ADVANCES IN POWER-TO-X: PROCESSES, SYSTEMS, AND DEPLOYMENT

EDITED BY: Valerie Eveloy, Luis M. Romeo, David Parra and Meysam Qadrdan

PUBLISHED IN: Frontiers in Energy Research

frontiers Research Topics

ISSN 1664-8714
ISBN 978-2-88966-859-5
DOI 10.3389/978-2-88966-859-5

About Frontiers

Frontiers is more than just an open-access publisher of scholarly articles: it is a pioneering approach to the world of academia, radically improving the way scholarly research is managed. The grand vision of Frontiers is a world where all people have an equal opportunity to seek, share and generate knowledge. Frontiers provides immediate and permanent online open access to all its publications, but this alone is not enough to realize our grand goals.

Frontiers Journal Series

The Frontiers Journal Series is a multi-tier and interdisciplinary set of open-access, online journals, promising a paradigm shift from the current review, selection and dissemination processes in academic publishing. All Frontiers journals are driven by researchers for researchers; therefore, they constitute a service to the scholarly community. At the same time, the Frontiers Journal Series operates on a revolutionary invention, the tiered publishing system, initially addressing specific communities of scholars, and gradually climbing up to broader public understanding, thus serving the interests of the lay society, too.

Dedication to Quality

Each Frontiers article is a landmark of the highest quality, thanks to genuinely collaborative interactions between authors and review editors, who include some of the world's best academicians. Research must be certified by peers before entering a stream of knowledge that may eventually reach the public - and shape society; therefore, Frontiers only applies the most rigorous and unbiased reviews.
Frontiers revolutionizes research publishing by freely delivering the most outstanding research, evaluated with no bias from both the academic and social point of view. By applying the most advanced information technologies, Frontiers is catapulting scholarly publishing into a new generation.

What are Frontiers Research Topics?

Frontiers Research Topics are very popular trademarks of the Frontiers Journals Series: they are collections of at least ten articles, all centered on a particular subject. With their unique mix of varied contributions from Original Research to Review Articles, Frontiers Research Topics unify the most influential researchers, the latest key findings and historical advances in a hot research area! Find out more on how to host your own Frontiers Research Topic or contribute to one as an author by contacting the Frontiers Editorial Office: frontiersin.org/about/contact

ADVANCES IN POWER-TO-X: PROCESSES, SYSTEMS, AND DEPLOYMENT

Topic Editors:
Valerie Eveloy, Khalifa University, United Arab Emirates
Luis M. Romeo, University of Zaragoza, Spain
David Parra, Université de Genève, Switzerland
Meysam Qadrdan, Cardiff University, United Kingdom

Citation: Eveloy, V., Romeo, L. M., Parra, D., Qadrdan, M., eds. (2021). Advances in Power-to-X: Processes, Systems, and Deployment. Lausanne: Frontiers Media SA. doi: 10.3389/978-2-88966-859-5

Table of Contents

frontiers in Energy Research

EDITORIAL
published: 13 April 2021
doi: 10.3389/fenrg.2021.650510

Editorial: Advances in Power-to-X: Processes, Systems, and Deployment

Valerie Eveloy[1]*, *Luis M. Romeo*[2]*, *David Parra*[3]* and *Meysam Qadrdan*[4]*

[1]Department of Mechanical Engineering, Khalifa University, Abu Dhabi, United Arab Emirates, [2]Department of Mechanical Engineering, University of Zaragoza, Zaragoza, Spain, [3]Energy Efficiency Group, Institute for Environmental Sciences and Forel Institute, University of Geneva, Genève, Switzerland, [4]School of Engineering, Cardiff University, Cardiff, United Kingdom

Keywords: power-to-X (PtX), power-to-gas (PtG), hydrogen, renewable energy, energy storage, CO_2 utilization, electrolysis, methanation

Editorial on the Research Topic

Advances in Power-to-X: Processes, Systems, and Deployment

INTRODUCTION

The storage of surplus electricity is critical to facilitate the large-scale integration of intermittent renewable technologies into energy systems. In this regard, power-to-X (PtX) technologies are a promising approach to convert and store excess renewable electricity in the form of synthetic fuels, chemicals, and other energy carriers, and to contribute decarbonizing difficult-to-abate sectors such as heavy/long-distance transport and industry (Lund et al., 2015). However, further development of PtX technologies faces sizeable challenges, including process efficiency limitations, limited availability of affordable (*quasi*) carbon-neutral carbon dioxide (CO_2) sources for hydrogenation, and economic aspects (Eveloy, 2019). Such challenges need to be overcome for PtX products to compete economically and in terms of environmental impact with conventional and other alternative energy vectors.

This Frontiers in Energy Research special issue seeks to present recent advancements, and identify challenges and future research needs in the area of PtX. The collection brings together nine research, review, and perspective articles contributed by researchers from academia, government, and industry based in Europe, Australia, and the United States. The topics of these articles are categorized herein into three areas, namely, PtX processes (4 articles), systems (3 articles), and deployment (2 articles).

PTX PROCESSES

The identification of optimum PtX energy vectors and synthesis pathways for a given application, based on technical and economic considerations, is being extensively pursued (Rego de Vasconcelos and Lavoie, 2019). In terms of energy carriers, hydrogen and methane produced using power-to-gas processes (Götz et al., 2016) have been the most widely investigated to date. Despite the need for additional process steps, equipment, and conversion losses relative to hydrogen, synthetic methane would be more readily supported by existing large-scale gas infrastructure (Lehner et al., 2014) than either pure or blended hydrogen, depending on blending regulations. A sustainable and affordable source of CO_2 is however required (Schiebahn et al., 2015). Although synthetic methane could provide a suitable source of CO_2, the direct use of biogas in power-to-methane processes without CO_2 separation from biogas could reduce process complexity, greenhouse gas (GHG) emissions, and cost, subject to biogas availability. Focusing on the direct use of biogas in power-to-methane

OPEN ACCESS

Edited and reviewed by:
Yulong Ding,
University of Birmingham,
United Kingdom

***Correspondence:**
Valerie Eveloy
valerie.eveloy@ku.ac.ae
Luis M. Romeo
luismi@unizar.es
David Parra
david.parra@unige.ch
Meysam Qadrdan
qadrdanm@cardiff.ac.uk

Specialty section:
This article was submitted to Process and Energy Systems Engineering, a section of the journal Frontiers in Energy Research

Received: *07 January 2021*
Accepted: *05 February 2021*
Published: *13 April 2021*

Citation:
Eveloy V, Romeo LM, Parra D and Qadrdan M (2021) Editorial: Advances in Power-to-X: Processes, Systems, and Deployment. Front. Energy Res. 9:650510. doi: 10.3389/fenrg.2021.650510

processes, Calbry-Muzyka and Schildhauer reviewed key challenges associated with the treatment of biogas impurities, and discussed both competing methanation reactor and final upgrading process concepts at a high technology readiness level recently demonstrated at relevant scales. A potential alternative direction to reduce the number of methane synthesis process steps, equipment size, GHG emissions, and cost is based on one-step, *in situ* solid oxide cell steam and CO_2 co-electrolysis. Focusing on such processes, Biswas et al. reviewed recent advancements and challenges in solid oxide cell materials, design, and optimized operating conditions. Ultimately, to effectively and comprehensively evaluate the potential of PtX technologies to contribute to meeting emission reduction targets, life cycle assessments are required (Sternberg and Bardow, 2015; Wevers et al., 2020). Schreiber et al. presented a life cycle assessment of high-temperature co-electrolysis–based power-to-syngas in the context of German Climate Action Plan 2050 energy scenarios. Generalizing the PtX concept (Bailera et al., 2017), solar-powered semiconductor-based artificial photosynthesis is another category of processes having the potential to reduce the complexity and increase the efficiency of water and/or CO_2 conversion processes to produce hydrogen, methane, syngas, liquid fuels (e.g., methanol), and chemicals (e.g., ammonia and formic acid). Mi and Sick provided a perspective on recent developments and techno-economic prospects of three major such process paths, namely, photocatalytic, photoelectrochemical, and photovoltaic-electrolysis, in terms of efficiency, stability and cost, and candidate promising semiconductor light absorber materials and catalysts.

PTX SYSTEMS

The design, evaluation, and optimization of PtX systems involve efforts at the prototype to plant or facility level, using a combination of experimentation and modeling. At the PtX prototype element level, Barton et al. experimentally characterized and modeled the dynamic performance of a novel nickel–iron battery-electrolyzer or "battolyser" prototype cell intended for both short-term (as a battery) and long-term energy storage (as an electrolyzer), either in remote mini-grid or national energy system applications. At the prototype level, bioelectrochemical power-to-methane reactors may offer a low-energy, single-step methanation route (i.e., without the need for preliminary hydrogen production) with simultaneous wastewater treatment. Molognoni et al. experimentally investigated the long-term performance of such a prototype reactor integrating CO_2 capture in wastewater *via* membrane contactors. At the facility level, combined cycle power plants in future renewable-dominated energy systems are expected to mainly serve as flexible regulating generators, the efficiency and economics of which could be adversely affected by low capacity/load utilization (Song et al., 2020). Bailera et al. investigated the use of power-to-methane under a range of combined cycle power plant start-up scenarios to virtually reduce plant minimum complaint load, hence augmenting electricity revenues and reducing specific CO_2 emissions.

PTX DEPLOYMENT

PtX techno-economic deployment studies and demonstration projects are critical to identify optimum plant configurations and their integration into energy systems, including supporting appropriate market structures and regulatory frameworks (Bailera et al., 2017; Eveloy and Gebreegziabher, 2018). The strategic role, cost, and value creation of PtX applications require to be carefully assessed to enable effective deployment strategies (Parra et al., 2019). Wulf et al. reviewed 220 PtX demonstration projects in Europe, in terms of commissioning time, location, capacity, electricity/CO_2 sources, electrolysis, and hydrogen post-processing technologies, and targeted PtX product applications, leading to recommendations on future PtX project strategies. Focusing on the management of wind generation in the 2030 Great Britain energy system, Ameli et al. evaluated an integrated, optimized approach to operate gas and electricity systems assisted with power-to-gas and other flexibility technologies, to reduce annual operating cost and GHG emissions, and improve the security of gas supply.

OUTLOOK

This Research Topic collection advances our understanding on the emerging and important role that PtX technologies are likely to play in future energy systems, as well as on challenges and future research needs in these areas. The further development of PtX technologies will ultimately depend on the level of decarbonization and renewable energy penetration in energy systems. Diversity in processes, products, and applications is essential to optimize the use of local resources in meeting local, national, and global energy/feedstock demands, while minimizing deployment risks. The Guest Editors hope that the readers of this collection will find the research presented informative and useful in pursuing their own research and development activities in the areas of PtX and sustainable energy systems.

AUTHOR CONTRIBUTIONS

VE wrote the initial editorial draft. LM, DP, and MQ critically reviewed the initial editorial draft.

ACKNOWLEDGMENTS

The guest editors express their gratitude to Frontiers in Energy Research editor in chief, section editors, and associate editor for their support and constructive feedback. The guest editors also thank all reviewers for their time and highly appreciated contributions in peer reviewing the authors' work. The guest editors especially thank the Review and Editorial Teams of Frontiers in Energy Research for their excellent support.

REFERENCES

Bailera, M., Lisbona, P., Romeo, L. M., and Espatolero, S. (2017). Power to gas projects review: lab, pilot and demo plants for storing renewable energy and CO_2. *Renew. Sustain. Energ. Rev.* 69, 292–312. doi:10.1016/j.rser.2016.11.130

Eveloy, V., and Gebreegziabher, T. (2018). A review of projected power-to-gas deployment scenarios. *Energies* 11 (7), 1824. doi:10.3390/en11071824

Eveloy, V. (2019). Hybridization of solid oxide electrolysis-based power-to-methane with oxyfuel combustion and carbon dioxide utilization for energy storage. *Renew. Sust. Energ. Rev.* 108, 550–571. doi:10.1016/j.rser.2019.02.027

Götz, M., Lefebvre, J., Mörs, F., McDaniel Koch, A., Graf, F., Bajohr, S, Reimert, R, and Kolb, T (2016). Renewable power-to-gas: a technological and economic review. *Renew. Energ.* 85, 1371–1390. doi:10.1016/j.renene.2015.07.066

Lehner, M., Tichler, R., Steinmüller, H., and Koppe, M. (2014). *Power-to-Gas: technology and business models*, Vol. 39. Berlin, Germany: Springer. doi:10.1007/978-3-319-03995-4

Lund, P. D., Lindgren, J., Mikkola, J., and Salpakari, J. (2015). Review of energy system flexibility measures to enable high levels of variable renewable electricity. *Renew. Sustain. Energ. Rev.* 45, 785–807. doi:10.1016/j.rser.2015.01.057

Parra, D., Valverde, L., Javier Pino, F., and Patel, M. K. (2019). A review on the role, cost and value of hydrogen energy systems for deep decarbonisation. *Renew. Sustain. Energ. Rev.* 101, 279–294. doi:10.1016/j.rser.2018.11.010

Rego de Vasconcelos, B., and Lavoie, J.-M. (2019). Recent advances in power-to-X technology for the production of fuels and chemicals. *Front. Chem.* 7, 392. doi:10.3389/fchem.2019.00392

Schiebahn, S., Grube, T., Robinius, M., Tietze, V., Kumar, B., and Stolten, D. (2015). Power to gas: technological overview, systems analysis and economic assessment for a case study in Germany. *Int. J. Hydrog. Energ.* 40, 4285–4294. doi:10.1016/j.ijhydene.2015.01.123

Song, X., Lin, C., Zhang, R., Jiang, T., and Chen, H. (2020). Two-stage stochastic scheduling of integrated electricity and natural gas systems considering ramping costs with power-to-gas storage and wind power. *Front. Energy Res.* 8:596774. doi:10.3389/fenrg.2020.596774

Sternberg, A., and Bardow, A. (2015). Power-to-What? - environmental assessment of energy storage systems. *Energy Environ. Sci.* 8, 389–400. doi:10.1039/c4ee03051f

Wevers, JB., Shen, L., and van der Spek, M. (2020). What Does It Take to Go Net-Zero-CO_2? A life cycle assessment on long-term storage of intermittent renewables with chemical energy carriers. *Front. Energy Res.* 8:104. doi:10.3389/fenrg.2020.00104

Conflict of Interest: The authors declare that the research was conducted in the absence of any commercial or financial relationships that could be construed as a potential conflict of interest.

frontiers in Energy Research

ORIGINAL RESEARCH
published: 07 July 2020
doi: 10.3389/fenrg.2020.00120

Coordinated Operation of Gas and Electricity Systems for Flexibility Study

Hossein Ameli[1]*, *Meysam Qadrdan*[2] *and Goran Strbac*[1]

[1] Control and Power Group, Imperial College, London, United Kingdom, [2] Institute of Energy, Cardiff University, Cardiff, United Kingdom

The increased interdependencies between electricity and gas systems driven by gas-fired power plants and gas electricity-driven compressors necessitates detailed investigation of such interdependencies, especially in the context of an increased share of renewable energy sources. In this paper, the value of an integrated approach for operating gas and electricity systems is assessed. An outer approximation with equality relaxation (OA/ER) method is used to deal with the optimization class of the mixed-integer non-linear problem of the integrated operation of gas and electricity systems. This method significantly improved the efficiency of the solution algorithm and achieved a nearly 40% reduction in computation time compared to successive linear programming. The value of flexibility technologies, including flexible gas compressors, demand-side response, battery storage, and power-to-gas, is quantified in the operation of integrated gas and electricity systems in GB 2030 energy scenarios for different renewable generation penetration levels. The modeling demonstrates that the flexibility options will enable significant cost savings in the annual operational costs of gas and electricity systems (up to 21%). On the other hand, the analysis carried out indicates that deployment of flexibility technologies appropriately supports the interaction between gas and electricity systems.

Keywords: integrated gas and electricity systems, operation, renewable generation variability, electricity and flexibilities, contingency

OPEN ACCESS

Edited by:
Francois M. A. Marechal, École Polytechnique Fédérale de Lausanne, Switzerland

Reviewed by:
Fabrizio Bezzo, University of Padova, Italy
Denny K. S. Ng, Heriot-Watt University Malaysia, Malaysia

***Correspondence:**
Hossein Ameli
h.ameli14@imperial.ac.uk

Specialty section:
This article was submitted to Process and Energy Systems Engineering, a section of the journal Frontiers in Energy Research

Received: *11 November 2019*
Accepted: *19 May 2020*
Published: *07 July 2020*

Citation:
Ameli H, Qadrdan M and Strbac G (2020) Coordinated Operation of Gas and Electricity Systems for Flexibility Study. Front. Energy Res. 8:120. doi: 10.3389/fenrg.2020.00120

1. INTRODUCTION

The share of variable Renewable Energy Sources (RES) in the power generation mix is increasing significantly in Great Britain (GB) to meet de-carbonization targets (National Grid Plc, 2016). Gas plants are expected to contribute to the management of the variability of renewable energy generation, which consequently will increase the interaction between gas and electricity systems and increase challenges associated with the management of gas storage and linepack in the gas transmission system. Therefore, operating the gas and electricity systems as an integrated energy system is increasingly important.

Battery storage, Demand-Side Response (DSR), power-to-gas (P2G), and flexible compressors can enhance the system flexibility needed to support more cost-effective balancing of electricity demand and supply. Furthermore, these options can participate in the provision of various ancillary services, including reserve and frequency regulation (Qadrdan et al., 2017b). Battery storage facilitates the integration of wind into the grid through managing variation of the peak plants,

such as gas-fired plants. The employment of DSR helps to deal with the variability of RES better, as energy consumption can be shifted, which can act as a virtual power plant (Ameli et al., 2017a,b). Furthermore, P2G technologies would make use of a surplus of renewable electricity by producing hydrogen via electrolyzers that would be injected into the gas system or stored in hydrogen storage facilities. Afterward, the hydrogen can be transported to the demand centers or provided to Combined Cycle Gas Turbines (CCGTs) to produce free-carbon electricity. In the gas system, flexible gas compressors improve gas delivery to the demand centers through changing the gas flow direction. Several studies, such as Troy et al. (2012) and Pudjianto et al. (2014), have evaluated the role of flexibility options in addressing the electricity balancing challenges caused by RES.

From whole energy system perspectives, by taking flexibilities into account, the interaction of gas and electricity systems was studied in Correa-Posada and Sanchez-Martin (2015), He et al. (2017), Zlotnik et al. (2017), Qadrdan et al. (2017a), Ameli et al. (2017c,d), and Wu et al. (2019). Zlotnik et al. (2017) developed coordinated modeling of interdependent gas and electricity systems for day-ahead scheduling of power dispatch and gas compressor operation. The efficiency of the model was validated by improvement in system operation and cost reduction. In Ameli et al. (2017d), the role of multi-directional compressors as one of the options in making the gas system more flexible was investigated in different operation methodologies of gas and electricity systems. It was demonstrated that increased flexibility in the gas system is beneficial for the whole energy system. In Sheikhi et al. (2015), an integrated demand-side response framework as a part of a smart energy hub was proposed. In this framework, the customer can modify the use of gas or electricity based on the gas and electricity prices. It was shown that this approach offers benefits for both customers and utilities in terms of costs and profits. In Yang et al. (2019), the coordination of different P2G conversions, including electrolysis and Steam Methane Reforming (SMR), and gas-fired plants in an integrated operation of gas and electricity networks was proposed. It was shown how this combined model can improve energy efficiency and reduce carbon emissions compared to the power-to-hydrogen-to-methane-to-pipeline approach. From a modeling point of view, it was not mentioned in detail how this optimization problem may be solved. In He et al. (2017), coordinated scheduling of gas and electricity systems considering P2G was investigated. Furthermore, another study (Akhtari and Baneshi, 2019) showed how the excess electricity generated by renewables can be used in the electrolysis process to produce hydrogen. The proposed method was tested in five different cities, and a decrease in carbon emissions was reported. In Wu et al. (2019), a hybrid multi-objective optimization approach was developed for the operation of integrated energy systems considering gas and electricity. In this approach, the price of electricity and cooling demands are considered. The results indicated fair treatment for all the players in the integrated energy system. In Zeng et al. (2016), a bi-directional energy flow between gas and electricity systems was proposed to realize high penetration of renewables and an increase in system flexibility. The effectiveness of the proposed method (i.e., solved by the Newton-Raphson method) was analyzed on an IEEE-9 test system and a 7-node gas system. In Correa-Posada and Sanchez-Martin (2015), a coupled model of natural gas and power systems aimed at providing energy adequacy was presented. Non-linear equations and constraints were linearized to solve a Mixed-Integer Linear Programming (MILP) problem. A weak point of this study was that linearizing the non-linearities piecewise causes a significant increase in the probability of data loss. In Gil et al. (2016), two coupling methodologies for gas and electricity markets in a European regulatory framework were presented. The first methodology was based on maximizing the profit of the electricity market, and the second approach was based on minimizing the operational cost of the natural gas system. It was demonstrated that if the modeling is accurate, the difference between these two methodologies may be negligible. In addition, in Zlotnik et al. (2017), different coordinated scheduling scenarios of natural gas and power systems were presented. The Unit Commitment (UC) problem of the generation units was not considered. This was done in order to reduce the model complexity by preventing binary variables in the optimization procedure, which may lead to inaccuracy. The authors of Deane et al. (2017) built and applied an integrated electricity and gas model for the European Union system. In this research, gas supply interruption scenarios were derived to examine the impacts on power system operation. As an example, it was shown that interruption of the Russian gas supply to the EU enhanced the average gas price by 28% and the electricity price by 12%. In Sardou et al. (2018), the role of microgrid aggregators in a coordinated operation strategy for gas and electricity systems was investigated. In Zhang et al. (2016), the role of demand response in providing energy balance was considered. A coordinated MILP strategy for natural gas and power systems was proposed. In this strategy, the power system was optimized, and then the natural gas constraints were checked for the feasibility of the solution. It was shown that this model increased the social welfare of the scenarios. However, through linearizing the gas flow equation piecewise, the complexity of the model is reduced, and accuracy may be lost. In the literature, different methods have been applied to linearize the general gas flow and propose a MILP formulation for the operation of a gas network (Correa-Posadaa and Sanchez-Martin, 2014; He et al., 2017; HU et al., 2017; Sirvent et al., 2017). Although piecewise linearization affects the time required to solve the problem considerably, the accuracy of each method (i.e., ability to find the optimal solution) significantly relies on the generating segments. On the other hand, some methods are not scalable and can only be used for a problem of a predetermined size (Correa-Posadaa and Sanchez-Martin, 2014).

The coupling of the binary variables representing the On/Off states of generating units and non-linear equations of gas flow in pipes and compressor power consumption makes the optimization of the integrated operation of gas and electricity systems a Mixed-Integer Non-Linear Programming (MINLP) problem, which is complex and challenging to

solve from the computational perspective (Floudas, 1995). In order to deal with the aforementioned complexity in solving the MINLP problem, several algorithms, such as Generalized Benders Decomposition (GBD), Outer Approximation (OA), Outer Approximation with Equality Relaxation (OA/ER), and generalized cross decomposition, have been developed (Floudas, 1995). Deterministic methods, such as Lagrangian Relaxation (LR) (Ongsakul and Petcharaks, 2004) and Benders Decomposition (BD) (Nasri et al., 2016), and also heuristic methods, such as an evolutionary algorithm (Chung et al., 2011) have been applied to solve MINLP problems in power systems. In Shabanpour-Haghighi and Seifi (2015), a solving technique based on a modified teaching–learning method for optimal power flow taking electricity, gas, and heat into account was proposed. This method was evaluated and compared with conventional evolutionary algorithms to highlight the effectiveness of the method. In He et al. (2017), co-optimization scheduling of gas and electricity systems was proposed. A decomposition method was applied to solve the electricity system sub-problem and gas system sub-problem separately.

The OA approach, which is the fundamental technique in this study, has been implemented in a few studies for dealing with the Unit Commitment (UC) problem (Yang et al., 2017) with AC power flow (Castillo et al., 2016) as well as security-constrained UC (Dai et al., 2016). The OA/ER decomposition method solves a binary relaxed primal problem [Non-Linear Problem (NLP)] and a relaxed master problem (MILP). The OA/ER decomposition method copes with non-linear inequalities and consequently creates sequences of lower and upper bounds. In the OA/ER approach, the non-linear equalities are converted to linear inequalities based on their associated Lagrangian multipliers. It is worth mentioning that the integrated operation of gas and electricity systems is solved by Successive Linear Programming (SLP) (Default solver of Xpress FICO, 2013) and investigated from different aspects in a few papers, such as Qadrdan et al. (2017a) and Ameli et al. (2017d). The MINLP problem of integrated operation of gas and electricity is non-convex, which implies the potential existence of multiple local optima.

Hence, in this paper, in order to deal with the complexity of the above-mentioned model, a solution algorithm is implemented based on the OA/ER approach to model the integrated operation of gas and electricity systems. The efficiency of this decomposition method is validated by comparing the computational performance in terms of optimization time and objective function with the SLP method. Furthermore, the role and value of the flexibility options, including DSR, electricity storage, flexible gas plants, P2G, and multi-directional compressors, in the cost-effective operation of the integrated systems for intact and contingency configurations (i.e., gas supply interruption) on a 2030 GB system are investigated. In this regard, to evaluate the sensitivity of the renewable penetration level to the flexibility options, different renewable generation and gas supply development scenarios in the presence of different installed capacities of flexibility options are defined to quantify the operation of the energy systems. To model the entire year, a demand clustering method is developed to reduce the size of the optimization problem, so that, through this method, the entire year is represented by 12 days.

2. GAS AND ELECTRICITY SYSTEMS INCLUDING A FLEXIBILITY OPERATIONAL MODEL

2.1. Formulation of Electricity System Operation

The constraints governing the electricity system over the time horizon ($t \in \mathcal{T}$) are represented by equations (1)–(11). These constraints include: minimum and maximum power generation limits for generators (1), Minimum Stable Generation (MSG) for thermal generators (2), maximum limit for power generation and provision of reserve by thermal generators (3), Minimum Up/Down Time (MUT/MDT) of generators (4)–(5), ramp up/down limits of generators (6), start-up cost of generators (7) (8), minimum reserve requirement (including the unserved reserve) (9) (Ameli et al., 2019), capacity of power transmission lines (10), and power balance at each time step (11).

$$\mathrm{P}_i^{\min} \le P_{i,t} \le \mathrm{P}_i^{\max},\ \forall i \in \mathcal{G} - \mathcal{K}, t \in \mathcal{T} \tag{1}$$

$$P_{i,t} \ge \sigma_{i,t} \cdot \mathrm{P}_i^{\min},\ \forall i \in \mathcal{K}, t \in \mathcal{T} \tag{2}$$

$$P_{i,t} + r_{i,t} \le \sigma_{i,t} \cdot \mathrm{P}_i^{\max},\ \forall i \in \mathcal{K}, t \in \mathcal{T} \tag{3}$$

$$\sigma_{i,\acute{t}} - \sigma_{i,\acute{t}-1} \le \sigma_{i,t};\ \acute{t} = [t - \Gamma_i^{\mathrm{up}} + 1, t-1],\ \forall i \in \mathcal{K}, t \in \mathcal{T} \tag{4}$$

$$\sigma_{i,\acute{t}-1} - \sigma_{i,\acute{t}} \le 1 - \sigma_{\mathrm{i,t}};\ \acute{t} = [t - \Gamma_i^{\mathrm{down}} + 1, t-1],\ \forall i \in \mathcal{K}, t \in \mathcal{T} \tag{5}$$

$$\left|P_{i,t} - P_{i,t-1}\right| \le \mu_i,\ \forall i \in \mathcal{K}, t \in \mathcal{T} \tag{6}$$

$$w_{i,t}^{\mathrm{su}} \ge \mathrm{C}_i^{\mathrm{su}} \cdot (\sigma_{i,t} - \sigma_{i,t-1}),\ \forall i \in \mathcal{K}, t \in \mathcal{T} \tag{7}$$

$$w_{i,t}^{\mathrm{su}} \ge 0,\ \forall i \in \mathcal{K}, t \in \mathcal{T} \tag{8}$$

$$\sum_{i=1}^{\mathcal{K}} r_{i,t} + \sum_{p=1}^{\mathcal{P}} r_{p,t}^{\mathrm{pump}} + ur_t \ge \max_{i \in \mathcal{K}} \left(\mathrm{P}_i^{\max}\right) + \alpha \cdot \sum_{b=1}^{\mathcal{B}} P_{b,t}^{\mathrm{wind}},\ \forall t \in \mathcal{T} \tag{9}$$

$$P_{x,t}^{\mathrm{line}} \le \mathrm{P}_x^{\mathrm{line,max}},\ \forall x \in \mathcal{L}_e, t \in \mathcal{T} \tag{10}$$

$$\sum_{i=1}^{\mathcal{G}} P_{i,t} + \sum_{b=1}^{\mathcal{B}} P_{b,t}^{\mathrm{wind}} + \sum_{p=1}^{\mathcal{P}} \left(P_{p,t}^{\mathrm{pump,with}} - P_{p,t}^{\mathrm{pump,inj}}\right) = \sum_{b=1}^{\mathcal{B}} \left(\mathrm{P}_{b,t}^{\mathrm{eload}} + P_{b,t}^{\mathrm{ecomp}} - P_{b,t}^{\mathrm{eshed}}\right),\ \forall t \in \mathcal{T} \tag{11}$$

where

$\mathcal{B}$	set of Busbars
$\mathcal{G}$	set of generation units
$\mathcal{K}$	set of thermal generation units
$\mathcal{L}_e$	set of electricity transmission lines
$\mathcal{P}$	set of pump-storage units
$\mathcal{T}$	time horizon
$\mathrm{P}_x^{\mathrm{line,max}}$	maximum capacity of line x (MW)
$\mathrm{P}_i^{\min}$	minimum power of generation unit i (MW)

$\mathrm{P}_i^{\max}$ maximum power of generation unit i (MW)

$P_{i,t}$ power output of generation unit i at time t (MW)

$P_{b,t}^{\text{ecomp}}$ power consumption of electrically driven compressors at busbar b and time t (MW)

$\mathrm{P}_{b,t}^{\text{eload}}$ electrical power demand at busbar b and time t (MW)

$P_{b,t}^{\text{eshed}}$ electrical load shedding at busbar b and time t (MW)

$P_{x,t}^{\text{line}}$ power flow of line x and time t (MW)

$P_{p,t}^{\text{pump,with}}$ power withdrawal of pump storage p to the grid at time t (MW)

$P_{p,t}^{\text{pump,inj}}$ power injection to pump storage p from the grid at time t (MW)

$P_{b,t}^{\text{wind}}$ wind power feed to the grid at busbar b and time t (MW)

$r_{i,t}$ reserve provided through generation unit i at time t (MW)

$r_{p,t}^{\text{pump}}$ reserve provided through pump unit p at time t (MW)

ur_t unserved reserve at time t (MW)

$w_{i,t}^{\text{su}}$ start-up cost function of generation unit i at time t (£)

α proportion of wind for reserve requirements

Γ_i^{down} minimum up time of generation unit i (h)

Γ_i^{up} minimum down time of generation unit i (h)

μ_i maximum ramp up/down power of generation unit i (MW/h)

C_i^{su} start-up cost coefficient of generation unit i (£)

$\sigma_{i,t}$ On/Off state of generation unit i at time t (1/0)

2.2. Formulation of Gas System Operation

The operation of the gas system over the time horizon ($t \in \mathcal{T}$) is modeled via constraints for gas flow along a pipe (12) (Osiadacz, 1987) (detailed formulation is presented in Ameli et al., 2019), power consumption by the compressors (14), changes in the gas system linepack (15), minimum and maximum pressure limits (16), and gas balance at each node and time step (17). In order to model a bi-directional gas flow, in the gas flow equation in (12), the term $Q_{x,t}^{\text{avg}\,1.854}$ is replaced by $Q_{x,t}^{\text{avg}} \cdot |Q_{x,t}^{\text{avg}}|^{0.854}$ (13).

$$\left(p_{x,t}^{\text{in}}\right)^2 - \left(p_{x,t}^{\text{out}}\right)^2 = \frac{18.43\ \mathrm{Le}_x}{\left(\eta_x^{\text{pipe}}\right)^2 \cdot \mathrm{D}_x^{4.848}}\ Q_{x,t}^{\text{avg}\,1.854},\ \forall x \in \mathcal{L}_g \tag{12}$$

$$\left(p_{x,t}^{\text{in}}\right)^2 - \left(p_{x,t}^{\text{out}}\right)^2 = \frac{18.43\ \mathrm{Le}_x}{\left(\eta_x^{\text{pipe}}\right)^2 \cdot \mathrm{D}_x^{4.848}}\ Q_{x,t}^{\text{avg}} \cdot |Q_{x,t}^{\text{avg}}|^{0.854},\quad \forall x \in \mathcal{L}_g, t \in \mathcal{T} \tag{13}$$

$$P_{x,t}^{\text{comp}} = \frac{\beta . Q_{x,t}^{\text{comp}}}{\eta^{\text{comp}}} . \left[\left(\frac{p_{x,t}^{\text{dis}}}{p_{x,t}^{\text{suc}}}\right)^{(1/\beta)} - 1\right],\ \forall x \in \mathcal{C}, t \in \mathcal{T} \tag{14}$$

$$L_{x,t} = L_{x,t-1} + \underbrace{\int_{t-1}^{t} \left(Q_{x,\tau-1}^{\text{in}} - Q_{x,\tau-1}^{\text{out}}\right) . d\tau}_{\partial L_{x,t}},\ \forall x \in \mathcal{L}_g, t \in \mathcal{T} \tag{15}$$

$$\mathrm{p}_x^{\min} \le p_{x,t} \le \mathrm{p}_x^{\max},\ \forall x \in \mathcal{M}, t \in \mathcal{T} \tag{16}$$

$$\begin{aligned} Q_{x,t}^{\text{supp}} &+ \left(\sum_{w=1}^{\mathcal{W}} \mathbf{M}_{w,x}^{\text{flow}} \cdot Q_{w,t}\right) + \left(Q_{x,t}^{\text{gstor,with}} - Q_{x,t}^{\text{gstor,inj}}\right) \\ &+ \left(\sum_{c=1}^{\mathcal{C}} \mathbf{M}_{c,x}^{\text{comp}} \cdot Q_{c,t}^{\text{comp}} - \sum_{c=1}^{\mathcal{C}-\mathcal{C}_e} \mathbf{M}_{c,x}^{\text{ecomp}} \cdot \zeta_{c,t}\right) \\ &= \left(\mathrm{Q}_{x,t}^{\text{gload}} + Q_{x,t}^{\text{gen}} - Q_{x,t}^{\text{gshed}}\right),\ \forall x \in \mathcal{M}, t \in \mathcal{T} \end{aligned} \tag{17}$$

where

$\mathcal{C}$ set of compressor nodes

$\mathcal{C}_e$ set of electrically driven compressors

$\mathcal{L}_g$ set of gas pipelines

$\mathcal{M}$ set of nodes

$\mathcal{W}$ set of flows

D_x diameter of the pipe x (mm)

$\mathbf{M}_{c,x}^{\text{comp}}$ compressor-node incident matrix of compressor c and node x

$\mathbf{M}_{c,x}^{\text{ecomp}}$ electrical compressor-node incident matrix of compressor c and node x

$\mathbf{M}_{w,x}^{\text{flow}}$ flow-node incident matrix of flow w and node x

$L_{x,t}$ linepack within pipeline x at time t (m^3)

Le_x length of pipe x (m)

$\mathrm{p}_x^{\max}$ upper bound of pressure at node x (Pascal)

$\mathrm{p}_x^{\min}$ lower bound of pressure at node x (Pascal)

$p_{x,t}$ pressure at node x and time t (Pascal)

$P_{c,t}^{\text{comp}}$ consumption power of compressor at node c and time t (MW)

$p_{c,t}^{\text{dis}}$ discharge pressure of compressor at node c and time t (Pascal)

$p_{x,t}^{\text{in}}$ pressure at in-take of pipeline x at time t (Pascal)

$p_{x,t}^{\text{out}}$ pressure at off-take of pipeline x at time t (Pascal)

$p_{c,t}^{\text{suc}}$ suction pressure of compressor at node c and time t (Pascal)

$Q_{w,t}$ volumetric gas flow w at time t (m^3/h)

$Q_{x,t}^{\text{avg}}$ average gas flow through pipeline x at time t (m^3/h)

$Q_{c,t}^{\text{comp}}$ gas flow through compressor at node c and time t (m^3/h)

$Q_{x,t}^{\text{in}}$ gas flow rate into pipeline x at time t (m^3/h)

$Q_{x,t}^{\text{gen}}$ required gas flow for power generation at node x and time t (m^3/h)

$Q_{x,t}^{\text{gload}}$ gas demand at node x and time t (m^3/h)

$Q_{x,t}^{\text{gstor,inj}}$ injected gas to storage facility at node x and time t (m^3/h)

$Q_{x,t}^{\text{gstor,with}}$ gas withdrawn from storage facility at node x and time t (m^3/h)

$Q_{x,t}^{\text{gshed}}$ gas load shedding at node x and time t (m^3/h)

$Q_{x,t}^{\text{out}}$ gas flow rate out of pipeline x at time t (m^3/h)

$Q_{x,t}^{\text{supp}}$ gas flow rate of terminal at node x and time t (m^3/h)

β polytropic exponent of a gas compressor (4.70 MJ/m^3)

η^{comp} efficiency of compressor units

η_x^{pipe} efficiency factor of pipe x (92%)

$\partial L_{x,t}$ changes in linepack at pipeline x and time t (m^3)

$\zeta_{c,t}$ amount of gas tapped by a compressor at node c and time t (m^3/h).

2.3. Coupling Components

The gas and electricity systems are coupled via gas-fired generators and electrically driven compressors. The electric power consumption of electrically driven compressors and the gas required for power generation are calculated by (14) and (18), respectively.

$$Q_{x,t}^{\text{gen}} = v_g \sum_{i=1}^{\mathcal{K}} \mathbf{M}_{x,i}^{\text{conn}} \cdot \frac{P_{i,t}}{\eta_i}, \ \forall x \in \mathcal{M}, t \in \mathcal{T} \tag{18}$$

where

$\mathbf{M}_{x,i}^{\text{conn}}$ node-generator incident matrix at node x and generation unit i

η_i efficiency of generation unit i

v_g energy conversion coefficient

2.4. Flexibility Options Modeling

2.4.1. Battery Storage

The operational characteristics of battery storage are modeled using equations (19)–(23) (Pudjianto et al., 2014; Ameli et al., 2020). A round trip efficiency of 80% is assumed for the battery storage. In this case, the reserve requirements and power balance equations of (9) and (11) are changed to (24) and (25), respectively. It is worth mentioning that, since the model is a least-cost optimization and attempts to minimize the cost, when an optimal solution is achieved, no simultaneous charge and discharge is happening.

$$E_{b,t}^{\text{estor}} = E_{b,t-1}^{\text{estor}} + \left(\eta^{\text{estor}}.P_{b,t}^{\text{estor,with}} - P_{b,t}^{\text{estor,inj}}\right) \cdot \text{ts}, \quad \forall b \in \mathcal{B}, t \in \mathcal{T} \tag{19}$$

$$P_{b,t}^{\text{estor,inj}} \le \text{P}_b^{\text{inj,max}}, \ \forall b \in \mathcal{B}, t \in \mathcal{T} \tag{20}$$

$$P_{b,t}^{\text{estor,with}} \le \text{P}_b^{\text{with,max}}, \ \forall b \in \mathcal{B}, t \in \mathcal{T} \tag{21}$$

$$E_{b,t}^{\text{estor}} \le \text{E}_b^{\text{max}}, \ \forall b \in \mathcal{B}, t \in \mathcal{T} \tag{22}$$

$$P_{b,t}^{\text{estor,inj}} \cdot \text{ts} \ + r_{b,t}^{\text{estor}} \cdot \text{ts} \le E_{b,t-1}^{\text{estor}}, \ \forall b \in \mathcal{B}, t \in \mathcal{T} \tag{23}$$

$$\sum_{i=1}^{\mathcal{K}} r_{i,t} + \sum_{i=1}^{\mathcal{P}} r_{i,t}^{\text{pump}} + \sum_{b=1}^{\mathcal{B}} r_{b,t}^{\text{estor}} + ur_t \ge \max_{i \in \mathcal{K}} \left(\text{P}_i^{\text{max}}\right) + \alpha \cdot \sum_{b=1}^{\mathcal{B}} P_{b,t}^{\text{wind}}, \ \forall t \in \mathcal{T} \tag{24}$$

$$\sum_{i=1}^{\mathcal{G}} P_{i,t} + \sum_{b=1}^{\mathcal{B}} P_{b,t}^{\text{wind}} + \sum_{i=1}^{\mathcal{P}} \left(P_{i,t}^{\text{pump,with}} - P_{i,t}^{\text{pump,inj}}\right) = \sum_{b=1}^{\mathcal{B}} \left(\text{P}_{b,t}^{\text{eload}} + P_{b,t}^{\text{ecomp}} - P_{b,t}^{\text{eshed}} - P_{b,t}^{\text{estor,with}} + P_{b,t}^{\text{estor,inj}}\right), \ \forall t \in \mathcal{T} \tag{25}$$

where

$E_{b,t}^{\text{estor}}$ energy level of electricity storage at busbar b and time t (MWh)

E_b^{max} maximum energy level of electricity storage at busbar b (MWh)

$P_{b,t}^{\text{estor,with}}$ power withdrawal of electricity storage to the grid at busbar b and time t (MW)

$P_{b,t}^{\text{estor,inj}}$ power injection to electricity storage from the grid at busbar b and time t (MW)

$\text{P}_b^{\text{max,with}}$ maximum power withdrawal of electricity storage to the grid at busbar b (MW)

$\text{P}_b^{\text{max,inj}}$ maximum power injection to electricity storage from the grid at busbar b (MW)

$r_{b,t}^{\text{estor}}$ reserve provided through electricity storage at busbar b and time t (MW)

η^{estor} round-trip efficiency of electricity storage.

2.4.2. Demand-Side Response (DSR)

A set of generic DSR constraints are implemented in the proposed model: the maximum amount of load that could be shifted (26), the change in load profile due to DSR (27), and temporal shifting of demand while considering potential losses (28) through the presented efficiency, as shifting demand could require an increase in overall energy consumption (Pudjianto et al., 2014). In the presence of DSR, (11) is replaced by (29).

$$P_{b,t}^{\text{dneg}} \le \psi \cdot \text{P}_{b,t}^{\text{eload}}, \ \forall b \in \mathcal{B}, t \in \mathcal{T} \tag{26}$$

$$P_{b,t}^{\text{dsr}} = \text{P}_{b,t}^{\text{eload}} - P_{b,t}^{\text{dneg}} + P_{b,t}^{\text{dpos}}, \ \forall b \in \mathcal{B}, t \in \mathcal{T} \tag{27}$$

$$\sum_{t=1}^{\mathcal{T}} P_{b,t}^{\text{dneg}} \leq \eta^{\text{dsr}} \cdot \sum_{t=1}^{\mathcal{T}} P_{b,t}^{\text{dpos}},\ \forall b \in \mathcal{B} \tag{28}$$

$$\sum_{i=1}^{\mathcal{G}} P_{i,t} + \sum_{b=1}^{\mathcal{B}} P_{b,t}^{\text{wind}} + \sum_{i=1}^{\mathcal{P}} \left(P_{i,t}^{\text{pump,with}} - P_{i,t}^{\text{pump,inj}}\right) = \sum_{b=1}^{\mathcal{B}} \left(P_{b,t}^{\text{dsr}} + P_{b,t}^{\text{ecomp}} - P_{b,t}^{\text{eshed}}\right),\ \forall t \in \mathcal{T} \tag{29}$$

where

$P_{b,t}^{\text{dneg}}$ reduction in electricity demand due to DSR at busbar b and time t (MW)

$P_{b,t}^{\text{dpos}}$ increase in electricity demand due to DSR at busbar b and time t (MW)

$P_{b,t}^{\text{dsr}}$ actual demand due to DSR at busbar b and time t (MW)

η^{dsr} DSR efficiency

ψ ratio of flexible electricity demand to total demand

2.4.3. Power-to-Gas (P2G)

Equations (30)–(32) describe the modeling of the P2G option with an efficiency of 70% (ITM Power, 2013). In (30), the energy content of hydrogen production by electrolyzer to its equivalent natural gas volume is presented. The amount of electricity used for hydrogen production is limited to the capacity of the electrolyzer (31). The amount of hydrogen that can be injected into the gas pipelines cannot exceed the maximum allowance (32). In this case, (11) and (17) are changed to (33) and (34), respectively.

$$P_{b,t}^{\text{e}\to\text{H}_2} \cdot \text{ts} = \nu \sum_{x=1}^{\mathcal{M}} \mathbf{M}_{b,x}^{\text{bus,node}} \cdot \eta^{\text{P2G}} \cdot Q_{x,t}^{\text{H}_2\to\text{g}},\ \forall b \in \mathcal{B}, t \in \mathcal{T} \tag{30}$$

$$P_{b,t}^{\text{e}\to\text{H}_2} \leq \text{P}_b^{\text{e}\to\text{H}_2\,\text{max}},\ \forall b \in \mathcal{B}, t \in \mathcal{T} \tag{31}$$

$$Q_{x,t}^{\text{H}_2\to\text{g}} \leq \Omega \cdot Q_{x,t}^{\text{available}},\ \forall x \in \mathcal{M}, t \in \mathcal{T} \tag{32}$$

$$\sum_{i=1}^{\mathcal{G}} P_{i,t} + \sum_{b=1}^{\mathcal{B}} P_{b,t}^{\text{wind}} + \sum_{i=1}^{\mathcal{P}} \left(P_{i,t}^{\text{pump,with}} - P_{i,t}^{\text{pump,inj}}\right) = \sum_{b=1}^{\mathcal{B}} \left(\text{P}_{b,t}^{\text{eload}} + P_{b,t}^{\text{ecomp}} - P_{b,t}^{\text{eshed}} + P_{b,t}^{\text{e}\to\text{H}_2}\right),\ \forall t \in \mathcal{T} \tag{33}$$

$$Q_{x,t}^{\text{supp}} + \left(\sum_{w=1}^{\mathcal{W}} \mathbf{M}_{w,x}^{\text{flow}} \cdot Q_{w,t}\right) + \left(Q_{x,t}^{\text{gstor,with}} - Q_{x,t}^{\text{gstor,inj}}\right) + \left(\sum_{c=1}^{\mathcal{C}} \mathbf{M}_{c,x}^{\text{comp}} \cdot Q_{c,t}^{\text{comp}} - \sum_{c=1}^{\mathcal{C}-\mathcal{C}_e} \mathbf{M}_{c,x}^{\text{ecomp}} \cdot \zeta_{c,t}\right) = \left(\text{Q}_{x,t}^{\text{gload}} + Q_{x,t}^{\text{gen}} - Q_{x,t}^{\text{gshed}}\right) - Q_{x,t}^{\text{H}_2\to\text{g}},\ \forall x \in \mathcal{M}, t \in \mathcal{T} \tag{34}$$

where

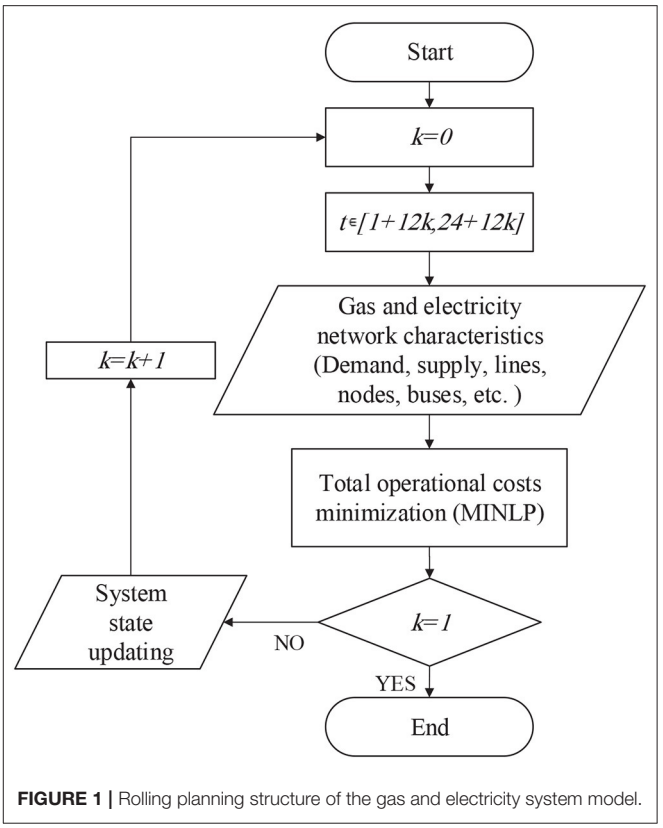

FIGURE 1 | Rolling planning structure of the gas and electricity system model.

$\mathbf{M}_{b,x}^{\text{bus.node}}$ bus-node incident matrix of busbar b and node x

$\text{P}_b^{\text{e}\to\text{H}_2\,\text{max}}$ maximum capacity of electrolyser at busbar b (MW)

$P_{b,t}^{\text{e}\to\text{H}_2}$ injected electric power to electrolyser at busbar b and time t (MW)

$Q_{x,t}^{\text{available}}$ available gas in node x and time t (mcm)

$Q_{x,t}^{\text{H}_2\to\text{g}}$ injected hydrogen from electrolyser to node x and time t (mcm)

η^{P2G} electrolyser efficiency

ν_{H_2} constant to convert energy content of hydrogen to its equivalent natural gas volume (90.9 m^3/MWh)

Ω maximum allowance of hydrogen injection to the natural gas system

2.4.4. Multi-Directional Compressors

Flexible multi-directional compressor stations can enhance flexibility and enable the gas system to deal with growing variability through optimally redirecting the gas flow. Detailed modeling of these units is presented in Ameli et al. (2017d).

3. MODELING METHODOLOGY

Figure 1 illustrates the structure of the model. The model minimizes the total operational cost of the gas and electricity systems, simultaneously. In the gas system, (a) cost of supply, (b)

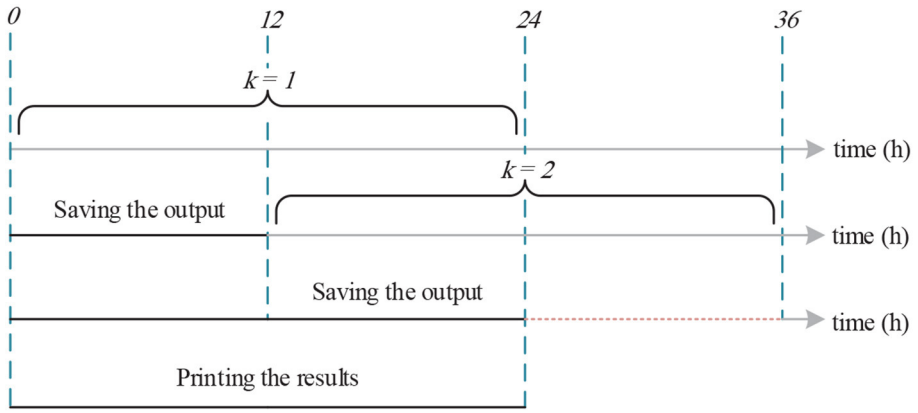

FIGURE 2 | Twelve-hours output saving strategy.

cost of unserved gas demand, and (c) cost of storage facilities and in the electricity system, (a) cost of power generation, (b) emission penalties, (c) unserved reserve, (d) cost of unserved electricity demand, and (e) start-up cost of the generators are taken into account (35).

$$Z = \sum_{t=1}^{\mathcal{T}} \left(\sum_{i=1}^{\mathcal{G}} \left(\mathrm{C}_i^{\mathrm{fuel}} + \mathrm{C}_i^{\mathrm{var}} \right) . P_{i,t} \cdot \mathrm{ts} + \sum_{i=1}^{\mathcal{K}} \mathrm{C}_i^{\mathrm{em}} . e_{i,t} + \left(\mathrm{C}^{\mathrm{ur}} . ur_t \cdot \mathrm{ts} \right) + \sum_{b=1}^{\mathcal{B}} \mathrm{C}^{\mathrm{eshed}} . P_{b,t}^{\mathrm{eshed}} \cdot \mathrm{ts} + \sum_{i=1}^{\mathcal{K}} w_{i,t}^{\mathrm{su}} + \sum_{x=1}^{\mathcal{Y}} \mathrm{C}^{\mathrm{gas}} . Q_{x,t}^{\mathrm{supp}} + \sum_{x=1}^{\mathcal{M}} \mathrm{C}^{\mathrm{gshed}} . Q_{x,t}^{\mathrm{gshed}} + \sum_{x=1}^{\mathcal{S}_g} \left(\mathrm{C}^{\mathrm{gstor,with}} . Q_{x,t}^{\mathrm{gstor,with}} - \mathrm{C}^{\mathrm{gstor,inj}} . Q_{x,t}^{\mathrm{gstor,inj}} \right) \right) \quad (35)$$

where

$\mathrm{C}_i^{\mathrm{fuel}}$	fuel cost of generation unit i (£/MW)
$\mathrm{C}_i^{\mathrm{var}}$	variable cost of generation unit i (£/MW)
$\mathrm{C}^{\mathrm{eshed}}$	cost of electrical load shedding (£/MW)
C^{em}	cost of produced GHG emissions of generation unit i (£/tons)
C^{gas}	cost of gas (£/mcm)
$C^{\mathrm{gstor,inj}}$	cost of gas injection to storage facilities (£/mcm)
$C^{\mathrm{gstor,with}}$	cost of gas withdrawal from storage facilities (£/mcm)
C^{gshed}	cost of gas load shedding (£/MW)
C^{ur}	cost of unserved reserve (£/MW)
$\mathcal{Y}$	set of gas terminal nodes
$\mathcal{S}_g$	set of gas storage facilities
Z	Objective function (£)

3.1. Temporal Structure of the Model

The operation of the gas and electricity systems is optimized using a day-ahead rolling planning approach. After solving the optimization problem for each iteration (i.e., 24 h), solutions representing the state of the system, e.g., On/Off states of the thermal generating units, linepack, and storage for the first 12 h of the iteration are saved (**Figure 2**). This is carried out in order to decrease the "end-of-optimization" effect and to model the storage facilities and unit commitment approach more realistically. Afterward, the solution of the state variables is used in time-dependent constraints when considering the following 24 h.

3.2. OA/ER Decomposition Method

The MINLP problem of the integrated operation of gas and electricity systems is solved using the OA/ER method. The structure of the OA/ER approach is presented in **Figure 3**. This structure represents the block "Total operational costs minimization" in **Figure 1**.

In each iteration, an upper bound and a lower bound of the objective function are generated to solve the MILNP problem. The upper bound is obtained from the primal problem, and the lower bound is obtained from the master problem. In the primal problem, the binary variables are fixed. The upper bound and the Lagrangian multipliers associated with the non-linear equality constraints are provided from the primal as input to the master problem. The master problem is derived through relaxing the non-linear equalities to linear inequalities via the use of the Lagrangian multipliers obtained in the primal problem. The master problem provides information about the lower bound and the updated values for binary variables that will be used in the next iteration of the primal problem. The lower bound and upper bound sequences converge as the iterations proceed. A detailed description of this approach is presented in Ameli et al. (2019).

For the sake of simplification, the sets of continuous variables and integer variables in the objective function of the electricity system are defined as:

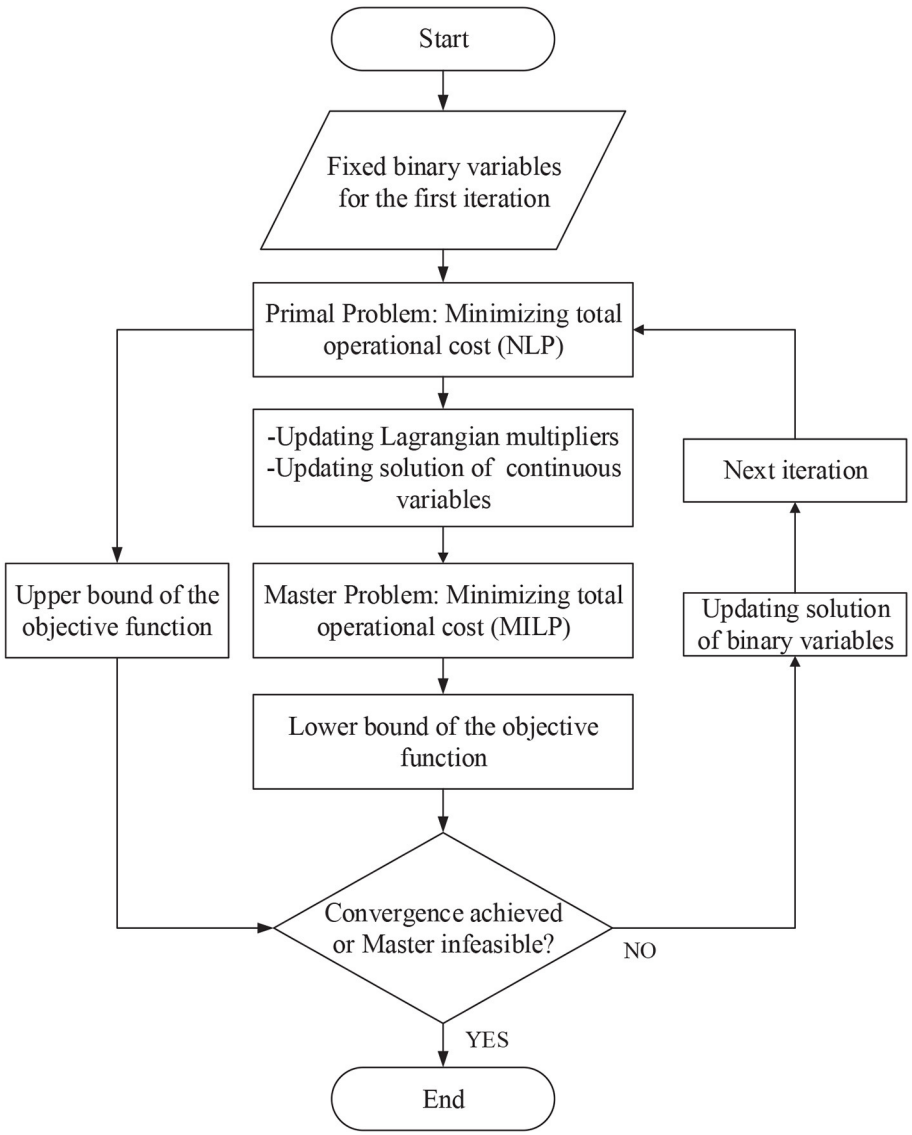

FIGURE 3 | Structure of OA/ER decomposition method.

$$\mathbf{X} = \left[P_{i,t},\, P^{\text{eshed}}_{b,t},\, e_{i,t},\, ur_t\right],\ \forall i \in \mathcal{G}, b \in \mathcal{B}, t \in \mathcal{T}$$
$$\mathbf{Y} = \left[w^{\text{su}}_{i,t}\right],\ \forall i \in \mathcal{K}, t \in \mathcal{T}.$$

the sets of variables in the objective function of the gas system are defined as:

$$\mathbf{U} = \left[Q^{\text{supp}}_{x,t},\, Q^{\text{gstorwith}}_{x,t},\, Q^{\text{gstorinj}}_{x,t},\, \partial L_{l,t},\, Q^{\text{gshed}}_{x,t}\right],$$
$$\forall x \in \mathcal{M}, l \in \mathcal{L}_g, t \in \mathcal{T}.$$

and the sets of variables in (12) and (14) are presented by:

$$\mathbf{S} = \left[p^{\text{in}}_{x,t},\, p^{\text{out}}_{x,t},\, Q^{\text{avg}}_{x,t}\right],\ \forall x \in \mathcal{L}_g, t \in \mathcal{T}$$
$$\mathbf{T} = \left[Q^{\text{comp}}_{x,t},\, p^{\text{dis}}_{x,t},\, p^{\text{suc}}_{x,t}\right],\ \forall x \in \mathcal{C}, t \in \mathcal{T}.$$

In this regard, in the objective function, $f(\mathbf{X})$ is representing the cost of the continuous variables in the electricity system, $g(\mathbf{Y})$ is representing the cost of the integer variables in the electricity system, $h(\mathbf{U})$ is representing the cost of the continuous variables in the gas system, $q(\mathbf{S})$ is representing the gas flow equation, and $r(\mathbf{T})$ is representing the compressor power consumption.

3.2.1. Primal Problem

In the primal problem, the binary variables of $w_{i,t}^{\mathrm{su}}$ are given as fixed values. Therefore, the MINLP function in (35) is converted to NLP (36). For the first iteration, initial values based on the optimization (using Xpress SLP solver FICO, 2013) described in Ameli et al. (2017d), were given as the values for $g(\mathbf{Y}^*)^{(1)}$. The * represents the values that are input to the problem. This selection of initial values makes the convergence process faster. For the next iteration of the primal problem, the fixed values of binary variables are provided subsequently by the master problem.

$$Z_{\mathrm{primal}}^{(\rho)} = f\left(\mathbf{X}^{(\rho)}\right) + h\left(\mathbf{U}^{(\rho)}\right) + g\left(\mathbf{Y}^{*(\rho)}\right), \forall \rho \in \mathcal{F} \tag{36}$$

where $\mathcal{F}$ is the total number iterations. At iteration ρ, if the primal problem is feasible, then information on the continuous variables in the gas system $h(\mathbf{U}^{*(\rho)})$ and in the electricity system $f(\mathbf{X}^{*(\rho)})$ is provided as input to the master problem. Additionally, the Lagrangian multipliers of the non-linear equations $\lambda_{q(\mathbf{S})}^{(\rho)}$ and $\lambda_{r(\mathbf{T})}^{(\rho)}$ are calculated and given as input to the master problem. If the primal problem is infeasible, a feasibility problem considering penalties would be solved to identify the feasible points.

The elements of the $\Phi_{q(\mathbf{S})}^{(\rho)}$ and $\Phi_{r(\mathbf{T})}^{(\rho)}$ matrices are presented in (37). These matrices provide information regarding the sign of the relaxed inequalities of the non-linear equations in the master problem.

$$\phi_{q(\mathbf{S})}^{(\rho)} = \left\{ \begin{array}{ll} -1 & \text{if} \quad \lambda_{q(\mathbf{S})}^{(\rho)} < 0 \\ +1 & \text{if} \quad \lambda_{q(\mathbf{S})}^{(\rho)} > 0 \\ 0 & \text{if} \quad \lambda_{q(\mathbf{S})}^{(\rho)} = 0 \end{array} \right\}$$

$$\text{and} \quad \phi_{r(\mathbf{T})}^{(\rho)} = \left\{ \begin{array}{ll} -1 & \text{if} \quad \lambda_{r(\mathbf{T})}^{(\rho)} < 0 \\ +1 & \text{if} \quad \lambda_{r(\mathbf{T})}^{(\rho)} > 0 \\ 0 & \text{if} \quad \lambda_{r(\mathbf{T})}^{(\rho)} = 0 \end{array} \right\} \tag{37}$$

3.2.2. Master Problem

The master problem formulation is presented by equations (38)-(43). In (38), the objective function of the master problem is presented. In (39), variable ξ is introduced to constrain the linearized objective function of the primal at the solution points of continuous variables. However, since the objective function is linear, it can be expressed as in (39).

$$Z_{\mathrm{master}}^{(\rho)} = g\left(\mathbf{Y}^{(\rho)}\right) + \xi, \forall \rho \in \mathcal{F} \tag{38}$$

$$\xi \geq f\left(\mathbf{X}^{*(\rho)}\right) + h\left(\mathbf{U}^{*(\rho)}\right), \forall \rho \in \mathcal{F} \tag{39}$$

The non-linear equalities of gas flow equation (12) and compressor power consumption (14) are relaxed to inequalities of (40) and (41), respectively.

$$\Phi_{q(\mathbf{S})}^{(\rho)} \cdot \left(q\left(\mathbf{S}^{*(\rho)}\right) + \left[\nabla q\left(\mathbf{S}^{*(\rho)}\right)\right] \cdot \left[\mathbf{S}^{(\rho)} - \mathbf{S}^{*(\rho)}\right]^T\right) \leq 0, \forall \rho \in \mathcal{F} \tag{40}$$

$$\Phi_{r(\mathbf{T})}^{(\rho)} \cdot \left(r\left(\mathbf{T}^{*(\rho)}\right) + \left[\nabla r\left(\mathbf{T}^{*(\rho)}\right)\right] \cdot \left[\mathbf{T}^{(\rho)} - \mathbf{T}^{*(\rho)}\right]^T\right) \leq 0, \forall \rho \in \mathcal{F} \tag{41}$$

In each iteration, the objective function of the master problem should be between the current objective function of the primal (upper bound) and the previous objective value of the master (lower bound) in order to proceed with convergence of the problem (42). The optimization is terminated when (43) is met or the master problem is infeasible, where ϵ is the convergence bound.

$$Z_{\mathrm{master}}^{(\rho-1)} \leq Z_{\mathrm{master}}^{(\rho)} \leq Z_{\mathrm{primal}}^{(\rho)}, \ \forall \rho \in \mathcal{F} \tag{42}$$

$$\left| Z_{\mathrm{master}}^{(\rho)} - Z_{\mathrm{primal}}^{(\rho)} \right| \leq \epsilon, \ \forall \rho \in \mathcal{F} \tag{43}$$

4. CASE STUDIES

The operation of a GB gas and electricity system with large penetration of wind generation is modeled for twelve representative days characterizing possible conditions for net electricity demand within the year in 2030.

The efficiency of the OA/ER decomposition method approach for solving the optimal operation problem of gas and electricity systems is assessed by comparing it to the commercial XPRESS SLP solver.

The efficacy of the flexibility options, namely (a) battery storage (*EStor*), (b) demand-side response (*DSR*), (c) Power-to-Gas (*P2G*), and (d) multi-directional compressors (*Multi*), to address electricity supply-demand balancing challenges is evaluated and compared to a reference (*Ref*) case in which no particular measure was considered to facilitate efficient integration of a large penetration of renewable generation.

TABLE 1 | Generation mix in GB 2030.

Generation technology	Capacity (GW)	Electricity cost (£/MWh)
Wind	47.3	–
Gas	33.7	2.2 + locational gas price
Solar	30.5	–
Interconnection	18.2	100
Nuclear	10.1	7
Pumped storage	4.8	variable
Coal	4.5	21.2
Biomass	3.8	70
Hydro	1.3	–
Other renewables	3.1	–
Other thermals	2	80

4.1. GB Gas and Electricity Systems

The power generation mix in this study is shown in **Table 1** and is based on the year 2030 of the "Gone Green" scenario of the National Grid (National Grid Plc, 2016). For gas-fired plants, variation in the cost of electricity production (2.2 /MWh) depending on the fuel price is taken into account.

The updated version of the GB 62-node National Transmission System (NTS) gas network (Qadrdan et al., 2010) and a 29-busbar electricity transmission system (Ameli et al., 2017d) are modeled. The data presented in Ameli et al. (2017d) are used as the base for hourly wind generation and non-electric gas demand in 2030. The gas demand for power generation is determined endogenously by (18). The electricity peak demand is assumed to be 85 GW, which is driven by the electrification of segments of the heat and transport sectors.

In the optimization problems of integrated operation of gas and electricity systems, about 43,000 variables including 3,500 binary variables are determined in each 24 h.

4.2. Demand Clustering Strategy

Due to the complexity of modeling the integrated operation of gas and electricity systems, it is computationally challenging to analyze the system for an entire year with an hourly time step (8,760 time steps in total). Instead, the net electricity demand profiles (i.e., renewable electricity generation deducted from electricity demand) for a number of characteristic days are selected, which represent the combination of electricity demand and renewable electricity generation. The clustering algorithm is presented in this section. At the beginning for each day, an equal weight of $\frac{1}{365}$ is considered. The net demand clustering algorithm is described as follows.

- **Step 1:** Calculating the distance between different net demand profiles through (44), where k is the counter.

$$\Delta_{i,j} = \sqrt{\sum_{t=1}^{\mathcal{T}} \left(P_{i,t}^{\text{net}} - P_{j,t}^{\text{net}}\right)^2}, \; k = \mathcal{N}_{\text{pr}}, \forall i,j \in \mathcal{H} \qquad (44)$$

- **Step 2:** Finding the two closest profiles.

$$\forall i,j \in \mathcal{H}: \;\; \Delta_{i^*,j^*} = \min_{i \neq j} \;\; \Delta_{i,j} \qquad (45)$$

- **Step 3:** Comparing the frequency of occurrence of the profiles in order to delete the profile with less frequency.
- **Step 4:** The frequency of the deleted profile is added to the closest profile, and $k = k - 1$.

$$\begin{aligned} \text{if } \varpi_{i^*} \geq \varpi_{j^*} \;\; &\rightarrow \;\; \text{profile } j^* \text{ is deleted} \\ &\rightarrow \;\; \varpi_i = \varpi_{i^*} + \varpi_{j^*}, \\ \text{if } \varpi_{i^*} < \varpi_{j^*} \;\; &\rightarrow \;\; \text{profile } i^* \text{ is deleted} \\ &\rightarrow \;\; \varpi_j = \varpi_{i^*} + \varpi_{j^*}. \end{aligned}$$

- **Step 5:** If $k = \mathcal{N}_{\text{dp}}$ then terminate. Otherwise, return to step 1.

where,

$\mathcal{H}$	set of the net demand profiles
$P_{t,i}^{\text{net}}$	net demand at time t of profile i (MW)
$\Delta_{i,j}$	distance between profile i and j
$\mathcal{N}_{\text{pr}}$	number of net demand profiles
ϖ_i	frequency of profile i
$\mathcal{N}_{\text{dp}}$	number of desired profiles

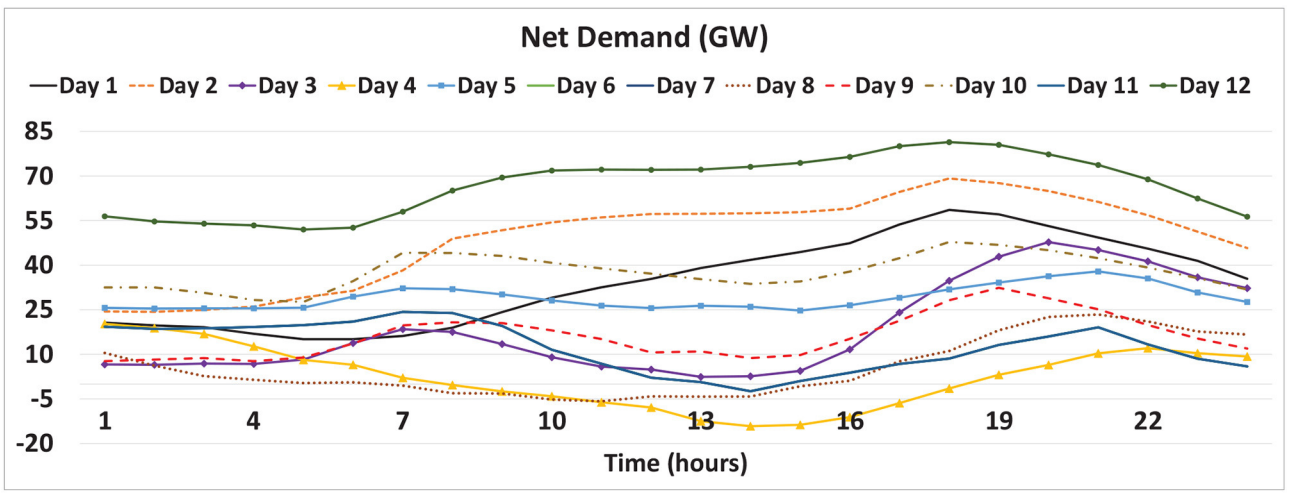

FIGURE 4 | Net demand profiles after the demand clustering strategy.

TABLE 2 | Representative days for the entire year.

Representative day	Actual day	Frequency
1	16	3
2	18	7
3	96	3
4	185	1
5	201	125
6	205	28
7	232	7
8	241	3
9	278	38
10	294	53
11	338	85
12	355	12

TABLE 3 | Computational performance for optimization of a day through different solving approaches.

	SLP	OA/ER
Computational time (min)	12.8	8.0
Operational cost (£ m)	148.1	147.9

In **Figure 4**, the net electricity demand profiles selected by the clustering algorithm are presented. The actual days in the year and the frequency of occurrence of the representative profiles are provided in **Table 2**. Some of the profiles that occur less frequently pose unique characteristics, e.g., Day 4 occurs only once in the whole year and represents a summer day in which a significant amount of electricity is generated by RES; therefore, net electricity demand is negative during most hours of the day.

4.3. Description of Flexibility Case Studies

To investigate the role and value of the flexibility options in supporting the cost-effective operation of gas and electricity systems, different combinations of available flexibility and level of wind generation penetration are considered. For each flexibility option, two different levels considered: low 4 GW installed capacity and high 12 GW installed capacity. For wind generation, three different levels of installed capacity, i.e., 23.6, 47.3, and 70.9 GW, are assumed.

5. RESULTS AND DISCUSSIONS

5.1. Computational Performance of the OA/ER Approach

The optimization problem was run on a computer with a 3.20 GHz Intel(R) Xeon(R) processor and 16 GB of RAM. The computational performance of the proposed OA/ER decomposition method was benchmarked against the SLP algorithm of Xpress solver (FICO, 2013). The employment of the OA/ER decomposition method significantly improved the efficiency of the solution algorithm, achieving a nearly 40% reduction in the computation time compared to the SLP method. In addition, the solution of the optimization (i.e., operational cost) was slightly improved. A summary of the computational characteristics for a day is presented in **Table 3**.

5.2. Performance of Flexibility Options in the Electricity System

5.2.1. Impacts of Increased Flexibility on Generation Dispatch

Figure 5 shows how the use of flexibility options affects the electricity outputs of different generation technologies through the change in electricity production with respect to the *Ref* Case. The application of flexibility options enhances the ability of the system to absorb more electricity from renewable sources. Consequently, due to more electricity being supplied from renewables, compared to the *Ref* case, the power from the expensive option (interconnection) as well as coal (i.e., characterized by high emissions) is reduced. Furthermore, the share of gas-fired plants increases to complement variable renewable generation. In **Figure 5A**, the significant role of high installation of DSR in accommodating more gas-fired plants is presented. This is due to the fact that, since the wind penetration is low, gas plants play the main part in supplying demand, and by shifting the demand optimally, around 5 TWh more electricity is provided by the gas-fired plants. Due to the small penetration of wind, electricity storage and P2G have a small impact on the electricity produced by different types of generators. In **Figure 5B**, although more electricity is absorbed by the grid, the gas plants are generating more. This is due to the fact that according to (23), the electricity storage is contributing to providing a reserve, and hence gas plants participate more in the supply-demand balance. **Figure 5C** shows that, due to the flexibility provided by electricity storage through optimal charging and discharging, the contribution of gas-fired plants and hydro is reduced. In *P2G* cases, the increased absorption of electricity from wind is primarily used for hydrogen production. Furthermore, to support the operation of the gas system during peak periods, up to 2.6 TWh/yr additional electricity, mainly from hydro (i.e., limited in the *Ref* case because of transmission congestion), is used for producing and injecting hydrogen into the gas system. As can be seen in **Figures 5B,C**, more electricity from hydrogen-based CCGTs is produced compared to the *Ref* case (up to 0.8 TWh/yr), which leads to less emissions from gas-fired plants.

It is shown that when increasing the penetration level of wind to the system, electricity storage plays a significant role in changing the power dispatch from different technologies. As presented in **Figure 5A**, this is demonstrated by integrating more wind into the system while decreasing the electricity from coal and interconnection and reducing the share of renewables, and there are decreases in all other generation technologies at higher shares of wind. For other flexibility options for all wind penetration levels, the generation from wind, gas-fired, and hydro plants increases, while the production of interconnectors and coal plants decreases. In *P2G* cases, the hydrogen produced through the excess of wind is injected into the gas pipelines as well as being used as a fuel for gas-fired plants.

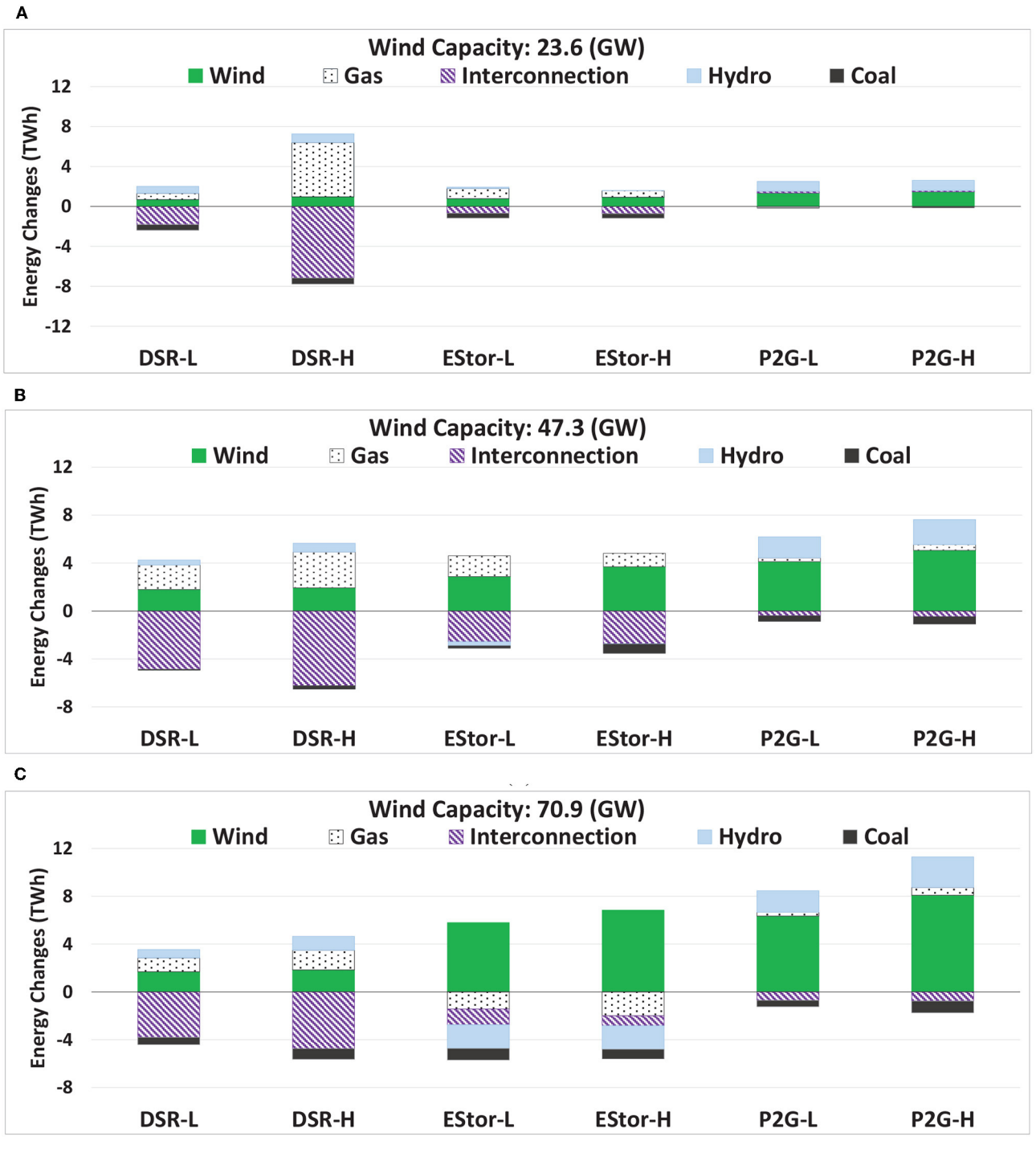

FIGURE 5 | Annual energy changes for different installed capacities of wind (compared to the *Ref* case): **(A)** 23.6 GW, **(B)** 46.7 GW, and **(C)** 70.9 GW.

5.2.2. Wind Curtailment

As expected, the increased level of flexibility reduces wind curtailment. The highest reductions in wind curtailment are achieved in the *P2G* and *EStor* cases. The annual reduction of wind curtailment is presented in **Figure 6A**.

5.2.3. Operational Costs

In **Figure 6B**, the annual gas and electricity operational cost savings compared to the *Ref* case are presented for different levels of wind penetration and the application of different flexibility options. The total operational costs of

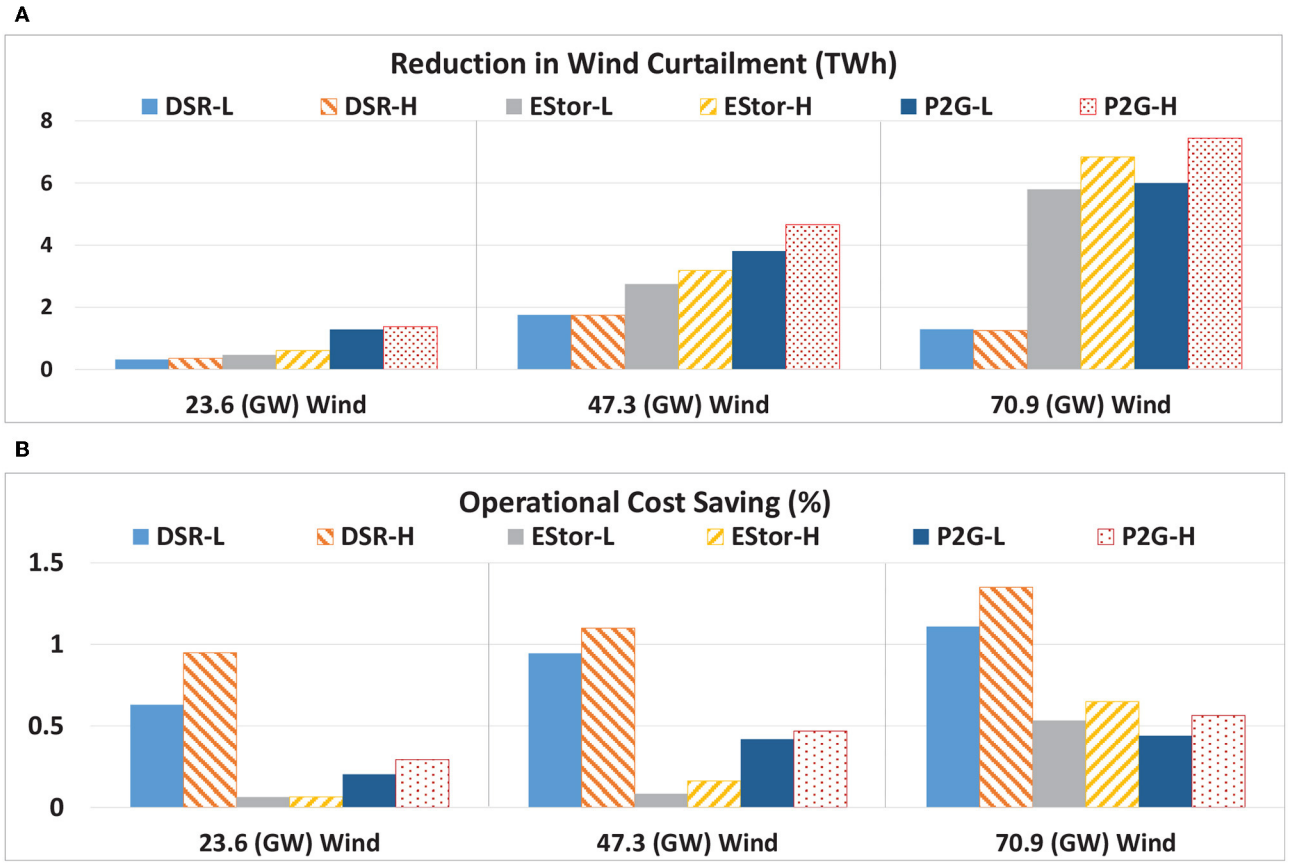

FIGURE 6 | (A) Cumulative wind curtailment reduction, and **(B)** annual operational cost savings of gas and electricity systems compared to the *Ref* case.

TABLE 4 | Total operational costs in the *Ref* case.

Wind penetration (GW)	Cost (£ bn)
23.6	30.9
47.3	29.3
70.9	28.2

gas and electricity systems for the *Ref* case are shown in **Table 4**.

The value of flexibility options increases when the penetration of wind generation increases. In *DSR* cases, due to the flexibility provided, demand is shifted mainly from peaks to off-peaks, which results in a significant decrease in electricity importation (**Figure 5**). As a result, the largest cost savings are achieved in *DSR* cases. Overall, the enhanced flexibility provided by DSR, electricity storage, and P2G increases the efficiency of system operation by reducing the challenges caused by RES.

It is worth mentioning that in the DSR modeling, the demand satisfaction constraints (i.e., related to customer behavior) is not taken into account (Pudjianto et al., 2014), and it is assumed that the part of demand that is flexible can be shifted when it is required by the system operator. In a case where demand satisfaction constraints should be considered, the cost savings would be lower.

5.3. Performance of Flexibility Options in the Gas System

If flexibility in the gas system is enhanced through multi-directional gas compressors, it is possible to deliver more gas to the gas plants. Consequently, the supply through coal decreases, and therefore the overall emissions and the total operational costs of the systems reduce. **Figure 7** demonstrates that enhancing the flexibility of the gas infrastructure in the integrated operation of gas and electricity systems increases the generation by gas-fired power plants and reduce wind curtailment, while the production from coal characterized by high emissions reduces. This delivers prevention of about 300 kilotonnes of CO_2 production.

It is worth mentioning that since there is enough gas supply to the system, under normal conditions, the multi-directional gas compressors do not play a major role in improving the operation of the system. This flexibility can enhance the energy system resiliency. Therefore, to highlight the role of multi-directional gas compressors, a stressed condition of the energy system considering two characteristics is derived: (a) when an increase

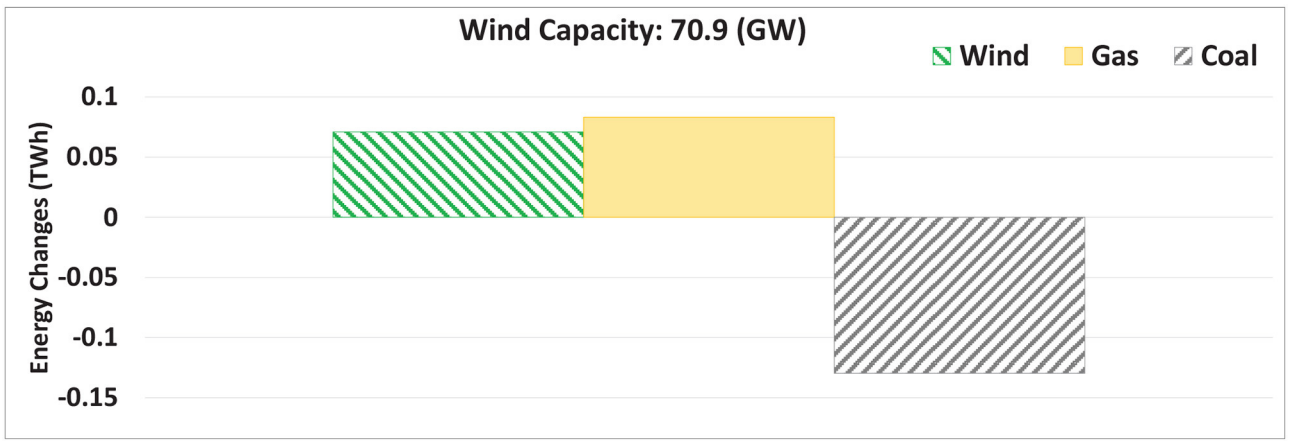

FIGURE 7 | Change in annual electricity generation in the *Multi* case in respect to the *Ref* case.

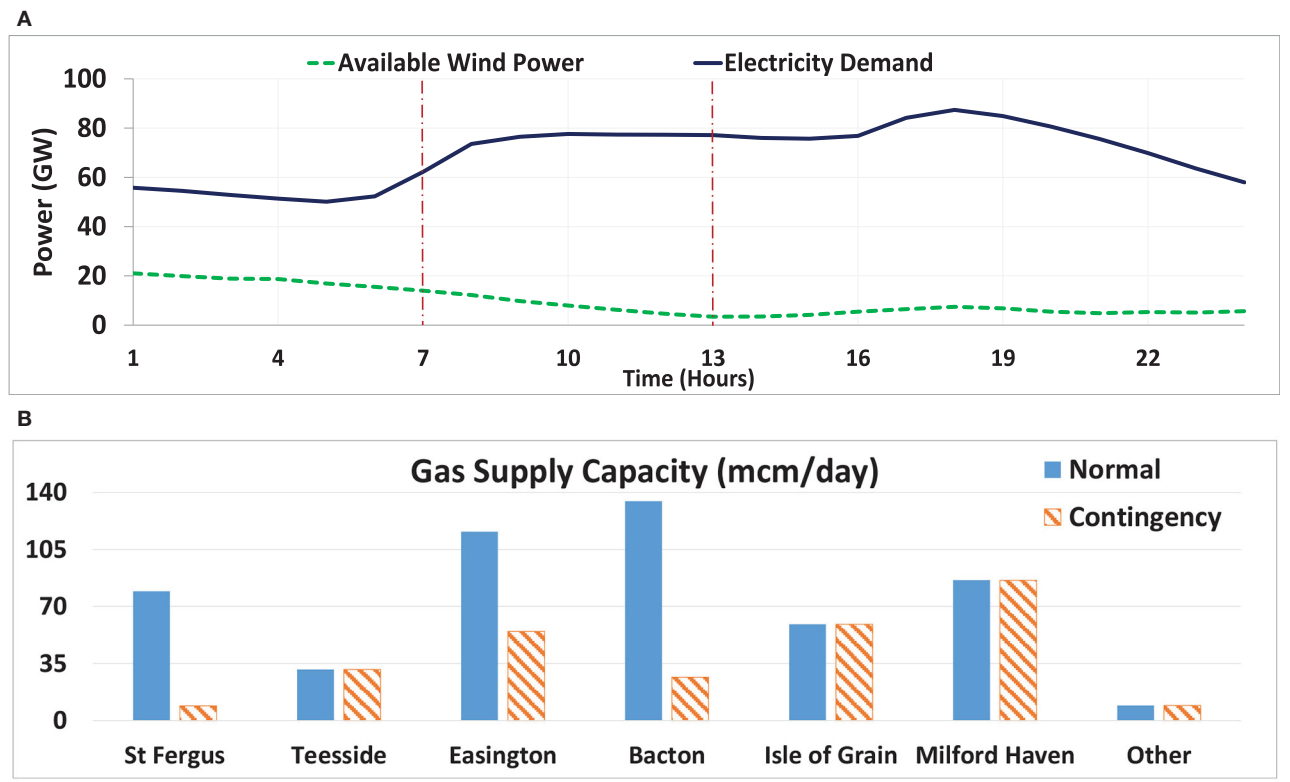

FIGURE 8 | (A) Electricity demand and available wind, and **(B)** gas terminal capacity on the day of supply interruption (other refers to Barrow, Burton point, and Theddlethrope).

in demand in morning hours coincides with a reduction in wind generation, as presented in **Figure 8A**, and (b) when gas supply capacities in the St Fergus, Bacton, and Easington gas terminals are constrained (**Figure 8B**).

5.3.1. Power Dispatch

The employment of flexibility options enables an effective balancing of electricity supply and demand during gas supply interruption and therefore reduces the need to import electricity (which is assumed to be at highest cost) or coal plants, which are characterized by high emissions. As seen in **Figure 9**, electricity from interconnectors and coal is reduced by up to 36 and 50 GWh compared to the *Ref* case in the two stress conditions, respectively. Hence, more accommodation of wind energy is facilitated, which leads to cost savings for both natural gas and power systems.

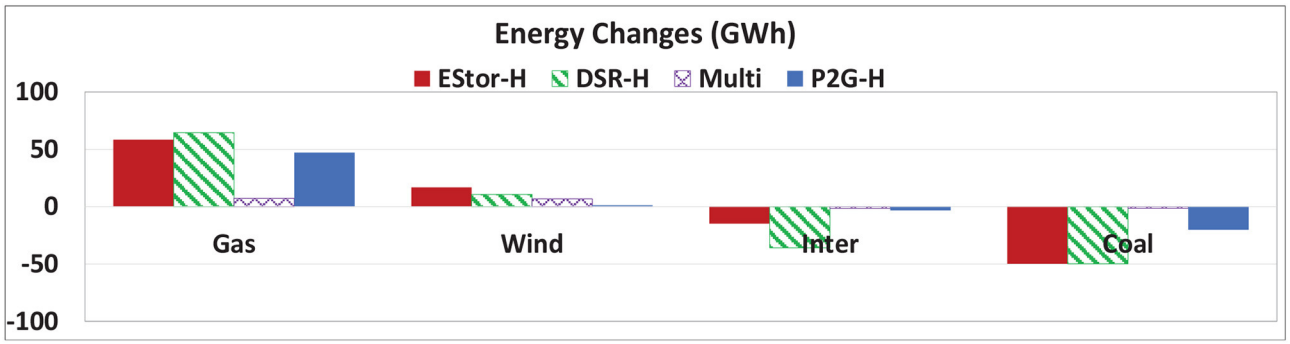

FIGURE 9 | Change in the electricity in presence of different flexibility options during the day of gas supply interruption compared to the *Ref* case.

5.3.2. Gas Compressor Performance

Multi-directional compressors play a key role in mitigating the impacts of gas supply interruption by redirecting gas flows and maintaining gas supply to gas-fired power plants that would be otherwise be affected by the supply interruption. As is presented in **Figure 10A**, in the *Multi* case, especially in the morning hours when a demand increase and a sudden wind drop coincide, the compressors operate more frequently to redirect the gas flow direction. In other cases, the compressor performance is almost the same as the *Ref* case, as the changes are small. This is due to the fact that, in these cases, the flexibility of the gas system infrastructure is not enhanced.

5.3.3. Locational Marginal Price of Gas

As was discussed, the large penetration of RES increases the interaction of gas and electricity networks. Therefore, changes in the level of wind generation will significantly influence the operation of the gas system. In the case of no interruption of gas supply, since there is still enough gas to meet the demand, gas Locational Marginal Prices (LMP) are around the gas price (0.35 £/cm). The gas system security will be impacted, particularly during interruption in the gas supply system. The index considered for the gas system security is the amount of non-served gas demand. In the *Ref* case, the gas supply interruption causes a loss of 0.033 mcm of gas demand. This results in a significant increase in the gas LMP, especially in Scotland after 11:00 a.m., when both gas and electricity demand are high (**Figure 10B**). The gas LMP in Scotland in the *Ref* case after 11 h is equal to the assumed Value of Lost Load (VoLL) (11.1 £/cm Chaudry et al., 2008). The use of flexibility options prevents gas load shedding during the supply interruption. As is shown in **Figure 10B**, the use of DSR and battery storage minimize the impact of the gas supply interruption on the gas LMP (0.46 £/cm). In the *Multi* case, the gas LMP is 0.72 £/cm, which indicates the efficacy of multi-directional compressors in gas delivery to demand centers. P2G prevents gas load shedding by producing hydrogen and injecting it into the gas system. However, the LMPs are high (3.4 £/cm) given that the wind generation is low and hydrogen injection therefore cannot help significantly to obviate the gas system congestion.

Overall, the modeling demonstrates that the investment in flexibility in gas infrastructure will be driven by increased requirements for flexibility in the electricity system. This will require closer coordination of operation and investment in both systems in order to facilitate cost-effective de-carbonization of the electricity system.

On the other hand, the case studies indicate that enhancing flexibility in gas and electricity networks could reduce the dependency between gas and electricity systems by addressing demand-supply balancing challenges as well as gas supply interruptions.

6. CONCLUSION

An outer approximation with equality relaxation method is proposed to effectively solve the optimization problem of the operation of integrated gas and electricity systems. The modeling approach developed is applied to demonstrate the benefits of an integrated approach to the operation of interdependent gas and electricity systems.

In addition, the modeling indicates that significant cost savings and corresponding emissions reduction can be achieved through enhancing the flexibility of the gas infrastructure. The value of different flexibility options (battery storage, demand-side response, power-to-gas, and multi-directional compressors) for the operation of gas and electricity systems were investigated for various scenarios representing different levels of wind generation penetration. It was demonstrated that flexibility options would enhance the ability of the system to accommodate wind generation and simultaneously reduce the operating cost of the gas and electricity systems by up to 21%.

It was demonstrated that during sudden drops in wind generation as well as gas supply interruptions, the flexibility options play important roles in enhancing the efficiency of system operation and the security of gas supply. The ability of the flexibility options to reduce the interaction between gas and electricity networks in an integrated strategy highlights the importance of reforming the current regulatory and

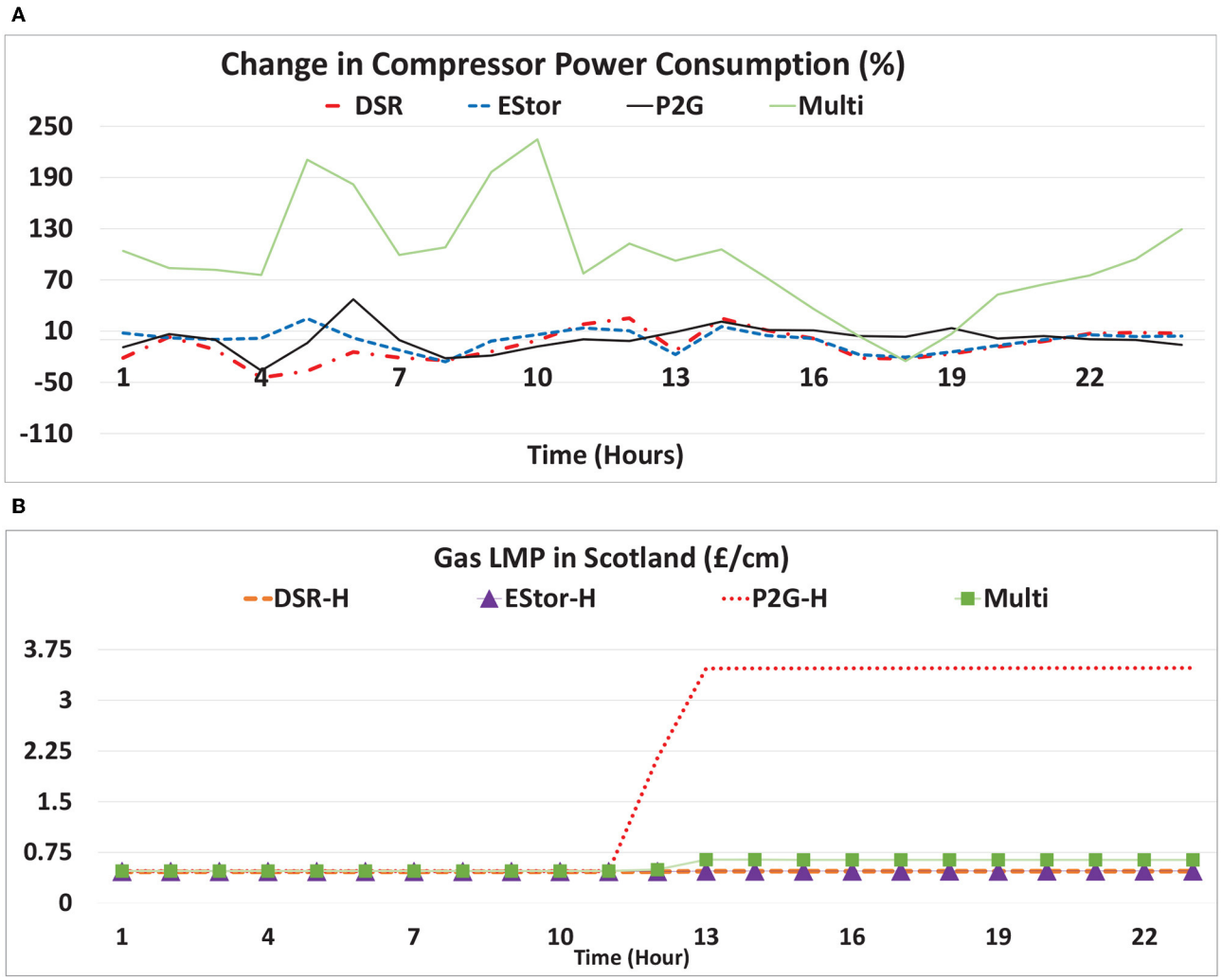

FIGURE 10 | (A) Change in power consumed by the gas compressors on the day of supply interruption compared to the *Ref* case, and **(B)** gas LMP in Scotland on the day of supply interruption.

market framework to coordinate operation and investment in both systems for a cost-effective transition to lower-carbon energy systems.

Future work will involve modeling of investment in different flexibility options and emission constraints in order to identify the optimal portfolio of these technologies that would achieve carbon targets at minimum whole-system costs. Furthermore, integrated analysis of local and national infrastructures will be important for considering alternative evolution pathways of the gas and electricity infrastructures.

DATA AVAILABILITY STATEMENT

The datasets generated for this study are available on request to the corresponding author.

AUTHOR CONTRIBUTIONS

HA conducted the modelings and run the optimization as well as writing the paper. MQ and GS provided the guidance as well as contributing in writing the paper. All authors contributed to the article and approved the submitted version.

FUNDING

The authors gratefully acknowledge the SysFlex project, which has received funding from the European Union's Horizon 2020 research and innovation program under award number 773505 as well as the EPSRC-funded program Integrated Development of Low-Carbon Energy Systems (IDLES) under award number EP/R045518/1.

REFERENCES

Akhtari, M. R., and Baneshi, M. (2019). Techno-economic assessment and optimization of a hybrid renewable co-supply of electricity, heat and hydrogen system to enhance performance by recovering excess electricity for a large energy consumer. *Energy Convers. Manag.* 188, 131–141. doi: 10.1016/j.enconman.2019.03.067

Ameli, H., Abbasi, E., Ameli, M. T., and Strbac, G. (2017a). A fuzzy-logic based control methodology for secure operation of a microgrid in interconnected and isolated modes. *Int. Trans. Electric. Energy Syst.* 27:e2389. doi: 10.1002/etep.2389

Ameli, H., Ameli, M. T., and Hosseinian, S. H. (2017b). Multi-stage frequency control of a microgrid in the presence of renewable energy units. *Electric Power Comp. Syst.* 45, 159–170. doi: 10.1080/15325008.2016.1247389

Ameli, H., Qadrdan, M., and Strbac, G. (2017c). Techno-economic assessment of battery storage and power-to-gas: a whole-system approach. *Energy Proc.* 142, 841–848. doi: 10.1016/j.egypro.2017.12.135

Ameli, H., Qadrdan, M., and Strbac, G. (2017d). Value of gas network infrastructure flexibility in supporting cost effective operation of power systems. *Appl. Energy* 202, 571–580. doi: 10.1016/j.apenergy.2017.05.132

Ameli, H., Qadrdan, M., and Strbac, G. (2019). Coordinated operation strategies for natural gas and power systems in presence of gas-related flexibilities. *IET Energy Syst. Integr.* 1, 3–13. doi: 10.1049/iet-esi.2018.0047

Ameli, H., Qadrdan, M., Strbac, G., and Ameli, M. T. (2020). Investing in flexibility in an integrated planning of natural gas and power systems. *IET Energy Syst. Integr.* 2, 101–111 doi: 10.1049/iet-esi.2019.0065

Castillo, A., Laird, C., Silva-Monroy, C. A., Watson, J. P., and O'Neill, R. P. (2016). The unit commitment problem with ac optimal power flow constraints. *IEEE Trans. Power Syst.* 31, 4853–4866. doi: 10.1109/TPWRS.2015.2511010

Chaudry, M., Jenkins, N., and Strbac, G. (2008). Multi-time period combined gas and electricity network optimisation. *Electric Power Syst. Res.* 78, 1265–1279. doi: 10.1016/j.epsr.2007.11.002

Chung, C. Y., Yu, H., and Wong, K. P. (2011). An advanced quantum-inspired evolutionary algorithm for unit commitment. *IEEE Trans. Power Syst.* 26, 847–854. doi: 10.1109/TPWRS.2010.2059716

Correa-Posada, C. M., and Sanchez-Martin, P. (2015). Integrated power and natural gas model for energy adequacy in short-term operation. *IEEE Trans. Power Syst.* 30, 3347–3355. doi: 10.1109/TPWRS.2014.2372013

Correa-Posadaa, C. M., and Sanchez-Martin, P. (2014). Gas network optimization: a comparison of piecewise linear models. *Chem. Eng. Sci.* 30, 1–24.

Dai, C., Wu, L., and Wu, H. (2016). A multi-band uncertainty set based robust scuc with spatial and temporal budget constraints. *IEEE Trans. Power Syst.* 31, 4988–5000. doi: 10.1109/TPWRS.2016.2525009

Deane, J., Ciaráin, M. O., and Gallachóir, B. O. (2017). An integrated gas and electricity model of the EU energy system to examine supply interruptions. *Appl. Energy* 193, 479–490. doi: 10.1016/j.apenergy.2017.02.039

FICO (2013). *Fico Xpress Optimisation Suite*. San Jose, CA.

Floudas, C. A. (1995). *Nonlinear and Mixed-Integer Optimization: Fundamentals and Applications*. Oxford, UK: Oxford University Press.

Gil, M., Duenas, P., and Reneses, J. (2016). Electricity and natural gas interdependency: comparison of two methodologies for coupling large market models within the european regulatory framework. *IEEE Trans. Power Syst.* 31, 361–369. doi: 10.1109/TPWRS.2015.2395872

He, C., Wu, L., Liu, T., and Shahidehpour, M. (2017). Robust co-optimization scheduling of electricity and natural gas systems via admm. *IEEE Trans. Sustain. Energy* 8, 658–670. doi: 10.1109/TSTE.2016.2615104

Hu, Y., Lian, H., Bie, Z., and Zhou, B. (2017). Unified probabilistic gas and power flow. *J. Mod. Power Syst. Clean Energy* 5, 400–411. doi: 10.1007/s40565-017-0284-1

ITM Power (2013). *Report and Financial Statements*. Technical report, Sheffield, United Kingdom.

Nasri, A., Kazempour, S. J., Conejo, A. J., and Ghandhari, M. (2016). Network-constrained ac unit commitment under uncertainty: a benders decomposition approach. *IEEE Trans. Power Syst.* 31, 412–422. doi: 10.1109/TPWRS.2015.2409198

National Grid Plc (2016). *UK Future Energy Scenarios, GB Gas and Electricity Transmission*. Technical Report July, Warwick, United Kingdom.

Ongsakul, W., and Petcharaks, N. (2004). Unit commitment by enhanced adaptive lagrangian relaxation. *IEEE Trans. Power Syst.* 19, 620–628. doi: 10.1109/TPWRS.2003.820707

Osiadacz, A. (1987). *Simulation and Analysis of Gas Networks*. Houston, TX: Gulf Publishing Company.

Pudjianto, D., Aunedi, M., Djapic, P., and Strbac, G. (2014). Whole-systems assessment of the value of energy storage in low-carbon electricity systems. *IEEE Trans. Smart Grid* 5, 1098–1109. doi: 10.1109/TSG.2013.2282039

Qadrdan, M., Ameli, H., Strbac, G., and Jenkins, N. (2017a). Efficacy of options to address balancing challenges: integrated gas and electricity perspectives. *Appl. Energy* 190, 181–190. doi: 10.1016/j.apenergy.2016.11.119

Qadrdan, M., Chaudry, M., Wu, J., Jenkins, N., and Ekanayake, J. (2010). Impact of a large penetration of wind generation on the GB gas network. *Energy Policy* 38, 5684–5695. doi: 10.1016/j.enpol.2010.05.016

Qadrdan, M., Cheng, M., Wu, J., and Jenkins, N. (2017b). Benefits of demand-side response in combined gas and electricity networks. *Appl. Energy* 192, 360–369. doi: 10.1016/j.apenergy.2016.10.047

Sardou, I. G., Khodayar, M. E., and Ameli, M. T. (2018). Coordinated operation of natural gas and electricity networks with microgrid aggregators. *IEEE Trans. Smart Grid* 9, 199–210. doi: 10.1109/TSG.2016.2547965

Shabanpour-Haghighi, A., and Seifi, A. R. (2015). Simultaneous integrated optimal energy flow of electricity, gas, and heat. *Energy Convers. Manag.* 101, 579–591. doi: 10.1016/j.enconman.2015.06.002

Sheikhi, A., Bahrami, S., and Ranjbar, A. M. (2015). An autonomous demand response program for electricity and natural gas networks in smart energy hubs. *Energy* 89, 490–499. doi: 10.1016/j.energy.2015.05.109

Sirvent, M., Kanelakis, N., Geißler, B., and Biskas, P. (2017). Linearized model for optimization of coupled electricity and natural gas systems. *J. Mod. Power Syst. Clean Energy* 5, 364–374. doi: 10.1007/s40565-017-0275-2

Troy, N., Flynn, D., and O'Malley, M. (2012). Multi-mode operation of combined-cycle gas turbines with increasing wind penetration. *IEEE Trans. Power Syst.* 27, 484–492. doi: 10.1109/TPWRS.2011.2163649

Wu, Q. H., Qin, Y. J., Wu, L. L., Zheng, J. H., Li, M. S., Jing, Z. X., et al. (2019). Optimal operation of integrated energy systems subject to the coupled demand constraints of electricity and natural gas. *CSEE J. Power Energy Syst.* 6, 1–14. doi: 10.17775/CSEEJPES.2018.00640

Yang, L., Jian, J., Dong, Z., and Tang, C. (2017). Multi-cuts outer approximation method for unit commitment. *IEEE Trans. Power Syst.* 32, 1587–1588. doi: 10.1109/TPWRS.2016.2584862

Yang, Z., Gao, C., and Zhao, M. (2019). Coordination of integrated natural gas and electrical systems in day-ahead scheduling considering a novel flexible energy-use mechanism. *Energy Convers. Manag.* 196, 117–126. doi: 10.1016/j.enconman.2019.05.109

Zeng, Q., Fang, J., Li, J., and Chen, Z. (2016). Steady-state analysis of the integrated natural gas and electric power system with bi-directional energy conversion. *Appl. Energy* 184, 1483–1492. doi: 10.1016/j.apenergy.2016.05.060

Zhang, X., Shahidehpour, M., Alabdulwahab, A., and Abusorrah, A. (2016). Hourly electricity demand response in the stochastic day-ahead scheduling of coordinated electricity and natural gas networks. *IEEE Trans. Power Syst.* 31, 592–601. doi: 10.1109/TPWRS.2015.2390632

Zlotnik, A., Roald, L., Backhaus, S., Chertkov, M., and Andersson, G. (2017). Coordinated scheduling for interdependent electric power and natural gas infrastructures. *IEEE Trans. Power Syst.* 32, 600–610. doi: 10.1109/TPWRS.2016.2545522

Conflict of Interest: The authors declare that the research was conducted in the absence of any commercial or financial relationships that could be construed as a potential conflict of interest.

frontiers in Energy Research

PERSPECTIVE
published: 10 July 2020
doi: 10.3389/fenrg.2020.00153

Taking a Shortcut: Direct Power-to-X Conversion

Zetian Mi[1] *and Volker Sick*[2]*

[1] Department of Electrical Engineering and Computer Science, University of Michigan, Ann Arbor, MI, United States,
[2] Department of Mechanical Engineering, University of Michigan, Ann Arbor, MI, United States

Power-to-X technologies provide avenues to help de-fossilize a range of large-scale technologies in the mobility, manufacturing, chemical, as well as energy delivery industries. This relates to energy carriers such as hydrogen and hydrocarbons as well as availability of feedstock materials, such as methanol. Technologies for solar and wind-generated electricity and subsequent electrochemical processing are available and are further developed for efficiency and yields. An alternative pathway can be pursued by fully integrating the electricity generation and chemical conversion into one device, thereby reducing technical complexity and removing inefficiencies due to multi-step cascading of processes. In this perspective article, we provide an overview on the recent developments and prospects of artificial photosynthesis, i.e., the chemical transformation of sunlight, water, and carbon dioxide into high-energy-rich fuels. Primary discussions will be focused on the recent development of scalable artificial photosynthesis technology using common semiconductors, e.g., silicon and gallium nitride, for solar fuel production. Technology advances for both hydrogen production from solar water splitting and liquid fuel generation from CO_2 reduction will be discussed. The basic operating principles and potential integration with existing and emerging energy infrastructures will be analyzed. The challenges, future prospects of achieving sustainable, large scale applications will also be presented.

Keywords: power-to-X, artificial photosynthesis, green hydrogen, solar fuels, de-fossilization

OPEN ACCESS

Edited by:
David Parra,
Université de Genève, Switzerland

Reviewed by:
Qinghua He,
Auburn University, United States
Edward P. Gatzke,
University of South Carolina, United States

***Correspondence:**
Volker Sick
vsick@umich.edu

Specialty section:
This article was submitted to Process and Energy Systems Engineering, a section of the journal Frontiers in Energy Research

Received: *03 March 2020*
Accepted: *17 June 2020*
Published: *10 July 2020*

Citation:
Mi Z and Sick V (2020) Taking a Shortcut: Direct Power-to-X Conversion. Front. Energy Res. 8:153. doi: 10.3389/fenrg.2020.00153

INTRODUCTION

Background, Needs, Challenges

Power-to-X technologies provide avenues to help de-fossilize a range of large-scale technologies in the mobility, manufacturing, chemical, as well as energy delivery industries. This relates to energy carriers such as hydrogen and hydrocarbons as well as availability of feedstock materials, such as methanol and other chemicals (Energy Transitions Commission, 2018; International Energy Agency, 2018; National Academies of Sciences Engineering and Medicine, 2019).

Current global production and use quantities for hydrogen exceed 70 million metric tons per year with key applications in fertilizer production, petroleum reforming, and the chemical industry (International Energy Agency, 2019). This demand will further grow substantially as hydrogen is considered ever more strongly as an energy carrier for mobility needs and mid- and long-term energy storage for renewable energy systems. Energy transition scenarios, especially looking at so-called hard-to-abate sectors include the use of hydrogen also for steel making, replacing coal-based

coke with hydrogen (Energy Transitions Commission, 2018). Projections are that global hydrogen markets could grow to $2.5T by 2050 (Alvéra, 2019).

In addition, rapidly growing opportunities to utilize CO_2 as a feedstock for carbon-based chemicals, polymers, as well as fuels, will increase the demand for hydrogen. Today, the overwhelming amount of hydrogen is produced via steam methane reforming that converts methane and water into hydrogen and carbon dioxide. Direct production of hydrogen from water via electrolysis eliminates the formation and release of carbon dioxide. In particular, with increasing availability of carbon-free energy this becomes an avenue for decarbonizing hydrogen production. It is also an enabling pathway to buffer and store surplus wind-, solar- and hydro-electricity.

In a similar manner, carbon-free electricity can be used to produce hydrocarbons that currently are derived from petroleum or coal and are used as fuels or base chemicals to make a wide range of everyday products (Artz et al., 2018; Hoppe et al., 2018; Kätelhön et al., 2019; Michailos et al., 2019). Fischer-Tropsch-like synthesis that starts with syngas can be tailored to work with carbon monoxide that is produced from carbon dioxide (Styring et al., 2015).

In order to advance technologies for hydrogen and hydrocarbon production, exciting opportunities were created in recent years that integrate the production of electricity and the chemical conversion of water, or conversion of water and carbon dioxide. After a brief status review, prospects and examples are presented for semiconductor-based artificial photosynthesis technologies that could reduce complexity and increase efficiency of conversion processes.

ARTIFICIAL PHOTOSYNTHESIS

Sunlight is the champion of energy sources: delivering more energy to the earth in an hour than world energy consumption is in a year and it may ultimately address the global energy problem: "The Terawatt Challenge" (Chu et al., 2017). The major obstacle, however, is how to develop an efficient, scalable, and cost-effective approach to store solar energy on demand on a global scale. Artificial photosynthesis, which mimics the natural photosynthesis and converts abundant solar energy into energy-rich chemicals and fuels, e.g., hydrogen (H_2) and carbon compounds such as carbon monoxide (CO), methanol (CH_3OH), formic acid (HCOOH), and methane (CH_4), schematically shown in **Figure 1**, offers a promising approach to storing solar energy in the form of chemicals and fuels, which can replace conventional fossil fuels widely used in our society today (Bolton, 1996; Turner et al., 2004). Take solar H_2 as an example: it can be utilized in fuel cells with water as the only emissions and can be readily employed as a feedstock for various large-scale industry processes, including methanol production via CO_2 hydrogenation reaction and ammonia synthesis via Haber-Bosch reaction. For large scale production it is essential to develop efficient and cost-effective artificial photosynthesis system that can compete with traditional methods using fossil fuels.

There are three major paths for solar powered artificial photosynthesis, including photocatalytic, photoelectrochemical (PEC), and photovoltaic-electrolysis (PV-E) systems. The PV-E approach integrates PV cells with appropriate catalysts to drive the chemical reaction. This approach has led to solar-to-hydrogen conversion efficiencies over 10% (Cox et al., 2014; Luo et al., 2014; Nakamura et al., 2015). However, its high cost has been considered a major limiting factor for large scale adoption. In a photoelectrochemical system, the light harvesting and electrochemical reaction process are integrated into a single unit (Pinaud et al., 2013; McKone et al., 2014; Ager et al., 2015). Recent techno-economic analysis suggested that the cost of PEC systems can be significantly reduced compared to PV-E systems (Pinaud et al., 2013; Sathre et al., 2014; Shaner et al., 2016). With further improved efficiency and reliability, it can potentially become highly competitive compared with conventional fossil-fuels. Compared to PV-E and PEC methods, the photocatalytic artificial photosynthetic system is a completely wireless approach, i.e., without the use of any electrical connection or components, to produce solar fuels (Fabian et al., 2015). In addition, it has no stringent requirement on the electrolyte. Recent studies have shown that seawater and possibly wastewater can be utilized without degrading the system performance (Guan et al., 2018a). As such, the manufacturing and operating cost can be drastically reduced, compared to both PV-E and PEC systems.

Critical components for PEC and photocatalytic systems include semiconductor light absorber (photoelectrode) and catalysts. The light-harvesting semiconductor materials, an essential component of the artificial leaf, plays a critical role in determining the efficiency, cost, and stability of artificial photosynthesis systems. The semiconductor light absorber should have a relatively small energy bandgap to absorb a large portion of the solar spectrum while offering sufficient potentials to efficiently drive the artificial photosynthesis chemical reaction, including water oxidation, proton reduction, and/or CO_2 reduction. In addition, the semiconductor light absorber should exhibit long-term stability in harsh chemical reactions, have low cost, and be non-toxic, and can be manufactured at large scale. In the past decades, numerous materials have been studied, but they often suffer from low efficiency and poor stability, and are not using industry-friendly materials and processing techniques (Fujishima and Honda, 1972; Hisatomi et al., 2014; Montoya et al., 2016).

Recently, significant advancements in efficient and artificial photosynthesis production of chemicals and fuels using industry-ready materials, e.g., gallium nitride (GaN) and silicon (Si) wafers, have been achieved (Kibria et al., 2015; Vanka et al., 2018; Vanka et al., 2019). The materials (GaN and Si) used to build such an artificial photosynthesis device have been widely used in industry: each year over 10,000 million square inches (or 6.5 million square meters) of Si wafers are produced, which serves as the backbone of the nearly $3-trillion consumer electronics market. GaN, the second most invested semiconductor material only next to Si, has been widely used industrially in solid-state lighting, blue/green laser diodes, and high-power electronic devices, whose market value will soon exceed $100 billion. Take GaN power transistor as an example,

they can support current densities on the order of tens of kA/cm^2 and hundreds of kilovolts, which are nearly five to six orders of magnitude larger than the photocurrent densities and voltage relevant for artificial photosynthesis devices. Therefore, this breakthrough research promises commercially viable large-scale production of clean chemicals and fuels from unassisted artificial photosynthesis.

Through nano-engineering, gallium nitride based semiconductors exhibit near-ideal electronic, optical, structural, and photocatalytic properties (Kibria and Mi, 2016) compared to other known semiconductor light absorbers for artificial photosynthesis (Kudo and Miseki, 2009). For III-nitride materials with thicknesses of 1 micrometer, nearly 100% of the incident photons above the energy bandgap can be absorbed. Moreover, the surfaces of GaN can be engineered to be N-rich, which can protect against photocorrosion and oxidation during harsh artificial photosynthesis chemical reaction (Kibria et al., 2016). Remarkable stability of up to 3,000 h continuous operation (i.e., over 500 days for usable sunlight ~5.5 h per day) has been demonstrated without any performance degradation (Guan et al., 2018b; Vanka et al., 2019). In addition, InGaN and Si can be designed to have complementary bandgaps to construct a two-photon tandem system, which is similar to the Z-scheme in natural photosynthesis. A nearly ideal tandem configuration, consisting of InGaN and Si with energy bandgap of 1.75 eV/1.13 eV has been demonstrated recently (Fan et al., 2017). A maximum solar-to-fuel efficiency up to 30% has been predicted for such a Z-scheme artificial photosynthesis system (Hu et al., 2013).

In what follows, we provide a few examples to briefly illustrate the potential of such artificial photosynthesis technologies

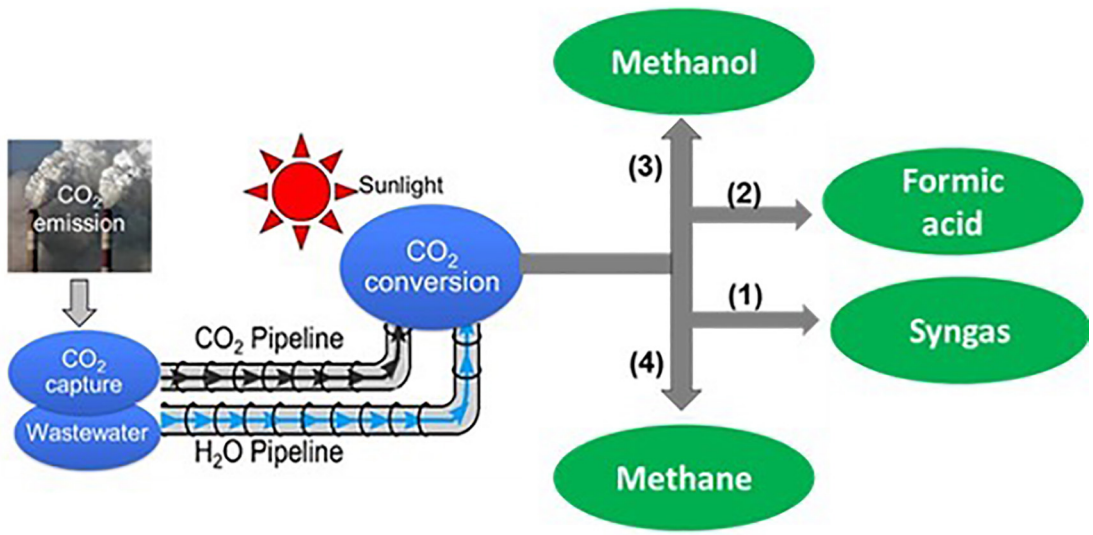

FIGURE 1 | Schematic illustration of the solar refinery system for converting CO_2 and wastewater into chemicals and fuels, including syngas (1), formic acid (2), methanol (3), and methane (4). The selective and efficient reduction of CO_2 to various chemicals and fuels can be potentially enabled by integrating suitable catalysts with semiconductor light absorbers.

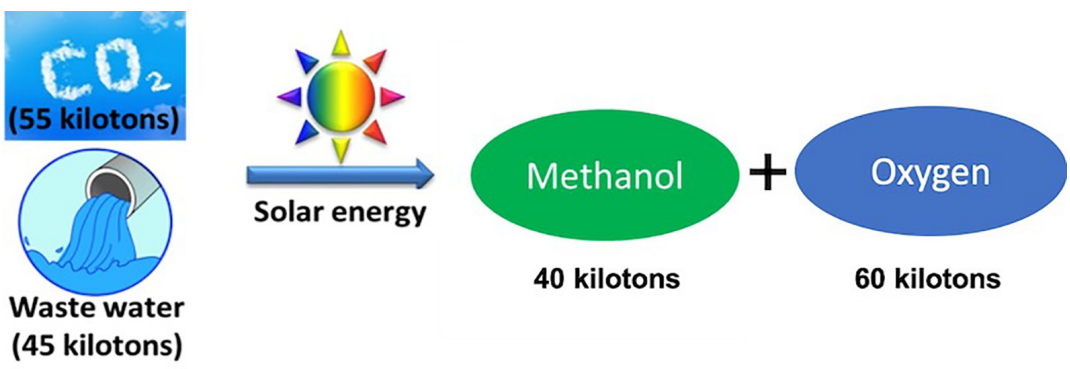

FIGURE 2 | Illustration of a 10 MW artificial photosynthesis plant, which can be potentially tuned to produce approximately 40 Kt of methanol and 60 Kt of O_2 per year.

(Alotaibi et al., 2016; Chu et al., 2018; Shan et al., 2019; Zhou et al., 2019, 2020).

Syngas, a mixture of carbon monoxide and hydrogen, is a key chemical feedstock to upgrade into methanol and long-chain hydrocarbons including synthetic jet, kerosene and diesel fuels, via established industrial process (e.g., Fischer–Tropsch reaction). Global syngas and derivatives market size is estimated to reach 213,100 MW thermal (MWth) by 2020 and will likely continue to grow in the future. It is important to note that direct transportation of syngas, however, may not be trivial. Therefore, the future commercialization of such a system for syngas generation will be likely integrated with chemical synthesis industry to minimize the direct transportation of syngas.

Methanol, known as the simplest alcohol, is also one of the most important feed stocks in chemical industry with an annual production of about 65 million tons. It is a very important precursor for producing various high-value commodity chemicals including gasoline, olefins, propylene, methylamines, and methyl ethers, by well-established technologies. Additionally, methanol itself can be used as bulk chemical as solvent, energy carrier, and gasoline additive. To date, however, methanol is mainly derived from fossil fuels, leading to great emission of CO_2 into the atmosphere. The direct hydrogenation of CO_2 into methanol presents a viable path for consuming large amounts of captured CO_2 due to the extensive market scale of methanol, especially using solar refinery.

Methane is the main component of natural gas and is widely used as fuel for domestic heating and electricity generation in gas turbines or steam generators. Moreover, methane is mainly used in Steam Methane Reforming (SMR) in industry for producing bulk hydrogen with a productivity of more than 50 million metric tons annually worldwide. However, the exploration of natural gas indicates great carbon emission. Recently, it has been demonstrated that methane can be produced with selectivity of up to 50% based on GaN-based materials from CO_2 and water (Zhou et al., 2020). The technology not only helps reduce carbon emissions but also offers great economic benefits.

The mass and energy balance of the CO_2 conversion system is analyzed based on the conversion of CO_2 to syngas, shown in Eq. (1).

$$CO_2 + H_2O + E_{solar} \rightarrow CO + H_2 + O_2 \quad (1)$$

Assuming 2400 h operation per year (8 h a day and 300 days), for a conversion plant with a 10 MW capacity, 55 Kt of CO_2 and 22.5 Kt of water will be consumed, and 35 Kt of CO, 2.5 Kt of H_2 and 40 Kt of O_2 will be produced. Similarly, 40 Kt of methanol or 20 Kt of methane can be produced from 55 Kt of CO_2 to 45 Kt of H_2O, illustrated in **Figure 2**. Here 10 MW energy is stored in the form of chemical bonds of syngas. Performance, cost, and direct integration with current energy and chemical industry infrastructures have been considered as some of the major challenges for this technology to be quickly adopted for commercial production of various chemicals and fuels, which can be mitigated with further research and development and through innovations in photocatalyst materials and system design and integration.

Summary

Artificial photosynthesis production of chemicals and fuels from some of the most abundant and free resources available on earth, i.e., sunlight, water, and carbon dioxide, is highly relevant for the societal transition to a sustainable and clean energy resource future. The GaN-based artificial photosynthetic system offers distinct advantages: the use of sunlight as the energy source, low cost and ambient operation, and leveraging well established semiconductor manufacturing processes. As such, it is expected that the development of artificial photosynthesis technology may follow the trend of solar cells and can be potentially scaled up in the near future. The products generated from this technology are chemicals and fuels such as hydrogen, oxygen, syngas, methane and methanol, which can be well integrated with current energy infrastructure, but with minimized environmental impact. The artificial photosynthesis technology is carbon negative with potentially the smallest greenhouse gas footprint compared to other competing approaches while meeting the increasing global energy demand.

AUTHOR CONTRIBUTIONS

ZM and VS contributed to the conception and design of this perspective. ZM is mainly responsible for the artificial photosynthesis section. VS provided the framework. Both authors contributed to the article and approved the submitted version.

FUNDING

VS is grateful for financial support from the Global CO_2 Initiative. VS and ZM appreciate support from the Blue Sky program at the College of Engineering at the University of Michigan.

ACKNOWLEDGMENTS

ZM expresses grateful thanks to Dr. Sheng Chu, Dr. Baowen Zhou, Dr. Mingxin Liu, and Dr. Faqrul Chowdhury for valuable discussions and for their help with analysis and technical input.

REFERENCES

Ager, J. W., Shaner, M. R., Walczak, K. A., Sharp, I. D., and Ardo, S. (2015). Experimental demonstrations of spontaneous, solar-driven photoelectrochemical water splitting. *Energy Environ. Sci.* 8, 2811–2824. doi: 10.1039/c5ee00457h

Alotaibi, B., Kong, X., Vanka, S., Woo, S. Y., Pofelski, A., Oudjedi, F., et al. (2016). Photochemical carbon dioxide reduction on Mg-doped Ga(In)N nanowire

arrays under visible light irradiation. *ACS Energy Lett.* 1, 246–252. doi: 10.1021/acsenergylett.6b00119

Alvéra, M. (2019). *Generation H: Healing the Climate with Hydrogen*. Milano: Mondadori Electa S.P.A.

Artz, J., Müller, T. E., Thenert, K., Kleinekorte, J., Meys, R., Sternberg, A., et al. (2018). Sustainable conversion of carbon dioxide: an integrated review of catalysis and life cycle assessment. *Chem. Rev.* 118, 434–504. doi: 10.1021/acs.chemrev.7b00435

Bolton, J. R. (1996). Solar photoproduction of hydrogen: a review. *Solar Energy* 57, 37–50. doi: 10.1016/0038-092x(96)00032-1

Chu, S., Li, W., Yan, Y., Hamann, T., Shih, I., Wang, D., et al. (2017). Roadmap on solar water splitting: current status and future prospects. *Nano Futures* 1:022001. doi: 10.1088/2399-1984/aa88a1

Chu, S., Ou, P. F., Ghamari, P., Vanka, S., Zhou, B. W., Shih, I., et al. (2018). Photoelectrochemical CO2 reduction into syngas with the metal/oxide interface. *J. Am. Chem. Soc.* 140, 7869–7877. doi: 10.1021/jacs.8b03067

Cox, C. R., Lee, J. Z., Nocera, D. G., and Buonassisi, T. (2014). Ten-percent solar-to-fuel conversion with nonprecious materials. *Proc. Natl. Acad. Sci. U.S.A.* 111, 14057–14061. doi: 10.1073/pnas.1414290111

Energy Transitions Commission (2018). *Mission Possible: Reaching Net-Zero Carbon Emissions From Harder-To-Abate Sectors by Mid-Century*. London: Energy Transitions Commission.

Fabian, D. M., Hu, S., Singh, N., Houle, F. A., Hisatomi, T., Domen, K., et al. (2015). Particle suspension reactors and materials for solar-driven water splitting. *Energy Environ. Sci.* 8, 2825–2850. doi: 10.1039/c5ee01434d

Fan, S., Shih, I., and Mi, Z. (2017). A monolithically integrated ingan nanowire/si tandem photoanode approaching the ideal bandgap configuration of 1.75/1.13 eV. *Adv. Energy Mater.* 7:1600952. doi: 10.1002/aenm.201600952

Fujishima, A., and Honda, K. (1972). Electrochemical photolysis of water at a semiconductor electrode. *Nature* 238:37. doi: 10.1038/238037a0

Guan, X., Chowdhury, F. A., Pant, N., Guo, L., Vayssieres, L., and Mi, Z. (2018a). Efficient unassisted overall photocatalytic seawater splitting on GaN-based nanowire arrays. *J. Phys. Chem. C* 122, 13797–13802. doi: 10.1021/acs.jpcc.8b00875

Guan, X., Chowdhury, F. A., Wang, Y., Pant, N., Vanka, S., Trudeau, M. L., et al. (2018b). Making of an industry-friendly artificial photosynthesis device. *ACS Energy Lett.* 3, 2230–2231. doi: 10.1021/acsenergylett.8b01377

Hisatomi, T., Kubota, J., and Domen, K. (2014). Recent advances in semiconductors for photocatalytic and photoelectrochemical water splitting. *Chem. Soc. Rev.* 43, 7520–7535. doi: 10.1039/c3cs60378d

Hoppe, W., Bringezu, S., and Wachter, N. (2018). Economic assessment of CO2-based methane, methanol and polyoxymethylene production. *J. CO2 Utilizat.* 27, 170–178. doi: 10.1016/j.jcou.2018.06.019

Hu, S., Xiang, C. X., Haussener, S., Berger, A. D., and Lewis, N. S. (2013). An analysis of the optimal band gaps of light absorbers in integrated tandem photoelectrochemical water-splitting systems. *Energy Environ. Sci.* 6, 2984–2993.

International Energy Agency (2018). *World Energy Outlook*. Paris: International Energy Agency.

International Energy Agency (2019). *The Future of Hydrogen*. Paris: International Energy Agency.

Kätelhön, A., Meys, R., Deutz, S., Suh, S., and Bardow, A. (2019). Climate change mitigation potential of carbon capture and utilization in the chemical industry. *Proc. Natl. Acad. Sci. U.S.A.* 116, 11187–11194. doi: 10.1073/pnas.1821029116

Kibria, M. G., Chowdhury, F. A., Zhao, S., Alotaibi, B., Trudeau, M. L., Guo, H., et al. (2015). Visible light-driven efficient overall water splitting using p-type metal-nitride nanowire arrays. *Nat. Commun.* 6:6797.

Kibria, M. G., and Mi, Z. (2016). Artificial photosynthesis using metal/nonmetal-nitride semiconductors: current status, prospects, and challenges. *J. Mater. Chem. A* 4, 2801–2820. doi: 10.1039/c5ta07364b

Kibria, M. G., Qiao, R., Yang, W., Boukahil, I., Kong, X., Chowdhury, F. A., et al. (2016). Atomic-scale origin of long-term stability and high performance of p-GaN nanowire arrays for photocatalytic overall pure water splitting. *Adv. Mater.* 28, 8388–8397. doi: 10.1002/adma.201602274

Kudo, A., and Miseki, Y. (2009). Heterogeneous photocatalyst materials for water splitting. *Chem. Soc. Rev.* 38, 253–278. doi: 10.1039/b800489g

Luo, J., Im, J.-H., Mayer, M. T., Schreier, M., Nazeeruddin, M. K., Park, N.-G., et al. (2014). Water photolysis at 12.3% efficiency via perovskite photovoltaics and Earth-abundant catalysts. *Science* 345, 1593–1596. doi: 10.1126/science.1258307

McKone, J. R., Lewis, N. S., and Gray, H. B. (2014). Will solar-driven water-splitting devices see the light of day? *Chem. Mater.* 26, 407–414. doi: 10.1021/cm4021518

Michailos, S., Mccord, S., Sick, V., Stokes, G., and Styring, P. (2019). Dimethyl ether synthesis via captured CO2 hydrogenation within the power to liquids concept: a techno-economic assessment. *Energy Conv. Manag.* 184, 262–276. doi: 10.1016/j.enconman.2019.01.046

Montoya, J. H., Seitz, L. C., Chakthranont, P., Vojvodic, A., Jaramillo, T. F., and Nørskov, J. K. (2016). Materials for solar fuels and chemicals. *Nat. Mater.* 16:70. doi: 10.1038/nmat4778

Nakamura, A., Ota, Y., Koike, K., Hidaka, Y., Nishioka, K., Sugiyama, M., et al. (2015). A 24.4% solar to hydrogen energy conversion efficiency by combining concentrator photovoltaic modules and electrochemical cells. *Appl. Phys. Express* 8:107101. doi: 10.7567/apex.8.107101

National Academies of Sciences Engineering and Medicine (2019). *Deployment of Deep Decarbonization Technologies: Proceedings of a Workshop*. Washington, DC: National Academies of Sciences Engineering and Medicine.

Pinaud, B. A., Benck, J. D., Seitz, L. C., Forman, A. J., Chen, Z. B., Deutsch, T. G., et al. (2013). Technical and economic feasibility of centralized facilities for solar hydrogen production via photocatalysis and photoelectrochemistry. *Energy Environ. Sci.* 6, 1983–2002.

Sathre, R., Scown, C. D., Morrow, W. R., Stevens, J. C., Sharp, I. D., Ager, J. W., et al. (2014). Life-cycle net energy assessment of large-scale hydrogen production via photoelectrochemical water splitting. *Energy Environ. Sci.* 7, 3264–3278. doi: 10.1039/c4ee01019a

Shan, B., Vanka, S., Li, T.-T., Troian-Gautier, L., Brennaman, M. K., Mi, Z., et al. (2019). Binary molecular-semiconductor p–n junctions for photoelectrocatalytic CO2 reduction. *Nat. Energy* 4, 290–299. doi: 10.1038/s41560-019-0345-y

Shaner, M. R., Atwater, H. A., Lewis, N. S., and Mcfarland, E. W. (2016). A comparative technoeconomic analysis of renewable hydrogen production using solar energy. *Energy Environ. Sci.* 9, 2354–2371. doi: 10.1039/c5ee02573g

Styring, P., Quadrelli, E. A., and Armstrong, K. (eds) (2015). *Carbon Dioxide Utilisation: Closing the Carbon Cycle*. Amsterdam: Elsevier.

Turner, J. A., Williams, M. C., and Rajeshwar, K. (2004). Hydrogen economy based on renewable energy sources. *Electrochem. Soc. Interface* 13:24.

Vanka, S., Arca, E., Cheng, S. B., Sun, K., Botton, G. A., Teeter, G., et al. (2018). High efficiency Si photocathode protected by multifunctional GaN nanostructures. *Nano Lett.* 18, 6530–6537. doi: 10.1021/acs.nanolett.8b03087

Vanka, S., Sun, K., Zeng, G., Pham, T. A., Toma, F. M., Ogitsu, T., et al. (2019). Long-term stability studies of a semiconductor photoelectrode in three-electrode configuration. *J. Mater. Chem. A* 7:27612. doi: 10.1039/c9ta09926c

Zhou, B., Kong, X., Vanka, S., Cheng, S., Pant, N., Chu, S., et al. (2019). A GaN:Sn nanoarchitecture integrated on a silicon platform for converting CO2 to HCOOH by photoelectrocatalysis. *Energy Environ. Sci.* 12, 2842–2848. doi: 10.1039/c9ee01339c

Zhou, B., Ou, P., Pant, N., Cheng, S., Vanka, S., Chu, S., et al. (2020). Highly efficient binary copper-iron catalyst for photoelectrochemical carbon dioxide reduction toward methane. *Proc. Natl. Acad. Sci. U.S.A.* 117, 1330–1338. doi: 10.1073/pnas.1911159117

Conflict of Interest: ZM is the co-founder of NS Nanotech Inc., and NX Fuels, Inc., which are in the businesses of developing and commercializing nanowire-based light emitting devices and artificial photosynthesis technology.

The remaining author declares that the research was conducted in the absence of any commercial or financial relationships that could be construed as a potential conflict of interest.

frontiers in Energy Research

ORIGINAL RESEARCH
published: 14 July 2020
doi: 10.3389/fenrg.2020.00151

Improved Flexibility and Economics of Combined Cycles by Power to Gas

Manuel Bailera[1], Begoña Peña[1], Pilar Lisbona[2] and Luis M. Romeo[1]*

[1] Escuela de Ingeniería y Arquitectura, Universidad de Zaragoza, Zaragoza, Spain, [2] Fundación Agencia Aragonesa Para la Investigación y el Desarrollo (ARAID), Zaragoza, Spain

Massive penetration of renewable energy in the energy systems is required to comply with existing CO_2 regulations. Considering current power pools, large shares of renewable energy sources imply strong efficiency and economic penalties in fossil fuel power plants as they are mainly operated to regulate the system and constant shutdowns are expected. Under this framework, the integration of a combined cycle power plant (CCPP) with an energy storage technology such as power to gas (PtG) is proposed to virtually reduce its minimum complaint load through the diversion of instantaneous excess electricity. Power to gas produces hydrogen through water electrolysis, which is later combined with CO_2 to produce methane. The main novelty of this study relies in the improved flexibility and economics of combined cycles by means of using power to gas as a tool to reduce the minimum complaint load. The principal objective of the study is the quantification of cost reduction under different scenarios of shutdowns and conventional start-ups. The case study analyses a combined cycle of 400 MW_e gross power with a minimum complaint load of 30% that can be virtually reduced to 20% by means of a 40- MW_e power-to-gas plant. Eight scenarios are defined to compare the reference case of conventional operation under hot, warm, and cold start-ups with power-to-gas-assisted operation. Additionally, PtG-assisted operation scenarios are analyzed with different loads (30–50–70%). These scenarios also include the consideration of a temporary peak of demand occurring in a period in which dispatch is below the minimum complaint load. Under this situation, the response time of conventional plants is very limited, while PtG-assisted CCPP can rapidly satisfy the peak. The techno-economic model quantifies the required fuel, gross and net power, and emissions as well as total costs and incomes under each scenario and net differential profit in an hourly basis. The analysis of the obtained results does not recommend the operation of the PtG-assisted CCPP at minimum complaint load for hot, warm, or cold start-ups. However, important marginal profits are achieved with the proposed system for part-loads operation over 50% for every sort of start-up, avoiding shutdowns and extending the capacity factor.

Keywords: flexibility, energy storage, power to gas, combined cycle, synthetic methane, CO_2 utilization

OPEN ACCESS

Edited by:
Tao Wang,
Zhejiang University, China

Reviewed by:
Menglian Zheng,
Zhejiang University, China
Robert J. Braun,
Colorado School of Mines, United States

****Correspondence:***
Manuel Bailera
mbailera@unizar.es

Specialty section:
This article was submitted to Carbon Capture, Storage, and Utilization, a section of the journal Frontiers in Energy Research

Received: *31 March 2020*
Accepted: *16 June 2020*
Published: *14 July 2020*

Citation:
Bailera M, Peña B, Lisbona P and Romeo LM (2020) Improved Flexibility and Economics of Combined Cycles by Power to Gas. Front. Energy Res. 8:151. doi: 10.3389/fenrg.2020.00151

Abbreviations: CCPP, combined cycle power plants; FFPP, fossil fuel power plants; FSNL, full speed no load; FL, full load; MCL, minimum complaint load; NSNL, no speed no load; O&M, operation and maintenance; PtG, power to gas; REF, reference case; RES, renewable energy sources; VMCL, virtual minimum complaint load.

INTRODUCTION

Aiming to reduce the greenhouse gas emissions below 40% of the 1990 levels (Paris Agreement of 2015) (United Nations Framework Convention on Climate Change [UNFCCC], 2015), the European Directive 2018/2001 promotes reaching 32% share of renewable energy sources (RES) by 2030 (European Commission, 2018). Moreover, RES share in European electricity production is expected to increase to 53% by 2050 (Capros et al., 2016). However, the transition toward a decarbonized society implies large amounts of variable RES in the energy system, wherein the balance between power generation and demand is difficult (Bailera and Lisbona, 2018; Lisbona et al., 2018). The problem of optimal dispatch and its connection with renewables or natural gas grids is being profusely analyzed in literature (Chen et al., 2018; He et al., 2018, 2020; Wang et al., 2019; Naval et al., 2020).

Traditionally, fossil-based regulation kept the frequency and the voltage of the grid within a stable range. Nowadays, power pools favor RES to the detriment of fossil-based electricity. However, generators and system operators control just 5–10% of the dispatch in RES power plants (the level of control in Spain is about 5%, in Sweden 6%, and in Germany 7%) (Pierre et al., 2011). Therefore, fossil fuel power plants (FFPP) are compelled to perform many start-ups, shutdowns, and load variations to meet demand. These cycling processes deteriorate the equipment, drop the efficiency, worsen specific CO_2 emissions, and increase the costs (Gilbert and Sovacool, 2017).

The implications of this issue have been analyzed in literature for energy systems worldwide. In northeastern China, Yin et al. (2017) studied the benefits of curtailing some wind power. They found that the overall income is optimized when the daily average wind curtailment is 2.17%. Despite curtailing some RES, the CO_2 emissions do not increase with respect to a scenario in which wind power is completely integrated in the grid. The extra amount of CO_2 that would be saved using the surplus wind power is canceled out by the high specific emissions of peak regulation in FFPP.

In Europe, de Groot et al. (2017) analyzed how the share of variable renewable technologies (VRE) influences on the performance of FFPP for different scenarios from 2005 to 2014 (de Groot et al., 2017). When renewable penetration is higher than 15%, they found that the yearly average efficiency of the combined cycle power plant (CCPP) drops by 20 points since full-load operating hours diminishes by 53%. Besides that, Van den Bergh and Delarue (2015) state that the implications of the overall cycling process (i.e., direct start, indirect start, outages, ramping, and efficiency decrease) are overlooked by system operators as they consider only the direct start. If the system operator considered total cycling costs when developing the optimal schedule for 25–40% VRE penetrations, the annual cycling costs of power plants could be reduced at 40%.

In western United States, Lew et al. (2013) studied scenarios with wind and solar penetrations up to 33%. They showed that the increment of emissions associated to cycling processes (+ 0.2% of total CO_2 emissions) has a small impact on the CO_2 saved because of the curtailment of fossil fuels (-34% of total CO_2 emissions). However, the cycling cost may increase to 1.28 US$ per MWh, which is not negligible in the context of reduced generation and revenue.

Actually, incomes from electricity will not cover production costs even if enough flexibility is achieved (Sjoerd Brouwer et al., 2015). Hentschel et al. (2016) showed that the profits barely change with faster ramp rates in combined cycles. Only the reduction of the minimum complaint load (MCL), the minimum load at which the plant can reliably operate before being disconnected out of the grid, may lead to relevant savings, thanks to avoiding the curtailment of incomes (Hentschel et al., 2016; Romeo et al., 2018). Under this framework, the authors propose to use power to gas (PtG) technology to virtually reduce the MCL of a given combined cycle. Instead of shutting down the combined cycle, the electricity production that exceeds demand may be diverted to the PtG energy storage. A similar concept was previously assessed by the authors, in which PtG displaces nuclear power to avoid part-load operation in coal-fired power plants (the average annual efficiency of the FFPP increased from 33.2 to 35.2%) (Bailera et al., 2019c).

Power to gas aggregates different technologies through which electricity is chemically stored in the form of gaseous or liquid chemicals and fuels (Andika et al., 2018; Brynolf et al., 2018; Buttler and Spliethoff, 2018; Allman et al., 2019; Anghilante et al., 2019). Among them, power to methane is one of the most promising long-term storage technologies for the versatility regarding applications and the use of current gas network infrastructures (Götz et al., 2015; Bailera and Lisbona, 2018; Eveloy and Gebreegziabher, 2018; Lewandowska-Bernat and Desideri, 2018; Wulf et al., 2018; Thema et al., 2019). These technologies not only will play an important role in decarbonization of the industry (Baier et al., 2018; Cormos et al., 2018; Di Salvo and Wei, 2019; Chauvy et al., 2020; Rosenfeld et al., 2020), transport (Schemme et al., 2017; Colbertaldo et al., 2019), and building (Bailera et al., 2019b) but also will be needed to balance the power generation with demand under high penetration of variable renewable energies (Bailera and Lisbona, 2018; Eveloy and Gebreegziabher, 2018; Wulf et al., 2018).

In the present work, power to gas uses the part of electricity that the CCPP cannot sell at the moment to produce hydrogen through water electrolysis. Then, this hydrogen is combined with CO_2 to produce methane through methanation (Gahleitner, 2013; Giglio et al., 2015; Götz et al., 2015; Jensen et al., 2015; Vandewalle et al., 2015; Bailera et al., 2017a,b; Becker et al., 2019). Several options have been proposed in literature for the supply of CO_2. Biogas is an attractive carbon source because it avoids the carbon capture stage and methanation heat could be used in the digestion process (Angelidaki et al., 2018; Anghilante et al., 2019). Nevertheless, the most common and simplest integration that directly uses CO_2 from carbon capture in the combined cycle is considered as more realistic for the application investigated. Besides that, in this work, the synthetic natural gas coming from the PtG process is used as fuel for the combined cycle itself to reduce the operating cost.

The novelty of this paper underlies in the improved flexibility and economics of combined cycles by using power to gas as method to reduce the minimum complaint load. The objective

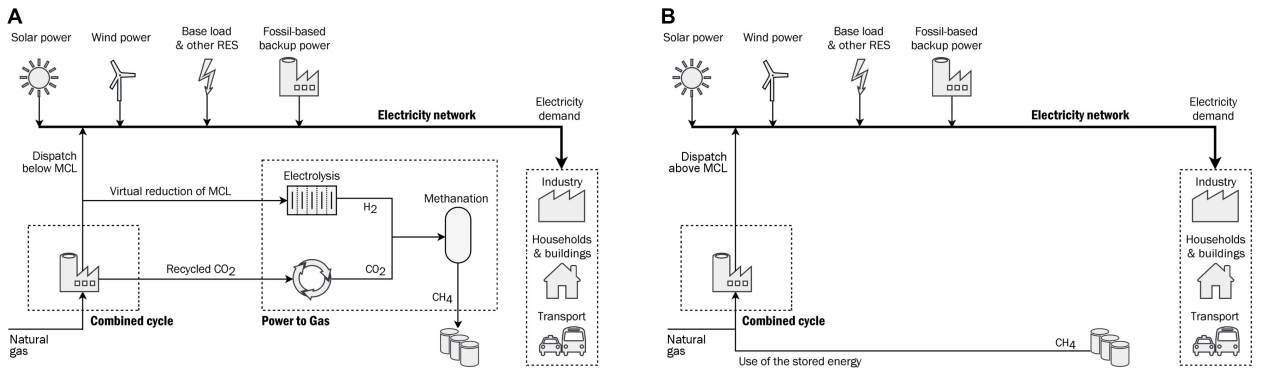

FIGURE 1 | Integration of power to gas and combined cycle power plant in the energy system: **(A)** Dispatch below minimum complaint load (MCL) diverting surplus electricity to power to gas. **(B)** Dispatch above MCL using stored energy.

is to compare and quantify this proposal with different scenarios of shutdowns and conventional start-ups.

CASE STUDY

In this study, we assess a combined cycle of 400 MW_e gross power. The auxiliaries of the plant consume 2.5% of this power output. The minimum complaint load is 30% (Nalbandian-Sugden, 2016), but it can be virtually reduced to 20% by using PtG. This power-to-gas plant manages up to 40 MW_e (i.e., 10% of the gross power of the CCPP). The overall efficiency of the energy storage is assumed constant at 60% (power to methane), accounting for polymer electrolyte membrane electrolysis (75% higher heating value, HHV) (Matute et al., 2019) and methanation (80% HHV) (Bailera et al., 2019a). **Figure 1** illustrates the system under study.

Operation of Combined Cycles

A power plant must follow different steps to modify its operating load. These processes depend on the start and end points between which the load is varied. This section describes the main cycling processes taken into account for the study and establishes some important assumptions during the operation of the combined cycle (Gonzalez-Salazar et al., 2018).

- Process 1 – start-up: The first process is the start-up of the plant. The turbine, which initially is stopped ("no speed, no load"), increases its speed up to synchronize the generator with the grid frequency ("full speed, no load"). Then, the load raises to the minimum complaint loads that fulfill safety and emission requirements. From this point upwards, the combined cycle may start generating power (**Figure 2**). The duration of the start-up varies, depending on how long the power plant has been stopped. Standby periods are classified in hot start (0–12 h offline), warm start (12–48 h offline), and cold start (> 48 h offline) (Smith et al., 2020). A standby of 6 h is considered for hot start, 24 h for warm start, and 48 h for cold start. We have also assumed 1-h period to full load for hot start, 2-h period to full load for warm start, and 3-h period to full load for cold start (Smith et al., 2020). Besides that, during start-up, the power output is constrained to the last one-third of the time, at a load equal to the MCL.
- Process 2 – ramping up/down: After start-up, the combined cycle can modify its load to any point between MCL and full load (FL) to satisfy demand. We assume 6% FL/min ramp rate (Gonzalez-Salazar et al., 2018), so passing from MCL to FL takes around 10–15 min. This duration is much shorter than for other processes and therefore neglected in the economic analysis.
- Process 3 – full load: Process 3 represents nominal operation, at which the efficiency of the power plant is the highest and the specific emissions are the lowest.
- Process 4 – minimum load: Process 4 describes the operation at minimum complaint load. This point has the lowest efficiency and the highest specific emissions.
- Process 5 – shutdown: When dispatch is no longer required, the combined cycle has to shut down. The load diminishes at 6% FL/min, so it takes 15–20 min to stop the plant when operating at full load. As simplification, we have also neglected the duration of this process for economic analysis.
- Process 6 – no operation: After shutdown, the combined cycle remains out of operation. There are no incomes throughout this period, so its duration should be minimized. Power to gas will help in avoiding this situation whenever demand is between 30% (MCL) and 20% of full load.

METHODOLOGY

The methodology section covers the scenarios of operation that are analyzed in this study and the techno-economical models used to characterize them. For each hour of the studied period, the load is assumed depending on the scenario described below. With the load, it is possible to calculate the net power production and input energy required. Hourly costs are calculated with this data. When power to gas is running, its power is subtracted from

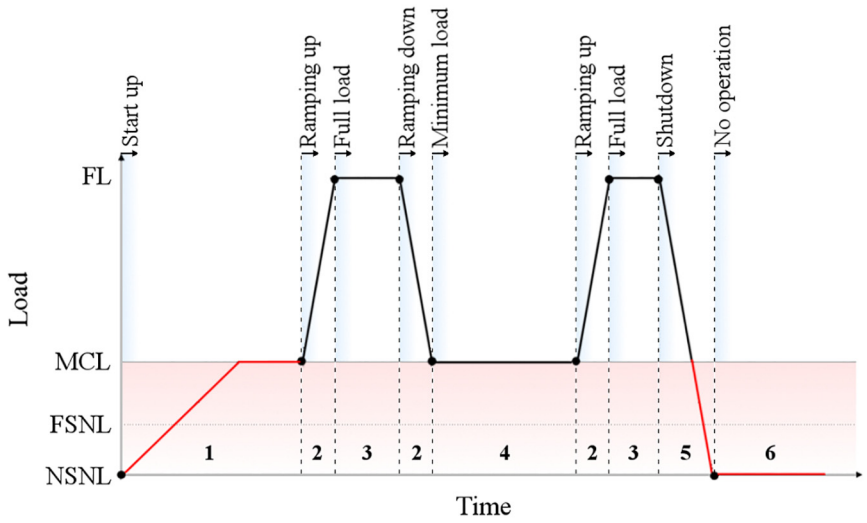

FIGURE 2 | Types of process during the operation of a combined cycle.

net power and natural gas is stored to be used in the full-load hours. The addition of hourly cost and incomes for the number of operational hours of the period and its comparison with the reference case are used as key variables of the work.

Scenarios

The definition of these scenarios allows the comparison of the conventional operation of combined cycles with the PtG-assisted operation of the hybrid system for situations in which electricity demand falls below the minimum complaint load (< 30% FL, i.e., < 120 MW_e). This situation may be due to an increase in RES production or simply a demand reduction. In the first case, it is supposed that there is no RES curtailment. Conventional CCPP have to shut down and follow a "no operation" period in which there are no incomes. On the other side, power-to-gas hybridization avoids shutdown if demand is still above 20% FL. The hybrid CCPP keeps operating at MCL, dispatching the 20% FL demanded by the grid (80 MW_e) and diverting the remaining 10% FL (40 MW_e) to the power-to-gas system (**Figure 3**). It has been assumed that the electrolyzers operation is on or off and there is no part-load operation for this equipment. Moreover, the time spent to get back to full-load operation is shorter in the hybrid system since there is no start-up.

The outage duration under conventional CCPP conditions determines the type of start-up (hot, warm, or cold start). According to that, eight scenarios are defined and grouped to compare the reference case of conventional operation with situations that take advantage of the power-to-gas storage system (**Table 1**). The time framework within which the analysis is performed (total time of scenario) is fixed in each group to compare equivalent situations. Additionally, scenarios 2, 4, and 7, corresponding to PtG-assisted operation, are analyzed with different loads (30, 50, and 70%). These scenarios are realistic as, although MCL is the typical scenario, it is also usual that the operator asks for increasing loads in the remaining (non-stopped) installations to meet the demand.

A third type of operation is analyzed in scenarios 5 and 8: a temporary peak of demand taking place in the middle of a dispatch that is below the minimum complaint load is considered. Under this situation, the response time of conventional CCPP is very limited since the plant should carry out a warm or cold start-up (**Figure 4**). Contrarily, the PtG-assisted CCPP is able to satisfy the peak rapidly since the plant keeps working at the virtual MCL. In the quantitative analysis, electricity is diverted to PtG until full-load operation is achieved, as depicted in **Figure 4**.

Efficiency Penalty and Emissions

The technical model quantifies the fuel required, the gross/net power produced, and the emissions, by energy and mass balances, in an hourly basis. All these values depend on the load at which the plant operates due to efficiency changes. It should be noted that despite the virtual MCL of the PtG-assisted CCPP being 20%, the actual load at which the plant operates in those situations is 30%.

Different equations to describe the variation in efficiency as a function of partial load can be found in literature (Sjoerd Brouwer et al., 2015). In combined cycles, a decrease of eight to 16 percentage points from full load to MCL is typical (Van den Bergh and Delarue, 2015; de Groot et al., 2017). For this study, we adopt Equation 1, a polynomic curve for the gross efficiency, which is adjusted to a set of different data by de Groot et al. (2017).

$$\eta_{gross} = -0.272 \cdot load^2 + 0.5742 \cdot load + 0.282 \qquad (1)$$

Data calculated from Equation (1), for the 400 MW_e CCPP of this study, are presented in **Table 2**. We assume that the specific CO_2 emission at full load is 337.7 kg/MWh. As thermal efficiency worsen, these emissions increase to 459.0 kg/MWh for the minimum complaint load (30%).

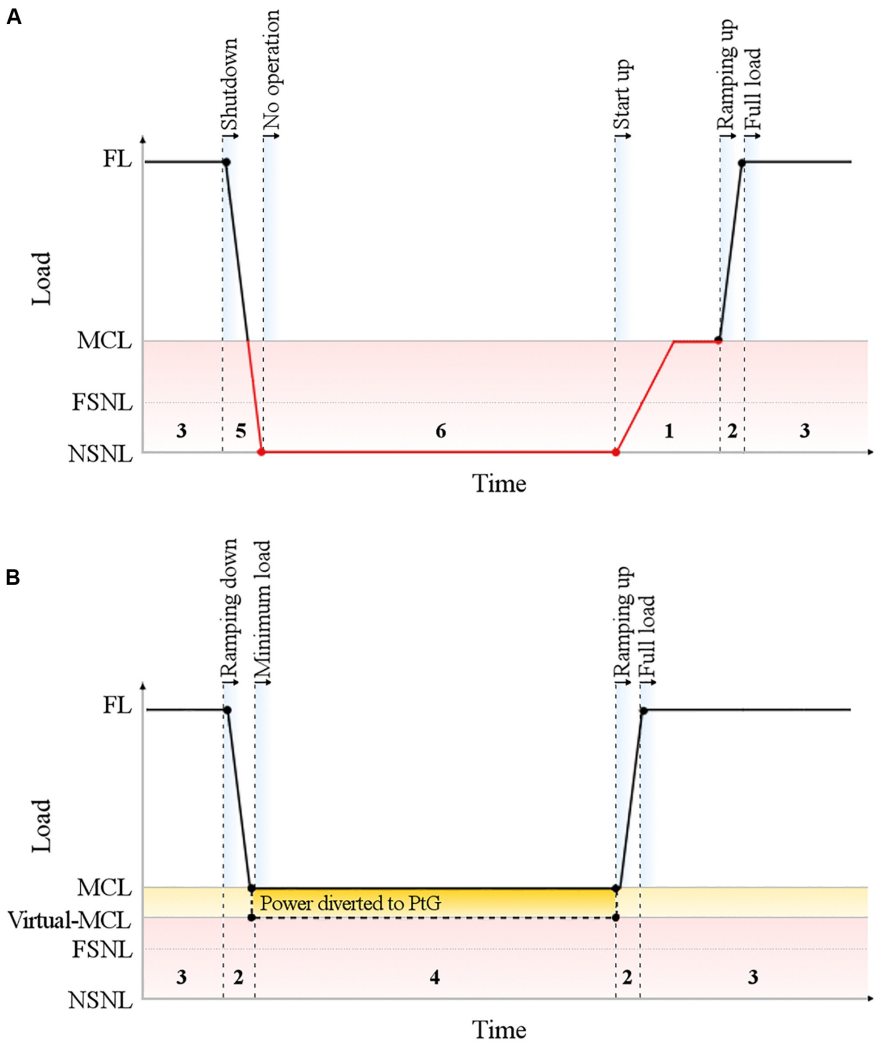

FIGURE 3 | Comparison between **(A)** conventional combined cycle power plant (CCPP) and **(B)** PtG-assisted CCPP while following an electric demand that falls below the minimum complaint load.

TABLE 1 | Selected scenarios for this work and types of operation.

Scenario	1	2	3	4	5	6	7	8
Outage (h)	6		24			48		
Start-up (h)	1 h (hot)		2 h (warm)			3 h (cold)		
Analyzed time framework (h)	24		48			96		
Comparison of:								
Conventional operation	✓	x	✓	x	x	✓	x	x
PtG-assisted operation	x	✓	x	✓	✓	x	✓	✓
PtG-assisted operation + load peak (peak duration)	x	x	x	x	✓ (12 h)*	x	x	✓ (24 h)*

**Duration of the peak of demand.*

Economics

In the economic model, we calculate the total cost (Equation 2) and incomes (Equation 3) of each type of operation, and then we compared them through the net differential profit. The model is defined in an hourly basis (e.g., hourly OPEX, CAPEX, CO_2 taxes, and fuel cost), as for the technical model. Besides that, for the specific situation in which the PtG-assisted CCPP works at the virtual MCL, we consider that the plant operating costs correspond to 30% part load (actual MCL), but the sale of electricity is limited to 20% of the power (virtual MCL).

$$\text{Total cost}\left[\frac{€}{h}\right] = \text{OPEX}\left[\frac{€}{h}\right] + \text{CAPEX}\left[\frac{€}{h}\right] \quad (2)$$

$$\text{Incomes } [€] = \text{net electricity production}\left[\text{kWh}\right] \cdot \text{electricity price}\left[\frac{€}{\text{kWh}}\right] \quad (3)$$

The CAPEX is assumed as 800 €/kW_e for the conventional CCPP (Nalbandian-Sugden, 2016) and 2,600 €/kW_e for the power-to-gas plant (Schiebahn et al., 2015; Lee et al., 2019). This value is a conservative figure that includes the sum of

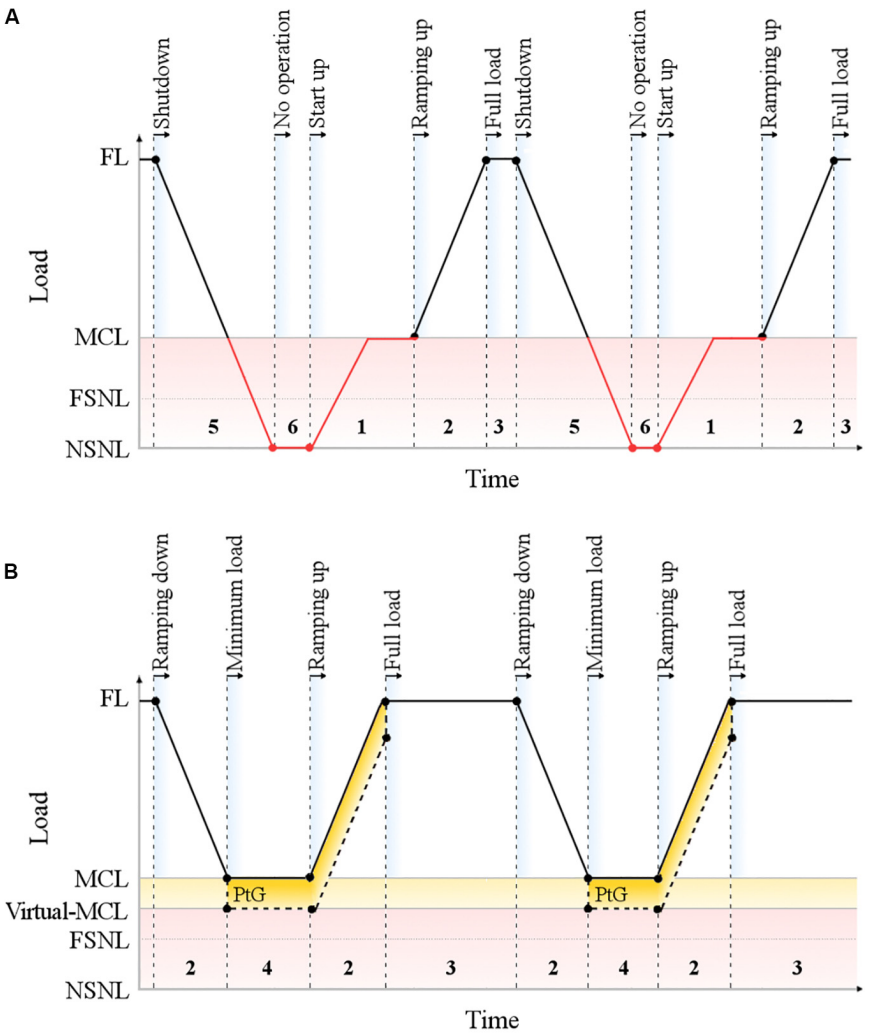

FIGURE 4 | Comparison between **(A)** conventional combined cycle power plant (CCPP) and **(B)** PtG-assisted CCPP while satisfying a peak of demand that takes place in the middle of a dispatch below the minimum complaint load.

the electrolyzer cost, between 500 (Schiebahn et al., 2015) and 1,200–2,000 €/kW_e (Lee et al., 2019), and methanation reactor plus compressors (Schiebahn et al., 2015). Moreover, regarding methane storage, the following assumptions can be made. The longest shutdown considered is 48 h, which corresponds to a storage of about 41.5 tons of methane (i.e., 576 MWh). The current commercial tanks for liquefied natural gas (LNG) are in the range of 30–50 tons (The Oxford Institute for Energy Studies, 2018; Linde, 2020), so we could even manage two to three consecutive 48-h shutdowns without emptying the tank. Therefore, the size proposed for our facility keeps within reasonable limits. In terms of cost, liquefaction plants range between 530 and 1,230 €/tpa (tons per annum) (The Oxford Institute for Energy Studies, 2018). As our plant requires a nominal capacity of liquefaction of 0.86 t/h, the corresponding LNG plant would cost 6.8 M€ (assuming 7,500 operating hours and 1,060 €/tpa for a conventional plant, although the liquefaction process in the PtG plant would operate much less hours). Thus, this cost is considered to be already included in the total cost of the PtG plant, which amounts to 104 M€.

TABLE 2 | Performance of a 400-MW_e combined cycle power plant *vs.* load.

Load factor (%)	Thermal efficiency gross (%)	Natural gas input power (MW_{th})	Specific CO_2 emissions (kg_{CO2}/MWh)
100	58.42	684.7	337.7
90	57.85	622.3	341.0
80	56.73	564.1	347.8
70	55.07	508.5	358.3
60	52.86	454.0	373.2
50	50.11	399.1	393.7
40	46.82	341.8	421.4
30	42.98	279.2	459.0

Regarding operation costs, fixed OPEX, fuel cost, and shutdowns are considered (Equation 4). Fixed OPEX is set at 25,000 €/MW_e/y (ACIL Tasman, 2009). Fuel cost (natural gas) is valued at 25 €/MWh_e, according to BP annual report and Netherlands market (BP Statistical Review of World Energy, 2019). Shutdowns are estimated at 14,000, 22,000, and 32,000 € for hot, warm, and cold start-ups, respectively (Kumar et al., 2012). The lifetime of the plant is assumed to be 25 years.

$$\text{OPEX}\left[\frac{€}{h}\right] = \text{fixed OPEX}\left[\frac{€}{h}\right] + \text{fuel costs}\left[\frac{€}{h}\right] \quad (4)$$

Thus, the specific cost of producing electricity is calculated by adding the OPEX and the CAPEX, distributed throughout 25 years. This electricity production cost ranges from 48.5 €/MWh_e (full load) to 72.1 €/MWh_e (MCL); for this reason, the electricity price has been set at 65 €/MWh. With lower values, installation is not feasible as the production costs would be higher than the selling price. This value has no important relevance because it also affects the reference case, and in every case, there is a reduction in the electricity production cost. Evidently, electricity price varies considerably throughout the time of day and country, but it is out of the scope of this first analysis to deal with every possibility of price, depending if the power-to-gas installation is in operation or not. We considered to isolate the effect of variable pool prices from the effect of the proposed idea. In **Table 3**, all the technical and economic data used in the model to calculate these values are gathered.

RESULTS

In this section, each conventional shutdown is compared with the continuous operation at MCL through the utilization of the power-to-gas storage system. The technical and the economic results are gathered in **Tables 4–8** for shutdowns of 6-, 12-, and 48-h duration in time frames of 24, 48, and 96 h, respectively.

TABLE 3 | Main assumptions of the model.

Variable	Value	References
Technical		
Gross power plant output (MW_e)	400	
Ancillaries consumption (%)	2.5	
Net power plant output (MW_e)	390	
Power to gas capacity (MW_e)	40	
Electrolyzer efficiency (%)	75	Matute et al., 2019
Economic		
CAPEX power plant (€/kW_e)	800	Nalbandian-Sugden, 2016
CAPEX power to gas (€/kW_e)	2,600	Schiebahn et al., 2015
Fixed OPEX (€/MW_e/y)	25,000	ACIL Tasman, 2009
Shutdown cost (€)		
Hot start-up	14,000	Kumar et al., 2012
Warm start-up	22,000	Kumar et al., 2012
Cold start-up	32,000	Kumar et al., 2012
Natural gas price (€/MWh_{th})	25	BP Statistical Review of World Energy, 2019
Electricity price (€/MWh_e)	65	Eurostat Statistics Explained, 2019

Scenarios 1 and 2: Hot Start-Up

For the reference case of short shutdown (6 h), a small economic loss is obtained with a specific cost of electricity at 65.44 €/MWh and CO_2 emissions at 4% above under full-load conditions. When the PtG system operates and the plant load is kept at minimum complaint load (30%), the profit is not significant and the specific cost of electricity is very similar to that obtained in the reference case. Total and specific emissions of CO_2 increase to 13.3 and 5.8%, respectively, due to the higher consumption of fuel and the lower energy efficiency.

If the PtG storage system remains in operation, the trend drastically changes as plant load is raised up to 50 or 70%. Specific CO_2 emissions diminish with regards the previous case (scenario 2a), being just 2% above the reference case for scenario 2c (70% FL). An important economic improvement is achieved as the net benefit now becomes positive and increases with load, reaching a marginal profit of roughly 700 and 1,400 €/h, respectively. The specific cost of electricity decreases by more than 2 and 4 €/MWh with respect to the reference scenario, which means a reduction of 3.4 and 6.6%, respectively. In all cases, the cumulative effect of the number of cycles incurred by the turbine and the heat recovery steam generator could be significant in cases of shutdowns and start-ups. This concept would certainly reduce the O&M costs of the combined cycle. From a cautious point of view, calculations do not consider this savings.

The respective marginal profits are above 16,000 and 34,000 €, respectively, per avoided shutdown for a period of 24 h. The significant increase in electricity sale incomes transforms the conventional shutdown situation with economic losses into a profitable operation. It has to be noted that the economic improvement of the alternative modes of operation (continuous MCL *via* PtG) is not directly related to the stored energy but to the avoidance of shutdown itself.

Scenarios 3 and 4: Warm Start-Up

In reference scenario 3, warm start-up with an outage period of 24 h is analyzed in a time frame of 48 h. Unlike what happened in scenario 1, the losses are now significant, with a negative net profit above 91,000 €. While the CO_2 emissions are quite similar, the specific cost of electricity increases up to 75.66 €/MWh, being 16% higher than that for hot start-up.

If the PtG system operates with minimum complain plant load (30%), the net profit is even more negative than in scenario 3, while the specific cost of electricity is slightly lower. The marginal profit with respect to the reference scenario is negative in this case (-119 €/h). Total and specific emissions of CO_2 increase to 42.9 and 14.5%, respectively, due to the higher consumption of fuel and a drop in energy efficiency of seven percentage points (pp).

Nevertheless, the outlook changes if the plant load increases (scenarios 4b–4c). Energy efficiency improves to 2 pp for 50% part-load operation and 2 pp more for 70% part-load with regards scenario 4a. Specific emissions decrease but are still 10 and 6% above the reference case, respectively. The economic results are

TABLE 4 | Conventional combined cycle power plant (CCPP) vs. PtG-assisted CCPP; hot start-up.

Summary of results		Reference 24 h			
		Scenario 1 Reference Hot 6 h	Scenario 2a PtG hot 6 h Load 30%	Scenario 2b PtG hot 6 h Load 50%	Scenario 2c PtG hot 6 h Load 70%
Input natural gas	MWh_{th}	11, 513.58	13, 044.85	14, 004.13	14, 879.00
Output energy	MWh_e	6, 474.00	6, 936.00	7, 560.00	8, 184.00
Energy efficiency	%	56.2	53.2	54.0	55.0
Total costs	€	423, 661.07	452, 930.19	477, 775.40	500, 434.55
CO_2 emissions	t CO_2	2, 271.40	2, 573.49	2, 762.73	2, 935.33
Specific CO_2 emissions	kg CO_2/MWh	350.85	371.03	365.44	358.67
Specific electricity cost	€/MWh	65.44	65.30	63.20	61.15
Energy, PtG	MWh		240.00	240.00	240.00
CH_4 energy storage	MWh		144.00	144.00	144.00
Cost increment	€		29, 269.12	54, 114.33	76, 773.47
Electricity increment	MWh_e		462.00	1, 086.00	1, 710.00
Additional electricity cost	€/MWh		63.35	49.83	44.90
Income from electricity (65€/MWh)	€	420, 810.00	450, 840.00	491, 400.00	531, 960.00
Profit	€	−2, 851.07	−2, 090.19	13, 624.60	31, 525.45
Marginal profit	€		760.88	16, 475.67	34, 376.53
Marginal profit/hour	€/h		31.70	686.49	1, 432.36

TABLE 5 | Conventional combined cycle power plant (CCPP) vs. PtG-assisted CCPP; warm start-up.

Summary of results		Reference 48 h			
		Scenario 3 Reference Warm 24 h	Scenario 4a Warm 12 h Load 30%	Scenario 4b Warm 12 h Load 50%	Scenario 4c Warm 12 h Load 70%
Input natural gas	MWh_{th}	15, 216.28	21, 746.86	24, 864.50	27, 707.83
Output energy	MWh_e	8, 541.00	10, 662.00	12, 690.00	14, 718.00
Total costs	€	646, 238.52	789, 820.90	870, 567.83	944, 210.05
CO_2 emissions	t CO_2	3, 001.87	4, 290.22	4, 905.27	5, 466.20
Specific CO_2 emissions	kg CO_2/MWh	351.47	402.38	386.55	371.40
Specific electricity cost	€/MWh	75.66	74.08	68.60	64.15
Energy PtG	MWh		480.00	480.00	480.00
CH_4 energy storage	MWh		288.00	288.00	288.00
Cost increment	€		143, 582.38	224, 329.31	297, 971.53
Electricity increment	MWh_e		2, 121.00	4, 149.00	6, 177.00
Additional electricity cost	€/MWh		67.70	54.07	48.24
Income from electricity (65€/MWh)	€	555, 165.00	693, 030.00	824, 850.00	956, 670.00
Profit	€	−91, 073.52	−96, 790.90	−45, 717.83	12, 459.95
Marginal profit	€		−5, 717.38	45, 355.69	103, 533.47
Marginal profit/hour	€/h		−119.11	944.91	2, 156.95

now positive. The specific cost of electricity shows a reduction of 9 and 15%, respectively. In spite of the negative net profit for scenario 4b, marginal profit is positive in both cases: 945 and 2,157 € per hour, respectively, which means total marginal profits of 45,000 and 103,000 € in the reference time framework of 48 h. These figures are 38 and 50% higher than those corresponding to the hot start-up.

As in the previous analysis, the economic improvement under the last two scenarios with continuous operation *via* PtG is not directly related to synthetic methane production but to the avoidance of shutdown itself.

Scenarios 6 and 7: Cold Start-Up

In reference scenario 6, long outages of 48 h related to cold start-ups are assessed within a total time frame of 96 h. The energy efficiency is similar to scenarios 1 and 3, while specific CO_2 emissions are slightly lower due to the different time intervals considered. The specific cost of electricity is 73.83 €/MWh, being 13% higher than that for the hot start-up. As it occurs in scenario 3, the losses are very important, with a negative net profit above 155,000 €.

When the PtG system is included in the analysis with minimum complain plant load (30%), the net profit is even

TABLE 6 | Conventional combined cycle power plant (CCPP) vs. PtG-assisted CCPP; cold start-up.

Summary of results		Reference 96 h			
		Scenario 6 Reference Cold 48 h	Scenario 7a Cold 48 h Load 30%	Scenario 7b Cold 48 h Load 50%	Scenario 7c Cold 48 h Load 70%
Input natural gas	MWh_{th}	31,243.52	44,304.69	50,300.16	55,768.10
Output energy	MWh_e	17,628.00	21,870.00	25,770.00	29,670.00
Total costs	€	1,301,481	1,607,765	1,763,048	1,904,667
CO_2 emissions	t CO_2	6,163.7	8,740.43	9,923.21	11,001.93
Specific CO_2 emissions	kg CO_2/MWh	349.66	399.65	385.07	370.81
Specific electricity cost	€/MWh	73.83	73.51	68.41	64.20
Energy PtG	MWh		960.00	960.00	960.00
CH_4 energy storage	MWh		576.00	576.00	576.00
Cost increment	€		306,284.42	461,566.98	603,186.63
Electricity increment	MWh_e		4,242.00	8,142.00	12,042.00
Additional electricity cost	€/MWh		72.20	56.69	50.09
Income from electricity (65€/MWh)	€	1,145,820	1,421,550	1,675,050	1,928,550
Profit	€	-155,661	-186,215	-87,998	23,882
Marginal profit	€		-30,554	67,663	179,543
Marginal profit/hour	€/h		-318.28	704.82	1,870.24

TABLE 7 | Comparison of different operation modes during the period of warm start-up.

Summary of results		Reference 48 h		
		Scenario 3 Reference Warm 24 h	Scenario 4a Warm 12 h Load 30%	Scenario 5 Warm 12 h Load 30–100%
Input natural gas	MWh_{th}	15, 216.28	21, 746.86	26, 900.68
Output energy	MWh_e	8, 541.00	10, 662.00	14, 418.00
Total costs	€	646, 238.52	789, 820.90	923, 298.42
CO_2 emissions	t CO_2	3, 001.87	4, 290.22	5, 306.96
Specific CO_2 emissions	kg CO_2/MWh	351.47	402.38	368.08
Specific electricity cost	€/MWh	75.66	74.08	64.04
Energy PtG	MWh		480.00	480.00
CH_4 energy storage	MWh		288.00	288.00
Cost increment	€		143, 582.38	277, 059.90
Electricity increment	MWh_e		2, 121.00	5, 877.00
Additional electricity cost	€/MWh		67.70	47.14
Income from electricity (65€/MWh)	€	555, 165.00	693, 030.00	937, 170.00
Profit	€	−91, 073.52	−96, 790.90	13, 871.58
Marginal profit	€		−5, 717.38	104, 945.10
Marginal profit/hour	€/h		−119.11	2, 186.36

more negative than in scenario 6, while the specific cost of electricity is very similar. The marginal profit with respect to the reference situation is negative for scenario 7a (-318 €/h). Total and specific emissions of CO_2 increase to 42 and 14%, respectively, due to the higher consumption of fuel and a drop in energy efficiency of 7 pp.

As presented for warm start-up, the results improve if plant load increases (scenarios 7b–7c). Energy efficiency improves by 2 pp for 50% part-load operation and 2 pp more for 70% part-load with regards scenario 7a. Specific emissions decrease but are still 10 and 6% above the reference case, respectively. The specific cost of electricity shows a reduction greater than 5 and 9 €/MWh at 50 and 70% part load, respectively. The marginal profit is positive in both cases: 705 and 1,870 € per hour, respectively, which means total marginal profits of 67,663 and 179,543 € per long shutdown avoided in the reference time framework of 96 h. For scenarios 7b and 7c, the total marginal profits are four and five times greater than the equivalent of hot start-up, respectively. As in the previous analysis, the economic improvement is mainly caused by the avoidance of shutdown itself.

Sensitivity Analysis

The study presented in the previous sections has compared the economic and the environmental impact of avoiding hot,

warm, and cold shutdowns through the utilization of a power-to-gas energy storage system. From the results, it is deduced that the most influential and uncertain economic parameter to reach profitability is the evolution of electricity demanded to the power plant. This figure depends in principle on the variable renewable generation and the total electricity demand. However, it has to be noted that the required power generation to a particular unit also depends on the availability of the other thermal power plants. Facilities with lower MCL, as those with energy storage systems, have advantage over their competitors and reduce cycling and the number of generation outages. Furthermore, the power initially assigned to those thermal plants which is still available under low demand would be augmented by assuming the power assigned to other thermal plants that have to stop. Therefore, it is highly probable that the former will not have to operate at its MCL for long periods.

Given the principal uncertainties regarding market regulation and power demanded to the PtG-assisted power plant, this section presents a sensitivity analysis to assess the effect of ramping up and down during the analyzed time frameworks. Two additional scenarios are compared to previous cases in **Tables 7**, **8**. Scenarios 5 and 8 show an alternative operation to the conventional warm and cold shutdowns gathered in scenarios 3 and 6. As it was illustrated in **Figure 4**, there is a transient increase in electricity demand that would hardly be assumed if the unit is off. On the contrary, the CCPP which is still working provides a fast response and can assume the required increase in load.

For scenario 5, the reference time period is still 48 h and full load is required for 12 h during the period in which the conventional power plant (without PtG) undergoes an outage of 24 h. The results are compared with the reference scenario 3 of warm start-up and with scenario 4a where 30% load is fixed. Energy efficiency and specific CO_2 emissions reach intermediate

TABLE 8 | Comparison of different operation modes during the period of cold start-up.

Summary of results		**Reference 96 h**		
		Scenario 6 Reference Cold 48 h	**Scenario 7a Cold 48 h Load 30%**	**Scenario 8 Cold 48 h Load 30–100%**
Input natural gas	MWh_{th}	31, 243.52	44, 304.69	55, 305.80
Output energy	MWh_e	17, 628.00	21, 870.00	29, 655.00
Total costs	€	1, 301, 481.13	1, 607, 765.55	1, 892, 694.30
CO_2 emissions	t CO_2	6, 163.72	8, 740.43	10, 910.73
Specific CO_2 emissions	kg CO_2/MWh	349.66	399.65	367.92
Specific electricity cost	€/MWh	73.83	73.51	63.82
Energy PtG	MWh		960.00	960.00
CH_4 energy storage	MWh		576.00	576.00
Cost increment	€		306, 284.42	591, 213.17
Electricity increment	MWh_e		4, 242.00	12, 027.00
Additional electricity cost	€/MWh		72.20	49.16
Income from electricity (65€/MWh)	€	1, 145, 820.00	1, 421, 550.00	1, 927, 575.00
Profit	€	−155, 661.13	−186, 215.55	34, 880.70
Marginal profit	€		−30, 554.42	190, 541.83
Marginal profit/hour	€/h		−318.28	1, 984.81

TABLE 9 | Economical comparison by varying the size of the power-to-gas installation for hot (6 h) and cold (48 h): scenarios 2c and 7c.

	Hot 6 h; 70%; scenario 2c						**Cold 24 h; 70%; scenario 7c**					
	Reference Hot 6 h	**10 MW**	**20 MW**	**30 MW**	**40 MW**	**50 MW**	**Reference Cold 24 h**	**10 MW**	**20 MW**	**30 MW**	**40 MW**	**50 MW**
Input natural gas	11,514	14,987	14,951	14,915	14,879	14,843	31,244	56,632	56,344	56,056	55,768	55,480
Output energy	6,474	8,364	8,304	8,244	8,184	8,124	17,628	31,110	30,630	30,150	29,670	29,190
Total costs	423,661	503,232	502,299	501,367	500,435	499,502	1,301,481	1,927,045	1,919,586	1,912,127	1,904,668	1,897,209
Cost increment		79,571	78,638	77,706	76,773	75,841		625,564	618,105	610,646	603,187	595,727
Income from electricity (65€/MWh)	420,810	543,660	539,760	535,860	531,960	528,060	1,145,820	2,022,150	1,990,950	1,959,750	1,928,550	1,897,350
Profit	−2,851	40,428	37,461	34,493	31,525	28,558	−155,661	95,105	71,364	47,623	23,882	141
Marginal profit		43,279	40,312	37,344	34,377	31,409		250,766	227,025	203,284	179,543	155,803
Marginal profit/hour		1,803	1,680	1,556	1,432	1,309		2,612	2,365	2,118	1,870	1,623

values: the former is 4.6 pp above scenario 4a, while the latter is 5% greater than the reference case. The improvement is significant from an economic point of view. The specific cost of electricity decreases almost 11 €/MWh and the marginal profit amounts to 105,000 € with respect to the reference case. Moreover, the net profit turns from negative to positive figures.

A similar trend is observed in **Table 8** for the cold start-up situations. Scenario 8 consists in a reference time framework of 96 h and an outage period of 48 h. During this period, the requested power suddenly increases up to 100% load during 24 h. The results are compared with reference scenario 6 of cold start-up and with scenario 7a where load is fixed at MCL. Energy efficiency and specific CO_2 emissions reach intermediate values. The efficiency is 4.3 pp above scenario 7a, while specific emissions increase to 5% regarding scenario 6. The improvement is also relevant from an economic point of view. The specific cost of electricity decreases by 10 €/MWh and the marginal profit amounts to 190,500 € with respect to the reference case. The net profit also becomes positive, being 2.5 times the benefit for warm start-up (scenario 5).

Another relevant variable that has to be analyzed in the sensitivity analysis is the power-to-gas size (electrolyzers plus methanation). As a reference case, 10% of the maximum load of the combined cycle was chosen for calculations in order to have enough flexibility to reduce the MCL and get the most of the operational hours in the power-to-gas installation. **Table 9** presents the summary of some economic results when the size of the power to gas varies between 10 and 50 MW. It can be concluded that lower sizes of the power-to-gas system led to better economic results in both, avoiding hot and cold shutdowns and start-ups. When the installation size is reduced, it means that more power is available to be sold. As the electricity price is high, the extra incomes surpass the slight increment of total costs. The incremental profit compared with the reference case (40 MW) is not a decisive quantity, around 5% in the case of scenario 7c and up to 20% in scenario 2c due to the low profit results in this case. Here the issue does not depend only on power to gas but also on the incremental flexibility of the combined cycle. For a single avoided stop, the economic results are better with low size of the system, but the flexibility gain is very limited and not enough to avoid the stop. The key variable is the incremental flexibility that determines the operational hours of the system and their feasibility. As it has been explained previously with the electricity prices, the casuistic is huge and specific studies have to be done in a case-by-case basis.

According to this study, important marginal profits, even net profit, can be achieved if combined cycle power plants utilize power-to-gas technology to avoid shutdowns and extend the capacity factor. The impact of cycling on energy efficiency is damped, but this measure entails a small increase in specific CO_2 emissions.

CONCLUSION

The integration of a combined cycle and a power-to-gas energy storage system is proposed in this study to increase CCPP flexibility of operation and improve economic results under energy systems with high shares of renewable energy sources. This combination allows for a virtual reduction of the minimum complaint load of the CCPP through the diversion of instantaneous excess electricity. The present case study analyses a 400-MW_e combined cycle with MCL of 30% that can be virtually reduced to 20% by means of a 40-MW_e PtG plant.

Eight scenarios were described to compare the reference case of conventional operation under hot, warm, and cold start-ups with power-to-gas-assisted operation. The results highlight that the hybrid system operating at MCL is not recommended for hot start-ups since the profit obtained is not significant in comparison to that of conventional operation. However, an increase in plant load operation of up to 50–70% dramatically modifies the trend, and a great reduction of specific CO_2 emissions is found together with a significant economic improvement. The observed variation is related to the large increase in electricity sale incomes which transforms the conventional shutdown situation with economic losses into a profitable operation.

The economic losses under warm start-up conventional operation are significant and the net profit is strongly negative. The hybrid system of PtG-assisted operation at MCL is still not recommended since its net profits are even more negative. Increments of plant load may again modify this behavior and energy efficiency is improved in higher part-load operation, showing positive economic results. The obtained marginal profits indicate that the hybrid system with CCPP operating with part loads over 50% is profitable and thus recommended.

The behavior of the hybrid system for cold start-up is analogous to the one described for warm start-ups. The economic losses of the reference cold start-up case are very important and the inclusion of the PtG system with the CCPP operating at MCL leads to an even more negative net profit. As presented for warm start-up, the results for higher CCPP loads are much more advantageous with the positive marginal profits. For all the studied cases, the largest amount of economic improvement is related to the avoidance of shutdown.

The analysis of results has pointed out that the most relevant and uncertain economic parameter to reach profitability is the evolution of the amount of electricity demanded to the CCPP. This value is initially related to the variable RES generation and the total electricity demand. It must be highlighted that low electricity demand may remove other thermal power generators with higher MCL of the power pool and leave more room for the participation of our hybrid proposal. Therefore, facilities with lower (real or virtual) MCL present certain advantage over their competitors and reduce cycling and the number of generation outages. To assess these uncertainties related to market regulation and power demanded to the PtG-assisted power plant, several sensitivity analyses have been performed to determine the effect of change load during the time in which the combined cycle should be stopped and the effect of the size of the power-to-gas system. Conclusions in both cases reinforce the finding that the casuistic is huge and specific studies have to be done in a case-by-case basis to achieve detailed and reliable feasibility studies.

According to the results obtained in this study, important marginal profits may be obtained when combined cycle power plants utilize power-to-gas technology to avoid shutdowns and extend the capacity factor. The impact of cycling on energy efficiency is avoided, but this measure entails a small increase in specific CO_2 emissions. The use of biogas as source of CO_2 for the methanation stage may contribute to balance carbon emissions (Allman et al., 2019; Anghilante et al., 2019). This option should be further investigated in future works because it would also increase the renewable share in the natural gas sector.

DATA AVAILABILITY STATEMENT

All datasets presented in this study are included in the article.

AUTHOR CONTRIBUTIONS

MB, BP, PL, and LR: conceptualization. MB and LR: methodology. MB, BP, and PL: writing. BP and LR: results. BP and PL: validation. MB: artwork. All authors contributed to the article and approved the submitted version.

FUNDING

The work described in this manuscript was supported by the R+D Spanish National Program from Ministerio de Economía y Competitividad, MINECO (Spanish Ministry of Economy and Competitiveness) and the European Regional Development Funds (European Commission), under project ENE2016-76850-R. This work was also supported by the Government of Aragon and co-financed by FEDER 2014-2020 "Construyendo Europa desde Aragón" (Research Group DGA T46_17R and project LMP134_18).

ACKNOWLEDGMENTS

We are thankful for the comments and advice given by the reviewers. They have improved the content of this work and pointed out some research directions of particular interest.

REFERENCES

ACIL Tasman (2009). *Fuel Resource, New Entry And Generation Costs In The NEM - Final Report*. Sydney: ACIL Tasman.

Allman, A., Palys, M. J., and Daoutidis, P. (2019). Scheduling-informed optimal design of systems with time-varying operation: a wind-powered ammonia case study. *Aiche J* 65:16434. doi: 10.1002/aic.16434

Andika, R., Nandiyanto, A. B. D., Putra, Z. A., Bilad, M. R., Kim, Y., Yun, C. M., et al. (2018). Co-electrolysis for power-to-methanol applications. *Renew. Sustain. Energy Rev.* 95, 227–241. doi: 10.1016/j.rser.2018.07.030

Angelidaki, I., Treu, L., Tsapekos, P., Luo, G., Campanaro, S., Wenzel, H., et al. (2018). Biogas upgrading and utilization: current status and perspectives. *Biotechnol. Adv.* 36, 452–466. doi: 10.1016/j.biotechadv.2018.01.011

Anghilante, R., Müller, C., Schmid, M., Colomar, D., Ortloff, F., Spörl, R., et al. (2019). Innovative power-to-gas plant concepts for upgrading of gasification bio-syngas through steam electrolysis and catalytic methanation. *Energy Convers. Manag.* 183, 462–473. doi: 10.1016/j.enconman.2018.12.101

Baier, J., Schneider, G., and Heel, A. (2018). A cost estimation for CO_2 reduction and reuse by methanation from cement industry sources in Switzerland. *Front. Energy Res.* 6:5. doi: 10.3389/fenrg.2018.00005

Bailera, M., Hanak, D. P., Lisbona, P., and Romeo, L. M. (2019a). Techno-economic feasibility of power to gas-oxy-fuel boiler hybrid system under uncertainty. *Int. J. Hydro. Energy* 44, 9505–9516. doi: 10.1016/j.ijhydene.2018.09.131

Bailera, M., Lisbona, P., Llera, E., Peña, B., and Romeo, L. M. (2019b). Renewable energy sources and power-to-gas aided cogeneration for non-residential buildings. *Energy* 181, 226–238. doi: 10.1016/j.energy.2019.05.144

Bailera, M., Lisbona, P., and Romeo, L. M. (2019c). Avoidance of partial load operation at coal-fired power plants by storing nuclear power through power to gas. *Int. J. Hydro. Energy* 44, 26063–26075. doi: 10.1016/j.ijhydene.2019.08.033

Bailera, M., Kezibri, N., Romeo, L. M., Espatolero, S., Lisbona, P., and Bouallou, C. (2017a). Future applications of hydrogen production and CO_2 utilization for energy storage: hybrid power to gas-oxycombustion power plants. *Int. J. Hydro. Energy* 42:123. doi: 10.1016/j.ijhydene.2017.02.123

Bailera, M., Lisbona, P., Romeo, L. M., and Espatolero, S. (2017b). Power to gas projects review: lab, pilot and demo plants for storing renewable energy and CO_2. *Renew. Sustain. Energy Rev.* 69, 292–312. doi: 10.1016/j.rser.2016.11.130

Bailera, M., and Lisbona, P. (2018). Energy storage in Spain: forecasting electricity excess and assessment of power-to-gas potential up to 2050. *Energy* 143, 900–910. doi: 10.1016/j.energy.2017.11.069

Becker, W. L., Penev, M., and Braun, R. J. (2019). Production of synthetic natural gas from carbon dioxide and renewably generated hydrogen: a techno-economic analysis of a power-to-gas strategy. *J. Energy Resour. Technol. Trans. ASME* 141:021901. doi: 10.1115/1.4041381

BP Statistical Review of World Energy (2019). BP. Full Report - BP Statistical Review of World Energy. Available online at: https://www.bp.com/content/dam/bp/business-sites/en/global/corporate/pdfs/energy-economics/statistical-review/bp-stats-review-2019-full-report.pdf

Brynolf, S., Taljegard, M., Grahn, M., and Hansson, J. (2018). Electrofuels for the transport sector: a review of production costs. *Renew. Sustain. Energy Rev.* 81, 1887–1905. doi: 10.1016/j.rser.2017.05.288

Buttler, A., and Spliethoff, H. (2018). Current status of water electrolysis for energy storage, grid balancing and sector coupling via power-to-gas and power-to-liquids: a review. *Renew. Sustain. Energy Rev.* 82, 2440–2454. doi: 10.1016/j.rser.2017.09.003

Capros, P., Vita, A., De Tasios, N., Siskos, P., Kannavou, M., Petropoulos, A., et al. (2016). *EU Reference Scenario 2016: Energy, Transport And GHG Emissions. Trends to 2050*. Brussels: European Union.

Chauvy, R., Dubois, L., Lybaert, P., Thomas, D., and De Weireld, G. (2020). Production of synthetic natural gas from industrial carbon dioxide. *Appl. Energy* 260:114249. doi: 10.1016/j.apenergy.2019.114249

Chen, S., Wei, Z., Sun, G., Wang, D., Zhang, Y., and Ma, Z. (2018). Stochastic look-ahead dispatch for coupled electricity and natural-gas networks. *Electr. Power Syst. Res.* 164, 159–166. doi: 10.1016/j.epsr.2018.07.038

Colbertaldo, P., Agustin, S. B., Campanari, S., and Brouwer, J. (2019). Impact of hydrogen energy storage on California electric power system: towards 100% renewable electricity. *Int. J. Hydro. Energy* 44, 9558–9576. doi: 10.1016/j.ijhydene.2018.11.062

Cormos, A. M., Dinca, C., Petrescu, L., Andreea Chisalita, D., Szima, S., and Cormos, C. C. (2018). Carbon capture and utilisation technologies applied to energy conversion systems and other energy-intensive industrial applications. *Fuel* 211, 883–890. doi: 10.1016/j.fuel.2017.09.104

de Groot, M., Crijns-Graus, W., and Harmsen, R. (2017). The effects of variable renewable electricity on energy efficiency and full load hours of fossil-fired power plants in the European Union. *Energy* 138, 575–589. doi: 10.1016/J.ENERGY.2017.07.085

Di Salvo, M., and Wei, M. (2019). Synthesis of natural gas from thermochemical and power-to-gas pathways for industrial sector decarbonization in California. *Energy* 182, 1250–1264. doi: 10.1016/j.energy.2019.04.212

European Commission (2018). *Directive (EU) 2018/2001 Of The European Parliament And Of The Council Of 11 December 2018 On The Promotion Of The Use Of Energy From Renewable Sources*. Brussels: European Commission.

Eurostat Statistics Explained (2019). *Eurostat. 2019. EU. Eurostat. Statistics Explained*. Brussels: Eurostat.

Eveloy, V., and Gebreegziabher, T. (2018). A review of projected power-to-gas deployment scenarios. *Energies* 11:1824. doi: 10.3390/en11071824

Gahleitner, G. (2013). Hydrogen from renewable electricity: an international review of power-to-gas pilot plants for stationary applications. *Int. J. Hydro. Energy* 38, 2039–2061. doi: 10.1016/j.ijhydene.2012.12.010

Giglio, E., Lanzini, A., Santarelli, M., and Leone, P. (2015). Synthetic natural gas via integrated high-temperature electrolysis and methanation: part I-energy performance. *J. Energy Storage* 1, 22–37. doi: 10.1016/j.est.2015.04.002

Gilbert, A. Q., and Sovacool, B. K. (2017). Benchmarking natural gas and coal-fired electricity generation in the United States. *Energy* 134, 622–628. doi: 10.1016/j.energy.2017.05.194

Gonzalez-Salazar, M. A., Kirsten, T., and Prchlik, L. (2018). Review of the operational flexibility and emissions of gas- and coal-fired power plants in a future with growing renewables. *Renew. Sustain. Energy Rev.* 82, 1497–1513. doi: 10.1016/J.RSER.2017.05.278

Götz, M., Lefebvre, J., Mörs, F., McDaniel Koch, A., Graf, F., Bajohr, S., et al. (2015). Renewable Power-to-Gas: a technological and economic review. *Renew. Energy* 85, 1–20.

He, G. X., Yan, H., Chen, L., and Tao, W. Q. (2020). Economic dispatch analysis of regional electricity-gas system integrated with distributed gas injection. *Energy* 201:117512. doi: 10.1016/j.energy.2020.117512

He, L., Lu, Z., Zhang, J., Geng, L., Zhao, H., and Li, X. (2018). Low-carbon economic dispatch for electricity and natural gas systems considering carbon capture systems and power-to-gas. *Appl. Energy* 224, 357–370. doi: 10.1016/j.apenergy.2018.04.119

Hentschel, J., Babić, U., and Spliethoff, H. (2016). A parametric approach for the valuation of power plant flexibility options. *Energy Rep.* 2, 40–47. doi: 10.1016/J.EGYR.2016.03.002

Jensen, S. H., Graves, C., Mogensen, M., Wendel, C., Braun, R., Hughes, G., et al. (2015). Large-scale electricity storage utilizing reversible solid oxide cells combined with underground storage of CO_2 and CH4. *Energy Environ. Sci.* 8, 2471–2479. doi: 10.1039/c5ee01485a

Kumar, N., Besuner, P., Lefton, S., Agan, D., and Hilleman, D. (2012). *Power Plant Cycling Costs. National Renewable Energy Laboratory*. Available online at: https://www.nrel.gov/docs/fy12osti/55433.pdf

Lee, B., Lee, H., Heo, J., Moon, C., Moon, S., and Lim, H. (2019). Stochastic techno-economic analysis of H2 production from power-to-gas using a high-pressure PEM water electrolyzer for a small-scale H2 fueling station. *Sustain Energy Fuels* 3, 2521–2529. doi: 10.1039/c9se00275h

Lew, D., Brinkman, G., Kumar, N., Lefton, S., Jordan, G., and Venkataraman, S. (2013). "Finding flexibility. cycling the conventional Fleet," in *Proceedings of the IEEE Power Energy Magazine*, Piscataway, NJ.

Lewandowska-Bernat, A., and Desideri, U. (2018). Opportunities of power-to-gas technology in different energy systems architectures. *Appl. Energy* 228, 57–67. doi: 10.1016/j.apenergy.2018.06.001

Linde (2020). *Natural Gas Filling Station 2020*. Dublin: Linde.

Lisbona, P., Frate, G. F., Bailera, M., and Desideri, U. (2018). Power-to-gas: analysis of potential decarbonization of spanish electrical system in long-term prospective. *Energy* 159, 656–668. doi: 10.1016/J.ENERGY.2018.06.115

Matute, G., Yusta, J. M., and Correas, L. C. (2019). Techno-economic modelling of water electrolysers in the range of several MW to provide grid services while generating hydrogen for different applications: a case study in Spain applied to mobility with FCEVs. *Int. J. Hydro. Energy* 44, 17431–17442. doi: 10.1016/j.ijhydene.2019.05.092

Nalbandian-Sugden, H. (2016). *Operating Ratio And Cost Of Coal Power Generation*. London: IEA Clean Coal Centre.

Naval, N., Sánchez, R., and Yusta, J. M. (2020). A virtual power plant optimal dispatch model with large and small-scale distributed renewable generation. *Renew. Energy* 151, 57–69. doi: 10.1016/j.renene.2019.10.144

Pierre, I., Bauer, F., Blasko, R., Dahlback, N., Dumpelmann, M., Kainurinne, K., et al. (2011). *Flexible Generation: Backing Up Renewables*. Available online at: https://www.google.com/url?sa=t&rct=j&q=&esrc=s&source=web&cd=&ved=2ahUKEwjv-IKvu7vqAhWJohQKHYWICFkQFjAAegQIAxAB&url=https%3A%2F%2Fwww3.eurelectric.org%2FDownload%2FDownload.aspx%3FDocumentFileID%3D71337&usg=AOvVaw3Idw040czr6Pa6RLx3uqsy

Romeo, L. M., Peña, B., Bailera, M., and Lisbona, P. (2018). "Analysis of the influence of Power-to-Gas systems in cyclic performance of fossil fuel power plants. ECOS 2018," in *Proceedingsof the 31st International Conference on Efficiency, Cost, Optimization, Simulation and Environmental Impact of Energy Systems*, Braga.

Rosenfeld, D. C., Böhm, H., Lindorfer, J., and Lehner, M. (2020). Scenario analysis of implementing a power-to-gas and biomass gasification system in an integrated steel plant: a techno-economic and environmental study. *Renew. Energy* 147, 1511–1524. doi: 10.1016/j.renene.2019.09.053

Schemme, S., Samsun, R. C., Peters, R., and Stolten, D. (2017). Power-to-fuel as a key to sustainable transport systems - an analysis of diesel fuels produced from CO_2 and renewable electricity. *Fuel* 205, 198–221. doi: 10.1016/j.fuel.2017.05.061

Schiebahn, S., Grube, T., Robinius, M., Tietze, V., Kumar, B., and Stolten, D. (2015). Power to gas: technological overview, systems analysis and economic assessment for a case study in Germany. *Int. J. Hydro. Energy* 40, 4285–4294. doi: 10.1016/j.ijhydene.2015.01.123

Sjoerd Brouwer, A., Van Den Broek, M., Seebregts, A., and Faaij, A. (2015). Operational flexibility and economics of power plants in future low-carbon power systems. *Appl. Energy* 156, 107–128. doi: 10.1016/j.apenergy.2015.06.065

Smith, R. W., Polukort, P., Maslak, C. E., Jones, C. M., and Gardiner, B. D. (2020). *GE Power Systems Advanced Technology Combined Cycles. Report from General Electric 592*. Atlanta, GA: GE Power Systems.

The Oxford Institute for Energy Studies (2018). *LNG Plant Cost Reduction 2014 - 18*. Oxford: The Oxford Institute for Energy Studies.

Thema, M., Bauer, F., and Sterner, M. (2019). Power-to-Gas: electrolysis and methanation status review. *Renew. Sustain. Energy Rev.* 112, 775–787. doi: 10.1016/j.rser.2019.06.030

United Nations Framework Convention on Climate Change [UNFCCC] (2015). *The Paris Agreement*. New York, NY: UNFCCC.

Van den Bergh, K., and Delarue, E. (2015). Cycling of conventional power plants: Technical limits and actual costs. *Energy Convers. Manag.* 97, 70–77. doi: 10.1016/j.enconman.2015.03.026

Vandewalle, J., Bruninx, K., and D'haeseleer, W. (2015). Effects of large-scale power to gas conversion on the power, gas and carbon sectors and their interactions. *Energy Convers. Manag.* 94, 28–39. doi: 10.1016/j.enconman.2015.01.038

Wang, X., Bie, Z., Liu, F., and Kou, Y. (2019). Robust dispatch for integrated electricity and natural gas system considering wind power uncertainty. *Energy Proc.* 159, 130–135. doi: 10.1016/j.egypro.2018.12.030

Wulf, C., Linßen, J., and Zapp, P. (2018). Review of power-to-gas projects in Europe. *Energy Proc.* 155, 367–378. doi: 10.1016/j.egypro.2018.11.041

Yin, S., Zhang, S., Andrews-Speed, P., and Li, W. (2017). Economic and environmental effects of peak regulation using coal-fired power for the priority dispatch of wind power in China. *J. Clean. Prod.* 162, 361–370. doi: 10.1016/j.jclepro.2017.06.046

Conflict of Interest: The authors declare that the research was conducted in the absence of any commercial or financial relationships that could be construed as a potential conflict of interest.

frontiers in Energy Research

ORIGINAL RESEARCH
published: 28 July 2020
doi: 10.3389/fenrg.2020.00174

How Operational Parameters Affect Electromethanogenesis in a Bioelectrochemical Power-to-Gas Prototype

Daniele Molognoni, Pau Bosch-Jimenez, Rubén Rodríguez-Alegre, Adrián Marí-Espinosa, Edxon Licon, Julia Gallego, Salvador Lladó, Eduard Borràs and Monica Della Pirriera*

Leitat Technological Center, Terrassa, Spain

Bioelectrochemical power-to-gas represents a novel solution for electrical energy storage, currently under development. It allows storing renewable energy surplus in the form of methane (CH_4), while treating wastewater, therefore bridging the electricity and natural gas (and wastewater) grids. The technology can be coupled with membrane contactors for carbon dioxide (CO_2) capture, dissolving the CO_2 in wastewater before feeding it to the bioelectrochemical system. This way, the integrated system can achieve simultaneous carbon capture and energy storage objectives, in the scenario of a wastewater treatment plant application. In this study, such technology was developed in a medium-scale prototype (32 L volume), which was operated for 400 days in different conditions of temperature, voltage and CO_2 capture rate. The prototype achieved the highest CH_4 production rate (147 $\pm$ 33 L m^{-3} d^{-1}) at the lowest specific energy consumption (1.0 $\pm$ 0.3 kWh m^{-3} CH_4) when operated at 25°C and applying a voltage of 0.7 V, while capturing and converting 22 L m^{-3} d^{-1} of CO_2. The produced biogas was nearer to biomethane quality (CH_4 > 90% v/v) when CO_2 was not injected in the wastewater. Traces of hydrogen (H_2) in the biogas, detectable during the periods of closed electrical circuit operation, indicated that hydrogenotrophic methanogenesis was taking place at the cathode. On the other hand, a relevant CH_4 production during the periods of open electrical circuit operation confirmed the presence of acetoclastic methanogenic microorganisms in the microbial community, which was dominated by the archaeal genus *Methanothrix* (*Euryarchaeota*). Different operational taxonomic units belonging to the bacterial *Synergistes* phylum were found at the anode and the cathode, having a potential role in organic matter degradation and H_2 production, respectively. In the panorama of methanation technologies currently available for power-to-gas, the performances of this bioelectrochemical prototype are not yet competitive, especially in terms of volumetric CH_4 production rate and power density demand. However, the possibility to obtain a high-quality biogas (almost reaching biomethane quality standards) at a minimal energy consumption represents a potentially favorable business scenario for this technology.

Keywords: carbon capture, electromethanogenesis, energy storage, methanation, microbial community, renewable energy

OPEN ACCESS

Edited by:
Luis M. Romeo, University of Zaragoza, Spain

Reviewed by:
Antonio Moran, Universidad de León, Spain
Kun Yu, Globalfoundries, United States

****Correspondence:***
Daniele Molognoni
dmolognoni@leitat.org

Specialty section:
This article was submitted to Carbon Capture, Storage, and Utilization, a section of the journal Frontiers in Energy Research

Received: *12 May 2020*
Accepted: *06 July 2020*
Published: *28 July 2020*

Citation:
Molognoni D, Bosch-Jimenez P, Rodríguez-Alegre R, Marí-Espinosa A, Licon E, Gallego J, Lladó S, Borràs E and Della Pirriera M (2020) How Operational Parameters Affect Electromethanogenesis in a Bioelectrochemical Power-to-Gas Prototype. Front. Energy Res. 8:174. doi: 10.3389/fenrg.2020.00174

INTRODUCTION

The European Commission fixed a target of 80% CO_2 emissions reduction by 2050 (European Commission, 2011). The challenge of economy decarbonization requires the development and implementation of massive amounts of renewable energy sources (RES) and methods for carbon capture and use (CCU). However, a high penetration of renewable energy in the electricity market requires the simultaneous deployment of energy storage systems, to cope with both short-term and long-term fluctuations of the electricity grid (Denholm et al., 2010). Nowadays, electrical batteries can provide a solution for the short-term storage of RES peaks, while pumped hydro or compressed air storage can deal with the long-term storage, although with large investment costs and construction efforts. The development of alternative technologies is required for long-term, high capacity and potentially strategic energy storage (Blanco and Faaij, 2018). Power-to-X (PtX) technologies can convert surplus electrical energy into more easily storable gas or liquid fuels. The PtX technologies currently at higher TRL (technology readiness level) are the ones producing H_2 or CH_4 as gaseous energy storage vectors (Bailera et al., 2017). Especially the methanation technologies, converting CO_2 to CH_4, were spotted by the energy industry, as the ones allowing an immediate integration into the existing infrastructure and the interconnection between electrical and natural gas distribution grids, with several advantages in terms of energy cost, system resilience and security (Zeng et al., 2016). Furthermore, for each CH_4 molecule produced, a CO_2 molecule is consumed, reducing the climate impacts of burning natural gas. Methanation can be performed through thermal, chemical, electrochemical, biological or bioelectrochemical processes (Geppert et al., 2016). Moreover, it can be efficiently coupled with a biogas upgrading unit for cheap CO_2 supply (Leonzio, 2019). This possibility opened the way to the idea of a distributed PtX application in wastewater treatment plants (WWTP), instead of centralized plants that would require huge piping of water and/or gaseous reactive streams (Inkeri et al., 2016).

In the recent years, bioelectrochemical systems (BES) emerged as a novel alternative for PtX plants (Geppert et al., 2016). BES use electro-active microorganisms as biocatalysts for wastewater treatment, with simultaneous recovery of energy and/or resources (Harnisch et al., 2011). The standard BES architecture is composed by an anode, where organic matter content of wastewater is oxidized, and a cathode, where a counter reaction occurs. In case of BES-based PtX, the desired energy vector is produced by the cathodic reaction. Cheng et al. (2009) were the first to propose cathodic reduction of CO_2 (dissolved into an aqueous medium) into CH_4 by an electromethanogenesis BES (hereafter, EMG-BES). The EMG process has been generally developed with double-chamber BES architectures, where anode and cathode are separated by an ionic exchange membrane, focusing on the optimization of the carbon conversion and Coulombic efficiency (Zhang et al., 2019) and aiming to a clear speciation of the microorganisms catalyzing the substrate oxidation at the anode, and the ones performing CO_2 reduction at the cathode (Mayer et al., 2019). The single-chamber EMG-BES represents a different approach for PtX, in the panorama of BES-based technologies. It can be coupled directly with anaerobic digestion (Park et al., 2018) and it reduces maintenance, energy losses and complexity of the reactor. This has proven to be effective for biomethane generation, from laboratory to prototype scale (Muñoz-Aguilar et al., 2018; Ceballos-Escalera et al., 2020). In both cases of single and double-chamber EMG-BES, the methanation process is performed within a single step process, not requiring preliminary H_2 production and occurring at mild temperature and pressure (25–35°C, 1–3 bar). Also, EMG-BES reactors treat wastewater at the same time than performing methanation, representing this an added value, compared with competitive PtX technologies. In this regard, EMG-BES can connect electrical, wastewater and natural gas grids, reducing overall energy cost and improving its resiliency. Previous studies summarized the factors affecting the performance of bioelectrochemical CH_4 production in EMG-BES: microbial communities, cathode potential, electrode materials, among them (Zhen et al., 2018; Noori et al., 2019; Zakaria and Dhar, 2019).

The single-chamber EMG-BES process requires the presence of both organic matter and CO_2 in wastewater, to sustain the complementary reactions of oxidation at the anode and reduction at the cathode. As organic matter oxidation generates CO_2, the process can be run efficiently with a regular feeding of wastewater, or sludge (Moreno et al., 2016; Xu et al., 2020). On the other hand, CO_2 injection can contribute to EMG (and generally to bioelectrochemical processes) by increasing the electrical conductivity of the medium, reducing cathode overpotentials and voltage requirements (Rodríguez-Alegre et al., 2019). Water scrubbing is the most used downstream technique for CO_2 capture, adopted by 33.8% of the European biogas upgrading plants (Batlle-Vilanova et al., 2019). Being a pressure-driven technology, it can present operational issues including channeling and flooding. On the other hand, the use of membrane contactors avoids such problems, being a diffusion-driven process. Moreover, the contactors have a compact and scalable architecture, allowing to reach high gas-liquid contact areas (Nogalska et al., 2017). The integration of membrane contactors with a stack of laboratory-scale EMG-BES reactors was previously tested by the authors, achieving good results in terms of CO_2 capture and CH_4 production (Rodríguez-Alegre et al., 2019).

To the authors' knowledge, no up-scaled studies have been reported previously about the integration of membrane contactors for CO_2 capture in wastewater, and single-chamber EMG-BES converting the dissolved CO_2 into biomethane. This study reports for the first time the long-term operation of a stack of EMG-BES cells fed with municipal wastewater, which was

Abbreviations: η_{COD}, organic matter removal efficiency; η_{CONV}, carbon conversion efficiency; BES, bioelectrochemical system; CCU, carbon capture and use; COD, chemical oxygen demand; EAB, electro-active bacteria; EMG, electromethanogenesis; HRT, hydraulic residence time; IC, inorganic carbon; OCV, open circuit voltage; OTU, operational taxonomic unit; PtX, power-to-X; RES, renewable energy source; SHE, standard hydrogen electrode; TC, total carbon; TRL, technology readiness level; VOC, volatile organic compound; WWTP, wastewater treatment plant.

integrated with a stack of membrane contactors for CO_2 capture in wastewater. The effect of different operational parameters was evaluated, among which temperature, applied voltage and CO_2 capture (ON/OFF). A complete assessment in terms of wastewater treatment efficiency, biomethane production rate and quality, current and power consumption was performed. Coulombic efficiency of anode and cathode, and the conversion efficiency of CO_2 to CH_4 were estimated. Finally, the microbial community colonizing different areas of the EMG-BES cells was evaluated, to get a better understanding of the potential metabolic reactions taking place in the biological reactor.

MATERIALS AND METHODS

The developed prototype was composed by a membrane-based CO_2 capture system coupled to a stack of EMG-BES cells for biomethane production and energy storage (**Figure 1**). Three polypropylene membrane contactors (3M Liqui-Cel^{TM} EXF-2.5 × 8, United States) of 2.5 m^2 each one were installed in parallel hydraulic configuration and used for CO_2 capture and dissolution in wastewater.

A medium-scale EMG-BES prototype was built by stacking 45 cells together, grouped by 3 into 15 single-chamber, membraneless reactor modules, as described by Ceballos-Escalera et al. (2020). The volume of each reactor module was 1.78 L (plus 5.2 L due to recirculation tank and piping volumes), reaching a total prototype volume of 32 L. Anode and cathode electrodes (170 cm^2 projected surface, each one) were made of thermally treated carbon felt (SGL group, Germany). The total anode/cathode surface was 0.77 m^2. The electrical connection to the external circuit was made by stainless steel current collectors. The stack was connected in parallel and powered at 0.7 V by an external power source (TENMA 72-2715, Farnell, Spain). An electrical monitoring system based on several shunt resistances, installed in series to each cell, and three 16-channels DAQ boards (PicoLog 1216, Farnell, Spain) allowed measuring the current consumed by each cell of the stack.

The modules were hydraulically connected in parallel, continuously recirculating the wastewater to a recirculation tank at a rate of 50 mL min^{-1} per module. A heating system (Huber thermostat CC-K6, Huber, Germany) was connected to the external jacket of the recirculation tank, allowing to control the operating temperature of the stack. Finally, the gas produced in the prototype was trapped by 3 external chambers (gas trap columns in **Figure 1**), each one connected to 5 reactor modules.

Wastewater Pre-treatment and CO_2 Capture Protocol

The stack of EMG-BES reactors was successfully inoculated in 68 days, using anaerobic sludge collected from the anaerobic digester at the local WWTP. Then, the stack was continuously fed with municipal wastewater (primary settler effluent, collected at the local WWTP). Preliminary batch tests identified a hydraulic residence time (HRT) of 22 h as the one guaranteeing the best performances in terms of current density consumption and CH_4 production rate (Ceballos-Escalera et al., 2020). However, due to practical constrains related to wastewater supply, adopted HRT was increased to 3.0 ± 0.5 days. The wastewater was initially pre-treated as detailed by Rodríguez-Alegre et al. (2019): wastewater was kept in a pre-treatment tank (60 L) at environmental temperature and basified to pH 13 by NaOH addition (35 mL of 3M NaOH solution per L of wastewater). After 24 h settling, the wastewater was poured to a homogenization tank (50 L) maintained at 4°C.

For a first experimental period (days 69–174), CO_2 capture in wastewater was not performed. Therefore, its pH was neutralized by addition of 26 mmol CH_3COOH per L, increasing the organic matter concentration to 1.3–1.4 g COD L^{-1} (where COD stands for chemical oxygen demand) and the conductivity to 10 mS cm^{-1}. A variable quantity of H_2SO_4 was used to reach a uniform pH of 7.5 (41 ± 14 mmol H_2SO_4 L^{-1}), before feeding the wastewater to the EMG-BES stack. For a second experimental period (days 175–400), the stack of membrane contactors was activated. Pure CO_2 (Carburos Metálicos, Spain) was introduced in the contactors on their lumen-side, from the bottom to the top, while NaOH-basified wastewater was pumped in counter current configuration on the shell side. The wastewater was continuously recirculated to the homogenization tank at a flowrate of 2 L min^{-1}. The pressure of influent CO_2 was set at 1 bar (manometer pressure), while its flowrate was regulated at 2 L min^{-1}. The pH of wastewater was continuously measured during the CO_2 capture process (by HQ40 multimeter, Hach Lange, Spain). The process was stopped when the wastewater reached a pH of 10, which should have allowed a total carbon (TC) concentration near 1 g L^{-1}, based on previous experience (Rodríguez-Alegre et al., 2019). Then, the wastewater pH was neutralized to 7.5 by addition of acetic acid (same amount as before) and H_2SO_4 (16 ± 5 mmol L^{-1}), before feeding it to the EMG-BES stack. The entire sequence of operations performed is resumed in **Figure 2**.

Operational Conditions Tested

The EMG-BES prototype was tested under different operational conditions. While the influent wastewater was not saturated with CO_2, two operation temperatures were tested. During days 69–132 the prototype was operated at 32°C, while for days 133–174 the temperature was decreased to 25°C. For both temperature conditions, both closed circuit (0.7 V) and open circuit voltage (OCV) tests were performed. For the rest of the experiment (days 175–400), the prototype was maintained in stable conditions (25°C, non-stop voltage application, CO_2 capture ON) to evaluate long-term performance. The **Table 1** resumes the tested operational conditions. Each condition is identified by a binary code, assigning letters A/B to the three independent parameters CO_2 capture, temperature and voltage.

Liquid and Gas Phase Characterization

Influent wastewater was sampled after the pre-treatment protocol (either the CO_2 capture was activated or not), to analyze its total and inorganic carbon concentration, TC and IC, respectively, (SHIMADZSU TOC-L CSH/CSN analyzer, Spain). The amount of absorbed CO_2 (for the condition BAB) could be estimated as the difference between TC values measured before and after

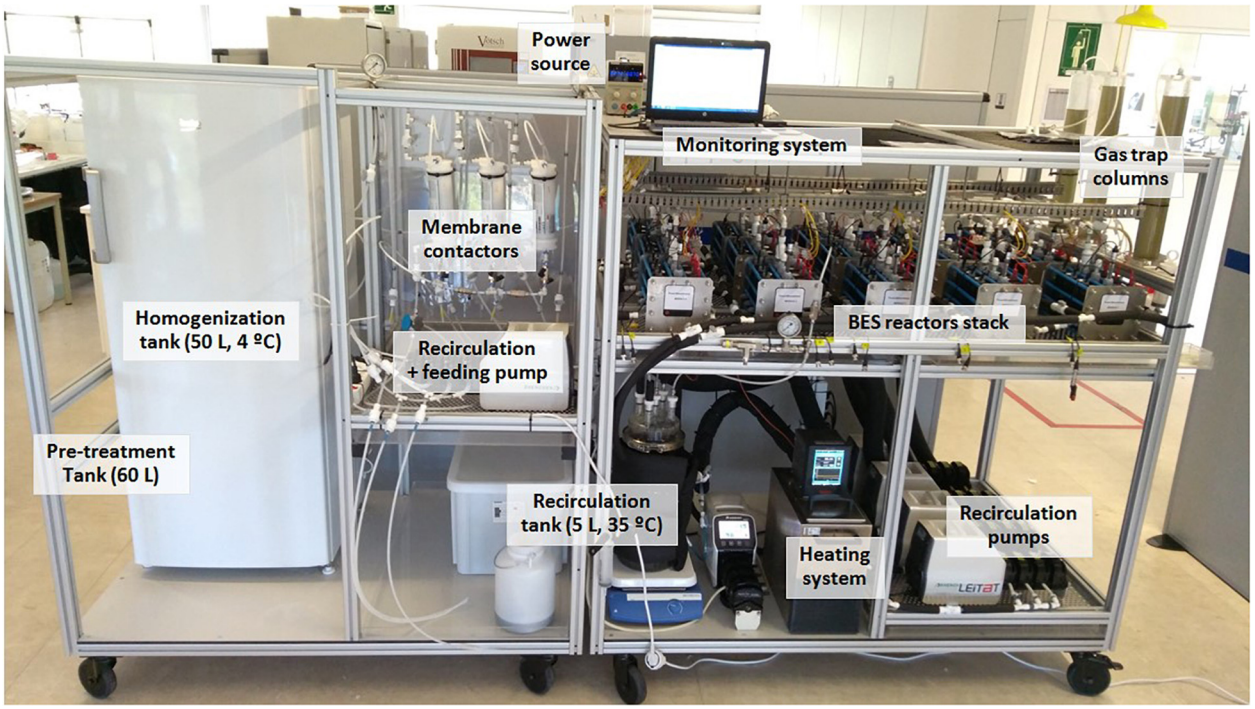

FIGURE 1 | Photo of the prototype. **Left side**: CO_2 capture system. **Right side**: EMG-BES stack.

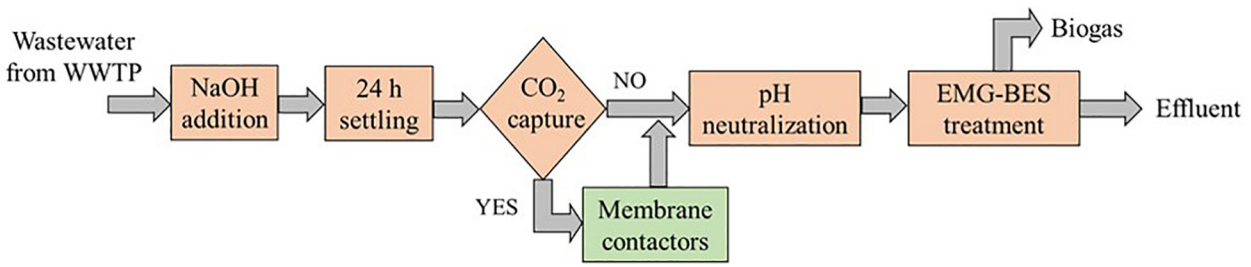

FIGURE 2 | Flow-chart showing the sequence of operations performed, from wastewater pre-treatment to CO_2 capture and EMG-BES stack operation.

the CO_2 saturation process. In addition, samples of effluent wastewater were collected twice a week. All the samples were characterized according to Standard Methods in terms of pH, conductivity (HQ40 multimeter, Hach Lange, Spain) and chemical oxygen demand (COD, by LCK 514 kits, Hach Lange, Spain) (APHA, 2005). For the last condition BAB, also the TC and IC concentrations of effluent wastewater were evaluated. Punctual sulfate (SO_4^{2-}) analysis of the effluent were performed during conditions AAB and BAB, to investigate the dynamics of sulfur species in the prototype.

Gas samples were collected regularly from the gas trap columns by means of Tedlar bags. Their volumetric content in terms of CO_2, CH_4, O_2, N_2, and H_2 was determined by a Micro-GC (Agilent 490, Spain) with dual channel cabinet and thermal conductivity detector. For the last condition BAB, also H_2S content of gas samples was determined. On day 365, a 10 L sample of the produced biogas was collected in a Tedlar bag. The content of volatile organic compounds (VOCs) was captured from the sample by means of a Tenax-TA tube, then desorbed at 280°C and analyzed by gas chromatography (GC) coupled to mass spectrometry (MS) (Agilent 7890B, Agilent Technologies, Spain).

TABLE 1 | Operational conditions tested.

Code	Time (days)	CO_2 capture (A = OFF/B = ON)	Temperature (A = 25/B = 32)	Voltage (A = OFF/B = ON)
ABB	69–132	OFF	32°C	ON
ABA	119–128	OFF	32°C	OFF
AAB	133–174	OFF	25°C	ON
AAA	150–156	OFF	25°C	OFF
BAB	175–400	ON	25°C	ON

The code identifies each condition by assigning letters A/B to the three independent parameters CO_2 capture, temperature and voltage.

Analysis and Calculations

The organic matter removal efficiency (η_{COD}) was determined by Eq. 1, where COD_{IN} and COD_{OUT} are the COD concentrations of influent and effluent wastewater, respectively.

$$\eta_{COD} = \frac{COD_{IN} - COD_{OUT}}{COD_{IN}} \cdot 100 \quad (1)$$

The CH_4 production rate was determined by multiplying the gas production rate (quantified daily through the measurement of the accumulated gas volume in the external columns) by its relative CH_4 content. A normalized value of CH_4 production could be achieved dividing it by the prototype volume.

Current density was calculated by dividing the electrical current by the cathode surface. Power demand of the stack was calculated by multiplying the consumed current by the applied voltage. The individual electrode potentials were measured periodically thanks to Ag/AgCl reference electrodes (+ 0.197 V vs. SHE, Xi'an Yima Opto-electrical Technology, China), installed inside each reactor module. The specific energy consumption of the EMG-BES reactor (in kWh m^{-3} CH_4) was calculated dividing the consumed electrical power by the CH_4 production rate. Anode and cathode Coulombic efficiencies were determined as explained by Ceballos-Escalera et al. (2020). All these variables (measured and/or calculated) were statistically treated in order to find the average and standard deviation values, for each operational condition tested.

Based on average current density data (dI), the maximum theoretical CH_4 production rate achievable by EMG was estimated (for the operation conditions ABB, AAB and BAB), assuming a cathodic Coulombic efficiency (CE_{cat}) of 100% (Eq. 2).

$$CH_4 \cdot prod \cdot EMG = \frac{CE_{cat} \cdot V_{mol} \cdot dI \cdot S}{c \cdot F \cdot V} \quad (2)$$

In Eq. 2, V_{mol} represents the molar volume of an ideal gas, calculated at the respective operation temperature (25 or 32°C), assuming a gas pressure of 1 atm. The term S refers to the total cathode surface (0.77 m^2), C are the e^- moles required to reduce 1 mol of CO_2 to CH_4 (8), F is the Faraday constant (96485 C mol^{-1}) and V is the prototype volume (32 L).

Moreover, the carbon conversion efficiency (η_{CONV}) from dissolved CO_2 to gaseous CH_4 was estimated (Eq. 3), as explained by Rodríguez-Alegre et al. (2019).

$$\eta_{CONV} = \frac{CH_4 \cdot prod \cdot EMG \cdot V}{V_{mol}} \cdot \frac{M_m}{IC_{IN} \cdot Q} \quad (3)$$

In Eq. 3, M_m is the molar mass of C (12 g mol^{-1}), IC_{IN} is the inorganic carbon concentration of influent wastewater and Q (L d^{-1}) is the measured feeding rate to the EMG-BES stack. The values of theoretical CH_4 production rate achievable by EMG were used, instead than measured CH_4 production values, as the excess amount would be due to acetoclastic methanogenesis, not contributing to CO_2 conversion.

For these two last parameters (CH_4 prod EMG and η_{CONV}), the standard deviation values were not calculated as their purpose was only orientative (not quantitative), as it will be explained in the section "Efficiency Parameters."

Microbial Community Analysis

In order to obtain a better understanding of the microbial populations growing in the EMG-BES prototype, the bacterial and archaeal communities associated with (*i*) bulk medium, (*ii*) anode biofilm and (*iii*) cathode biofilm were determined by 16S rRNA gene sequence analysis. On day 211 the reactor module 15 was opened and biofilm samples were collected from all anode and cathode electrodes, together with two biomass samples from the bulk electrolyte.

The samples were centrifuged and stored at −20°C prior to community analysis. DNA was extracted from each sample using the Norgen Total Genomic DNA Purification kit (Norgen Biotek, Canada). PCR amplification of the bacterial (and archaeal) 16S rRNA gene V4 region was carried out with the barcoded primers 515F and 806R, using the DNA extracted from each sample (Caporaso et al., 2012). Amplicons were sequenced on an Illumina MiSeq. The amplicon sequencing data were processed with the software SEED v2.1 (Větrovský et al., 2018). Briefly, pair-end reads were merged using fast-join (Aronesty, 2013). Chimeric sequences were detected and deleted, and sequences were clustered using UPARSE implemented within Usearch, at a 97% similarity level (Edgar, 2013). The most abundant sequence was selected for each cluster, and the closest hits at a genus level were identified using BLAST against the GenBank database. From 16S rRNA in DNA, bacterial and archaeal genome count estimates were calculated based on the 16S copy numbers in the closest available sequenced genome as described previously (Větrovský and Baldrian, 2013). Relative abundance bar chart, heatmap and statistics comparing abundance between bulk medium, anode biofilm and cathode biofilm (multiple *t* tests) were performed using the software GraphPad v7.04. Significant differences between samples were confirmed by a probability value (p) minor than 0.05. Sequencing data are available in the SRA database with accession number PRJNA627951.

RESULTS AND DISCUSSION

The prototype was long-term operated for 400 days. The effects of different operational parameters were evaluated, as presented in the following sections "Methane Production Rate and Electrical Current Consumption," "Wastewater Treatment," "Biogas Composition," "Microbial Community Analysis," and "Efficiency Parameters."

Methane Production and Electrical Current Consumption

For the majority of the time, the EMG-BES stack was electrically connected in parallel at 0.7 V applied voltage. The potentials of anode and cathode electrodes, in all the reactor modules, were stable for the whole experiment duration (−0.4 V and −1.1 V vs. Ag/AgCl, respectively). **Figure 3** presents the statistical distribution of the experimental values obtained for CH_4 production rate (A) and current density (B), in the

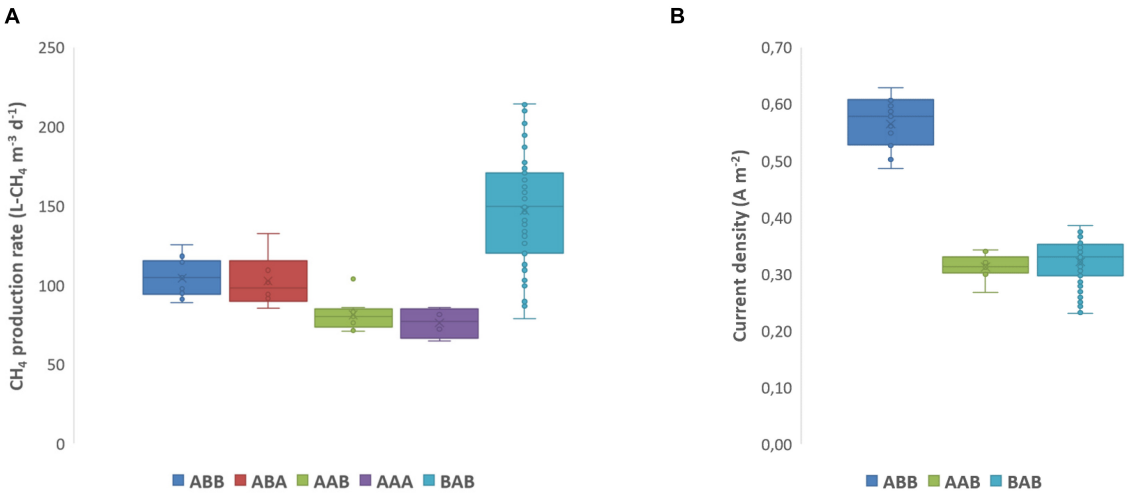

FIGURE 3 | CH_4 production rate **(A)** and current density **(B)** measured in tested operation conditions. ABB condition refers to days 90 to 118, when stationary phase was reached; current density was null in ABA and AAA conditions (OCV tests).

different experimental conditions tested. While the membrane contactors for CO_2 capture were disconnected, two operational temperatures were tested (32 and 25°C), in both closed and open electrical circuit conditions. At 32°C the CH_4 production reached 105 ± 11 L m^{-3} d^{-1}, with a simultaneous current consumption of 0.56 ± 0.04 A m^{-2}. However, the current density was not stable and slowly diminished over time, as shown in **Supplementary Figure S1**. That was due to the competitive growth of acetoclastic methanogens in the electrolyte medium, competing with electro-active bacteria (EAB) for acetate as unique substrate, as previously reported (Ceballos-Escalera et al., 2020). At 25°C both CH_4 production rate and current consumption decreased (22 and 45% reduction, respectively), due to a slower microbial metabolism. At both temperatures, when excluding the EMG process, i.e., during the OCV tests (conditions ABA and AAA), the CH_4 production rate slightly decreased compared with the periods applying voltage (conditions ABB and AAB), as shown in **Figure 3A**. This reduction was lower than the theoretical CH_4 production achievable by EMG (see **Supplementary Table S1**), due to the microbial competition and dynamic equilibrium existing between electroactive and acetoclastic methanogenic populations. This behavior was previously reported when coupling anaerobic methanogenesis and EMG processes (Zhao et al., 2014). Even so, the surplus CH_4 production obtained applying voltage (versus the base production in OCV) allowed the calculation of the energy storage efficiency of EMG-BES technology, which was estimated around 42–47% (for calculation details, see the work of Ceballos-Escalera et al., 2020). Strategies to reduce the competition of acetoclastic methanogenesis in the reactor, among other factors, must be developed to ensure an efficient conversion of electricity to CH_4 by electro-active microorganisms (Flores-Rodriguez and Min, 2020).

On the other hand, it is interesting to note the significant increase of CH_4 production achieved in the last condition BAB, when the CO_2 capture process was activated. The membrane contactors allowed to dissolve CO_2 in the influent wastewater, increasing the inorganic carbon availability from 170 ± 17 to 509 ± 241 mg-IC L^{-1}. The average CH_4 production, which was equal to 81 ± 9 L m^{-3} d^{-1} during condition AAB, increased by 81% reaching an average value of 147 ± 33 L m^{-3} d^{-1}. However, the wide whiskers in **Figure 3A** denote a fairly unstable production (see also **Supplementary Figure S1**). The increment of CH_4 production was not matched by an equivalent increase of current density, as shown in **Figure 3B**. Therefore, it can be inferred that the surplus CH_4 achieved by activating the CO_2 capture process was not due to an increased activity of EAB at the cathode. Indeed, considering a hypothetical cathodic Coulombic efficiency of 100%, only 14% of the measured CH_4 production could be ascribed to EMG in condition BAB (see the difference between CH_4 prod. rate and CH_4 prod. EMG for condition BAB, in **Supplementary Table S1**).

Wastewater Treatment

Figure 4A shows the evolution of sulfate concentration in the influent wastewater, for the tested operation conditions. Sulfates presence was mainly due to wastewater pre-treatment, where H_2SO_4 was adopted for pH neutralization (see **Figure 2**). This neutralization was needed to balance NaOH addition, which in turn was required to increase the pH and efficiently dissolve the CO_2 in the wastewater (Rodríguez-Alegre et al., 2019). The same amount of NaOH was added for all the tested conditions, in order to replicate the same pre-treatment process, with and without CO_2 capture. This turned into a significantly higher acid requirement during first conditions, resulting in an average SO_4^{2-} concentration of 4.1 ± 0.9 g L^{-1} (condition AAB). Sulfates could act as alternative electron acceptors for the reduction process at the cathode, producing H_2S and/or elemental sulfur (Coma et al., 2013) and resulting in a lower CH_4 production rate and cathodic Coulombic efficiency (Batlle-Vilanova et al., 2015), when CO_2 capture process was not active

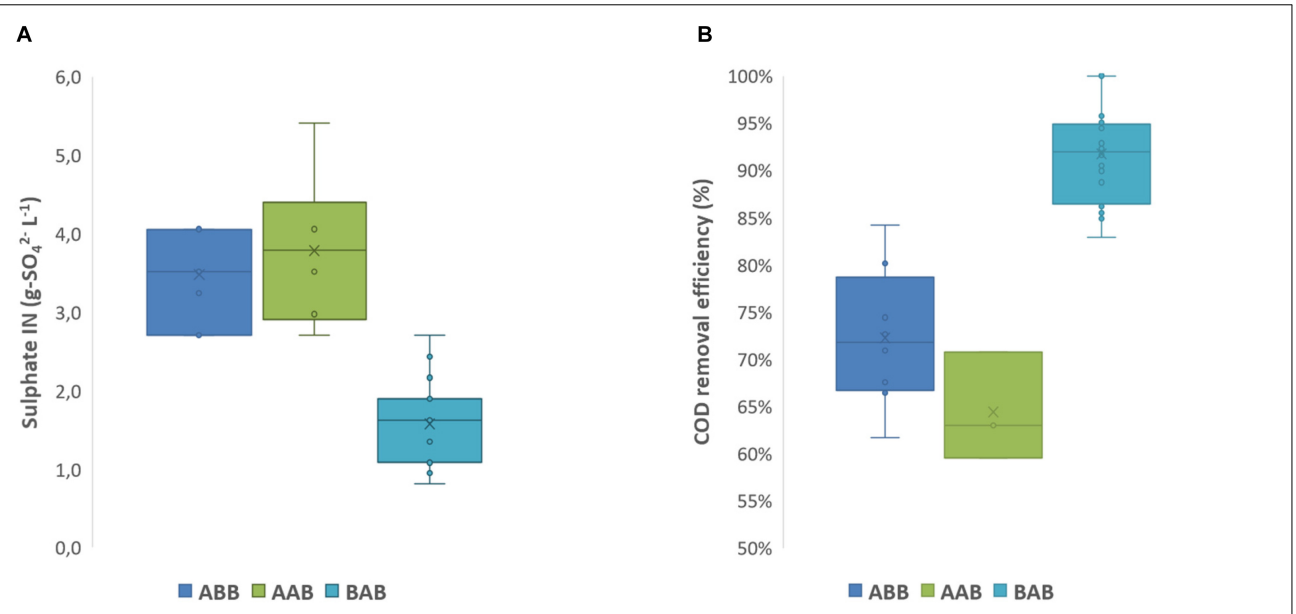

FIGURE 4 | Sulfate concentration of influent wastewater **(A)** and COD removal efficiency **(B)** measured in tested operation conditions. ABB condition refers to days 90 to 118, when stationary phase was reached. ABA and AAA conditions are not reported here as not significative.

(see **Supplementary Figure S2**). Sulfate analysis at the effluent confirmed that 14% of it was removed, or accumulated inside the prototype, during condition AAB. The produced H_2S could in turn inhibit the EMG process, affecting also the organic matter removal on the anode side (**Supplementary Figure S3**). Indeed, the average COD removal efficiency increased from 64 ± 5% to 91 ± 5% passing from condition AAB to BAB, when reducing H_2SO_4 addition to wastewater (**Figure 4B**). In this last condition (BAB), sulfates removal/conversion rate in the prototype was highly reduced, and the effluent revealed a slightly higher SO_4^{2-} concentration than the influent wastewater (1.8 ± 0.7 vs. 1.6 ± 0.5 g L^{-1}), likely due to the re-oxidation to sulfate of the elemental sulfur previously accumulated in the reactor.

The ratio IC/TC of the wastewater varied depending on the activation of the CO_2 capture process. The influent IC/TC ratio was approximately 26–35% without CO_2 capture, and increased to 50% when membrane contactors were activated (**Supplementary Table S1**). Then, while organic matter was oxidized at the anode of EMG-BES cells, additional CO_2 was released into the wastewater. The same CO_2 was reduced at the cathode to CH_4, resulting in the (partial) volatilization of the carbon content of wastewater. During the last condition BAB (the only one with available IC/TC data for influent and effluent), an average TC removal of 41% was estimated. The carbon remaining in the wastewater after the EMG-BES treatment (0.6 ± 0.2 g-TC L^{-1}) was mostly inorganic (IC/TC ratio of 91%). Only 7% of the inorganic carbon load was valorized to CH_4 (see Section "Efficiency Parameters"). Strategies to valorize the residual CO_2 of the effluent wastewater must be developed, in order to avoid its later emission to the atmosphere.

The pH and conductivity trends were similar along all the experiment duration. While the pH increased around 1 point from the influent to effluent section of the prototype (due to H^+ consumption during EMG process), the conductivity remained stable (**Supplementary Table S1**). No major variations were expected for these parameters, due to: (*i*) single-chamber EMG-BES architecture, (*ii*) natural buffering effect of used wastewater, and (*iii*) low current densities achieved.

Biogas Composition

The composition of the biogas produced by the prototype was routinely measured in terms of volumetric content of elemental gases. **Figure 5** shows the average biogas composition for the different operation conditions. Generally, more than the 85% (v/v) of the biogas was composed by CH_4, demonstrating that EMG-BES technology could store electricity in form of a valuable energy vector, near the quality standards of biomethane, i.e., $O_2 < 1\%$, $H_2 < 2\%$, $O_2 + CO_2 + N_2 < 5\%$ (DIN EN 16723-1, 2017). The relevant presence of N_2 in the biogas (6–11%) was due to air intrusion in the reactor, which could not be maintained completely airtight. On the other hand, the O_2 content of biogas was always minor than 1%, as it was likely reduced to water at the cathode or consumed by heterotrophic bacteria, that were present due to the mixed microbial culture used as inoculum (Ceballos-Escalera et al., 2020). Th eventual inhibition effect of O_2 over the electromethanogenic population is still unclear at this stage and will require further research to elucidate its impact on the overall process efficiency.

When the EMG-BES stack was electrically powered (and membrane contactors were not active), almost no CO_2 could be found in the biogas effluent (0.5% in ABB, 0.04% in AAB condition). While a minor part of the inorganic carbon was valorized to CH_4 (see section "Efficiency Parameters"), the most

of it remained trapped in the effluent wastewater, in form of bicarbonate, due to the high pH (**Supplementary Table S1**). Interestingly, some CO_2 was released when EMG was stopped, i.e., during the OCV tests (1.2% in ABA, 2.4% at AAA condition), as it could not be converted to CH_4 and due to the slightly lower pH of the effluent. A few H_2 was detected in the produced biogas, at a higher amount during electrical closed-circuit operation (0.01‰ in ABB, 0.004‰ in AAB condition) compared with the OCV tests. This suggests that H_2 was produced at the cathode, operating indeed at a low potential (−1.1 V vs. Ag/AgCl) compared with the thermodynamic limit required for H_2 evolution (−0.6 V vs. Ag/AgCl). The H_2 was likely consumed at the same moment of its generation by hydrogenotrophic methanogens, this explaining the extremely low concentrations detected in the biogas (Villano et al., 2010).

When the CO_2 capture process was active, CO_2 was constantly detected in the biogas, sometimes at non-negligible concentration (1.8 ± 1.5%). Indeed, the CO_2 was intentionally dissolved in excess in the wastewater, compared with cathodic reduction capacity, in order to achieve non-limiting EMG conditions (Rodríguez-Alegre et al., 2019). Interestingly, also H_2 was detected at the relatively high volumetric concentration of 0.02‰. Hydrogen sulfide was likely always present in the biogas (0.4 ± 0.2‰), as the result of sulfates reduction at the cathode, but its determination could be implemented only for the last condition (BAB), and no values are available for the previous period.

On day 365, a significant volume of biogas was collected, in order to analyze its content of VOCs. Contaminants belonging to the family of alcohols, ketones, non-aromatic hydrocarbons, silicon and sulfur compounds, were found at concentrations higher than 100 μg m^{-3}. Their presence was likely related to the adopted wastewater, which was collected at a municipal WWTP and surely contained some industrial discharges. All the contaminants were found at concentrations lower than threshold values for biomethane quality (**Supplementary Table S2**), confirming the good quality of the produced biogas.

Microbial Community Analysis

The bacterial and archaeal communities associated with bulk medium, anode and cathode biofilm were determined for the reactor module 15 (arbitrarily chosen). The **Figure 6** reports the relative abundance of identified phyla. The biomass contained in the bulk medium was strongly dominated by the Archaea phylum *Euryarchaeota* (60.2 ± 1.8%). Members of this phylum are well known CH_4 producers (Blasco-Gómez et al., 2017), while some of them are also recognized as sulfate reducing bacteria (SRB) (Muyzer and Stams, 2008). On the other hand, the abundance

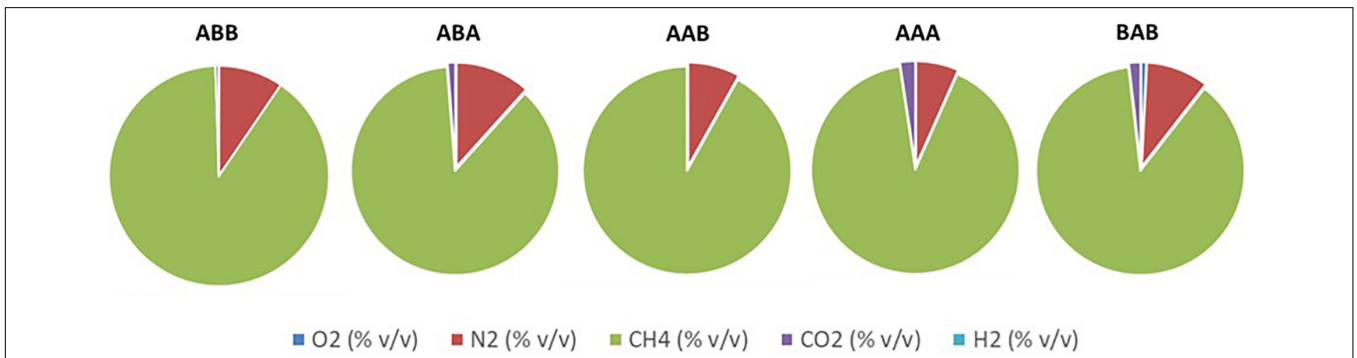

FIGURE 5 | Average biogas composition measured in the tested operation conditions.

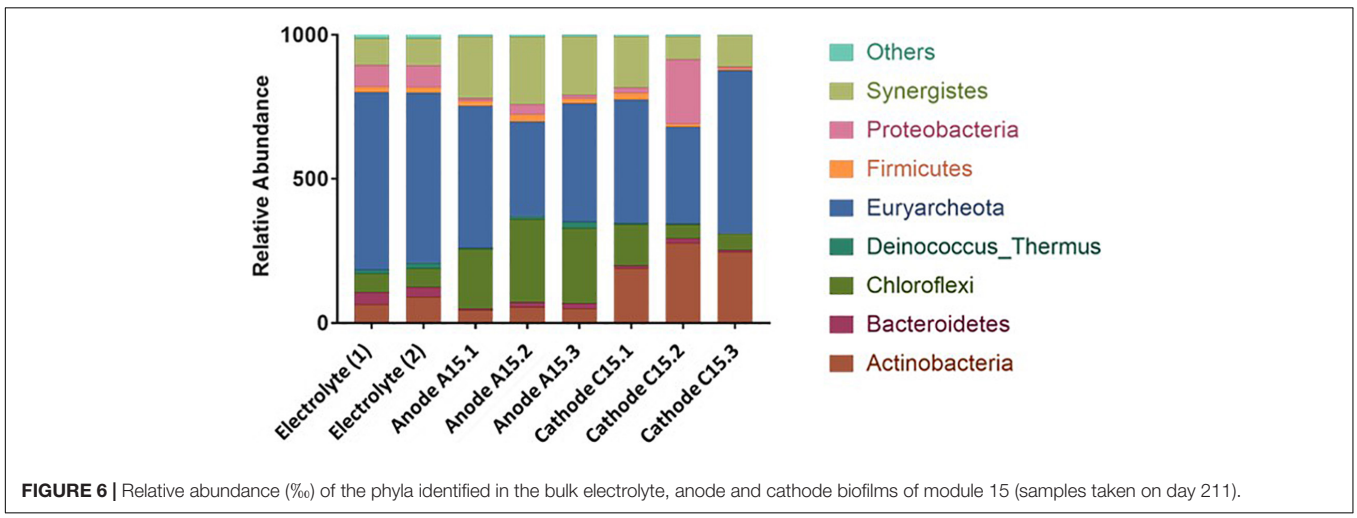

FIGURE 6 | Relative abundance (‰) of the phyla identified in the bulk electrolyte, anode and cathode biofilms of module 15 (samples taken on day 211).

of the phylum *Euryarchaeota* (41.2 ± 8.2%) significantly decreased (p = 0.003) in the biofilm of the anodes, where the *Synergistes* (21.7 ± 1.6%) and *Chloroflexi* (25.2 ± 4.2%) phyla concurrently increased their presence (p = 0.003 and p = 0.013, respectively). *Synergistes* are significant contributors in the degradation of sludge for the production of biogas, in anaerobic digesters (Rivière et al., 2009). The *Chloroflexi* phylum is also common in anaerobic digesters (Flores-Rodriguez and Min, 2020). The presence of these two phyla on the anode (although treating wastewater) likely originated from the inoculum sludge and formed symbiotic relationships. On the cathode samples, *Euryarchaeota* (44.4 ± 11.6%) and *Synergistes* (12.3 ± 5.0%) were still the dominant phyla. As previously mentioned, *Euryarchaeota* were surely responsible of CH_4 production by EMG, and were likely participating in sulfate reduction. *Synergistes* are known also to be responsible of H_2 production in anaerobic digesters (Rivière et al., 2009), and could contribute in this case to H_2 evolution at the cathode, confirming the indications coming from biogas composition analysis (see section "Biogas Composition"). However, in comparison with the wastewater filling the reactor and the anode, *Actinobacteria* became the dominant phylum in the cathode (23.7 ± 4.5%, p = 0.019 and p = 0.002, respectively). *Actinobacteria* was previously reported as dominant phylum on biocathodes performing EMG, co-responsible of H_2 production hereby taking place (Fu et al., 2015).

In order to obtain a deeper insight into the microbial diversity, **Figure 7** shows the relative abundance of the 20 most abundant Operational Taxonomic Units (OTUs) found in the different samples. This way, it can be observed that OTU 1, belonging to the genus *Methanothrix* (*Euryarchaeota*) was the most abundant genus within all the samples, and especially in the bulk medium (58.1 ± 1.4%, p = 0.026 vs. anode, p = 0.044 vs. cathode). *Methanothrix* can use both acetate and CO_2 for CH_4 production (Enzmann et al., 2018; Liu et al., 2019), thereby confirming the coexistence of acetoclastic methanogenesis and EMG processes in the prototype. OTU 11 and OTU 7, belonging to the genera *Thermovirga* (*Synergistes*) and *Levilinea* (*Chloroflexi*), were more abundant in the anodes (7.9 ± 0.1% and 0.9 ± 0.1%, respectively, p = 0.005 and p = 0.011 vs. bulk medium, p = 0.053 and p = 0.016 vs. cathode). *Thermovirga* was previously reported to accelerate hydrolysis of long-chain fatty acids in anaerobic fermentation reactors, providing low-chain molecules to methanogens for CH_4 production (Du et al., 2019) and possibly explaining the relevant presence of *Methanothrix* on the anode (36.4 ± 5.7%, not previously reported for similar systems). Equal considerations are valid for *Levilinea* (Zakaria and Dhar, 2019), which was previously reported in the anode bacterial community of microbial electrolysis cells treating waste activated sludge from municipal WWTPs (Zhao et al., 2016). Apart from *Methanothrix* (32.4 ± 8.4%), the cathode samples revealed the

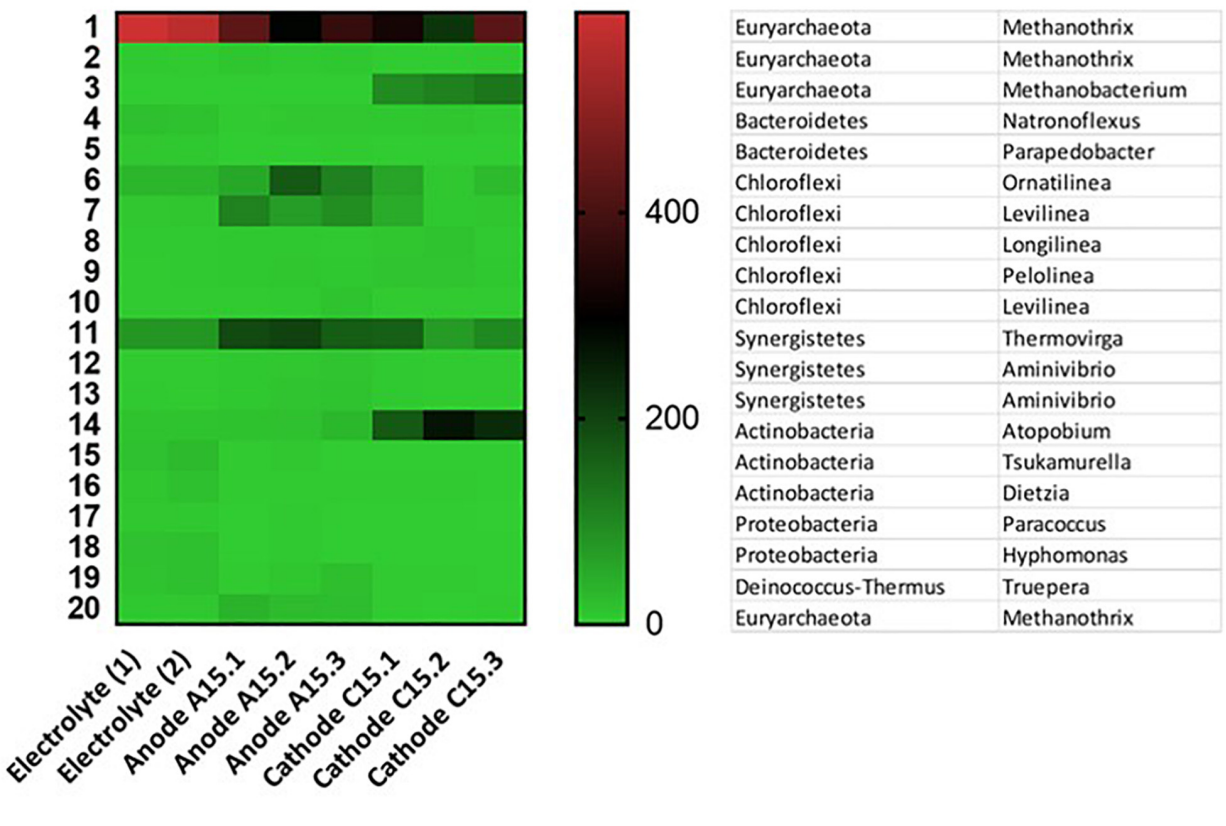

FIGURE 7 | Relative abundance (‰) of the 20 most abundant microorganisms (OTUs) identified in the electrolyte (2 replicates), anode and cathode biofilms of module 15.

significant presence of OTU 14 and OTU 3, belonging to the genera *Atopobium* (*Actinobacteria*) and *Methanobacterium* (*Euryarchaeota*) (1.3 ± 0.01% and 0.1 ± 0.01%, respectively, $p = 0.011$ and $p = 0.003$ vs. bulk medium; $p = 0.002$ and $p < 0.001$ vs. anode). While *Methanobacterium* is a well-known H_2-consuming methanogen and was often reported in the microbial community of EMG biocathodes (Flores-Rodriguez and Min, 2020; Xu et al., 2020; among others), *Atopobium* was not previously reported and its role is not clear at this stage. In conclusion, the description of the microbial community colonizing the EMG-BES prototype indicated the biological syntrophic relationships between its more relevant members and, as a consequence, the opportunities of such bioelectrochemical system for the simultaneous achievement of electricity storage, CO_2 conversion to CH_4 and wastewater treatment, due to the metabolic potential of the microbial diversity inhabiting this particular ecosystem. The presence of microorganisms linked to the sulfur cycle opens a potential new field of research, to elucidate the relationship between them and the electromethanogenic population.

Efficiency Parameters

The Coulombic efficiency of anode and cathode was estimated for the different tested conditions. Once the current density stabilized, the anode Coulombic efficiency remained stable (16 ± 2% at condition AAB, 14 ± 4% at condition BAB), showing that CO_2 capture activation did not offer a competitive advantage to oxidative EAB at the anode. On the other hand, the cathode Coulombic efficiency increased from 399 ± 49% (AAB) to 694 ± 226% (BAB). As explained by Ceballos-Escalera et al. (2020), cathode Coulombic efficiencies higher than 100% indicate situations where the measured CH_4 production is higher than that achievable only by EMG, i.e., acetoclastic methanogenesis became with time the main pathway of acetate degradation in the prototype (Zhao et al., 2014). However, it is meaningful to observe that the specific energy consumption of EMG-BES cells reached its optimum during condition BAB, i.e., when CO_2 was injected in the wastewater. A minimum energy input of 1.0 ± 0.3 kWh was necessary to produce 1 m^{-3} CH_4 (compared with 1.6 ± 0.2 kWh m^{-3} CH_4 for condition AAA). This confirmed the validity of the EMG-BES technology, already proofed at laboratory stage by Rodríguez-Alegre et al. (2019), merging the two complementary needs of carbon capture and electricity storage.

In this regard, the CCU potential of the integrated technology of membrane contactors and EMG-BES cells was estimated in terms of (maximum) carbon conversion efficiency from dissolved CO_2 to gaseous CH_4. The 30% of inorganic carbon was potentially converted to CH_4 during condition ABB (see Eq. 3 for calculation details). Reducing the temperature from 32°C to 25°C, only 15% of the inorganic carbon load could be converted. Injecting additional CO_2 to the wastewater (condition BAB), only 7% of the carbon was valorized, confirming the values obtained in the laboratory by Rodríguez-Alegre et al. (2019). It must be noted that the estimation of this parameter is not easy, as organic and inorganic carbon can undergo different metabolic processes at both anode and cathode of an EMG-BES reactor. Therefore, the values of carbon conversion efficiency hereby commented should not be taken as quantitative, but only orientative.

CONCLUSION

A bioelectrochemical power-to-gas prototype was long-term operated (400 days), integrating membrane contactors for CO_2 capture in wastewater with a stack of BES cells performing electromethanogenesis. Different operational conditions were tested, acting on parameters like temperature, applied voltage and CO_2 capture (ON/OFF). The prototype achieved the highest CH_4 production rate (147 ± 33 L m^{-3} d^{-1}), with a high gas quality (CH_4 > 85% v/v) and the lowest energy consumption (1.0 ± 0.3 kWh m^{-3} CH_4), when operated at 25°C and 0.7 V, while capturing and converting 22 L m^{-3} d^{-1} of CO_2. Only 7% of the injected carbon load could be valorized to CH_4, because CO_2 was dissolved in excess in the wastewater, compared with cathodic reduction capacity, in order to achieve non-limiting EMG. Traces of H_2 in the biogas, detectable during the periods of closed electric circuit, indicated that hydrogenotrophic methanogenesis was taking place at the cathode. On the other hand, a relevant CH_4 production during the periods of open electric circuit confirmed the presence of acetoclastic methanogenic microorganisms in the microbial community. This was dominated by the archaea *Methanothrix* (*Euryarchaeota*). Different microorganisms belonging to the *Synergistes* phylum were found at the anode and the cathode, having a potential role in organic matter degradation and H_2 production, respectively. In the panorama of methanation technologies currently available for PtX, the performances of this EMG-BES prototype are not yet competitive, especially because of a low CH_4 production rate, a limited current/power density demand (<10 W m^{-3}) and a low CO_2 conversion efficiency (7–30%). On the other hand, the possibility to obtain a high-quality biogas (near biomethane quality) at a minimal energy consumption leads to a potentially favorable business scenario for this technology, compared with biological methanation or anaerobic digestion.

DATA AVAILABILITY STATEMENT

The datasets presented in this study can be found in online repositories. The names of the repository/repositories and accession number(s) can be found below: https://www.ncbi.nlm.nih.gov/, PRJNA627951.

AUTHOR CONTRIBUTIONS

DM, PB-J, EB, EL, and RR-A contributed to the prototype design and construction. AM-E and RR-A (among others) performed periodical CO_2 saturation of wastewater and took care of the maintenance of the membrane contactors. DM performed experiments on the EMG-BES stack, collected and elaborated the experimental data. JG and SL performed the microbial

community analysis. DM wrote the first draft of the manuscript, while all authors contributed to its revision, read and approved the submitted version. MD, PB-J, and EB managed funding acquisition and project direction. All authors contributed to the article and approved the submitted version.

FUNDING

This work has been financially supported by the Spanish Ministry of Economy and Competitiveness under the project Power2Biomethane (RTC-2016-5024-3, 2016).

ACKNOWLEDGMENTS

The authors wish to acknowledge David Gali, Olga Gomez Navarro, and the other Leitat collaborators who took part in the Power2Biomethane project.

SUPPLEMENTARY MATERIAL

The Supplementary Material for this article can be found online at: https://www.frontiersin.org/articles/10.3389/fenrg.2020.00174/full#supplementary-material

REFERENCES

APHA (2005). *Standard Methods for the Examination of Water and Wastewater*, 19th Edn. Washington, DC: American Public Healt Association.

Aronesty, E. (2013). Comparison of sequencing utility programs. *TOBIOIJ* 7, 1–8. doi: 10.2174/1875036201307010001

Bailera, M., Lisbona, P., Romeo, L. M., and Espatolero, S. (2017). Power to Gas projects review: lab, pilot and demo plants for storing renewable energy and CO2. *Renew. Sust. Energ. Rev.* 69, 292–312. doi: 10.1016/j.rser.2016.11.130

Batlle-Vilanova, P., Puig, S., Gonzalez-Olmos, R., Vilajeliu-Pons, A., Balaguer, M. D., and Colprim, J. (2015). Deciphering the electron transfer mechanisms for biogas upgrading to biomethane within a mixed culture biocathode. *RSC Adv.* 5, 52243–52251. doi: 10.1039/c5ra09039c

Batlle-Vilanova, P., Rovira-Alsina, L., Puig, S., Balaguer, M. D., Icaran, P., Monsalvo, V. M., et al. (2019). Biogas upgrading, CO2 valorization and economic revaluation of bioelectrochemical systems through anodic chlorine production in the framework of wastewater treatment plants. *Sci. Total Environ.* 690, 352–360. doi: 10.1016/j.scitotenv.2019.06.361

Blanco, H., and Faaij, A. (2018). A review at the role of storage in energy systems with a focus on Power to Gas and long-term storage. *Renew. Sust. Energ. Rev.* 81, 1049–1086. doi: 10.1016/j.rser.2017.07.062

Blasco-Gómez, R., Batlle-Vilanova, P., Villano, M., Balaguer, M., Colprim, J., and Puig, S. (2017). On the edge of research and technological application: a critical review of electromethanogenesis. *Int. J. Mol. Sci.* 18, 874–874.

Caporaso, J. G., Lauber, C. L., Walters, W. A., Berg-Lyons, D., Huntley, J., Fierer, N., et al. (2012). Ultra-high-throughput microbial community analysis on the Illumina HiSeq and MiSeq platforms. *ISME J.* 6, 1621–1624. doi: 10.1038/ismej.2012.8

Ceballos-Escalera, A., Molognoni, D., Bosch-Jimenez, P., Shahparasti, M., Bouchakour, S., Luna, A., et al. (2020). Bioelectrochemical systems for energy storage: a scaled-up power-to-gas approach. *Appl. Energ.* 260:114138. doi: 10.1016/j.apenergy.2019.114138

Cheng, S., Xing, D., Call, D. F., and Logan, B. E. (2009). Direct biological conversion of electrical current into methane by electromethanogenesis. *Environ. Sci. Technol.* 43, 3953–3958. doi: 10.1021/es803531g

Coma, M., Puig, S., Pous, N., Balaguer, M. D. D., and Colprim, J. (2013). Biocatalysed sulphate removal in a BES cathode. *Bioresour. Technol.* 130, 218–223. doi: 10.1016/j.biortech.2012.12.050

Denholm, P., Ela, E., Kirby, B., and Milligan, M. (2010). *Role of Energy Storage with Renewable Electricity Generation*. Golden, CO: National Renewable Energy Lab.

DIN EN 16723-1 (2017). *Natural gas and Biomethane for use in Transport and Biomethane for Injection in the Natural Gas Network - Part 1: Specifications for Biomethane for Injection in the Natural Gas Network*. Berlin: German Institute for Standardisation.

Du, S., Sun, C., Ding, A., Chen, W., Zhang, M., Cheng, R., et al. (2019). Microbial dynamics and performance in a microbial electrolysis cell-anaerobic membrane bioreactor. *J. Zhejiang Univ. Sci. A* 20, 533–545. doi: 10.1631/jzus.a1900009

Edgar, R. C. (2013). UPARSE: highly accurate OTU sequences from microbial amplicon reads. *Nat. Methods* 10, 996–998. doi: 10.1038/nmeth.2604

Enzmann, F., Mayer, F., Rother, M., and Holtmann, D. (2018). Methanogens: biochemical background and biotechnological applications. *AMB Exp.* 8:1.

European Commission (2011). *European Energy Roadmap 2050*. Available online at: https://ec.europa.eu/energy/sites/ener/files/documents/2012_energy_roadmap_2050_en_0.pdf (accessed June 5, 2019).

Flores-Rodriguez, C., and Min, B. (2020). Enrichment of specific microbial communities by optimum applied voltages for enhanced methane production by microbial electrosynthesis in anaerobic digestion. *Bioresour. Technol.* 300:22624.

Fu, Q., Kuramochi, Y., Fukushima, N., Maeda, H., Sato, K., and Kobayashi, H. (2015). Bioelectrochemical analyses of the development of a thermophilic biocathode catalyzing electromethanogenesis. *Environ. Sci. Technol.* 49, 1225–1232. doi: 10.1021/es5052233

Geppert, F., Liu, D., van Eerten-Jansen, M., Weidner, E., Buisman, C., and ter Heijne, A. (2016). Bioelectrochemical power-to-gas: state of the art and future perspectives. *Trends Biotechnol.* 34, 879–894. doi: 10.1016/j.tibtech.2016.08.010

Harnisch, F., Aulenta, F., and Schröder, U. (2011). "Microbial fuel cells and bioelectrochemical systems," in *Comprehensive Biotechnology* (Amsterdam: Elsevier), 643–659. doi: 10.1016/b978-0-08-088504-9.00462-1

Inkeri, E., Sihvonen, T., Karjunen, H., Tynjälä, T., Tähtinen, M., and Weiss, R. (2016). "Integration of power-to-gas process to wastewater treatment plant with biogas production," in *Conference Proceedings of the 10th International Renewable Energy Storage Conference (IRES 2016)*, Düsseldorf, 11.

Leonzio, G. (2019). Power to gas systems integrated with anaerobic digesters and gasification systems. *Waste Biomass Valor* [Epub ahead of print].

Liu, C., Sun, D., Zhao, Z., Dang, Y., and Holmes, D. E. (2019). Methanothrix enhances biogas upgrading in microbial electrolysis cell via direct electron transfer. *Bioresour. Technol.* 291:121877. doi: 10.1016/j.biortech.2019.121877

Mayer, F., Enzmann, F., Lopez, A. M., and Holtmann, D. (2019). Performance of different methanogenic species for the microbial electrosynthesis of methane from carbon dioxide. *Bioresour. Technol.* 289:121706. doi: 10.1016/j.biortech.2019.121706

Moreno, R., San-Martín, M. I., Escapa, A., and Morán, A. (2016). Domestic wastewater treatment in parallel with methane production in a microbial electrolysis cell. *Renew. Energy* 93, 442–448. doi: 10.1016/j.renene.2016.02.083

Muñoz-Aguilar, R., Molognoni, D., Bosch-Jimenez, P., Borràs, E., Della Pirriera, M., and Luna, Á (2018). Design, operation, modeling and grid integration of power-to-gas bioelectrochemical systems. *Energies* 11, 1947–1947.

Muyzer, G., and Stams, A. J. M. (2008). The ecology and biotechnology of sulphate-reducing bacteria. *Nat. Rev. Microbiol.* 6, 441–454. doi: 10.1038/nrmicro1892

Nogalska, A., Trojanowska, A., and Garcia-Valls, R. (2017). Membrane contactors for CO2 capture processes – critical review. *Phys. Sci. Rev.* 2 [Epub ahead of print].

Noori, M. T., Vu, M. T., Ali, R. B., and Min, B. (2019). Recent advances in cathode materials and configurations for upgrading methane in bioelectrochemical systems integrated with anaerobic digestion. *Chemi. Eng. J.* 3292:123689. doi: 10.1016/j.cej.2019.123689

Park, J.-G., Lee, B., Park, H., and Jun, H. (2018). Long-term evaluation of methane production in a bio-electrochemical anaerobic digestion reactor according to the organic loading rate. *Bioresour. Technol.* 273, 478–486. doi: 10.1016/j.biortech.2018.11.021

Rivière, D., Desvignes, V., Pelletier, E., Chaussonnerie, S., Guermazi, S., Weissenbach, J., et al. (2009). Towards the definition of a core of

microorganisms involved in anaerobic digestion of sludge. *ISME J.* 3, 700–714. doi: 10.1038/ismej.2009.2

Rodríguez-Alegre, R., Ceballos-Escalera, A., Molognoni, D., Bosch-Jimenez, P., Galí, D., Licon, E., et al. (2019). Integration of membrane contactors and bioelectrochemical systems for CO2 Conversion to CH4. *Energies* 12, 361–361.

Větrovský, T., and Baldrian, P. (2013). The variability of the 16S rRNA Gene in bacterial genomes and its consequences for bacterial community analyses. *PLoS One* 8:e57923. doi: 10.1371/journal.pone.0057923

Větrovský, T., Baldrian, P., and Morais, D. (2018). SEED 2: a user-friendly platform for amplicon high-throughput sequencing data analyses. *Bioinformatics* 34, 2292–2294. doi: 10.1093/bioinformatics/bty071

Villano, M., Aulenta, F., Ciucci, C., Ferri, T., Giuliano, A., and Majone, M. (2010). Bioelectrochemical reduction of CO2 to CH4 via direct and indirect extracellular electron transfer by a hydrogenophilic methanogenic culture. *Bioresour. Technol.* 101, 3085–3090. doi: 10.1016/j.biortech.2009.12.077

Xu, X.-J., Wang, W.-Q., Chen, C., Xie, P., Liu, W.-Z., Zhou, X., et al. (2020). Bioelectrochemical system for the enhancement of methane production by anaerobic digestion of alkaline pretreated sludge. *Bioresour. Technol.* 304:123000. doi: 10.1016/j.biortech.2020.123000

Zakaria, B. S., and Dhar, B. R. (2019). Progress towards catalyzing electromethanogenesis in anaerobic digestion process: fundamentals, process optimization, design and scale-up considerations. *Bioresour. Technol.* 289:121738. doi: 10.1016/j.biortech.2019.121738

Zeng, Q., Fang, J., Li, J., and Chen, Z. (2016). Steady-state analysis of the integrated natural gas and electric power system with bi-directional energy conversion. *Appl. Energ.* 184, 1483–1492. doi: 10.1016/j.apenergy.2016.05.060

Zhang, Z., Song, Y., Zheng, S., Zhen, G., Lu, X., Takuro, K., et al. (2019). Electro-conversion of carbon dioxide (CO2) to low-carbon methane by bioelectromethanogenesis process in microbial electrolysis cells: the current status and future perspective. *Bioresour. Technol.* 279, 339–349. doi: 10.1016/j.biortech.2019.01.145

Zhao, Z., Zhang, Y., Chen, S., Quan, X., and Yu, Q. (2014). Bioelectrochemical enhancement of anaerobic methanogenesis for high organic load rate wastewater treatment in a up-flow anaerobic sludge blanket (UASB) reactor. *Sci. Rep.* 4, 6658–6658.

Zhao, Z., Zhang, Y., Yu, Q., Ma, W., Sun, J., and Quan, X. (2016). Enhanced decomposition of waste activated sludge via anodic oxidation for methane production and bioenergy recovery. *Int. Biodeterior. Biodegradation* 106, 161–169. doi: 10.1016/j.ibiod.2015.10.020

Zhen, G., Zheng, S., Lu, X., Zhu, X., Mei, J., Kobayashi, T., et al. (2018). A comprehensive comparison of five different carbon-based cathode materials in CO2 electromethanogenesis: long-term performance, cell-electrode contact behaviors and extracellular electron transfer pathways. *Bioresour. Technol.* 266, 382–388. doi: 10.1016/j.biortech.2018.06.101

Conflict of Interest: The authors declare that the research was conducted in the absence of any commercial or financial relationships that could be construed as a potential conflict of interest.

frontiers in Energy Research

REVIEW
published: 08 September 2020
doi: 10.3389/fenrg.2020.570112

A Review on Synthesis of Methane as a Pathway for Renewable Energy Storage With a Focus on Solid Oxide Electrolytic Cell-Based Processes

Saheli Biswas[1], *Aniruddha P. Kulkarni*[2]*, *Sarbjit Giddey*[2] *and Sankar Bhattacharya*[1]

[1] Department of Chemical Engineering, Monash University, Melbourne, VIC, Australia, [2] CSIRO Energy, Clayton South, VIC, Australia

Environmental issues related to global warming are constantly pushing the fossil fuel-based energy sector toward an efficient and economically viable utilization of renewable energy. However, challenges related to renewable energy call for alternative routes of its conversion to fuels and chemicals by an emerging Power-to-X approach. Methane is one such high-valued fuel that can be produced through renewables-powered electrolytic routes. Such routes employ alkaline electrolyzers, proton exchange membrane electrolyzers, and solid oxide electrolyzers, commonly known as solid oxide electrolysis cells (SOECs). SOECs have the potential to utilize the waste heat generated from exothermic methanation reactions to reduce the expensive electrical energy input required for electrolysis. A further advantage of an SOEC lies in its capacity to co-electrolyze both steam and carbon dioxide as opposed to only water, and this inherent capability of an SOEC can be harnessed for *in situ* synthesis of methane within a single reactor. However, the concept of *in situ* methanation in SOECs is still at a nascent stage and requires significant advancements in SOEC materials, particularly in developing a cathode electrocatalyst that demonstrates activity toward both steam electrolysis and methanation reactions. Equally important is the appropriate reactor design along with optimization of cell operating conditions (temperature, pressure, and applied potential). This review elucidates those developments along with research and

OPEN ACCESS

Edited by:
Valerie Eveloy, Khalifa University, United Arab Emirates

Reviewed by:
Søren Højgaard Jensen, Aalborg University, Denmark
Tong Liu, Wuhan University, China

***Correspondence:**
Aniruddha P. Kulkarni
Aniruddha.Kulkarni@csiro.au

Specialty section:
This article was submitted to Hydrogen Storage and Production, a section of the journal Frontiers in Energy Research

Received: *06 June 2020*
Accepted: *18 August 2020*
Published: *08 September 2020*

Citation:
Biswas S, Kulkarni AP, Giddey S and Bhattacharya S (2020) A Review on Synthesis of Methane as a Pathway for Renewable Energy Storage With a Focus on Solid Oxide Electrolytic Cell-Based Processes. Front. Energy Res. 8:570112. doi: 10.3389/fenrg.2020.570112

Abbreviations: AEL, alkaline electrolytic cell; ASR, area-specific resistance; BOP, balance of plant; CCS, carbon capture and sequestration; DME, dimethyl ether; e^-, electron; F, Faraday's constant (96,485 C mol^{-1}); F–T, Fischer–Tropsch; ΔG, Gibb's free energy (kJ mol^{-1}); ΔG^0, Gibb's free energy at 298 K, 1 atm; GDC, gadolinia-doped ceria; GHG, greenhouse gas; H^+, hydrogen ion; ΔH, change in enthalpy (kJ mol^{-1}); ΔH^0, change in enthalpy at 298 K, 1 atm; H-SOEC, proton-conducting solid oxide electrolytic cell; HT, high temperature; I, current (A); IEA, International Energy Agency; K_{eql}, equilibrium constant; $K_{eql}{}^0$, equilibrium constant at 298 K, 1 atm; LNG, liquefied natural gas; LSCF, strontium- and cobalt-doped lanthanum ferrite; LSCM, strontium- and cobalt-doped lanthanum manganite; LSMG, strontium- and magnesium-doped lanthanum gallate; LSF, strontium-doped lanthanum ferrite; LST, lanthanum-doped strontium titanate; LT, low temperature; MR, methanation reactor; n, number of electrons transferred during electrolysis; NEMCA, non-Faradaic electrochemical modification of catalytic activity; NTP, normal temperature and pressure of 298 K, 1 atm; O^{2-}, oxide ion; OH^-, hydroxyl ion; P, partial pressure (atm); PEM, proton exchange membrane; PV, photovoltaic; R, universal gas constant (8.314 J mol^{-1} K); R_{act}, resistance due to activation overpotential (ohm); R_{conv}, gas conversion overpotential (ohm); R_{diff}, resistance due to diffusion overpotential (ohm); R_{ohm}, ohmic resistance (ohm); R_{pol}, polarization resistance (ohm); R&D, research and development; RE, renewable energy; RTE, round trip efficiency; ΔS, change in entropy (kJ mol^{-1} K^{-1}); ΔS^0, change in entropy at 298 K, 1 atm (kJ mol^{-1} K^{-1}); ScSZ, scandia-stabilized zirconia; SDC, samaria-doped ceria; SOEC, solid oxide electrolytic cell; SR, Sabatier reactor; T, temperature (K); T^0, normal temperature (298 K); TPB, triple-phase boundary; V_0, minimum thermodynamic voltage required for electrolysis (V); V_n, Nernst potential (V); V_{OP}, actual cell operating voltage (V); WGSR, water–gas shift reactor; X-ray near-edge structure, X-ray absorption near-edge structure; YSZ, yttria-stabilized zirconia; η, energy efficiency.

development opportunities in this space. Also presented here is an efficiency comparison of different routes of synthetic methane production using SOECs in various modes, that is, as a source of hydrogen, syngas, and hydrogen/carbon dioxide mixture, and for *in situ* methane synthesis.

Keywords: renewable fuel, power-to-X, hydrogen, methane, solid oxide electrolyzer

INTRODUCTION

The global energy consumption has been increasing ever since the dawn of industrialization. Such an increase can be attributed to the expeditious economic growth across the globe and the rising population. World Energy Outlook 2019 [International Energy Agency (IEA) 2019 executive summary] and others (Criqui and Kouvaritakis, 2000; Newell et al., 2018) report that in 2018, worldwide energy consumption increased by 2.3%, which is almost twice the average rate of growth since 2010. The deleterious aftermath of such higher energy consumption is an overall CO_2 emission of 33.1 Gt, which is 1.7% higher than that in 2017. This is equivalent to 2.4 ppm rise in the total concentration of atmospheric CO_2 as stated by the IEA (Capuano, 2018) and others (Saracoglu et al., 2018). According to studies conducted by National Aeronautics and Space Administration (NASA) and recent UN reports, such a steady acceleration of CO_2 levels will increase the earth's temperature by 1.5°C by 2052, leading to the melting of the Arctic ice and subsequent perilous rise in sea level. Such effects coupled with the gradual depletion of fossil fuels has made a compelling case for the development and deployment of renewable energy (RE) sources such as solar, wind, tidal, and geothermal energy.

A substantial reduction in the manufacturing and capital costs associated with solar and wind energy plants has been observed in the last decade. Renewables 2018 (Saracoglu et al., 2018) predicts that by 2023, there would be 1,460 TW h of electricity generation from solar photovoltaic and 1,880 TW h of electricity generation from offshore and onshore wind turbines (Renewables, 2018). An analysis of the world energy scenario in terms of fuel type shows that consumption of renewables has expanded at an annual growth rate of about 12% over the past 10 years, driven by the move of electricity generation toward renewables (Tanaka, 2010).

Despite impressive numbers, inherent intermittency and uneven geographical distribution of RE sources remain a barrier for a solid commercial case of clean energy technologies, and therefore, reliance on fossil fuel continues. As such, the key enablers for renewable technology will be pathways for efficient and cost-effective storage as well as transportation of RE from the supply areas rich in RE to the demand areas like cities and industrial establishments. In this context, the conversion of RE into storable and transportable energy carriers is being considered a promising avenue to balance the energy supply–demand equation.

An emerging technology in this area is broadly defined as Power-to-X, where X can be a fuel such as hydrogen, ammonia, methanol, and dimethyl ether, or a commodity chemical like lubricants and aviation fuels (Foit et al., 2017; Rego de Vasconcelos and Lavoie, 2019; Dueñas et al., 2020). Hydrogen is a zero carbon-emission fuel with high gravimetric energy density (33.3 kW h/kg) that can be synthesized using various electrolytic, photocatalytic, or solar thermochemical processes (Chen and Shangguan, 2013; Acar and Dincer, 2019) and can be efficiently converted back to energy without carbon emission. However, the major hurdles in a hydrogen-based RE economy are difficulties in the storage and transportation of hydrogen owing to energy-intensive processes of compression or liquefaction and boil-off losses during transportation. For instance, up to 12% of the energy content of hydrogen is lost while compressing the gas to the required pressures (Makridis, 2017; Bruce et al., 2018). Although hydrogen has a very high gravimetric heat content (lower heating value (LHV) of 33.3 kWh/kg), its volumetric heat content is very low (2.73 Wh/L). Further, several challenges related to the mechanical properties of storage materials need to be addressed (Christian et al., 2013; Prabhukhot Prachi et al., 2016).

A last link of the supply chain technology is the conversion of hydrogen back to energy that also needs substantial bottoms-up development. Most of the current infrastructure for utilization of carbon fuels such as gasoline, diesel, or natural gas cannot be used with hydrogen in high concentration due to issues related to hydrogen embrittlement, flame travel distance, and a high autoignition temperature (Verhelst and Wallner, 2009).

In response to these challenges, storing and transporting energy in the form of hydrogen carriers appears interesting, where methane is being considered one of the promising and practical energy cum hydrogen carriers due to its moderately high heat content (LHV of 13 kW h/kg) as compared to other prospective alternatives such as gasoline (LHV of 12 kW h/kg) and ammonia (LHV of 5.2 kW h/kg), lower compression energy (0.56 kW h/kg at the usual compression pressure of 350 bar) (Makridis, 2017), and facile synthesis using RE and waste CO_2 (**Figure 1A**).

Methane is a primary constituent of natural gas (50–90%) and can be effectively used for any application where natural gas is being currently used. Apart from this, methane finds potential application in different chemicals production as well. Global Energy Statistical Yearbook states that from 2010 to 2018, global natural gas consumption increased by 11%, and the IEA has predicted that this value will rise to almost 55% with a total gas consumption of ~53,330 TW h by 2040 (Capuano, 2018). Recently, there has been an interest in utilizing methane as a probable RE carrier, especially in the context of Australia's abundant RE potential and its vision as an exporter of the same to other countries.

Several processes to produce methane from feedstock (typically CO_2 and H_2) are under investigation. These include thermochemical (Mills and Steffgen, 1974; Anderson et al., 1984; Schulz, 1999; Junaedi et al., 2014; El Sibai et al., 2015), photocatalytic (Kondratenko et al., 2013; Wang K. et al., 2017;

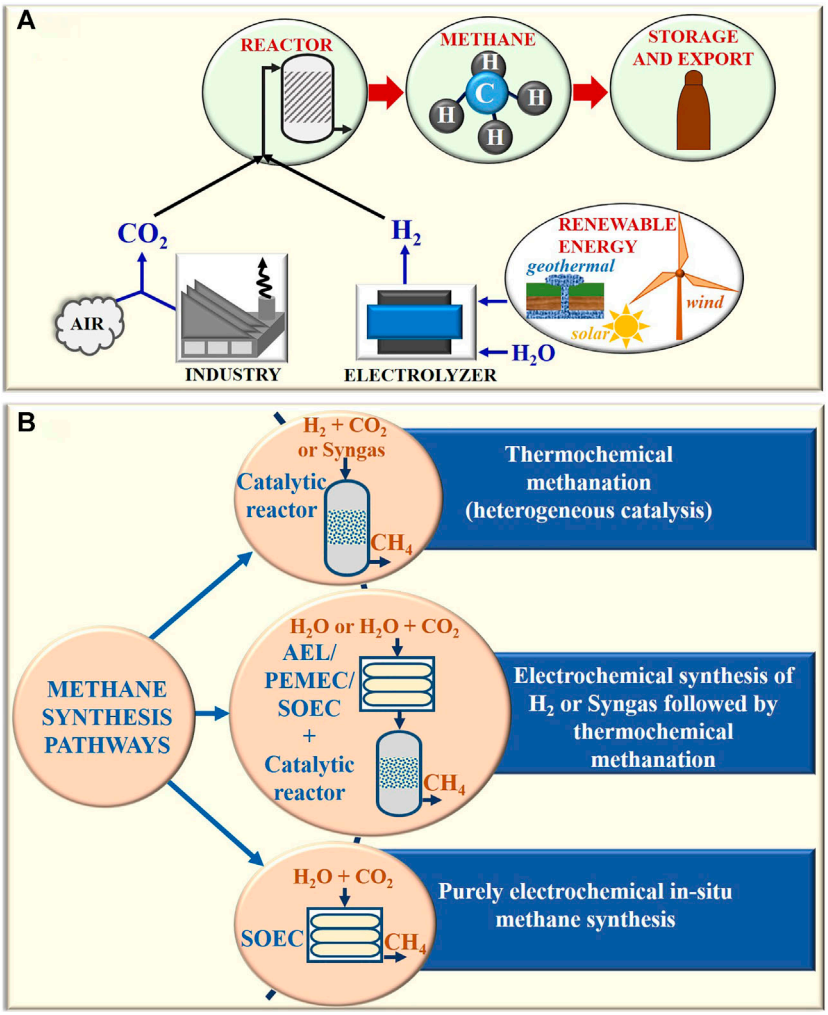

FIGURE 1 | A) Methane synthesis through renewables-powered electrochemical reactors. **(B)** Three major pathways of methane synthesis.

Murugesan et al., 2020), electrochemical (Kondratenko et al., 2013; Clausen et al., 2019; Kofler et al., 2019), and biogenic (Hobson et al., 1981; Cimon et al., 2020) routes. Among these, thermochemical methanation is perhaps the most extensively studied and currently used for synthetic methane manufacturing. The process can utilize hydrogen generated non-renewably through natural gas and oil reforming processes, or renewably by electrolysis, photocatalysis, plasma reforming, thermochemical water splitting, dark fermentation, and biophotolysis (Acar and Dincer, 2019). The hydrogen production technologies have been presented in the literature in great depths, with a plethora of reviews on materials, methods, and techno-economics thereof (Nikolaidis and Poullikkas, 2017; Acar and Dincer, 2019; Zhu et al., 2019).

In the genre of electrolytic routes, a comparatively early-stage technology that offers scalable, economic, and highly efficient solution to produce either pure hydrogen or syngas (a mixture of CO and H_2) for methanation is based upon solid oxide electrolysis. More interestingly, it can be used to directly synthesize methane from steam and CO_2 co-electrolysis with a right combination of electrocatalyst and process conditions. However, this route of methane synthesis is not yet well established, with a dearth of knowledge on the fundamental mechanism, reaction pathways, and development of materials tailored to improve the reaction kinetics, product selectivity, and process efficiency. Further, the scale and lifetime of solid oxide electrolyzers remain limited compared to those of more established alkaline and proton exchange membrane (PEM) electrolyzers.

For methane synthesis using solid oxide electrolytic cell (SOEC) coupled with a thermochemical methanator, the challenges are essentially those related to hydrogen and syngas production in SOECs. This review elucidates those issues followed by a brief discussion on the emerging area of one-step methane generation in SOEC via co-electrolysis of steam (instead of hydrogen) and CO_2. An efficiency comparison of methane synthesis using SOEC in all possible configurations has also been presented at the end. For such comparison, previous studies (Jensen et al., 2015; Luo et al., 2018; Wang et al., 2018; Wang L. et al., 2019) have focused on SOECs

only as a source of hydrogen and syngas (H_2/CO), but here we have considered SOECs as a source of H_2/CO_2 mixture and for *in situ* methanation as well.

MAJOR PATHWAYS OF METHANE SYNTHESIS

As opposed to other emerging hydrogen carriers, the infrastructure for the synthesis, storage, transport, and utilization of methane is fairly well-established. Several pathways of methane synthesis have emerged over the past few decades that can be broadly categorized as shown in **Figure 1B** and have been briefly described in this review with a detailed discussion on SOECs. Synthetic methane production routes can be classified as follows:

(1) Purely thermochemical process in a catalytic reactor using biosyngas or industrial syngas, or other non-electrolytic sources of H_2 and CO_2 (discussed in *Purely Thermochemical Route of Methane Synthesis*)
(2) Combined thermo-electro-chemical process where H_2 produced from electrolytic routes [using alkaline electrolytic cells (AELs) or PEM electrolytic cells (PEMECs) or solid oxide electrolytic cells (SOECs)] or syngas produced from steam/CO_2 co-electrolysis in SOECs is utilized for thermochemical methanation in a conventional catalytic reactor (discussed in *Combined Thermo-Electro-Chemical Route of Methane Synthesis* and *Challenges and Advancement in the Electrolytic Production of Hydrogen and Syngas in Solid Oxide Electrolytic Cell Integrated With Thermochemical Reactor for Methane Synthesis*)
(3) Purely electrochemical process of *in situ* methane synthesis in high-temperature SOECs (discussed in *State of the Art of Purely Electrochemical In Situ Methane Synthesis in Solid Oxide Electrolytic Cell*)

As can be well perceived from the above classifications, synthetic methane production requires a source of carbon along with an electrolytic or non-electrolytic source of hydrogen. Several industrial processes yield highly pure and concentrated CO_2 off-gas, which can be separated from impurities and sequestered (Farla et al., 1995). These processes include production of alcohols (ethanol and methanol), ammonia synthesis, synthetic fuel production, and production of several organic chemicals. Other sources of CO_2 in high concentration include iron and steel plants (Kim and Worrell, 2002) and cement industries (Taylor et al., 2006). Process heaters, fluidized catalytic cracking units, and steam methane reforming of hydrogen production units in refineries (Van Straelen et al., 2010) are also important sources of CO_2.

A naïve yet promising process for producing CO_2 is direct air capture, which is an industrial process of trapping CO_2 from the ambience with subsequent conversion to pure CO_2 stream that can be either sequestered or recycled back for other industrial processes (**Figure 2**). Processes available for this emerging technology include absorption of CO_2 by ion exchange membranes with humidity-swing regeneration (Lackner, 2003), solid amines on a mesoporous silica substrate (Gray et al., 2008), and alkaline aqueous solution (Keith, 2009).

PURELY THERMOCHEMICAL ROUTE OF METHANE SYNTHESIS

Most of the current industrial applications of methane are essentially in petroleum or natural gas markets, and as such, synthetic methanation is limited to removal of CO_2 and CO during steam methane reforming in processes such as ammonia production. Typically, methanation is carried out in a thermochemical catalytic reactor in the temperature range of 250–350°C and 25 bar pressure by either CO_2 hydrogenation (Mills and Steffgen, 1974; Wei and Jinlong, 2011; Junaedi et al., 2014; El Sibai et al., 2015) via the Sabatier process (Eq. 1) or CO hydrogenation (Anderson et al., 1984; Schulz, 1999; Van Der Laan and Beenackers, 1999; Méndez and Ancheyta, 2020) via the Fischer–Tropsch process (Eq. 2). Reaction kinetics and product selectivity are heavily affected by the type of catalyst and support, whereas overall reactor efficiency depends on its design and operating conditions, all of which have been widely studied till date and are not within the scope of our present discussion, and readers are referred to reviews and books (Mills and Steffgen, 1974; Rönsch et al., 2016; Mebrahtu et al., 2019).

Both CO_2 and CO methanation are highly exothermic reactions accompanied by a reduction in volume, thus favorable at high pressures and low temperatures (LTs).

$$CO_2 + 4H_2 = CH_4 + 2H_2O\left(\Delta H_{1,023K} = -164\,\text{kJ mol}^{-1}\right) \quad (1)$$

$$CO + 3H_2 = CH_4 + H_2O\left(\Delta H_{1,023K} = -206.1\,\text{kJ mol}^{-1}\right) \quad (2)$$

$$CO_2 + H_2 = CO + H_2O\left(\Delta H_{1,023K} = 41.2\,\text{kJ mol}^{-1}\right) \quad (3)$$

As can be determined from Eqs 1 and 2, the stoichiometric methanation of CO_2 and CO is accompanied by the evolution of 2.03 and 2.55 kW h heat per cubic meter of methane produced at normal temperature and pressure of 298 K.

The thermodynamics and kinetics of both CO and CO_2 methanation processes have been widely studied by many

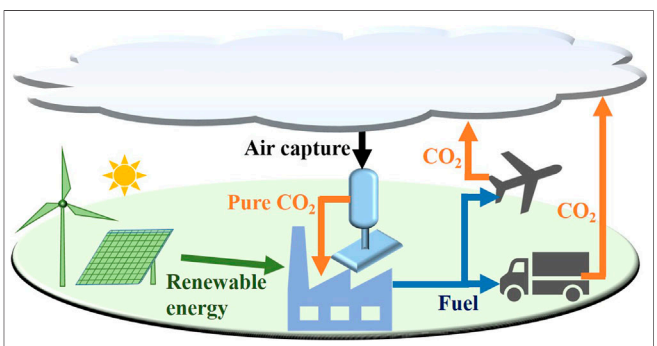

FIGURE 2 | Exhaust from vehicles and other sources of greenhouse gas can be captured from air, and the CO_2 thus separated can be recycled back to fuel synthesis sources.

researchers (Gao et al., 2012; Sahebdelfar and Takht Ravanchi, 2015; Rönsch et al., 2016). As reported by Gao et al. (2012), a maximum yield of CH_4 (>90%) from CO methanation is obtained in the temperature range of 200–300°C. In case of the Sabatier reaction as well, methane yield maintains a steady value (>90%) for temperatures up to 300°C, irrespective of pressure. Above 450°C, the reverse water gas shift (RWGS) reaction (Eq. 3) becomes dominant due to its endothermic nature and results in an upsurge of the CO by-product with a commensurate decrease in methane yield. Thus, the overall process of CO_2 conversion is dictated by competing reactions 1 and 3.

A perfect combination of LT, high pressure, appropriate H_2:CO_2 ratio, and suitable catalyst plays an important role for maximum methane yield from the Sabatier reaction. Compared to CO_2, CO hydrogenation is more exothermic and releases 3.58 MW h heat for each ton of methane produced, and reaction kinetics is also expected to be faster as the reactivity of CO is likely to be higher than that of CO_2 molecule. Thus, methane synthesis from renewably produced syngas might be a better option instead of CO_2 hydrogenation with only hydrogen produced renewably (Sabatier process), as further discussed in *Energy Efficiency of Methane Synthesis via Different Electrochemical Routes*.

COMBINED THERMO-ELECTRO-CHEMICAL ROUTE OF METHANE SYNTHESIS

Green hydrogen generation for synthetic methane production has been widely studied using different electrolysis cells or electrolyzers that have been developed over the past few decades. These electrolyzers can be classified based upon the type of electrolyte (aqueous or solid) and ionic species transported during electrolysis, and operating temperature regimes as shown in **Figures 3A,B**. The aqueous solution-based electrolytes were the original choice for electrolytes, and the most technologically matured electrolyzer design, AEL is based upon an aqueous electrolyte which transports hydroxyl ions (OH^-). Further, the family of electrolyzers based upon solid membrane electrolytes emerged where electrolytes are nonporous solids, which can either be proton (H^+) or oxide ion (O^{2-}) conductors. This group of electrolyzers can operate over a wide range of temperature and can be broadly classified into low temperature (LT; <100°C), intermediate temperature (100–500°C), and high temperature (HT; >500°C). In addition to these common types, electrolyzers based upon molten carbonate electrolytes have been evaluated to some extent

A

Electrolyzer type	Anodic reaction	Ionic species	Cathodic reaction
AEL	$2OH^- \rightarrow 0{\cdot}5O_2 + H_2O + 2e^-$	OH^-	$2H_2O + 2e^- \rightarrow H_2 + 2OH^-$
Low T (PEM)	$H_2O \rightarrow 0.5O_2 + 2H^+ + 2e^-$	H^+	$2H^+ + 2e^- \rightarrow H_2$
Intermediate T (proton conducting ceramic)	$H_2O \rightarrow 0.5O_2 + 2H^+ + 2e^-$	H^+	$2H^+ + 2e^- \rightarrow H_2$
High T (SOEC)	$O^{2-} \rightarrow 0.5O_2 + 2e^-$	O^{2-}	$H_2O + 2e^- \rightarrow H_2 + O^{2-}$

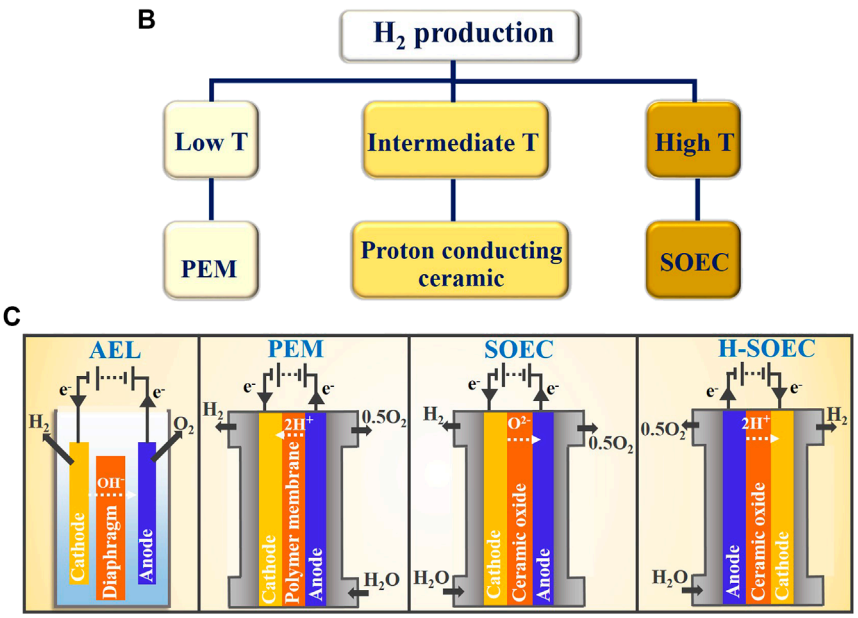

FIGURE 3 | A) Ionic species for different types of electrolyzers. **(B)** Temperature-based classification of electrolyzers used for solid electrolytic routes of hydrogen synthesis. **(C)** Basic working principle of alkaline electrolytic cells, proton exchange membrane, solid oxide electrolytic cells, and proton-conducting solid oxide electrolytic cells.

where the electrolyte is a molten carbonate material which operates at temperatures above 600°C (Hu, 2016; Hu et al., 2016).

PEMECs are most widely used for LT operation. Polymer composite electrolyte membranes, beta alumina-based electrolyte membranes, and proton-conducting solid oxide electrolytic cells (H-SOECs) are used for intermediate temperature range and emerging solid oxide electrolytic cells (SOECs) used for HT operation (**Figure 3B**). The basic working principles of AELs, PEMECs, SOECs, and H-SOECs are depicted in **Figure 3C**. Each of these electrolyte systems is at a different stage of technological maturity and comes with its own merits and demerits as discussed in reviews (Carmo et al., 2013; Santos et al., 2013; Rashid et al., 2015). In the section below, we have briefly discussed AEL and PEM technology followed by a detailed discussion on SOEC technology.

Alkaline Electrolyzer

AELs have existed ever since the dawn of electrolysis and witnessed remarkable improvements over many decades, which make AELs suitable for large-scale hydrogen production with capacities as high as 500–760 Nm^3/h (Vandenborre et al., 1980; Vermeiren et al., 1998; Ulleberg, 2003; Ursua et al., 2012).

The setup is relatively simple with two electrodes, usually a mild steel cathode and an Ni anode immersed in a liquid alkaline electrolyte (20–30% potassium hydroxide, KOH), and separated by a porous diaphragm permeable to both OH^- ions and water molecules. The operating temperature of AELs varies from 70 to 90°C, and hydrogen can be produced at pressures from 1 to 30 bar (Ursua et al., 2012). However, few of the shortcomings of AELs include corrosiveness of the electrolyte that reduces cell lifetime, and a low current density (100–300 mA per cm^2 of the electrode area) due to high ohmic losses which increase plant footprint (Mazloomi and Sulaiman, 2012). Current density is an important figure of merit used for comparison of the electrolytic systems as it is directly proportional to the rate of hydrogen production. More importantly, the limited ability of AELs for dynamic response to the fluctuations in the electricity supply is a key issue when it is powered by RE sources like solar and wind, which are intermittent in nature. Any additional requirement for energy storage devices such as batteries and related electronics significantly increases the capital and process costs, leading to an increased levelized cost of hydrogen production. Some opportunities for further improvement of this electrolyzer are in the improvement of diaphragm materials and electrocatalysts.

Proton Exchange Membrane Electrolyzer

To overcome the limitations of AELs, the concept of replacing the electrolytic solution by a solid polymeric membrane having proton conductivity emerged, and the electrolyzer came to be known as PEMEC, more popularly PEM (Xu and Scott, 2010; Carmo et al., 2013; Paidar et al., 2016; Jayakumar, 2019; Yang et al., 2019). In PEM electrolyzers, oxygen is released at the anode, and the H^+ ions migrate to the cathode through the solid nonporous polymeric membrane, where they recombine with e^- to release hydrogen gas. As the anode and cathode are separated by the polymeric electrolyte membrane, this guarantees minimum gas crossover with the yield of very high purity hydrogen. The most commonly used polymer membrane electrolyte material is Nafion sold by Dupont Ltd. On the anode side, a titanium (Ti)-based electrode mesh or foam with iridium (Ir)-based oxygen evolution electrocatalyst is used, and on the cathode side, platinum (Pt) metal nanoparticles supported on a high surface area carbon support are used. With improvements in design and materials, the PEM technology has made substantial progress, and the operating current densities can be as high as 1.5 A cm^{-2} and hydrogen can be produced at pressures above 30 bar (Ayers et al., 2010). The design of PEM is relatively compact and modular in nature, allowing for flexibility in scale and configuration of the system. Considerable progress has been made over the past decade in terms of technological maturity with systems up to 3 MW scale available commercially. Despite such progress, key technical challenges still remain unsolved, which include high costs associated with components fabrication, reliance on precious metal group catalysts, and performance degradation over the lifetime requiring incremental electrical energy input.

The levelized cost of hydrogen production per kilogram by PEM is in the range of $ 6.08–7.43 and for AEL, about $4.78–5.84 (Bruce et al., 2018). These costs are expected to decrease as the scale of the system increases. The cost of hydrogen from electrolysis is somewhat challenging considering the variables involved; however, it is generally agreed that cost of electricity is a major contributor with up to 65% of the cost of hydrogen (James et al., 2016; McDonagh et al., 2018). Clearly, the reduction in electrical energy input and lower cost of electricity can bring a shift change in the cost of electrolysis.

The minimum theoretical energy required for water electrolysis with PEM or AEM is about 40 kW h/kg of hydrogen. On top of that, losses associated with electrolyte resistance and electrode reactions (electrode polarization) and system-level losses add up. The total energy required at the system level can be as high as 5 kW h per Nm^3 of hydrogen, which equates to about a whopping 60 kW h/kg of hydrogen.

SOECs have a great potential to overcome the limitations of AELs and PEM, in particular energy requirements (Luo et al., 2018; Wang L. et al., 2019). Further, it allows electrolysis of not only water but also CO_2 and co-electrolysis of steam/CO_2 mixture (Bandi et al., 1995; Laguna-Bercero, 2012; Hansen, 2015; Zheng et al., 2017). SOEC operation at HTs (above 600°C) requires a substantially lower electric energy input per kilogram of fuel produced due to favorable cell thermodynamics, which has been elaborated in a subsequent section. A detailed comparison of the characteristics of AELs, PEMECs, and SOECs is available in the literature (Bertuccioli et al., 2014; Bhandari et al., 2014; Peterson and Miller, 2016; Schmidt et al., 2017; Buttler and Spliethoff, 2018).

BASIC WORKING PRINCIPLE OF SOLID OXIDE ELECTROLYTIC CELLS AND THEIR APPLICATION IN SYNTHETIC METHANE PRODUCTION

Figure 4A shows the basic working principle of SOECs. The electrodes are separated by a dense ion-conducting ceramic

membrane. The feed gases, that is, steam or CO_2 or both, are supplied to the cathode where it reacts with electrons provided by an external power supply to produce H_2 and CO, respectively, and oxygen ions, which are transported through an ion-conducting electrolyte to the anode, where they combine and release the electrons (e^-) again (Bandi et al., 1995; Zheng et al., 2017; Pandiyan et al., 2019). The electrochemical reactions taking place in the SOECs are given as follows:

Cathode

i. Steam electrolysis:

$$H_2O + 2e^- \rightarrow H_2 + O^{2-} \left(\Delta H_{1,023K} = 241\ \text{kJ mol}^{-1}\right) \quad (4)$$

ii. CO_2 electrolysis:

$$CO_2 + 2e^- \rightarrow CO + O^{2-} \left(\Delta H_{1,023K} = 282.5\ \text{kJ mol}^{-1}\right) \quad (5)$$

iii. Steam/CO_2 co-electrolysis:

$$CO_2 + H_2O + 4e^- \rightarrow CO + H_2 + 2O^{2-} \left(\Delta H_{1,023K} = 523.5\ \text{kJ mol}^{-1}\right) \quad (6)$$

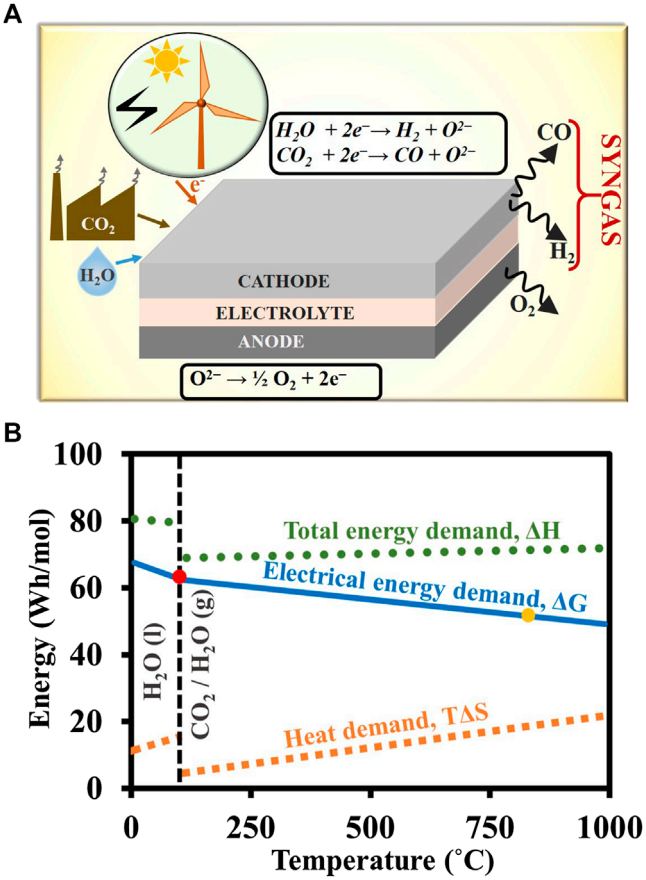

FIGURE 4 | A) Primary reactions taking place in a SOEC during H_2O/CO_2 co-electrolysis. **(B)** ΔH, ΔG, and $T\Delta S$ of steam/CO_2 splitting as a function of temperature. The red and yellow dots denote the typical operating temperature of a standard alkaline electrolytic cells/proton exchange membrane and SOEC.

Anode

$$\text{Oxygen evolution: } O^{2-} \rightarrow 1/2O_2 + 2e^- \quad (7)$$

The voltage gradient across the ion-conducting membrane drives the reaction, and the minimum operating voltage (V_0) required for the process is equal to the change in the Gibbs free energy (ΔG):

$$\Delta G = \Delta H - T\Delta S, \quad (8)$$

where ΔH is the enthalpy change given by the heat of the reaction and $T\Delta S$ is the supply of external heat, T being the temperature and ΔS the entropy change.

As can be forecasted from Eq. 8, with an increase in T, ΔH remains almost unaffected, while ΔG (electrical energy input) decreases almost linearly with T (**Figure 4B**) since both steam and CO_2 decomposition are highly endothermic reactions (Eqs 4 and 5). Hansen (2015) reported that the ratio of ΔG to ΔH is about 93% at 80°C and about 77% at 750°C. This reduction in ΔG is significant, as it constitutes over 64% of the total cost of electrolytic hydrogen production, as discussed earlier. More importantly, the heat ($T\Delta S$) can be sourced either as low-grade waste heat from industrial processes, or as high-grade heat from the solar thermal concentrators.

The operating voltage of the cell is governed by its ohmic resistance and resistances offered by the activation of electrodes, charge transfer, diffusion of the reactant and the product gases, and gas conversion. All these resistances together are often referred to as area-specific resistance of the cell and dictate the efficiency and, in turn, the cost of fuel production.

Solid Oxide Electrolytic Cell Materials, Designs, and Modes of Operation for Methane Synthesis

The solid oxide electrolyte in SOECs can be either an oxygen ion conductor or a proton conductor. A major development of SOECs revolves around oxygen ion-conducting electrolytes, but there has been renewed interest in proton-conducting electrolytes for SOEC application (Ding et al., 2019; Duan et al., 2019; Vøllestad et al., 2019). Despite the impressive performance, H-SOECs are still at infancy and limited to the laboratory scale relative to the oxygen ion conductor-based technology.

Most of the materials and methods of fabrication for SOECs are derived from those used for solid oxide fuel cells (SOFCs), which is already a commercialized technology. For state-of-the-art SOECs, choice of the electrolyte is an oxygen ion-conducting ceramic known as 8 mol% yttria (Y_2O_3)-stabilized zirconia (ZrO_2) or YSZ (Smart and Weissbart, 1967; Bandi et al., 1995; Graves et al., 2011). As shown in **Figure 4A**, the electrolyte is sandwiched between the fuel electrode (cathode) and the oxygen electrode (anode). Cathodes are generally composed of porous composites (commonly known as cermets) of Ni metal with YSZ, which is made by mixing NiO with YSZ. The state-of-the-art anode (oxygen evolution electrode) materials for SOECs are lanthanum strontium manganite ($La_{0.8}Sr_{0.2}MnO_{3-\delta}$, commonly known as LSM) and YSZ composite (Kim et al., 2001; Chen et al.,

2004; Murakami et al., 2010; Kaur et al., 2018b), or lanthanum strontium cobalt ferrite ($La_{0.8}Sr_{0.2}Co_{0.2}Fe_{0.8}O_{3\delta}$, commonly known as LSCF) (Laguna-Bercero et al., 2011; Zheng et al., 2014). Several new materials are being developed and trialed as SOEC electrodes such as mixed conductor perovskites (Ebbesen and Mogensen, 2009; Laguna-Bercero, 2012). In particular, there has been significant research on new cathode materials (Wang Y. et al., 2017) with regard to methanation, as discussed in *Challenges and Advancement in the Electrolytic Production of Hydrogen and Syngas in Solid Oxide Electrolytic Cell Integrated With Thermochemical Reactor for Methane Synthesis*.

SOECs can be fabricated in two different configurations, namely, planar and tubular (Shi et al., 2015), as shown in **Figures 5A,B**. Planar cells are in the form of square or rectangular flat plates or circular discs (**Figure 5A**) that can be stacked on top of one another and interconnected in series with metallic or ceramic plates referred to as interconnects, which are electronic conductors in both reducing and oxidizing atmospheres. The planar cells can either be electrode supported (Knibbe et al., 2010) where the anode is first prepared followed by casting a thinner layer of electrolyte atop (**Figure 5C**), or electrolyte supported (Ursua et al., 2012; Ghaib and Ben-Fares, 2018) where the electrolyte is first fabricated followed by electrode coating (**Figure 5D**). In electrode-supported cells, the electrolyte is few microns thick, which remarkably reduces the ohmic resistance. However, such thin electrolytes are vulnerable to mechanical stresses and prone to failure under continually variable loading conditions which are common with renewables. Another design under consideration is a metal-supported cell where a porous metallic plate acts as a support and very thin layers of electrode and electrolyte can be coated on it (Tucker, 2010; Leah et al., 2017).

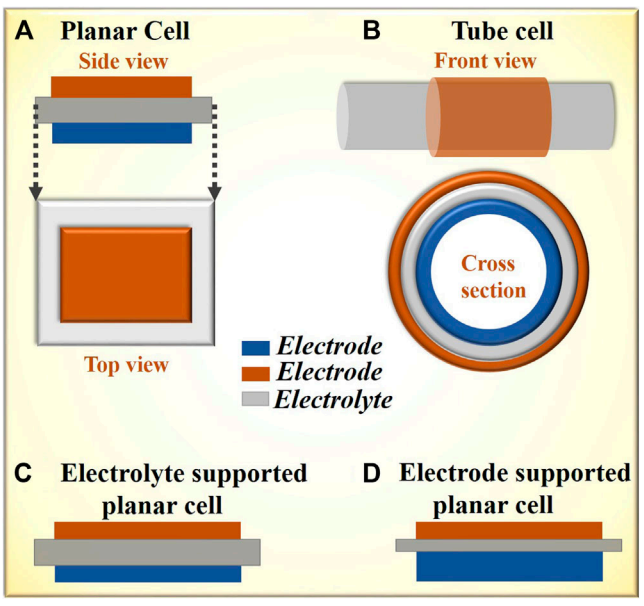

FIGURE 5 | Schematic of a typical planar cell **(A)** and tube cell **(B)**. Schematic of electrolyte-supported **(C)**, and electrode-supported cells **(D)**.

The planar design ensures high volumetric hydrogen production and a facile fabrication process. However, major concerns include issues with the hermetic sealing required to separate fuel gas from the air and compressive stresses lowering the ability of stack to cope up with thermal cycling.

Alternatively, a tubular design (**Figure 5B**) is available, where either an electrolyte or a cathode (fuel electrode) is formed in the shape of a tube, typically by processes such as isostatic bag pressing, extrusion, or freeze casting. Once the starting component is prepared, the remaining electrodes/electrolytes can be coated by a variety of processes, including dip coating, spray coating, or brush painting. The tubular cells are freestanding and can be stacked side by side in a row or as a bundle of several tubes. In the case of electrolyte-supported tubular cells, the requirements for sealing are less stringent, and the ability to cope with thermal cycling is shown to be better (Kaur et al., 2018a). The downsides of this tubular geometry are a lower volumetric current density leading to a larger footprint of the system and issues with designing and fabrication of current collectors for current collection from the tube interior.

SOECs can be operated in four different modes or configurations for methane synthesis as shown in **Table 1**. The first two modes belong to thermo-electro-chemical routes of methane synthesis, whereas modes 3 and 4 constitute purely electrochemical pathways (**Figure 1B**). In modes 1 and 2, SOECs simply act as a source of hydrogen or syngas coupled with a separate conventional SR or methanation reactor (MR), respectively, whereas modes 3 and 4 encompass methanation carried out in a single reactor without the need for a separate downstream process. The differences between modes 3 and 4 are the operating temperature and role of cathode toward the entire process. In mode 3, the cathode itself acts as a methanation catalyst, or the catalyst is in direct physical contact with the cathode, referred to as bilayer electrodes. With bilayer cathodes, both steam/CO_2 co-electrolysis and methanation occur on the

TABLE 1 | Different modes of operation of SOECs for methane synthesis.

Mode	Process description
Mode 1	SOEC supplies hydrogen produced by steam electrolysis to a conventional Sabatier reactor. Heat from the Sabatier reactor can be used for the SOEC reactor (i.e., steam production and maintaining temperature).
Mode 2	SOEC supplies syngas produced by steam/CO_2 electrolysis to a conventional methanation reactor. Heat from the methanation reactor can be used for the SOEC reactor (i.e., steam production, heating reactant gases, and maintaining temperature).
Mode 3	*In situ* methanation in a single temperature zone cell where both steam/CO_2 co-electrolysis and methanation occur on the cathode itself. One-step process without a downstream reactor.
Mode 4	*In situ* methanation in a dual temperature zone cell where syngas generation from steam/CO_2 co-electrolysis occurs on the cathode maintained at a high temperature followed by its methanation on a catalyst bed kept at a lower temperature, but both housed inside the same cell.

cathode itself, the key feature being that the SOEC can be maintained at one single temperature. Contrarily, in mode 4, the catalyst is placed as a separate bed in proximity of the electrode (at some distance from the electrode) in cooler regions of the cell but still within the same cell. So, in this case, the cell features two zones: a high-temperature electrolysis zone, where syngas is produced from co-electrolysis, followed by a catalyst-laden lower temperature zone, where the syngas along with unconverted CO_2 undergoes methanation. As is expected, the energy efficiency and cost of methane production will vary for each of these pathways (Luo et al., 2018), and a comparison on the same has been provided in detail in *Energy Efficiency of Methane Synthesis via Different Electrochemical Routes*.

Challenges and Advancement in the Electrolytic Production of Hydrogen and Syngas in Solid Oxide Electrolytic Cells Integrated With Thermochemical Reactor for Methane Synthesis

For modes 1 and 2, mentioned above, the materials and design challenges are very similar to the state-of-the-art SOECs, and research has been progressing at different paces consistent with "waves" in hydrogen research and development (R&D) in general. The advantageous use of SOECs with reduced electrical energy input has been experimentally demonstrated almost 40 years ago by Erdle et al. (1992), followed by Quandt and Streicher (1986) in the 1980s. The key technical issues for SOECs as hydrogen or syngas generators include limited lifetime due to degradation at the electrodes, sealing issues, and high capital costs. Capital cost is a function of several factors, such as production volume and scale of the units, and material supply chain. One might expect a drastic reduction in capital costs with improved cell designs such as microtubular cells (Lei et al., 2017; Chen et al., 2019; Monzón and Laguna-Bercero, 2019), advent of new manufacturing processes such as 3D printing (Huang et al., 2017; Wei et al., 2019), and advanced automation which can be implied if the technology gains market acceptance. The challenges associated with materials are more fundamental in nature, and the degradation mechanism in SOECs is not yet well understood. It is generally agreed that more R&D is warranted toward designing new electrode materials like double perovskites (Shin et al., 2015; Afroze et al., 2019; Tian et al., 2020) or modification of existing electrodes. When CO_2 is added to steam for generation of syngas (mode 2), the issues related to the stability of the electrode become even more challenging.

SOEC cathodes have been under intense investigation over the recent few years as both energy-intensive reactions in SOECs, namely, steam and CO_2 splitting (Eqs 4 and 5), occur on this electrode. The state-of-the-art cathode material is a porous cermet comprising YSZ and metallic nickel, as mentioned earlier in *Solid Oxide Electrolytic Cell Materials, Designs, and Modes of Operation for Methane Synthesis*. Ni provides the electronic conduction pathways and catalytic activity, while the YSZ matrix prevents Ni particle grain growth and provides ionic conduction pathways leading to an increased triple-phase boundary area (Bandi et al., 1995; Sridhar and Vaniman, 1997; Holtappels et al., 1999; Graves et al., 2011). Although Ni-YSZ is the common choice of fuel electrode due to the high catalytic activity of Ni in H–H (Bourcet and Tantardini, 1994) bond breaking, its pitfalls include accelerated coarsening, agglomeration, and migration away from the electrode–electrolyte interface particularly under electrolysis condition; limited catalytic activity for CO_2 splitting; poor stability under variable loading conditions; and reduced mechanical strength in the presence of steam (Hauch et al., 2008; Knibbe et al., 2010b; Iwanschitz et al., 2010; Chen et al., 2013; Khan et al., 2016; Wang Y. et al., 2019). As Ni gets oxidized upon exposure to steam or CO_2, an additional supply for partial recycling of generated H_2 is required to maintain Ni in the metallic state. Product gas circulation is not a critical challenge in small lab-scale experiments; however, at the system level, it could pose significant challenges as it adds to the complexity of the plant. If the operation of SOECs is desired without recirculation of the product gas, the operating window must ensure that oxygen partial pressure in the inlet chamber (cathode chamber) always remains below 10^{-14} bar. This, in turn, requires SOEC operation with or above particular current densities. In the case of fluctuating electricity supply, such a requirement may lead to curtailing of hydrogen/syngas production if the availability of electricity cannot meet the minimal demand. Alternatively, a complex system control or a backup power can be used, however, at a substantial capital cost penalty. Usually, operation with recirculated gas like hydrogen requires a low steam-to-hydrogen ratio in the feed gas with the hydrogen content above 10%, preferably up to 20% hydrogen with steam. Significant degradation in the performance has been reported by Eguchi et al. (1996) at a higher steam concentration. In a similar observation for CO_2 electrolysis, Green et al. (2008) have shown that for a decreasing CO_2/CO ratio (creating a more reducing environment), polarization resistance offered by an Ni-YSZ cathode first decreases and then increases, which is contrary to the general expectation. This is due to the Ni-catalyzed Boudouard reaction leading to enhanced coke deposition that dampens cathode activity. Thus, steam electrolysis demands the cathode to be stable in low H_2 partial pressures, but co-electrolysis or CO_2 electrolysis poses the additional challenge that cathode should be CO tolerant and coking resistant. Thus, a considerable portion of the current SOEC material development focuses on the development of an alternative cathode which will be stable under a variety of operating conditions.

The development strategies involve either a modification of the Ni-YSZ or a complete substitution with new materials. The modification includes either tailoring of the microstructure or addition of a catalytic phase to the Ni-YSZ, which can improve the catalytic performance of Ni toward CO_2 splitting. Some researchers (Ishihara et al., 2010; Wang et al., 2013; Hong et al., 2015; Kim et al., 2016; Neofytidis et al., 2019; Yu et al., 2020) have tried to evaluate the alloying of Ni with a second metal as promoter, which alters the work function of Ni, thereby improving its catalytic activity toward steam or CO_2 splitting and minimizing issues related to carbon deposition. For example,

Ishihara et al. (2010) reported that a Ni–Fe bimetallic cathode serves well for steam electrolysis in intermediate temperature SOECs, possibly because Fe effectively increases the rate of H_2 formation. Wang et al. (2013) explored a bimetallic Ni-Fe cathode (with YSZ) for electrolysis of CO_2 and reported a significant reduction in carbon deposition compared to bare Ni during a test period of 12 h. Issues such as product recirculation requirement and Ni migration may still persist, and long-term testing is required.

As for the complete substitution of Ni-YSZ, a wide variety of materials such as perovskites, fluorites, and composites have been studied as prospective cathodes for both hydrogen and syngas generation (Wang Y. et al., 2017; Wang Y. et al., 2019; Jiang, 2019; Pandiyan et al., 2019). Since the key role of Ni in Ni-YSZ is to provide electronic conduction and catalytic activity toward electroreduction, a pertinent alternative is to seek perovskites that can potentially exhibit these two features. Such ceramics, mainly fluorites and perovskites, belong to the genre of mixed ionic electronic conductors. A plethora of investigations on perovskite electrodes have been reported for SOFCs (Zhu and Deevi, 2003a; Faes et al., 2012; Mahato et al., 2015); however, for SOECs, the number of publications and patents in the area have started increasing only over the past few years.

Yang and Irvine (2008) used strontium and cobalt-stabilized lanthanum manganite ($La_{0.8}Sr_{0.2}Cr_{0.5}Mn_{0.5}O_{3-\delta}$, commonly referred as LSCM) as the cathode with YSZ as the electrolyte and lanthanum strontium ferrite ($La_{0.7}Sr_{0.3}FeO_3$, commonly LSF) as the oxygen electrode for steam electrolysis, and achieved start-up from a very low hydrogen concentration (4% by volume) without having to overcome high ohmic and polarization resistances as witnessed in Ni-based cathodes prior to the reduction of NiO to Ni. Another example is doped titanium oxide or titanate cathodes. Titanate perovskites (Yang et al., 2014; Gan et al., 2016; Barnett et al., 2019; Dogu et al., 2019) have been investigated for several years as an alternative to Ni-YSZ. Titanates lack catalytic activity for electrolysis, and the addition of a second catalytic phase becomes necessary. Marina and Pederson (2008) reported a composite ceria–titanate cathode ($La_{0.35}Sr_{0.65}TiO_3$-$Ce_{0.5}La0.5O_2$) which demonstrated substantially lower polarization resistance (0.2–0.28 $\Omega\,cm^2$) than Ni-YSZ (0.4 $\Omega\,cm^2$). Ceria provides additional catalytic activity, and the titanate phase provides electronic conductivity.

Recently, Deka et al. (2019) used Ni- and Co-doped lanthanum strontium ferrite (LSF) cathode for co-electrolysis at 800°C. Co-electrolysis performed for 110 h on a $La_{0.7}Sr_{0.3}Ni_{0.1}Co_{0.1}Fe_{0.8}O_3$ cathode showed appreciable stability of this composition to coking. Co-doped LSF showed the lowest Faradaic efficiency, whereas Ni-doped LSF gave ~100% Faradaic efficiency (see **Table 2** for the performance). Their *in situ* X-ray near-edge structure studies revealed that during co-electrolysis, Co ions may get oxidized, thereby decreasing the number of oxygen vacancies in the material and lowering its electrochemical activity. Moreover, unlike Ni-doped cathodes, Co-doped ones showed evidence of graphitic carbon formation that could have further reduced the electrochemical performance of the cell.

Doped ceria-based fluorite oxides and related composite cathodes have been gaining popularity over the last few years. It is generally accepted that Ceria (CeO_2), and in particular aliovalent metal (gadolinium, samarium, or praseodymium)-doped ceria such as gadolinia-doped ceria (GDC) or samaria-doped ceria, is immune to coking due to the presence of highly mobile surface oxygen species that react with any deposited carbon and suppress coke build-up through gasification (Livermore et al., 2000; Goodenough and Huang, 2007; Cimenti and Hill, 2010; Lee et al., 2016; Elleuch and Halouani, 2020). The presence of such mobile oxygen species is the synergistic effect of oxygen vacancies imparted by the dopant and the *in situ* reduction of Ce^{4+} to Ce^{3+} at HTs and in a reducing atmosphere. Although not as widely studied for CO_2 electrolysis or co-electrolysis, ceria-based electrodes have already proven their merit in SOFCs. Yue and Irvine (2012) compared the cathode performance of LSCM/YSZ and LSCM/GDC composites for CO_2 electrolysis and concluded that GDC itself undergoes reduction under applied load, thus offering much lesser polarization resistance and enhanced cathode activity than YSZ. Doped ceria has a conductivity of up to 1 s/cm in a reducing atmosphere, and as such, either mixing with an electronically conducting phase is required or an additional current collection layer needs to be coated on the top of the ceria cathode. Recently, LSM and GDC composite was evaluated by Kaur et al. (2018b) as an SOEC cathode for CO_2 electrolysis, and it not only exhibited better electrochemical performance but was also found to be significantly more stable. The LSM and related structures provided required electronic conductivity. Kulkarni et al. (2017) observed that at 800°C, a Pd-doped $La_{0.8}Sr_{0.2}Co_{0.2}Fe_{0.8}O_{3-\delta}$ (LSCF) cathode with samaria-doped ceria interlayer and YSZ electrolyte rendered a high Faradaic efficiency of 97% with minimal overpotential losses (**Table 2**) for CO_2 electrolysis. Ag-GDC composites were evaluated for electrolysis of CO_2 (Xie et al., 2015). Ag possesses high electrical conductivity and chemical stability in oxidizing atmospheres above 200°C, and GDC has high ionic conductivity and good catalytic properties toward CO_2 reduction in CO/CO_2 atmospheres, and their composite has shown promising results for CO_2 electrolysis. However, any adverse effect of the cell performance due to evaporation of Ag and possible electromigration needs to be evaluated in long-term tests.

Another important component that has drawn sufficient research interest is the SOEC electrolyte. As of date, YSZ is the most commonly used electrolyte (Graves et al., 2011b; Hansen, 2015b) due to its high ionic conductivity (~0.016 s/cm) along with thermal and chemical stability at the usual operating temperatures of SOECs (800–1,000°C). However, it fails to exhibit sufficient ionic conductivity in the intermediate temperature range (500–800°C), which is a major drawback. There are some reports even on the failure of the YSZ electrolyte, which is otherwise thought to be stable under SOFC operating conditions (Graves et al., 2015; Park et al., 2019).

Over the past few decades, substantial efforts have been made to develop an oxygen ion conductor electrolyte which works at

TABLE 2 | Key cathodes and electrolytes tested for co-electrolysis and CO_2 electrolysis at atmospheric pressure.

Group	Cathode|electrolyte|anode	Cathode gas	*T* (K)	Current density in mA cm^{-2}/ (Faradaic efficiency in %)	Notes
Faro et al. (2019)	Ni/YSZ|GDC-YSZ|LSM **$Gd_{0.2}Ce_{0.8}O_{1.95}$ (GDC)**	H_2O/CO_2	798–973	350/(60)	–
Deka et al. (2019)	LSNiF|YSZ|LSM-YSZ; LSCoF|YSZ|LSM-YSZ **Ni-doped $La_{0.7}Sr_{0.3}FeO_3$ (LSNiF)** **Co-doped $La_{0.7}Sr_{0.3}FeO_3$ (LSCoF)**	H_2O/CO_2	1,073	7/(LSNiF ~ 100 LSF ~ 80 LSCoF ~ 65)	H_2 production: LSNiF > LSF > LSCoF CO production: LSF > LSCoF > LSNiF
Graves et al.(2011)	Ni/YSZ|YSZ|LSM-YSZ	H_2O/CO_2	1,023–1,123	250–1,000/–	Low current density: Cathode degradation (0.005–0.008 mV h^{-1}) dominated; High current densities: anode degradation (0.1 mV h^{-1}) dominated
Pu et al. (2016)	LSCM|BCZY|LSCM **$La_{0.8}Sr_{0.2}Cr_{0.5}Mn_{0.5}O_{3-\delta}$ (LSCM)** **$BaCe_{0.5}Zr_{0.3}Y_{0.2}O_{3-\delta}$ (BCZY)**	H_2O/CO_2	723–873	330/(90)	Current density higher than YSZ
Kulkarni et al. (2017)	Pd-LSCF with SDC interlayer |YSZ|LSCF-Ag **$La_{0.8}Sr_{0.2}Co_{0.2}Fe_{0.8}$ $O_{3-\delta}$ (LSCF)** **$Sm_{0.2}Ce_{0.8}O_{1.9}$ (SDC)**	H_2O/CO_2	1,073	360/(97)	Overpotential losses, 200 mV at 350 mA cm^{-2}
Wang et al. (2015)	Ni-Fe-LSFM|LSGM|BLC64 **$Ba_{0.6}La_{0.4}CoO_{3+\delta}$ (BLC64)** **$La_{0.6}Sr_{0.4}Fe_{0.8}Mn_{0.2}O_3$ (LSFM)** **$La_{0.9}Sr_{0.1}Ga_{0.8}Mg_{0.2}O_3$ (LSGM)**	Dry CO_2	973–1,173	2,320/(96.5)	Cathodes stable for 100 h at 1.3 V
Zhou et al. (2018)	LSFV-GDC|YSZ|LSM-YSZ **$La_{0.5}Sr_{0.5}Fe_{1-x}V_xO_{3-\delta}$ (LSFV) with ($0 < x < 0.15$)**	Dry CO_2	1,073	620/(89.5)	Compared to LSF, $LSFV_{0.05}$ gave 51.2% increase in current density at 1.6 V and 30% reduction in cell degradation
Zhang et al. (2016)	Ce-LSCrF-YSZ|YSZ-GDC|LSCoF-GDC **$La_{0.8}Sr_{0.2}Co_{0.2}Fe_{0.8}O_{3-\delta}$ (LSCoF)** **$La_{0.65}Sr_{0.3}Ce_{0.05}Cr_{0.5}Fe_{0.5}O_{3-\delta}$ (Ce-LSCrF)**	Dry CO_2	1,123	1,130/(87)	Ce doping increased CO_2 adsorption and its conversion to CO
Cumming et al. (2016)	SCT-SDC|YSZ|LSM-YSZ **$Sr_{0.7}Ce_{0.2}TiO_{3\pm\delta}$ (SCT)**	H_2O–CO_2	923–1,123	263/–	–
Ye et al. (2017)	NiO-CZI|CZI|CZI-LSM **$CaZr_{0.9}In_{0.1}O_{3-\delta}$ (CZI)**	H_2O	1,123	182/(95)	Cell degraded by 35 mA cm^{-2} (18%) over a period of 8 h

Specific electrode/electrolyte compositions have been provided in bold.

even lower temperatures. For instance, Ishihara et al. (2010) used a lanthanum gallate ($LaGaO_3$)-based electrolyte for steam electrolysis, which gave optimistic results for intermediate temperatures. Strontium- and magnesium-stabilized lanthanum gallate ($La_{0.8}Sr_{0.2}Ga_{0.8}Mg_{0.2}O_{3-\delta}$, commonly LSGM) also exhibits good ionic conductivity at intermediate temperatures, but it reacts with the Ni of fuel electrode, manifested by the formation of a $LaNiO_3$ layer on the electrode surface. Other materials include scandia-stabilized zirconia (ScSZ) (Mat et al., 2019; Pesaran et al., 2019; Pham et al., 2019; Zhigachev et al., 2019; Wang et al., 2020); however, the high cost of scandium (several times higher than that of yttria) is a major issue for practical applications. Another prominent electrolyte family is ceria-based materials (Jaiswal et al., 2019; Raza et al., 2020). The technical issues with these electrolytes for SOEC application are their propensity toward electronic conduction under high applied potential or reducing atmosphere, phase stability in the presence of steam and CO_2, and lower mechanical strength than YSZ. Thus, as of now, YSZ continues to be the choice of electrolyte material for commercial SOECs and the most widely used electrolyte for laboratory-scale studies. **Table 2** shows observations from some of the key cathodes and electrolytes that have been tested for co-electrolysis and CO_2 electrolysis.

The established air electrodes for SOFCs are also materials of choice for SOEC anodes, as previously mentioned in *Solid Oxide Electrolytic Cell Materials, Designs, and Modes of Operation for Methane Synthesis*. However, rapid degradation due to electrode delamination and changes in electrode–electrolyte interfacial phase assemblage has been reported with LSM-YSZ composites (Chen and Jiang, 2011; Graves et al., 2011; Rashkeev and Glazoff, 2012; Kim et al., 2013; Graves et al., 2015). It is now well-established that a high current density leads to the build-up of high internal oxygen partial pressure at the anode–electrolyte interface, resulting in the entrapment of nano-sized oxygen bubbles that finally causes microstructural damage and electrode delamination (Virkar, 2010; Tietz et al., 2013; Graves et al., 2015; Chatzichristodoulou et al., 2016; Khan et al., 2017). In response to the degradation issues, LSCF-based materials, which are mixed ionic electronic conductors, are being evaluated in SOECs (Guan et al., 2006; Hjalmarsson et al., 2013; Kim and Choi, 2014; Singh et al., 2015). According to one such research conducted by Singh et al. (2015), CO_2 electrolysis was carried out at 1,000°C using Ni–GDC cathode and YSZ electrolyte with two different anodes (LSCF and LSM-YSZ). Under open circuit conditions, LSCF showed much lower anodic polarization resistance (~0.074 $\Omega\,cm^2$) than LSM/YSZ (~0.13 $\Omega\,cm^2$). Also, the LSCF anode remained stable for a constant operation of 9 h at a current density of 1.2 A cm^{-2}. In another work by GE (Guan et al., 2006) using Ni-YSZ as fuel electrode, YSZ as electrolyte, and different perovskites as oxygen electrodes for steam electrolysis at 800°C and 1.3 V for 100 h, the cell degradation rate followed the order: LSCF < LSF < LSM. Although LSCF shows promising results at intermediate current densities, long-term stability testing at high current density is still under investigation. As oxygen evolution is relatively less energy intensive in SOECs, the research emphasis in on engineering the porosity and microstructure of the cathodes (Chatzichristodoulou et al., 2016; Khan et al., 2017) to avoid delamination from the electrolyte. Also, changes in cell operating conditions are being explored. For example, Graves et al. (2015) recently proposed that electrolysis-induced degradation can be reduced by reversibly switching between electrolysis and fuel-cell modes. They reported that for steam electrolysis at a current density of 1 A cm^{-2}, the cell voltage increased from 1.33 to 1.73 V for 420 h of constant operation, whereas in the reversible mode operation (1 h electrolysis followed by 5 h fuel-cell mode), the cell voltage during the electrolysis part of the cycles remained stable at 1.33 V over the same span of 420 h.

In addition to electrodes and electrolyte, there are issues associated with cost reduction of interconnects and sealing stability in the presence of steam and gases like CO_2 (Zhu and Deevi, 2003b; Lessing, 2007). These are persistent issues with SOFC technology; however, they can be more challenging for SOECs as understandings on the performance and degradation behavior of these components in SOECs are limited. The typical sealing being explored in planar SOEC stacks is edge seal, glass seal, or compressive seal (Lessing, 2007). For the edge sealing, typically a metal frame of ferritic stainless steel is used. Most sealing metal frames have thermal expansion coefficients higher than zirconia (10.5 $K^{-1} \times 10^{-6}\,K^{-1}$), which led to the development of chromium (Cr)-based alloys with lower thermal expansion coefficients. However, Cr gets oxidized to Cr_2O_3 followed by vaporization and condensation on the electrode and electrolyte surfaces, increasing cell resistance. Thus, low Cr content iron-based steels are presently used for edge sealing and interconnect because of their low cost, easy fabrication methods, and reasonably low thermal expansion coefficient. The development work is also continuing with ceramic materials and coatings like doped lanthanum chromate ($LaCrO_3$) which has the potential to attenuate the Cr poisoning effect of metallic interconnects (Cable et al., 2011). Other major challenges include stack design and assemblage, and optimization of manufacturing processes at scale. These challenges are not specific to synthetic methane production but need focused R&D to meet the performance and life targets for SOECs at a realistic price point. These issues are discussed in detail in SOFC reviews (Balachandran et al., 1989; Lessing, 2007; Shaigan et al., 2010; Ebbesen et al., 2014; Mahato et al., 2015; Mah et al., 2017; Pandiyan et al., 2019; Wang Y. et al., 2019), which apply to SOECs as well.

State of the Art of Purely Electrochemical *In Situ* Methane Synthesis in Solid Oxide Electrolytic Cells

A relatively large body of literature work is available on SOEC cathodes for hydrogen or CO, or more recently on syngas production; however, very limited experimentation has been carried out on the *in situ* synthesis of hydrocarbons where the cathode needs to play an additional role of synthetic catalyst to promote reactions such as methanation. Lately, researchers have

started investigating *in situ* methane synthesis in SOECs in a single reactor (Jensen et al., 2003; Bierschenk et al., 2011; Xie et al., 2011; Li et al., 2013; Chen et al., 2014; Chen et al., 2017; Lei et al., 2017; Jensen et al., 2019; Luo et al., 2020) with only CO_2 and steam as feedstock (**Figure 6**) employing either mode 3 or 4 as described in this section.

Xie et al. (2011) were one of the first to perform *in situ* methanation using a composite of lanthanum-doped strontium titanate ($La_{0.2}Sr_{0.8}TiO_{3+\delta}$, commonly LST) and GDC as cathode on YSZ electrolyte and LSM/YSZ composite anode. They used an additional layer of iron catalyst placed in direct contact with the cathode (**Figure 6A**). At 650°C, about 2.8% methane was generated at atmospheric pressure. They suggested that methane yield can be further improved with adequate optimization of reactor design, proper manipulation of pressure, possibly by the usage of backpressure, and catalyst infiltration into cathode instead of placing it atop the cathode.

The effect of temperature, as encountered in *in situ* methanation, is still ambiguous and has been systematically studied by only a few researchers. According to some studies, *in situ* methane synthesis should be carried out in dual-temperature zone SOECs (mode 4 described in *Basic Working Principle of Solid Oxide Electrolytic Cells and Their Application in Synthetic Methane Production*), where the high-temperature region favors endothermic steam/CO_2 co-electrolysis, whereas a catalyst-laden cooler region within the same cell favors exothermic methanation reactions of the *in situ*-generated syngas (**Figure 6B**). In one such design, Chen et al. (2014) conducted *in situ* methanation using an Ni-YSZ cathode, YSZ electrolyte, and LSM-YSZ anode, where the SOEC part was operated at 800°C and 1.3 V, and the temperature was gradually decreased to 250°C in the Fischer–Tropsch (F–T) regime. Methane yield remained almost constant from 200 to 400°C for the F-T section, followed by a sharp decrease with

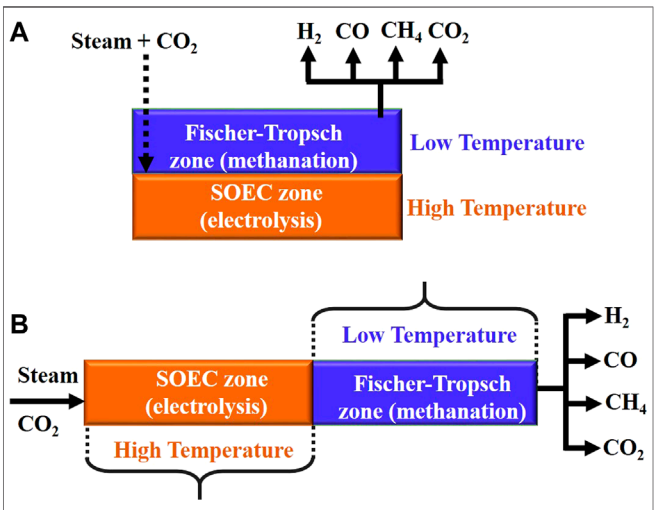

FIGURE 6 | *In situ* methane synthesis in SOEC in a single temperature zone configuration with catalyst layer above the cathode **(A)** and dual temperature zone configuration with catalyst beside the cathode **(B)**.

further increase in temperature up to 800°C, as HT does not favor exothermic CO methanation reaction (Eq. 2); rather, it promotes methane steam reforming (Eq. 9), which is a competing reaction occurring in the F–T section.

$$CH_4 + H_2O = CO + 3H_2 \ (\Delta H_{1,023K} = 206\,kJ\,mol^{-1}) \quad (9)$$

In the SOEC section, as expected, increasing the operating temperature improved the ionic conductivity of the electrolyte, thereby sprucing up the methane output flux. In another study by Lei et al. (2017) using a microtubular SOEC consisting of Ni-YSZ cathode, YSZ electrolyte, and LSM-YSZ anode, the electrolysis zone was operated at 800°C and the temperature decreased to 200°C in the F–T regime. They obtained a methane yield of 23.1% with an inlet gas composition of 21.3% CO_2, 58.7% H_2, and 20.0% H_2O under an electrolysis current density of 0.32 A cm^{-2}. Luo et al. (2020) recently proposed a mechanism for *in situ* methanation in dual-temperature zone SOECs. They said it takes place in three active regions: on the high-temperature zone cathode surface driven by the reaction between inflowing hydrogen and CO_2, on the cathode–electrolyte interface driven by rapid hydrogenation of the CO produced from the electroreduction of CO_2, and on the low-temperature zone cathode surface driven by purely heterogeneous catalyst-mediated CO_2/CO methanation.

Regarding the role of temperature, another school of thought advocates the use of a single temperature (550–650°C) zone SOEC, where methanation occurs on or in the near vicinity of the cathode itself (mode 3 described in *Basic Working Principle of Solid Oxide Electrolytic Cells and Their Application in Synthetic Methane Production*). Li et al. (2013) used a button-cell configuration with Ni-YSZ cathode, ScSZ electrolyte, and LSM-ScSZ composite anode at 650°C and reported trace amount (0.29%) of methane formation. On similar lines, Bierschenk et al. (2011) showed that reducing SOEC operating temperature from 750 to 600°C increases methane yield from a merely traceable amount to 14.3%. They further predicted from thermodynamic calculations that increasing the pressure to 10 atm would further raise the yield to 26.7%. Jensen et al. (2003) showed that the equilibrium methane yield can be raised to over 50% at 650°C and an operating pressure >15 bar, and this conclusion also indicates that an intermediate temperature SOEC should be more suitable for methane synthesis. They proposed that co-electrolysis carried out at a pressure as high as 150 atm and 650°C would generate 85% CH_4 and 15% H_2 with minimal CO and CO_2. Jensen et al. (2019) further carried out *in situ* methanation in an SOFCMAN 301 stack with 30 NiO-YSZ|YSZ|GDC|LSCF-GDC planar cells maintained at 700°C and 18.7 bar. They reported a methane yield of 18% at a current density of 0.17 A cm^{-2}. In another study, Luo et al. (2020) carried out *in situ* methanation in a tubular reactor with a Ni-YSZ|Ni-ScSZ bilayer cathode, ScSZ electrolyte, and LSM-ScSZ composite anode under varying conditions of pressure. They showed that under an applied current of 2 A, methane yield of 7% at 1 atm increased to 28.7% at 4 atm. However, with technology related to *in situ* methanation in SOECs being at a nascent stage, the effect of pressure on methane yield is debated. Contrary to calculations of Jensen and coworkers, Chen et al. (2017) observed that from 1 to

2.7 bar, the conversion ratio of methane increased and then remained unchanged with further increase in pressure. They explained this phenomenon in terms of the synergistic effect of pressure on methanation reaction rate and current density. On one hand, methanation, being a volume contraction reaction (Eqs 1 and 2), is favored at high pressure, and on the contrary, increase in pressure increases the required voltage for steam and CO_2 co-electrolysis, thereby slightly reducing the current density that pulls down the syngas production rate.

In addition to temperature and pressure effects, investigations on reaction pathways are also equivocal. Li et al. (2013) proposed that under higher applied voltage, CO generated *in situ* dissociates and deposits on the cathode surface as carbon that undergoes hydrogenation to methane. Another interesting possibility is a combinative effect of electric field and catalytic activity on the reaction kinetics by a phenomenon termed as a non-Faradaic electrochemical modification of catalytic activity (NEMCA). In the context of SOECs, it is believed that catalytic activity is enhanced due to the promotion of the work function of catalytic surfaces generated by oxygen ion pumping to/from the electrolyte onto the catalyst surface (Yentekakis and Bebelis, 1992; Yentekakis et al., 1994; Varkaraki et al., 1995; Yentekakis et al., 1995; Frantzis et al., 2000; Cavalca, 2006; Anastasijevic, 2009; Fan, 2012; Theleritis et al., 2012; González-Cobos et al., 2017; López et al., 2019). Unlike structural promoters that improve the dispersion and the chemical stability of the active catalyst phase, electronic promoters directly enhance the catalytic activity of the catalyst itself (**Figure 7A**).

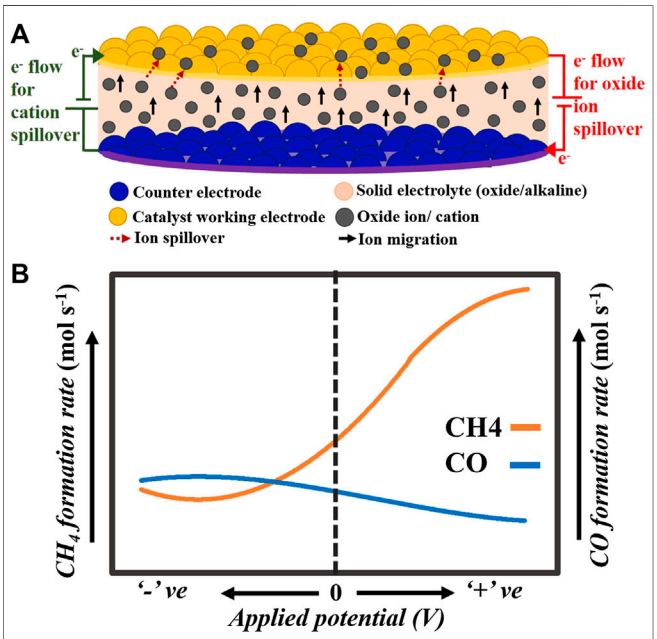

FIGURE 7 | A) Schematic of the basic working principle of non-Faradaic electrochemical modification of catalytic activity effect when ions (oxide ions or cations) are pumped to the catalyst working electrode. **(B)** Pictorial depiction of the trends followed by methane and CO production rates when CO_2 hydrogenation is carried out over a range of negative to positive polarization of the active catalyst surface. Here, both the *y* axes have the same scale.

For *in situ* methanation, Anastasijevic (2009) investigated CO_2 hydrogenation in light of the NEMCA effect using Ru||YSZ||Au between 200 and 300°C under an anodic polarization of −1.3–1.3 V. Under open-circuit conditions, the rate of CH_4 formation was 10^{-4} mmol s^{-1}, which increased to ~2.4 mmol s^{-1} × 10^{-4} mmol s^{-1} under an applied potential of 1.3 V and decreased to ~0.6 mmol s^{-1} × 10^{-4} mmol s^{-1} under −1.3 V. However, the formation rate and selectivity of CO exhibited exactly opposite trends, as shown in **Figure 7B**. There was a monotonic decrease in the rate of CO formation from ~0.7 mmol s^{-1} × 10^{-4} mmol s^{-1} under −1.3 V to ~0.5 mmol s^{-1} × 10^{-4} mmol s^{-1} under 1.3 V. The authors concluded that supplying O^{2-} to the Ru catalyst surface increases its work function, which, in turn, strengthens the Ru–H bond and weakens the Ru–CO bond. This suppresses RWGS (Eq. 3) and promotes methanation, thereby increasing methane yield. Contrarily, stripping O^{2-} away from the Ru surface decreases its work function, promoting RWGS, and hence CO formation. In another study, Fujiwara et al. (2018) conducted steam/CO_2 co-electrolysis on button cells at 600°C using Ni-GDC cathodes, LSCF-GDC anodes, and Hionic™ substrate (oxide ion conductor) electrolyte. The cathodes were doped with Pd and Ru (0.3 mmol/g Ni-GDC). They reported that both CO_2 conversion and methane selectivity increased with an increase in applied potential up to ~4 V, which they explained in light of the NEMCA effect. According to them, polarization enriched the cathode surface with electrons, which could have enhanced its catalytic activity toward CO_2 conversion via the RWGS reaction (Eq. 3). Nevertheless, there is a dearth of studies that address the NEMCA effect on CO_2 methanation, especially for *in situ* methane synthesis in SOECs.

A summary of the key findings of *in situ* methanation studies carried out till date is provided in **Table 3**. The crux of the researches conducted so far on *in situ* methanation in SOECs is that all of temperature, pressure, operating voltage, inlet gas composition, and most essentially electrode and/or electrocatalyst play pivotal roles in determining the yield of methane. However, to interpret and optimize the operating parameters and determine the type of methanation electrocatalyst that would render the highest yield, a clear perception of the actual reaction mechanism is imperative. Thus, the application of SOECs to produce methane requires further R&D activities focused on a clear perception of the governing reactions, and reaction kinetics thereof, choice of electrode–electrolyte–catalyst combination, and finally, optimization of the operating conditions. Nonetheless, it is worth mentioning that *in situ* methanation is one of the most efficient ways for synthetic methane production. We have presented a comparison of the energy efficiency of *in situ* methanation in SOECs with four other routes of methane synthesis in the following section.

ENERGY EFFICIENCY OF METHANE SYNTHESIS VIA DIFFERENT ELECTROCHEMICAL ROUTES

In this section, we compare the energy requirements and efficiencies of five different routes of methane synthesis

TABLE 3 | Studies on *in situ* methanation have been listed in terms of electrode/electrolyte combination, operation temperature and pressure, type of methanation catalyst employed, and yield of CH_4 obtained.

Group	Cathode|electrolyte|anode	Pressure (bar)	Temperature (K)		CH_4 yield (%)	Catalyst	Notes
			SOEC zone	F–T zone			
Xie et al. (2011)	LST-GDC|GDC|LSM-YSZ	1	923	573	2.8	Fe	Fe promotes synthesis of C_{2+} HCs
Chen et al. (2014)	Ni-YSZ|YSZ|LSM-YSZ	1	1,073	523	11.8	Ni	Ni gets oxidized to NiO and decreases CH_4 yield
Lei et al. (2017)	Ni-YSZ|YSZ|LSM-YSZ	1	1,073	473	23.1	Ni in Ni-YSZ	
Luo et al. (2020)	Ni-YSZ|Ni-ScSZ|YSZ|LSM-YSZ	4	823	823	28.7	Ni in Ni-YSZ and Ni-ScSZ	
Li et al. (2013)	Ni-YSZ|ScSZ|LSM-ScSZ	1	923	923	0.29	Ni in Ni-YSZ	
Bierschenk et al. (2011)	Ni-YSZ|YSZ|LSM-YSZ	1	823	823	14.3	Ni in Ni-YSZ	
Jensen et al. (2003)	Ni-YSZ|YSZ|LSM-YSZ	1	923	923	0.58	Ni in Ni-YSZ	
Jensen et al. (2019)	NiO-YSZ|YSZ|GDC ILSCF-GDC	18.7	973	973	18	Ni in NiO-YSZ	
Chen et al. (2017)	Ni-YSZ|YSZ|LSM-YSZ	3	1,023	523	17	Ni	

(**Figure 8**) which involve the use of PEM, AELs, and SOEC electrolyzers. For SOECs, we considered different modes of operation. In route 1, water electrolysis is carried out in AELs or PEM at near-standard operating conditions (80°C and 1 bar) to produce hydrogen, which along with CO_2 is fed to a Sabatier reactor (SR) for methane synthesis. In route 2, steam electrolysis is carried out in SOECs to produce hydrogen, which is fed to a SR for methane generation. In route 3, steam and CO_2 are co-electrolyzed in SOECs to generate syngas, which is supplied to a MR for methane synthesis. Route 4 involves *in situ* synthesis of methane in a two-temperature zone SOEC, where syngas generation from co-electrolysis of steam–CO_2 occurs in the high-temperature zone followed by its subsequent methanation in the low-temperature zone. In route 5, dry CO_2 electrolysis in SOECs produces CO that undergoes WGS reaction with steam in a thermochemical reactor to generate a H_2/CO_2 mixture that then undergoes methanation in a subsequent SR.

So routes 2–5 involve SOECs, here assumed to be at 800°C and 1 bar, which can be essentially operated in multiple configurations for methane synthesis. It can be used as a source of hydrogen (route 1) or CO (route 5) or syngas (route 3) that undergoes subsequent methanation in a SR or a MR operated at 250°C and 25 bar pressure in the presence of state-of-the-art Ni catalyst. Further, it is possible to use SOECs for one-step methanation (route 4) directly from steam and CO_2.

The schematic of the five routes considered here are shown in **Figure 8** and their corresponding energy efficiencies in **Figure 9A**. The process energy efficiencies (η) are calculated by employing basic enthalpy balance:

$$\text{Process energy efficiency } (\eta) = \frac{\text{Energy content of product}}{\text{Total energy input}} \times 100 \tag{10}$$

It is to be noted now that SOECs provide the opportunity to recycle back the exothermic heat of methanation reactions (Eqs 1 and 2); however, the recirculation of heat requires an additional balance of plant which can increase capital costs. So, for each of routes 2, 3, and 5, two cases of η and energy demand are portrayed (**Figures 9A,B**): one with heat recycled back from SR or MR to the SOEC being operated at 800°C and the other one with no such heat recycle, whereas routes 1 and 4 have only one value of η; for route 1, there is no scope for heat recycle with AELs/PEM, and for route 4, exothermic heat is generated *in situ* within the SOEC itself and is thus available at all times.

Although methane itself is a well-established fuel, it can also be used as a source of hydrogen (at energy penalty) using an established steam methane reforming process in conventional thermochemical reactors or membrane separation catalytic reactors (Kim et al., 2018; Simakov and Román-Leshkov, 2018). When methane was produced via routes 1, 2, and 5 (Eq. 10), the energy efficiency of the process was estimated to be approximately 67, 73, and 80%, respectively, whereas the highest efficiency of ~89% was calculated for *in situ* methanation (route 4), as shown in **Figure 9A**. The round-trip efficiency (RTE) of producing methane from hydrogen and back

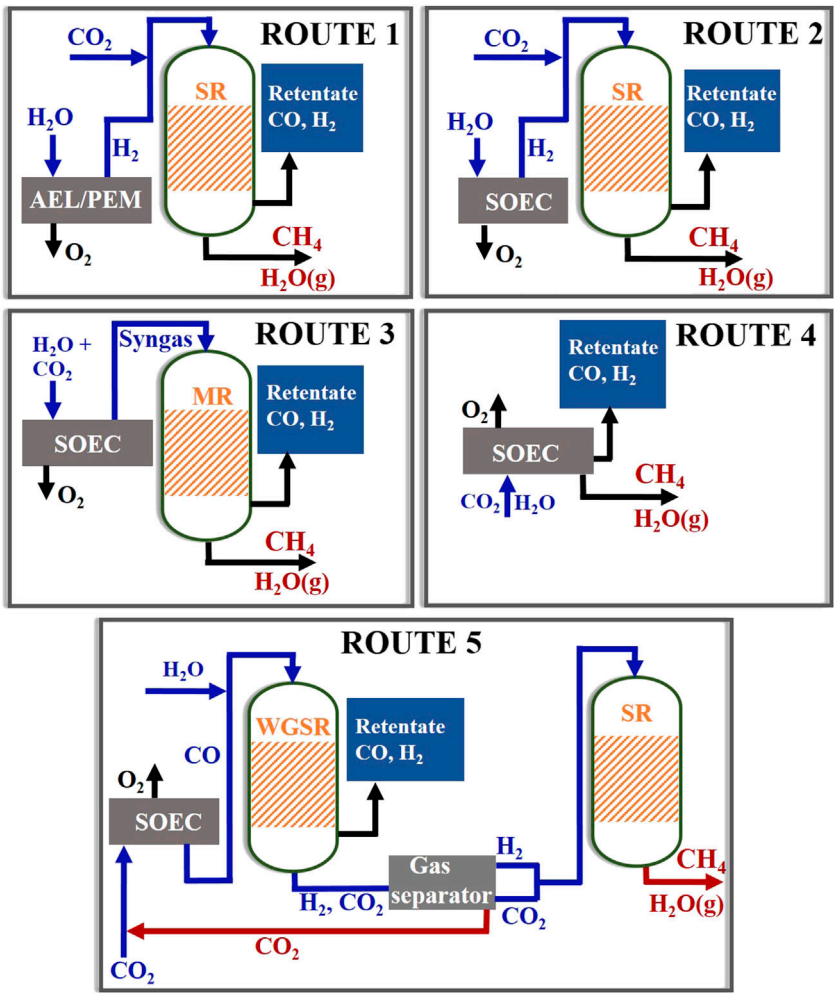

FIGURE 8 | Schematics of five different routes of methane synthesis using electrolysis. Here, SR, MR, WGS, and HE stand for Sabatier reactor, methanation reactor, water–gas shift reactor, and heat exchanger, respectively.

to hydrogen through steam reforming (**Figure 9C**) was also maximum for route 4 (~62%), followed by route 3 (~58%). Similar RTE (~65%) was reported by Jensen et al. (2015) while operating solid oxide cells in reversible mode at near-atmospheric pressure. They modeled the system where methane was synthesized as well as utilized using the same device. However, at high pressure (15 bar), higher efficiencies of up to 70% were reported by them. In another similar study, Butera et al. (2019) reported that during the reversible operation of solid oxide cells at higher pressures, the RTE can be further increased to 80% through proper adjustment of the H/C ratio of the gases being purged into the cell during both electrolysis and fuel-cell modes.

From preliminary energy balance calculations and considering minimal balance of plant requirements, it can be stated that *in situ* methanation in SOECs is the most efficient yet relatively cheaper option for methane synthesis as well as hydrogen recovery. For large-scale methane producing plants, the capital costs associated with the integration of separate reactors is substantial. In contrast, *in situ* methanation in SOECs eliminates the need for separate reactors and auxiliary components, which makes the system relatively compact and reduces plant footprint.

Calculations are based on the following major assumptions:

- During actual cell operation, voltage and current density would dictate the input energy, and thus the energy efficiency of the process. However, what have been reported here are simplistic calculations purely based on thermodynamics, so no current density is involved in this case.
- System losses incurred from the integration of various components such as catalytic recuperator, condenser, humidifier, and gas splitter have not been considered here.
- Heat loss from reactor and pipelines is 5% of the total heat generated due to exothermic reactions occurring in the SR or MR or WGSR (heat exchanger efficiency 95%).
- 90% of each of the gases produced through electrolysis is available for further reactions.

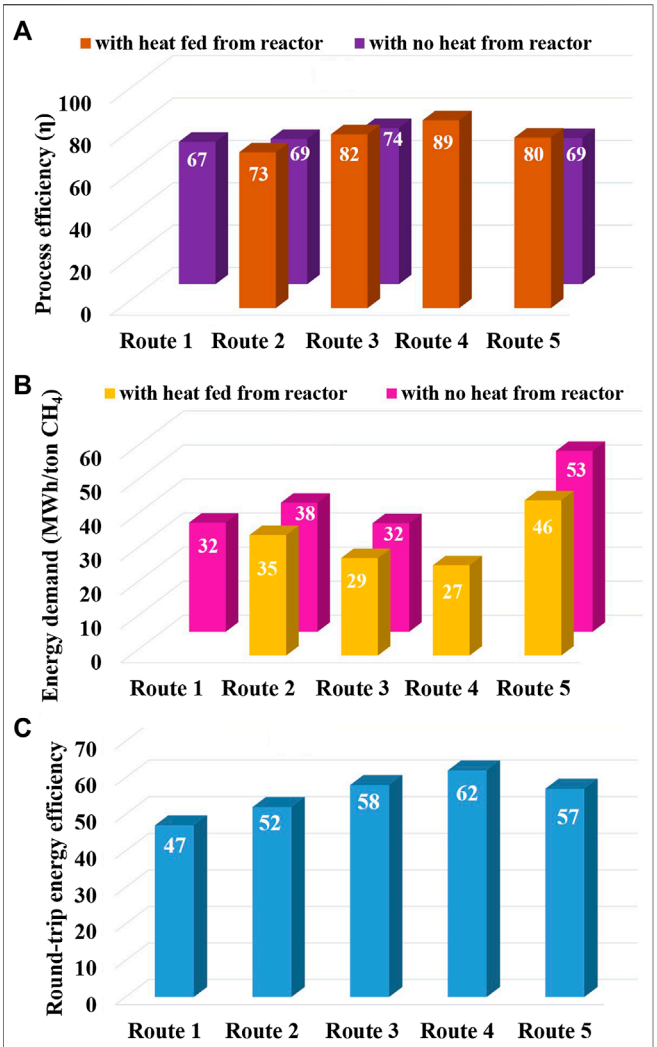

FIGURE 9 | A) Process efficiencies of five different routes of CH_4 synthesis. **(B)** Energy requirements of five different routes of CH_4 synthesis. **(C)** The round-trip efficiency of the five different routes of methane synthesis.

- 100% of the products generated in the SR, MR, and WGSR are obtained at the reactor outlets.
- In route 5, H_2/CO_2, produced in the WGSR at the ratio of 1:1, flows to the gas separator from where H_2/CO_2 at a ratio of 4:1 is sent to the SR and the remaining CO_2 is recycled back to the SOEC.
- Electrolyzers are thermally insulated and prevent heat loss to the surrounding.
- For RTE, no losses have been considered for methane compression and transportation, and efficiency of the steam methane reformer for converting methane to hydrogen is 70%.
- RTE calculations are based on the best-case scenario, that is, with heat recycled back from the SR or MR to the SOEC.
- LHV has been used for both methane (55 KJ/g) and hydrogen (120 KJ/g).

CONCLUDING REMARKS AND TECHNOLOGY OUTLOOK

An ever-increasing global energy demand with subsequent development in solar and wind energy systems has made the compelling case for investigations on renewably powered synthetic reactors for the production of hydrogen and hydrogen carriers as a means of energy storage and transport.

Methane, the major component of natural gas, is one of the favorite contenders if the carbon source is waste CO_2 produced from industrial or biological processes, or collected from the atmosphere using direct air capture technology, and hydrogen is sourced using renewable sources of energy. Methane itself is a well-established fuel but can potentially be a part of a circular hydrogen economy acting as a source of hydrogen that can be transported over long distances for various applications. The steam methane reforming for hydrogen production is a well-established process.

Methane can be synthesized in a SR from CO_2 and hydrogen. CO_2 can be acquired from carbon capture and sequestration stations and hydrogen from electrolysis of water in AELs or PEM. AEM and PEM are becoming mature technologies for hydrogen production, but both suffer from certain shortcomings, the major one being the high electrical energy demand. In such a pretext, SOECs are being considered eligible candidates for methane synthesis. Although some preliminary research corroborates the huge potential of *in situ* methane synthesis in SOECs, rigorous investigations on the electrochemical and chemical reaction mechanisms and kinetics, and cell material behavior under the process conditions are required to advance the technology. A balance between SOEC kinetics and a thermodynamically favorable operating window for methane synthesis needs to be achieved, which is a nontrivial challenge.

The areas requiring detailed inspection and development include electrocatalytically active materials selection, cell design, the establishment of overall mechanism and reaction pathways of methanation processes, and optimization of process conditions.

One of the prime constraints of SOEC is the high-temperature operation that tends to reduce the cell materials lifetime and is counterproductive for methanation reaction. This calls for innovation of novel materials as electrolytes that will possess appreciable ionic conductivity at intermediate temperatures (350–600°C), good chemical stability to endure the redox environment of the SOEC and finally excellent adhesion to the electrodes. Development of electrode materials (cathode) with the desired combination of electrocatalytic properties, mechanical strength, phase stability and electrical conductivity at SOEC operating temperature and environment is another prerequisite.

The choice for cathode materials for one-step methane synthesis (on the same electrode) becomes even more challenging as in addition to the requirements for electrodes to perform co-electrolysis, the activity of methanation also needs to be considered. Materials need to be chosen such that they have low CO adsorption energies so that the CO produced *in situ* can undergo further hydrogenation to yield methane. Oxygen

evolution being relatively less energy intensive in SOECs, the research emphasis is on engineering the porosity and microstructure of the anodes to avoid delamination from the electrolyte, rather than materials itself.

A second limitation of methane synthesis using SOECs is that the rate-limiting step for electrolysis of CO_2 or co-electrolysis of CO_2/H_2O mixture in SOECs has not yet been unanimously established or determined. For syngas production through co-electrolysis, the role of CO_2 electrolysis (Eq. 5) vs. RWGS reaction (Eq. 3) as the major pathway of CO generation is still debated. As of date, two notions prevail regarding the role of the RWGS reaction in the co-electrolysis of steam and CO_2. Some researchers believe that with steam electrolysis being much faster than CO_2 electrolysis, only H_2O splits into hydrogen which then undergoes RWGS reaction with CO_2 to produce CO, as RWGS is thermodynamically more favorable. However, others believe that CO_2 is electrolyzed to CO. Establishment of the reaction mechanism for *in situ* methanation poses additional challenges as it follows a complex pathway consisting of primarily four different steps: 1) dissociative adsorption of CO_2 on the electrode followed by either its hydrogenation to CH_4 (methanation) or CO (RWGS), or even surface reduction to CO; 2) electroreduction of CO_2 to CO at the triple-phase boundary; 3) hydrogenation of the CO produced *in situ* through steps 1 and 2 to CH_4; and 4) electroreduction of the steam generated during *in situ* methanation to prevent dissociation of methane via steam reforming. The kinetically slowest and hence rate-limiting step will be dictated by the electro-kinetics of the whole process subject to temperature, and such understanding is required to enable material design and optimization of processing conditions to enhance reaction kinetics and methane yield to practical levels.

Other parameters requiring optimization are SOEC operating conditions such as temperature, pressure, current density, voltage, and inlet gas composition. The effect of temperature is still debated; most of the investigations conducted with dual-temperature zone SOECs show that the operation of the SOEC section at higher temperatures improves syngas generation, which would consequently enhance methane yield in the subsequent low-temperature F–T section. However, some other investigations clearly indicate that a single temperature zone SOEC operated at an intermediate temperature ensures improved methane yield. Equally ambiguous is the effect of pressure as discussed in *State of the Art of Purely Electrochemical In Situ Methane Synthesis in Solid Oxide Electrolytic Cells*. The contribution of the NEMCA effect toward the enhanced catalytic activity of electrocatalysts during *in situ* methane synthesis is also yet to be established.

A sustainable operation meeting the required SOEC kinetics in the temperature range suitable for methanation (300–500°C) warrants the development of new materials and cell designs functioning effectively in the temperature range. The electrochemical performance targeted for the electrodes and the electrolyte will vary with the design, and this will in turn affect the costs associated with the cell fabrication process. The electrolyte-supported cells can be limited in current densities (proportional to hydrogen or syngas production); however, the production costs are usually lower than that of anode-supported cells. On the other hand, the electrode-supported cells can be operated at very high current densities, even exceeding 1 A cm^{-2}; however, cost and lifetime are the key challenges. In the opinion of the authors, the capital costs of US$1,000 per kilogram (hydrogen) at 1 MW scale can make a compelling commercial case for SOECs, considering competing technologies and hydrogen cost targets.

In a nutshell, exhaustive studies and improvisation, therefore, can make *in situ* methanation in SOECs an indispensable part of Power-to-Methane technology that is bound to play a key role in the future energy sector.

AUTHOR CONTRIBUTIONS

SahB, major write up and review; AK, conception, outline, major write up, and review; SG, critical review, content suggestions, and proofreading; SanB, critical review, content suggestions, and proofreading.

FUNDING

This work received funding from the Australian Renewable Energy Agency (ARENA) as part of ARENA's Research and Development Program—Renewable Hydrogen for Export, and also from CSIRO Hydrogen Energy Systems Future Science Platform, CSIRO Research Office, and a PhD scholarship from Monash University. The funder was not involved in the study design; collection, analysis, and interpretation of data; the writing of the manuscript; or the decision to submit it for publication.

ACKNOWLEDGMENTS

The authors would also like to thank Daniel Fini for an internal review of the manuscript.

REFERENCES

Acar, C., and Dincer, I. (2019). Review and evaluation of hydrogen production options for better environment. *J. Clean. Prod.* 218, 835–849. doi:10.1016/j.jclepro.2019.02.046

Afroze, S., Karim, A., Cheok, Q., Eriksson, S., and Azad, A. K. (2019). Latest development of double perovskite electrode materials for solid oxide fuel cells: a review. *Front. Energy* 13, 770–797. doi:10.1007/s11708-019-0651-x

Anastasijevic, N. A. (2009). NEMCA—from discovery to technology. *Catal. Today* 146, 308–311. doi:10.1016/j.cattod.2009.02.020

Anderson, R. B., Kölbel, H., and Rálek, M. (1984). *The Fischer–Tropsch synthesis*. New York, NY: Academic Press

Ayers, K. E., Anderson, E. B., Capuano, C., Carter, B., Dalton, L., Hanlon, G., et al. (2010). Research advances towards low cost, high efficiency PEM electrolysis. *ECS Trans.* 33, 3–15.

Balachandran, U., Dorris, S., Picciolo, J., Poeppel, R., Mcpheeters, C., and Minh, N. (1989). "Material and fabrication challenges in the development of monolithic

solid oxide fuel cells," in Proceedings of the 24th intersociety energy conversion engineering conference (Piscataway, NJ: IEEE), 1541–1545.

Bandi, A., Specht, M., Weimer, T., and Schaber, K. (1995). CO_2 recycling for hydrogen storage and transportation—electrochemical CO_2 removal and fixation. *Energy Convers. Manag.* 36, 899–902. doi:10.1016/0196-8904(95)00148-7

Barnett, S. A., Zhang, S.-L., Zhu, T., Lu, M. Y., and Mogni, L. V. (2019). "Titanate-based electrodes for solid oxide cells," in 236th ECS meeting, Atlanta, GA, October 13–17, 2019.

Bertuccioli, L., Chan, A., Hart, D., Lehner, F., Madden, B., and Standen, E. (2014). Final report. Study on development of water electrolysis in the EU. The Fuel Cells and Hydrogen Joint Undertaking.

Bhandari, R., Trudewind, C. A., and Zapp, P. (2014). Life cycle assessment of hydrogen production via electrolysis: a review. *J. Clean. Prod.* 85, 151–163. doi:10.1016/j.jclepro.2013.07.048

Bierschenk, D. M., Wilson, J. R., and Barnett, S. A. (2011). High efficiency electrical energy storage using a methane-oxygen solid oxide cell. *Energy Environ. Sci.* 4, 944–951. doi:10.1039/c0ee00457j

Bourcet, A., and Tantardini, G. F. (1994). A theoretical study of the adsorption dynamics of hydrogen on Ni(111) surface. *J. Electron. Spectros. Relat. Phenomena* 69, 55–64. doi:10.1016/s0368-2048(14)80008-x

Bruce, S., Temminghoff, M., Hayward, J., Schmidt, E., Munnings, C., Palfreyman, D., et al. (2018). *National hydrogen roadmap*. Australia: CSIRO.

Butera, G., Jensen, S. H., and Clausen, L. R. (2019). A novel system for large-scale storage of electricity as synthetic natural gas using reversible pressurized solid oxide cells. *Energy* 166, 738–754. doi:10.1016/j.energy.2018.10.079

Buttler, A., and Spliethoff, H. (2018). Current status of water electrolysis for energy storage, grid balancing and sector coupling via power-to-gas and power-to-liquids: a review. *Renew. Sust. Energ. Rev.* 82, 2440–2454. doi:10.1016/j.rser.2017.09.003

Cable, T. L., Setlock, J. A., Farmer, S. C., and Eckel, A. J. (2011). Regenerative performance of the NASA symmetrical solid oxide fuel cell design. *Int. J. Appl. Ceram. Technol.* 8, 1–12. doi:10.1111/j.1744-7402.2009.02477.x

Capuano, L. (2018). *International energy outlook 2018 (IEO2018)*. Washington, DC: US Energy Information Administration (EIA), 21.

Carmo, M., Fritz, D. L., Mergel, J., and Stolten, D. (2013). A comprehensive review on PEM water electrolysis. *Int. J. Hydrog. Energy* 38, 4901–4934. doi:10.1016/j.ijhydene.2013.01.151

Cavalca, C. (2006). Method for low temperature, high activity and selectivity catalytic conversion using electrochemical (NEMCA) cells. Google Patents 20060131179.

Chatzichristodoulou, C., Chen, M., Hendriksen, P. V., Jacobsen, T., and Mogensen, M. B. (2016). Understanding degradation of solid oxide electrolysis cells through modeling of electrochemical potential profiles. *Electrochim. Acta* 189, 265–282. doi:10.1016/j.electacta.2015.12.067

Chen, B., Xu, H., and Ni, M. (2017). Modelling of SOEC-FT reactor: pressure effects on methanation process. *Appl. Energy* 185, 814–824. doi:10.1016/j.apenergy.2016.10.095

Chen, K., and Jiang, S. P. (2011). Failure mechanism of (La,Sr)MnO_3 oxygen electrodes of solid oxide electrolysis cells. *Int. J. Hydrog. Energy* 36, 10541–10549. doi:10.1016/j.ijhydene.2011.05.103

Chen, L., Chen, F., and Xia, C. (2014). Direct synthesis of methane from CO_2–H_2O co-electrolysis in tubular solid oxide electrolysis cells. *Energy Environ. Sci.* 7, 4018–4022. doi:10.1039/c4ee02786h

Chen, M., Liu, Y.-L., Bentzen, J. J., Zhang, W., Sun, X., Hauch, A., et al. (2013). Microstructural degradation of Ni/YSZ electrodes in solid oxide electrolysis cells under high current. *J. Electrochem. Soc.* 160, F883–F891. doi:10.1149/2.098308jes

Chen, X., Khor, K., and Chan, S. (2004). Electrochemical behavior of La(Sr)MnO_3 electrode under cathodic and anodic polarization. *Solid State Ion.* 167, 379–387. doi:10.1016/j.ssi.2003.08.049

Chen, X., and Shangguan, W. (2013). Hydrogen production from water splitting on CdS-based photocatalysts using solar light. *Front. Energy* 7, 111–118. doi:10.1007/s11708-012-0228-4

Chen, Y., Luo, Y., Shi, Y., and Cai, N. (2019). Theoretical Modeling of methane production in pressurized micro-tubular R-SOFC. *Energy Procedia* 158, 2164–2169. doi:10.1016/j.egypro.2019.01.615

Christian, F., Edith, D., Selly, A., Adityawarman, D., and Indarto, A. (2013). Application of nanotechnologies in the energy sector: a brief and short review. *Front. Energy* 7, 6–18. doi:10.1007/s11708-012-0219-5

Cimenti, M., and Hill, J. M. (2010). Importance of pyrolysis and catalytic decomposition for the direct utilization of methanol in solid oxide fuel cells. *J. Power Sources* 195, 54–61. doi:10.1016/j.jpowsour.2009.07.007

Cimon, C., Kadota, P., and Eskicioglu, C. (2020). Effect of biochar and wood ash amendment on biochemical methane production of wastewater sludge from a temperature phase anaerobic digestion process. *Bioresour. Technol.* 297, 122440. doi:10.1016/j.biortech.2019.122440

Clausen, L. R., Butera, G., and Jensen, S. H. (2019). Integration of anaerobic digestion with thermal gasification and pressurized solid oxide electrolysis cells for high efficiency bio-SNG production. *Energy* 188, 116018. doi:10.1016/j.energy.2019.116018

Criqui, P., and Kouvaritakis, N. (2000). World energy projections to 2030. *Ijgei* 14, 116–136. doi:10.1504/ijgei.2000.004385

Cumming, D. J., Thompson, A. R., and Rothman, R. H. (2016). Nickel impregnated cerium-doped strontium titanate fuel electrode: direct carbon dioxide electrolysis and co-electrolysis. *J. Electrochem. Soc.* 163, F3057. doi:10.1149/2.0081611jes

Deka, D. J., Gunduz, S., Fitzgerald, T., Miller, J. T., Co, A. C., and Ozkan, U. S. (2019). Production of syngas with controllable H_2/CO ratio by high temperature co-electrolysis of CO_2 and H_2O over Ni and Co-doped lanthanum strontium ferrite perovskite cathodes. *Appl. Catal. B Environ.* 248, 487–503. doi:10.1016/j.apcatb.2019.02.045

Ding, H., Wu, W., and Ding, D. (2019). Advancement of proton-conducting solid oxide fuel cells and solid oxide electrolysis cells at Idaho national laboratory (INL). *ECS Trans.* 91, 1029–1034. doi:10.1149/09101.1029ecst

Dogu, D., Gunduz, S., Meyer, K. E., Deka, D. J., Co, A. C., and Ozkan, U. S. (2019). CO_2 and H_2O electrolysis using solid oxide electrolyzer cell (SOEC) with La and Cl-doped strontium titanate cathode. *Catal. Lett.* 149, 1743–1752. doi:10.1007/s10562-019-02786-8

Duan, C., Kee, R., Zhu, H., Sullivan, N., Zhu, L., Bian, L., et al. (2019). Highly efficient reversible protonic ceramic electrochemical cells for power generation and fuel production. *Nat Energy* 4, 230–240. doi:10.1038/s41560-019-0333-2

Dueñas, D. M. A., Riedel, M., Riegraf, M., Costa, R., and Friedrich, K. A. (2020). High temperature co-electrolysis for power-to-X. *Chem. Ing. Tech.* 92, 45–52. doi:10.1002/cite.201900119

Ebbesen, S. D., Jensen, S. H., Hauch, A., and Mogensen, M. B. (2014). High temperature electrolysis in alkaline cells, solid proton conducting cells, and solid oxide cells. *Chem. Rev.* 114, 10697–10734. doi:10.1021/cr5000865

Ebbesen, S. D., and Mogensen, M. (2009). Electrolysis of carbon dioxide in solid oxide electrolysis cells. *J. Power Sources* 193, 349–358. doi:10.1016/j.jpowsour.2009.02.093

Eguchi, K., Hatagishi, T., and Arai, H. (1996). Power generation and steam electrolysis characteristics of an electrochemical cell with a zirconia- or ceria-based electrolyte. *Solid State Ion.* 86–88, 1245–1249. doi:10.1016/0167-2738(96)00295-0

El Sibai, A., Rihko-Struckmann, L., and Sundmacher, K. (2015). "Synthetic methane from CO_2: dynamic optimization of the Sabatier process for power-to-gas applications," in *Computer aided chemical engineering* (Amsterdam, Netherlands: Elsevier).

Elleuch, A., and Halouani, K. (2020). "Intermediate-temperature solid oxide fuel cell fueled by biofuels," *Intermediate temperature solid oxide fuel cells* (Amsterdam, Netherlands: Elsevier).

Erdle, E., Dönitz, W., Schamm, R., and Koch, A. (1992). Reversibility and polarization behaviour of high temperature solid oxide electrochemical cells. *Int. J. Hydrogen Energy* 17, 817–819. doi:10.1016/0360-3199(92)90026-s

Faes, A., Hessler-Wyser, A., Zryd, A., and Van Herle, J. (2012). A review of RedOx cycling of solid oxide fuel cells anode. *Membranes* 2, 585–664. doi:10.3390/membranes2030585

Fan, Q. (2012). Biofuel production by high temperature non-faradaic electrochemical modification of catalysis. Google Patents 20100258447.

Farla, J. C. M., Hendriks, C. A., and Blok, K. (1995). Carbon dioxide recovery from industrial processes. *Clim. Change* 29, 439–461. doi:10.1007/bf01092428

Faro, M. L., Zignani, S., Trocino, S., Antonucci, V., and Aricò, A. (2019). New insights on the co-electrolysis of CO_2 and H_2O through a solid oxide electrolyser operating at intermediate temperatures. *Electrochim. Acta* 296, 458–464.

Foit, S. R., Vinke, I. C., de Haart, L. G. J., and Eichel, R.-A. (2017). Power-to-Syngas: an enabling technology for the transition of the energy system? *Angew. Chem. Int. Ed.* 56, 5402–5411. doi:10.1002/anie.201607552

Frantzis, A., Bebelis, S., and Vayenas, C. G. (2000). Electrochemical promotion (NEMCA) of CH_4 and C_2H_4 oxidation on Pd/YSZ and investigation of the origin of NEMCA via AC impedance spectroscopy. *Solid State Ion.* 36–137, 863–872. doi:10.1016/s0167-2738(00)00528-2

Fujiwara, N., Kikuchi, R., Takagaki, A., and Oyama, S. T. (2018). "Development OF solid oxide electrolysis cell cathodes for direct methanation IN CO_2/H_2O CO-electrolysis," in Grand renewable energy proceedings, Japan, June 17–22, 2018 (Japan: Japan Council for Renewable Energy), 225.

Gan, L., Ye, L., Tao, S., and Xie, K. (2016). Titanate cathodes with enhanced electrical properties achieved via growing surface Ni particles toward efficient carbon dioxide electrolysis. *Phys. Chem. Chem. Phys.* 18, 3137–3143. doi:10.1039/c5cp06742a

Gao, J., Wang, Y., Ping, Y., Hu, D., Xu, G., Gu, F., et al. (2012). A thermodynamic analysis of methanation reactions of carbon oxides for the production of synthetic natural gas. *RSC Adv.* 2, 2358–2368. doi:10.1039/c2ra00632d

Ghaib, K., and Ben-Fares, F.-Z. (2018). Power-to-Methane: a state-of-the-art review. *Renew. Sustain. Energy Rev.* 81, 433–446. doi:10.1016/j.rser.2017.08.004

González-Cobos, J., Valverde, J. L., and DE Lucas-Consuegra, A. (2017). Electrochemical vs. chemical promotion in the H_2 production catalytic reactions. *Int. J. Hydrogen Energy* 42, 13712–13723. doi:10.1016/j.ijhydene.2017.03.085

Goodenough, J. B., and Huang, Y. (2007). Alternative anode materials for solid oxide fuel cells. *J. Power Sources* 73, 1–10.

Graves, C., Ebbesen, S. D., Jensen, S. H., Simonsen, S. B., and Mogensen, M. B. (2015). Eliminating degradation in solid oxide electrochemical cells by reversible operation. *Nat. Mater.* 14, 239–244. doi:10.1038/nmat4165

Graves, C., Ebbesen, S. D., and Mogensen, M. (2011). Co-electrolysis of CO_2 and H_2O in solid oxide cells: performance and durability. *Solid State Ion.* 192, 398–403. doi:10.1016/j.ssi.2010.06.014

Gray, M. L., Champagne, K. J., Fauth, D., Baltrus, J. P., and Pennline, H. (2008). Performance of immobilized tertiary amine solid sorbents for the capture of carbon dioxide. *Int. J. Greenh. Gas Con.* 2, 3–8. doi:10.1016/s1750-5836(07)00088-6

Green, R., Liu, C., and Adler, S. (2008). Carbon dioxide reduction on gadolinia-doped ceria cathodes. *Solid State Ion.* 179, 647–660. doi:10.1016/j.ssi.2008.04.024

Guan, J., Ramamurthi, B., Ruud, J., Hong, J., Riley, P., and Minh, N. (2006). High performance flexible reversible solid oxide fuel cell. GE Global Research Center Final Report for DOE Cooperative Agreement DE-FC36-04GO-14351.

Hansen, J. B. (2015). Solid oxide electrolysis—a key enabling technology for sustainable energy scenarios. *Faraday Discuss.* 182, 9–48. doi:10.1039/c5fd90071a

Hauch, A., Ebbesen, S. D., Jensen, S. H., and Mogensen, M. (2008). Solid oxide electrolysis cells: microstructure and degradation of the Ni/yttria-stabilized zirconia electrode. *J. Electrochem. Soc.* 155, B1184–B1193. doi:10.1149/1.2967331

Hjalmarsson, P., Sun, X., Liu, Y.-L., and Chen, M. (2013). Influence of the oxygen electrode and inter-diffusion barrier on the degradation of solid oxide electrolysis cells. *J. Power Sources* 223, 349–357. doi:10.1016/j.jpowsour.2012.08.063

Hobson, P. N., Bousfield, S., and Summers, R. (1981). *Methane production from agricultural and domestic wastes*. Berlin, Germany: Springer.

Holtappels, P., De Haart, L., Stimming, U., Vinke, I. C., and Mogensen, M. (1999). Reaction of CO/CO_2 gas mixtures on Ni–YSZ cermet electrodes. *J. Appl. Electrochem.* 29, 561–568. doi:10.1023/a:1003446721350

Hong, H. S., Lee, S., and Lee, C. S. (2015). Characterization of (Ni–Cu)/YSZ cermet composites fabricated using high-energy ball-milling: effect of Cu concentration on the composite performance. *Ceram. Int.* 41, 6122–6126.

Hu, L. (2016). *Molten carbonate fuel cells for electrolysis*. Stockholm, Sweden: KTH Royal Institute of Technology.

Hu, L., Lindbergh, G., and Lagergren, C. (2016). Performance and durability of the molten carbonate electrolysis cell and the reversible molten carbonate fuel cell. *J. Phys. Chem. C* 120, 13427–13433. doi:10.1021/acs.jpcc.6b04417

Huang, W., Finnerty, C., Sharp, R., Wang, K., and Balili, B. (2017). High-performance 3D printed microtubular solid oxide fuel cells. *Adv. Mater. Technol.* 2, 1600258. doi:10.1002/admt.201600258

Ishihara, T., Jirathiwathanakul, N., and Zhong, H. (2010). Intermediate temperature solid oxide electrolysis cell using $LaGaO_3$ based perovskite electrolyte. *Energy Environ. Sci.* 3, 665–672. doi:10.1039/b915927d

Iwanschitz, B., Sfeir, J., Mai, A., and Schütze, M. (2010). Degradation of SOFC anodes upon redox cycling: a comparison between Ni/YSZ and Ni/CGO. *J. Electrochem. Soc.* 157, B269–B278. doi:10.1149/1.3271101

Jaiswal, N., Tanwar, K., Suman, R., Kumar, D., Upadhyay, S., Parkash, O., et al. (2019). A brief review on ceria based solid electrolytes for solid oxide fuel cells. *J. Alloys Compd.* 781, 984–1005. doi:10.1016/j.jallcom.2018.12.015

James, B., Desantis, D., and Saur, G. (2016). Final report: hydrogen production pathways cost analysis (2013–2016). US Department of Energy. Report DOE-StrategicAnalysis-6231-1.

Jayakumar, A. (2019). A comprehensive assessment on the durability of gas diffusion electrode materials in PEM fuel cell stack. *Front. Energy* 173, 1–14.

Jensen, S. H., Graves, C., Mogensen, M., Wendel, C., Braun, R., Hughes, G., et al. (2015). Large-scale electricity storage utilizing reversible solid oxide cells combined with underground storage of CO_2 and CH_4. *Energy Environ. Sci.* 8, 2471–2479. doi:10.1039/c5ee01485a

Jensen, S. H., Høgh, J. V. T., Barfod, R., and Mogensen, M. B. (2003). "High temperature electrolysis of steam and carbon dioxide," in Risø international energy conference 2003, Risø, Denmark, May 19-21, 2003, 204–215.

Jensen, S. H., Langnickel, H., Hintzen, N., Chen, M., Sun, X., Hauch, A., et al. (2019). Reversible operation of a pressurized solid oxide cell stack using carbonaceous gases. *J. Energy Storage* 22, 106–115. doi:10.1016/j.est.2019.02.003

Jiang, S. P. (2019). Development of lanthanum strontium cobalt ferrite perovskite electrodes of solid oxide fuel cells—a review. *Int. J. Hydrog. Energy* 44, 7448–7493. doi:10.1016/j.ijhydene.2019.01.212

Junaedi, C., Hawley, K., and Roychoudhury, S. (2014). Sabatier process and apparatus for controlling exothermic reaction. Google Patents US20120029095A1.

Kaur, G., Kulkarni, A. P., and Giddey, S. (2018a). CO_2 reduction in a solid oxide electrolysis cell with a ceramic composite cathode: effect of load and thermal cycling. *Int. J. Hydrogen Energy* 43, 21769–21776. doi:10.1016/j.ijhydene.2018.10.014

Kaur, G., Kulkarni, A. P., Giddey, S., and Badwal, S. P. S. (2018b). Ceramic composite cathodes for CO_2 conversion to CO in solid oxide electrolysis cells. *Appl. Energy* 221, 131–138. doi:10.1016/j.apenergy.2018.03.176

Keith, D. W. (2009). Why capture CO_2 from the atmosphere? *Science* 325, 1654–1655. doi:10.1126/science.1175680

Khan, M. S., Lee, S.-B., Song, R.-H., Lee, J.-W., Lim, T.-H., and Park, S.-J. (2016). Fundamental mechanisms involved in the degradation of nickel-yttria stabilized zirconia (Ni-YSZ) anode during solid oxide fuel cells operation: a review. *Ceram. Int.* 42, 35–48. doi:10.1016/j.ceramint.2015.09.006

Khan, M. S., Xu, X., Zhao, J., Knibbe, R., and Zhu, Z. (2017). A porous yttria-stabilized zirconia layer to eliminate the delamination of air electrode in solid oxide electrolysis cells. *J. Power Sources* 359, 104–110. doi:10.1016/j.jpowsour.2017.05.049

Kim, C.-H., Han, J.-Y., Lim, H., Lee, K.-Y., and Ryi, S.-K. (2018). Hydrogen production by steam methane reforming in membrane reactor equipped with Pd membrane deposited on NiO/YSZ/NiO multilayer-treated porous stainless steel. *J. Membr. Sci.* 563, 75–82. doi:10.1016/j.memsci.2018.05.037

Kim, J., Ji, H.-I., Dasari, H. P., Shin, D., Song, H., Lee, J.-H., et al. (2013). Degradation mechanism of electrolyte and air electrode in solid oxide electrolysis cells operating at high polarization. *Int. J. Hydrogen Energy* 38, 1225–1235. doi:10.1016/j.ijhydene.2012.10.113

Kim, J., Kim, G.-D., Moon, J.-W., Park, Y.-I., Lee, W.-H., Kobayashi, K., et al. (2001). Characterization of LSMâ"YSZ composite electrode by ac impedance spectroscopy. *Solid State Ion.* 143, 379–389. doi:10.1016/s0167-2738(01)00877-3

Kim, S. J., and Choi, G. M. (2014). Stability of LSCF electrode with GDC interlayer in YSZ-based solid oxide electrolysis cell. *Solid State Ion.* 262, 303–306. doi:10.1016/j.ssi.2014.01.001

Kim, S.-W., Park, M., Kim, H., Yoon, K. J., Son, J.-W., Lee, J.-H., et al. (2016). Catalytic effect of Pd–Ni bimetallic catalysts on high-temperature co-electrolysis of steam/CO_2Mixtures. *J. Electrochem. Soc.* 163, F3171. doi:10.1149/2.0251611jes

Kim, Y., and Worrell, E. (2002). International comparison of CO_2 emission trends in the iron and steel industry. *Energy Policy* 30, 827–838. doi:10.1016/s0301-4215(01)00130-6

Knibbe, R., Traulsen, M. L., Hauch, A., Ebbesen, S. D., and Mogensen, M. (2010). Solid oxide electrolysis cells: degradation at high current densities. *J. Electrochem. Soc.* 157, B1209–B1217. doi:10.1149/1.3447752

Kofler, R., Butera, G., Jensen, S. H., and Clausen, L. R. (2019). "Novel hybrid electricity storage system producing synthetic natural gas by integrating

biomass gasification with pressurized solid oxide cells," in 32nd international conference on efficiency, cost, optimization, simulation and environmental impact of energy systems, Wrocław, Poland, June 23–28, 2019.

Kondratenko, E. V., Mul, G., Baltrusaitis, J., Larrazábal, G. O., and Pérez-Ramírez, J. (2013). Status and perspectives of CO_2 conversion into fuels and chemicals by catalytic, photocatalytic and electrocatalytic processes. *Energy Environ. Sci.* 6, 3112–3135. doi:10.1039/c3ee41272e

Kulkarni, A. P., Giddey, S., and Badwal, S. P. S. (2017). Efficient conversion of CO_2 in solid oxide electrolytic cells with Pd doped perovskite cathode on ceria nanofilm interlayer. *J. CO_2 Util.* 17, 180–187. doi:10.1016/j.jcou.2016.11.014

Lackner, K. S. (2003). Climate change: a guide to CO_2 sequestration. *Science* 300, 1677–1678. doi:10.1126/science.1079033

Laguna-Bercero, M. A. (2012). Recent advances in high temperature electrolysis using solid oxide fuel cells: a review. *J. Power Sources* 203, 4–16. doi:10.1016/j.jpowsour.2011.12.019

Laguna-Bercero, M. A., Kilner, J. A., and Skinner, S. J. (2011). Development of oxygen electrodes for reversible solid oxide fuel cells with scandia stabilized zirconia electrolytes. *Solid State Ion.* 192, 501–504. doi:10.1016/j.ssi.2010.01.003

Leah, R. T., Bone, A., Hammer, E., Selcuk, A., Rahman, M., Clare, A., et al. (2017). Development progress on the Ceres power steel cell technology platform: further progress towards commercialization. *ECS Trans.* 78, 87. doi:10.1149/07801.0087ecst

Lee, J. G., Jeon, O. S., Hwang, H. J., Jang, J., Lee, Y., Hyun, S. H., et al. (2016). Durable and high-performance direct-methane fuel cells with coke-tolerant ceria-coated Ni catalysts at reduced temperatures. *Electrochim. Acta* 191, 677–686. doi:10.1016/j.electacta.2016.01.091

Lei, L., Liu, T., Fang, S., Lemmon, J. P., and Chen, F. (2017). The co-electrolysis of CO_2–H_2O to methane via a novel micro-tubular electrochemical reactor. *J. Mater. Chem.* 5, 2904–2910. doi:10.1039/c6ta10252b

Lessing, P. A. (2007). A review of sealing technologies applicable to solid oxide electrolysis cells. *J. Mater. Sci.* 42, 3465–3476. doi:10.1007/s10853-006-0409-9

Li, W., Wang, H., Shi, Y., and Cai, N. (2013). Performance and methane production characteristics of H_2O–CO_2 co-electrolysis in solid oxide electrolysis cells. *Int. J. Hydrog. Energy* 38, 11104–11109. doi:10.1016/j.ijhydene.2013.01.008

Livermore, S. J. A., Cotton, J. W., and Ormerod, R. M. (2000). Fuel reforming and electrical performance studies in intermediate temperature ceria-gadolinia-based SOFCs. *J. Power Sources* 86, 411–416. doi:10.1016/s0378-7753(99)00493-0

López, E. R., Dorado, F., and de Lucas-Consuegra, A. (2019). Electrochemical promotion for hydrogen production via ethanol steam reforming reaction. *Appl. Catal. B Environ.* 243, 355–364. doi:10.1016/j.apcatb.2018.10.062

Luo, Y., Shi, Y., Chen, Y., Li, W., Jiang, L., and Cai, N. (2020). Pressurized tubular solid oxide H_2O/CO_2 co-electrolysis cell for direct power-to-methane. *AIChE J.* 66, e16896.

Luo, Y., Wu, X.-Y., Shi, Y., Ghoniem, A. F., and Cai, N. (2018). Exergy analysis of an integrated solid oxide electrolysis cell-methanation reactor for renewable energy storage. *Appl. Energy* 215, 371–383. doi:10.1016/j.apenergy.2018.02.022

Mah, J. C. W., Muchtar, A., Somalu, M. R., and Ghazali, M. J. (2017). Metallic interconnects for solid oxide fuel cell: a review on protective coating and deposition techniques. *Int. J. Hydrogen Energy* 42, 9219–9229. doi:10.1016/j.ijhydene.2016.03.195

Mahato, N., Banerjee, A., Gupta, A., Omar, S., and Balani, K. (2015). Progress in material selection for solid oxide fuel cell technology: a review. *Prog. Mater. Sci.* 72, 141–337. doi:10.1016/j.pmatsci.2015.01.001

Makridis, S. (2017). Hydrogen storage and compression. arXiv:1702.06015 [Preprint]. Available at: https://arxiv.org/abs/1702.06015 (Accessed July 7, 2020).

Marina, O. A., and Pederson, L. R. (2008). Composite solid oxide fuel cell anode based on ceria and strontium titanate. Google Patents US7468218B2.

Mat, Z. A., Nadaraja, S. K., Zakaria, Z., Hassan, S. H. A., Kar, Y. B., Tan, C. Y., et al. (2019). Fabrication and characterization of YSZ/ScSZ bilayer electrolyte for intermediate temperature-solid oxide fuel cell (IT-SOFC) application. *Int. J. Integr. Eng.* 1, 201–208.

Mazloomi, S. K., and Sulaiman, N. (2012). Influencing factors of water electrolysis electrical efficiency. *Renew. Sustain. Energy Rev.* 16, 4257–4263. doi:10.1016/j.rser.2012.03.052

Mcdonagh, S., O'Shea, R., Wall, D. M., Deane, J. P., and Murphy, J. D. (2018). Modelling of a power-to-gas system to predict the levelised cost of energy of an advanced renewable gaseous transport fuel. *Appl. Energy* 215, 444–456. doi:10.1016/j.apenergy.2018.02.019

Mebrahtu, C., Krebs, F., Abate, S., Perathoner, S., Centi, G., and Palkovits, R. (2019). "CO_2 methanation: principles and challenges," in *Studies in surface science and catalysis* (Amsterdam, Netherlands: Elsevier).

Méndez, C. I., and Ancheyta, J. (2020). Modeling and control of a Fischer–Tropsch synthesis fixed-bed reactor with a novel mechanistic kinetic approach. *Chem. Eng. J.* 390, 124489. doi:10.1016/j.cej.2020.124489

Mills, G. A., and Steffgen, F. W. (1974). Catalytic methanation. *Catal. Rev.* 8, 159–210. doi:10.1080/01614947408071860

Monzón, H., and Laguna-Bercero, M. A. (2019). CO_2 and steam electrolysis using a microtubular solid oxide cell. *J. Phys. Energy* 2, 014005. doi:10.1088/2515-7655/ab4250

Murakami, K., Matsui, T., Kikuchi, R., Muroyama, H., and Eguchi, K. (2010). Activation of LSM electrode related to the potential oscillation under cathodic polarization. *J. Electrochem. Soc.* 157, B880–B884. doi:10.1149/1.3374407

Murugesan, P., Narayanan, S., and Manickam, M. (2020). "Photocatalytic conversion of carbon dioxide into hydrocarbons," in *Conversion of carbon dioxide into hydrocarbons* (Berlin, Germany: Springer).

Neofytidis, C., Ioannidou, E., Sygellou, L., Kollia, M., and Niakolas, D. K. (2019). Affecting the H_2O electrolysis process in SOECs through modification of NiO/GDC: experimental case of Au–Mo–Ni synergy. *J. Catal.* 373, 260–275. doi:10.1016/j.jcat.2019.04.002

Newell, R., Iler, S., and Raimi, D. (2018). Global energy outlook comparison methods: 2019 update. Resources for the Future, April, 26.

Nikolaidis, P., and Poullikkas, A. (2017). A comparative overview of hydrogen production processes. *Renew. Sustain. Energy Rev.* 67, 597–611. doi:10.1016/j.rser.2016.09.044

Paidar, M., Fateev, V., and Bouzek, K. (2016). Membrane electrolysis-history, current status and perspective. *Electrochim. Acta* 209, 737–756. doi:10.1016/j.electacta.2016.05.209

Pandiyan, A., Uthayakumar, A., Subrayan, R., Cha, S. W., and Krishna Moorthy, S. B. (2019). Review of solid oxide electrolysis cells: a clean energy strategy for hydrogen generation. *Nanomater. Energy* 8, 2–22. doi:10.1680/jnaen.18.00009

Park, B.-K., Zhang, Q., Liu, Q., Voorhees, P. W., and Barnett, S. A. (2019). *Understanding of solid oxide electrolysis cell degradation: the role of the electrode overpotential. Meeting abstracts*. Pennington, NJ: The Electrochemical Society, 1890.

Pesaran, A., Jaiswal, A., and Wachsman, E. D. (2019). "Bilayer electrolytes for low temperature and intermediate temperature solid oxide fuel cells: a review," in *Energy storage and conversion materials* (Croydon, UK: Royal Society of Chemistry), 1–41.

Peterson, D., and Miller, E. (2016). *Hydrogen production cost from solid oxide electrolysis*. Hinton, IA: United States Department of Energy.

Pham, T. T., Tu, H. P., Dao, T. D., To, T. D., Doan, D. C. T., and Dang, M. C. (2019). Fabrication of an anode functional layer for an electrolyte-supported solid oxide fuel cell using electrohydrodynamic jet printing. *Nanotechnology* 10, 015004. doi:10.1088/2043-6254/aafdab

Prabhukhot Prachi, R., Wagh Mahesh, M., and Gangal Aneesh, C. (2016). A review on solid state hydrogen storage material. *Adv. Energy Power* 4, 11.

Pu, T., Tan, W., Shi, H., Na, Y., Lu, J., and Zhu, B. (2016). Steam/CO_2 electrolysis in symmetric solid oxide electrolysis cell with barium cerate-carbonate composite electrolyte. *Electrochim. Acta* 190, 193–198. doi:10.1016/j.electacta.2015.12.220

Quandt, K., and Streicher, R. (1986). Concept and design of a 3.5 MW pilot plant for high temperature electrolysis of water vapor. *Int. J. Hydrogen Energy* 11, 309–315. doi:10.1016/0360-3199(86)90149-7

Rashid, M. M., AL Mesfer, M. K., Naseem, H., and Danish, M. (2015). Hydrogen production by water electrolysis: a review of alkaline water electrolysis, PEM water electrolysis and high temperature water electrolysis. *Int. J. Eng. Adv. Technol.* 4, 2249–8958.

Rashkeev, S. N., and Glazoff, M. V. (2012). Atomic-scale mechanisms of oxygen electrode delamination in solid oxide electrolyzer cells. *Int. J. Hydrogen Energy* 37, 1280–1291. doi:10.1016/j.ijhydene.2011.09.117

Raza, R., Zhu, B., Rafique, A., Naqvi, M. R., and Lund, P. (2020) Functional ceria-based nanocomposites for advanced low-temperature (300–600°C) solid oxide fuel cell: a comprehensive review. *Mater. Today Energy* 15, 100373. doi:10.1016/j.mtener.2019.100373

Rego de Vasconcelos, B., and Lavoie, J.-M. (2019). Recent advances in power-to-X technology for the production of fuels and chemicals. *Front. Chem.* 7, 392.

Renewables (2018). Analysis and forecast to 2023, France 2018, IEA.

Rönsch, S., Schneider, J., Matthischke, S., Schlüter, M., Götz, M., Lefebvre, J., et al. (2016). Review on methanation—From fundamentals to current projects. *Fuel* 166, 276–296. doi:10.1016/j.fuel.2015.10.111

Sahebdelfar, S., and Takht Ravanchi, M. (2015). Carbon dioxide utilization for methane production: a thermodynamic analysis. *J. Petrol. Sci. Eng.* 134, 14–22. doi:10.1016/j.petrol.2015.07.015

Santos, D. M. F., Sequeira, C. A. C., and Figueiredo, J. L. (2013). Hydrogen production by alkaline water electrolysis. *Quím. Nova* 36, 1176–1193. doi:10.1590/s0100-40422013000800017

Saracoglu, B. O., Ohunakin, O. S., Adelekan, D. S., Gill, J., Atiba, O. E., Okokpujie, I. P., et al. (2018). A framework for selecting the location of very large photovoltaic solar power plants on a global/supergrid. *Energy Rep.* 4, 586–602. doi:10.1590/s0100-40422013000800017.

Schmidt, O., Gambhir, A., Staffell, I., Hawkes, A., Nelson, J., and Few, S. (2017). Future cost and performance of water electrolysis: an expert elicitation study. *Int. J. Hydrog. Energy* 42, 30470–30492. doi:10.1016/j.ijhydene.2017.10.045

Schulz, H.. (1999). Short history and present trends of Fischer–Tropsch synthesis. *Appl. Catal. Gen.* 186, 3–12. doi:10.1016/s0926-860x(99)00160-x

Shaigan, N., Qu, W., Ivey, D. G., and Chen, W. (2010). A review of recent progress in coatings, surface modifications and alloy developments for solid oxide fuel cell ferritic stainless steel interconnects. *J. Power Sources* 195, 1529–1542. doi:10.1016/j.jpowsour.2009.09.069

Shi, X., Luo, Y., Li, W., Ni, M., and Cai, N. (2015). "Energy efficiencies in ASEAN region," in *Handbook of Clean Energy Systems* (Hoboken, NJ: Wiley), 1–19. doi:10.1002/9781118991978.hces146

Shin, T. H., Myung, J.-H., Verbraeken, M., Kim, G., and Irvine, J. T. S. (2015). Oxygen deficient layered double perovskite as an active cathode for CO_2 electrolysis using a solid oxide conductor. *Faraday Discuss.* 182, 227–239. doi:10.1039/c5fd00025d

Simakov, D. S. A., and Román-Leshkov, Y. (2018). Highly efficient methane reforming over a low-loading Ru/γ-Al_2O_3 catalyst in a Pd–Ag membrane reactor. *AIChE J.* 64, 3101–3108. doi:10.1002/aic.16094

Singh, V., Muroyama, H., Matsui, T., Hashigami, S., Inagaki, T., and Eguchi, K. (2015). Feasibility of alternative electrode materials for high temperature CO_2 reduction on solid oxide electrolysis cell. *J. Power Sources* 293, 642–648. doi:10.1016/j.jpowsour.2015.05.088

Smart, W., and Weissbart, J. (1967). Study of electrolytic dissociation of CO2–H2O using a solid oxide electrolyte, NASA CR-680.

Sridhar, K., and Vaniman, B. T. (1997). Oxygen production on Mars using solid oxide electrolysis. *Solid State Ion.* 93, 321–328. doi:10.1016/s0167-2738(96)00513-9

Tanaka, N. J. (2010). World energy outlook 2010, Beijing, China, November 17, 2010 (Paris, France: International Energy Agency).

Taylor, M., Tam, C., and Gielen, D. (2006). "Energy efficiency and CO_2 emissions from the global cement industry," in IEA-WBCSD workshop, Paris, September 4–5, 2006 (Paris, France: International Energy Agency), 61–67.

Theleritis, D., Souentie, S., Siokou, A., Katsaounis, A., and Vayenas, C. G. (2012). Hydrogenation of CO_2 over Ru/YSZ electropromoted catalysts. *ACS Catal.* 2, 770–780. doi:10.1021/cs300072a.

Tian, Y., Liu, Y., Wang, W., Jia, L., Pu, J., Chi, B., et al. (2020). High performance and stability of double perovskite-type oxide $NdBa_{0.5}Ca_{0.5}Co_{1.5}Fe_{0.5}O_{5+}$ as an oxygen electrode for reversible solid oxide electrochemical cell. *J. Energy Chem.* 43, 108–115. doi:10.1016/j.jechem.2019.08.010

Tietz, F., Sebold, D., Brisse, A., and Schefold, J. (2013). Degradation phenomena in a solid oxide electrolysis cell after 9,000 h of operation. *J. Power Sources* 223, 129–135. doi:10.1016/j.jpowsour.2012.09.061

Tucker, M. C. (2010). Progress in metal-supported solid oxide fuel cells: a review. *J. Power Sources* 195, 4570–4582. doi:10.1016/j.jpowsour.2010.02.035

Ulleberg, O. (2003). Modeling of advanced alkaline electrolyzers: a system simulation approach. *Int. J. Hydrogen Energy* 28, 21–33. doi:10.1016/s0360-3199(02)00033-2

Ursua, A., Gandia, L. M., and Sanchis, P. (2012). Hydrogen production from water electrolysis: current status and future trends. *Proc. IEEE* 100, 410–426. doi:10.1109/jproc.2011.2156750

Vøllestad, E., Strandbakke, R., Tarach, M., Catalán-Martínez, D., Fontaine, M.-L., Beeaff, D., et al. (2019). Mixed proton and electron conducting double perovskite anodes for stable and efficient tubular proton ceramic electrolysers. *Nat. Mater.* 18, 752–759. doi:10.1038/s41563-019-0388-2

Van Der Laan, G. P., and Beenackers, A. (1999). Kinetics and selectivity of the Fischer–Tropsch synthesis: a literature review. *Catal. Rev.* 41, 255–318. doi:10.1081/cr-100101170

Van Straelen, J., Geuzebroek, F., Goodchild, N., Protopapas, G., and Mahony, L. (2010). CO_2 capture for refineries, a practical approach. *Int. J. Greenh. Gas Con.* 4, 316–320. doi:10.1016/j.ijggc.2009.09.022

Vandenborre, H., Leysen, R., and Baetsle, L. (1980). Alkaline inorganic-membrane-electrolyte (IME) water electrolysis. *Int. J. Hydrog. Energy* 5, 165–171. doi:10.1016/0360-3199(80)90093-2

Varkaraki, E., Nicole, J., Plattner, E., Comninellis, C., and Vayenas, C. (1995). Electrochemical Promotion of IrO_2 catalyst for the gas phase combustion of ethylene. *J. Appl. Electrochem.* 5, 978–981. doi:10.1007/bf00241594

Verhelst, S., and Wallner, T. (2009). Hydrogen-fueled internal combustion engines. *Prog. Energy Combust. Sci.* 35, 490–527. doi:10.1016/j.pecs.2009.08.001

Vermeiren, P., Adriansens, W., Moreels, J., and Leysen, R. (1998). Evaluation of the Zirfon® separator for use in alkaline water electrolysis and Ni–H_2 batteries. *Int. J. Hydrog. Energy*. 23, 321–324. doi:10.1016/s0360-3199(97)00069-4

Virkar, A. V. (2010). Mechanism of oxygen electrode delamination in solid oxide electrolyzer cells. *Int. J. Hydrog. Energy* 35, 9527–9543. doi:10.1016/j.ijhydene.2010.06.058

Wang, K., Fang, Z., Huang, X., Feng, W., Wang, Y., Wang, B., et al. (2017). Enhanced selectivity of methane production for photocatalytic reduction by the piezoelectric effect. *Chem. Commun.* 53, 9765–9768. doi:10.1039/c7cc05112c

Wang, L., Pérez-Fortes, M., Madi, H., Diethelm, S., Herle, J. V., and Maréchal, F. (2018). Optimal design of solid-oxide electrolyzer based power-to-methane systems: a comprehensive comparison between steam electrolysis and co-electrolysis. *Appl. Energy* 211, 1060–1079. doi:10.1016/j.apenergy.2017.11.050

Wang, L., Chen, M., Küngas, R., Lin, T.-E., Diethelm, S., Maréchal, F., et al. (2019). Power-to-fuels via solid-oxide electrolyzer: operating window and techno-economics. *Renew. Sustain. Energy Rev.* 110, 174–187. doi:10.1016/j.rser.2019.04.071

Wang, S., Inoishi, A., Hong, J.-E., Ju, Y.-W., Hagiwara, H., Ida, S., et al. (2013). Ni–Fe bimetallic cathodes for intermediate temperature CO_2 electrolyzers using a $La_{0.9}Sr_{0.1}Ga_{0.8}Mg_{0.2}O_3$ electrolyte. *J. Mater. Chem. A* 1, 12455–12461. doi:10.1039/c3ta11863k

Wang, S., Tsuruta, H., Asanuma, M., and Ishihara, T. (2015). Ni–Fe–La(Sr)Fe(Mn)O_3 as a new active cermet cathode for intermediate-temperature CO_2 electrolysis using a $LaGaO_3$-based electrolyte. *Adv. Energy Mater.* 5, 1401003. doi:10.1002/aenm.201401003

Wang, Y., Li, W., Ma, L., Li, W., and Liu, X. (2019). Degradation of solid oxide electrolysis cells: phenomena, mechanisms, and emerging mitigation strategies—a review. *J. Mater. Sci. Technol.* 55, 35–55. doi:10.1016/j.jmst.2019.07.026

Wang, Y., Liu, T., Lei, L., and Chen, F. (2017). High temperature solid oxide H_2O/CO_2 co-electrolysis for syngas production. *Fuel Process. Technol.* 161, 248–258. doi:10.1016/j.fuproc.2016.08.009

Wang, Y.-P., Gao, J.-T., Chen, W., Li, C.-X., Zhang, S.-L., Yang, G.-J., et al. (2020). Development of ScSZ electrolyte by very low pressure plasma spraying for high-performance metal-supported SOFCs. *J. Therm. Spray Technol.* 29, 223–231. doi:10.1007/s11666-019-00970-1

Wei, L., Zhang, J., Yu, F., Zhang, W., Meng, X., Yang, N., et al. (2019). A novel fabrication of yttria-stabilized-zirconia dense electrolyte for solid oxide fuel cells by 3D printing technique. *Int. J. Hydrog. Energy* 44, 6182–6191. doi:10.1016/j.ijhydene.2019.01.071

Wei, W., and Jinlong, G. (2011). Methanation of carbon dioxide: an overview. *Front. Chem. Sci. Eng.* 5, 2–10. doi:10.1007/s11705-010-0528-3

Xie, K., Zhang, Y., Meng, G., and Irvine, J. T. S. (2011). Direct synthesis of methane from CO_2/H_2O in an oxygen-ion conducting solid oxide electrolyser. *Energy Environ. Sci.* 4, 2218–2222. doi:10.1039/c1ee01035b

Xie, Y., Xiao, J., Liu, D., Liu, J., and Yang, C. (2015). Electrolysis of carbon dioxide in a solid oxide electrolyzer with silver-gadolinium-doped ceria cathode. *J. Electrochem. Soc.* 162, F397–F402. doi:10.1149/2.0501504jes

Xu, W., and Scott, K. (2010). The effects of ionomer content on PEM water electrolyser membrane electrode assembly performance. *Int. J. Hydrog. Energy* 35, 12029–12037. doi:10.1016/j.ijhydene.2010.08.055

Yang, G., Yu, S., Kang, Z., Dohrmann, Y., Bender, G., Pivovar, B. S., et al. (2019). A novel PEMEC with 3D printed non-conductive bipolar plate for low-cost hydrogen production from water electrolysis. *Energy Conv. Manag.* 182, 108–116. doi:10.1016/j.enconman.2018.12.046

Yang, L., Xie, K., Wu, L., Qin, Q., Zhang, J., Zhang, Y., et al. (2014). A composite cathode based on scandium doped titanate with enhanced electrocatalytic activity towards direct carbon dioxide electrolysis. *Phys. Chem. Chem. Phys.* 16, 21417–21428. doi:10.1039/c4cp02229g

Yang, X., and Irvine, J. T. S. (2008). $(La_{0.75}Sr_{0.25})_{0.95}Mn_{0.5}Cr_{0.5}O_3$ as the cathode of solid oxide electrolysis cells for high temperature hydrogen production from steam. *J. Mater. Chem.* 18, 2349–2354. doi:10.1039/b800163d

Ye, X.-F., Wen, Y. B., Yang, S. J., Lu, Y., Luo, W. H., Wen, Z. Y., et al. (2017). Study of $CaZr_{0.9}In_{0.1}O_{3-\delta}$ based reversible solid oxide cells with tubular electrode supported structure. *Int. J. Hydrog. Energy* 42, 23189–23197. doi:10.1016/j.ijhydene.2017.07.195

Yentekakis, I. V., and Bebelis, S. (1992). Study of the NEMCA effect in a single-pellet catalytic reactor. *J. Catal.* 137, 278–283. doi:10.1016/0021-9517(92)90157-D

Yentekakis, I. V., Jiang, Y., Neophytides, S., Bebelis, S., and Vayenas, C. G. (1995). Catalysis, electrocatalysis and electrochemical promotion of the steam reforming of methane over Ni film and Ni-YSZ cermet anodes. *Ionics* 1, 491–498. doi:10.1007/bf02375296

Yentekakis, I. V., Moggridge, G., Vayenas, C., and Lambert, R. (1994). *In situ* controlled promotion of catalyst surfaces via NEMCA: the effect of Na on the Pt-catalyzed CO oxidation. *J. Catal.* 146, 292–305. doi:10.1016/0021-9517(94)90033-7

Yu, J., Men, H. J., Qu, Y. M., and Tian, N. (2020). Performance of Ni–Fe bimetal based cathode for intermediate temperature solid oxide electrolysis cell. *Solid State Ion.* 346, 115203. doi:10.1016/j.ssi.2019.115203

Yue, X., and Irvine, J. T. S. (2012). Alternative cathode material for CO_2 reduction by high temperature solid oxide electrolysis cells. *J. Electrochem. Soc.* 159, F442–F448. doi:10.1149/2.040208jes

Zhang, Y.-Q., Li, J.-H., Sun, Y.-F., Hua, B., and Luo, J.-L. (2016). Highly active and redox-stable Ce-doped LaSrCrFeO-based cathode catalyst for CO_2 SOECs. *ACS Appl. Mater. Interfaces* 8, 6457–6463. doi:10.1021/acsami.5b11979

Zheng, Y., Chen, T., Li, Q., Wu, W., Miao, H., Xu, C., et al. (2014). Achieving 360 NL h^{-1} hydrogen production rate through 30-cell solid oxide electrolysis stack with LSCF-GDC composite oxygen electrode. *Fuel Cells* 14, 1066–1070. doi:10.1002/fuce.201400051

Zheng, Y., Wang, J., Yu, B., Zhang, W., Chen, J., Qiao, J., et al. (2017). A review of high temperature co-electrolysis of H_2O and CO_2 to produce sustainable fuels using solid oxide electrolysis cells (SOECs): advanced materials and technology. *Chem. Soc. Rev.* 46, 1427–1463. doi:10.1039/c6cs00403b

Zhigachev, A. O., Zhigacheva, D. V., and Lyskov, N. V. (2019). Influence of yttria and ytterbia doping on phase stability and ionic conductivity of ScSZ solid electrolytes. *Mater. Res. Express* 6, 105534. doi:10.1088/2053-1591/ab3ed0

Zhou, Y., Zhou, Z., Song, Y., Zhang, X., Guan, F., Lv, H., et al. (2018). Enhancing CO_2 electrolysis performance with vanadium-doped perovskite cathode in solid oxide electrolysis cell. *Nanomater. Energy* 50, 43–51. doi:10.1016/j.nanoen.2018.04.054

Zhu, W. Z., and Deevi, S. C. (2003a). A review on the status of anode materials for solid oxide fuel cells. *Mater. Sci. Eng.* 362, 228–239. doi:10.1016/s0921-5093(03)00620-8

Zhu, W. Z., and Deevi, S. C. (2003b). Development of interconnect materials for solid oxide fuel cells. *Mater. Sci. Eng.* 348, 227–243. doi:10.1016/s0921-5093(02)00736-0

Zhu, X., Li, S., Shi, Y., and Cai, N. (2019). Recent advances in elevated-temperature pressure swing adsorption for carbon capture and hydrogen production. *Prog. Energy Combust. Sci.* 75, 100784. doi:10.1016/j.pecs.2019.100784

Conflict of Interest: The authors declare that the research was conducted in the absence of any commercial or financial relationships that could be construed as a potential conflict of interest.

frontiers in Energy Research

REVIEW
published: 25 September 2020
doi: 10.3389/fenrg.2020.00191

Review of Power-to-X Demonstration Projects in Europe

Christina Wulf, Petra Zapp and Andrea Schreiber*

Institute of Energy and Climate Research – Systems Analysis and Technology Evaluation, Forschungszentrum Jülich, Jülich, Germany

At the heart of most Power-to-X (PtX) concepts is the utilization of renewable electricity to produce hydrogen through the electrolysis of water. This hydrogen can be used directly as a final energy carrier or it can be converted into, for example, methane, synthesis gas, liquid fuels, electricity, or chemicals. Technical demonstration and systems integration are of major importance for integrating PtX into energy systems. As of June 2020, a total of 220 PtX research and demonstration projects in Europe have either been realized, completed, or are currently being planned. The central aim of this review is to identify and assess relevant projects in terms of their year of commissioning, location, electricity and carbon dioxide sources, applied technologies for electrolysis, capacity, type of hydrogen post-processing, and the targeted field of application. The latter aspect has changed over the years. At first, the targeted field of application was fuel production, for example for hydrogen buses, combined heat and power generation, and subsequent injection into the natural gas grid. Today, alongside fuel production, industrial applications are also important. Synthetic gaseous fuels are the focus of fuel production, while liquid fuel production is severely under-represented. Solid oxide electrolyzer cells (SOECs) represent a very small proportion of projects compared to polymer electrolyte membranes (PEMs) and alkaline electrolyzers. This is also reflected by the difference in installed capacities. While alkaline electrolyzers are installed with capacities between 50 and 5000 kW (2019/20) and PEM electrolyzers between 100 and 6000 kW, SOECs have a capacity of 150 kW. France and Germany are undertaking the biggest efforts to develop PtX technologies compared to other European countries. On the whole, however, activities have progressed at a considerably faster rate than had been predicted just a couple of years ago.

Keywords: Power-to-Gas, Power-to-X, hydrogen, methanation, electrolysis, R&D project, review

OPEN ACCESS

Edited by:
Luis M. Romeo,
University of Zaragoza, Spain

Reviewed by:
Ligang Wang,
École Polytechnique Fédérale de Lausanne, Switzerland
Xiao-Yu Wu,
University of Waterloo, Canada
Manuel Bailera,
University of Zaragoza, Spain

****Correspondence:***
Christina Wulf
c.wulf@fz-juelich.de

Specialty section:
This article was submitted to Hydrogen Storage and Production, a section of the journal Frontiers in Energy Research

Received: *06 April 2020*
Accepted: *17 July 2020*
Published: *25 September 2020*

Citation:
Wulf C, Zapp P and Schreiber A (2020) Review of Power-to-X Demonstration Projects in Europe. Front. Energy Res. 8:191. doi: 10.3389/fenrg.2020.00191

Abbreviations: CO_2, carbon dioxide; H_2, hydrogen; H_2O, water; ADEME, Agence de l'environnement et de la maîtrise de l'énergie; CCU, carbon capture and use; CCS, carbon capture and storage; CHP, combined heat and power; CUTE, Clean Urban Transport for Europe; DAC, direct air capture; DME, dimethyl ether; DVGW, German Technical and Scientific Association for Gas and Water; DWV, German Hydrogen and Fuel-Cell Association; EU, European Union; IEA, International Energy Agency; IPCEI, Important Project of Common European interest; MWT, municipal waste treatment; n.s., not specified; OME, polyoxymethylene dimethyl ether; PEM, polymer electrolyte membrane; PtG, Power-to-Gas; PtX, Power-to-X; R&D, research & development; RE, renewable energy; SOEC, solid oxide electrolyzer cell; SPE, solid polymeric electrolyte; UK, United Kingdom; VRE, variable renewable energy.

INTRODUCTION

Future energy systems with high shares of renewable energies and aims to achieve the goals set out in the Paris Agreement will place a high demand on energy storage systems. Furthermore, electricity will be increasingly used in the heat, transport, and industry sectors, i.e., sector coupling (e.g., Ram et al., 2019), which will – to some extent – require transformation into other energy forms.

Electricity can be used directly in other sectors, for example with battery electric vehicles, or it can be processed into other energy carriers that are more versatile in their use and can be better stored. Such concepts are known as Power-to-X (PtX), since electrical energy is transformed into different products. A key stage of this concept is the production of hydrogen by water splitting in an electrolyzer. Often, hydrogen or further processed methane are the final products. These concepts are referred to as Power-to-Gas (PtG), a name often used synonymously with all PtX applications.

In **Figure 1**, an overview of basic PtX process chains is given. The focal point of most pathways is the electrolysis process to produce hydrogen. The required electricity often comes from variable renewable energy (VRE) generation, for example wind or photovoltaics, either directly or in the form of certificates (e.g., Pearce, 2015; Bauer, 2016; BIGH2IT, 2017; Büssers, 2019), and less frequently from the grid. The use of grid electricity, however, often contradicts the original idea behind PtX – to use and store renewable energy (RE) – as electricity produced from fossil fuels still makes up a considerable share of most national grids. Projects using grid electricity either focus on hydrogen production or processing (Moser et al., 2018), or they aim to provide peak shaving electricity to the grid (Hänel et al., 2019).

If further processing is emphasized, carbon dioxide is a necessary feedstock to process hydrogen into other energy carriers or industrial products such as methane or chemicals (Hendriksen, 2015; MefCO2, 2019). To foster a climate-friendly energy system, non-fossil fuel carbon dioxide sources should, of course, be favored. However, in some research projects, fossil carbon is used due to it being easily accessible from existing test facilities for carbon capture and use (CCU; Moser et al., 2018). In future, fossil fuel-based power plants will be less, or not at all, available. The knowledge gained from such projects, however, can be used for other power plants, such as municipal waste treatment (MWT). Other carbon dioxide sources include industrial processes [(CCU P2C Salzbergen) BMWi, 2019], the anaerobic digestion of biomass (e.g., Rubio et al., 2016; Sveinbjörnsson and Münster, 2017), direct air capture (DAC; BMBF, 2018), and other biogenic sources.

Alongside methanation, other options for hydrogen-based fuels are methanol, Fischer–Tropsch diesel (BMBF, 2018), or dimethyl ether (DME; Moser et al., 2018). Another possibility is the production of synthesis gas, a mixture of hydrogen and carbon monoxide, in a reversed water–gas shift reaction or co-electrolysis (Andika et al., 2018; Wang et al., 2019). This technology splits water electrochemically and simultaneously produces synthesis gas from the hydrogen and the added carbon dioxide in a single process.

There is a diverse range of applications for hydrogen or hydrogen-based products. Hydrogen and fuels can be used in mobility applications (HyFLEET:Cute, 2009), for re-electrification in combined heat and power (CHP) plants (Exytron, 2019), or in industrial applications, for example refineries (H&R, 2017) or steel production [H2Stahl (BMWi, 2019)]. Furthermore, hydrogen can substitute fossil fuel-based feedstocks in the chemical industry [(CCU P2C Salzbergen) BMWi, 2019].

Another way to use electricity across multiple sectors is through direct conversion into heat, which is a standard application in many cases, for example heat pumps. In industrial applications, an increasing number of electrode boilers have been installed over the last few years. However, an analysis of this kind of technology is beyond the scope of this article.

As the number of PtX projects has increased, so too has the number of reviews. A first overview of PtX projects was published by Gahleitner (2013). It focused on global projects from laboratory scale to demonstration plants. Gahleitner identified 64 projects, 48 of which included a detailed assessment. Bailera et al. (2017) analyzed lab, pilot, and demonstration projects on a global scale. They identified 66 projects, highlighting 23 of them and focusing on catalytic methanation. A first overview focusing on Europe was given in an earlier publication by Wulf et al. (2018). We explicitly excluded lab projects, and still found 128 projects in 16 countries. One year later, Thema et al. (2019) published a review with 153 projects from 22 different countries on a global scale, also including lab projects and older projects dating back to 1988. They also included a cost and capacity projection for installed electrolyzers until 2050 as well as geospatial data. Although the authors included an analysis of the countries involved, there was no detailed discussion on this subject. Based on Task 38 of the International Energy Agency's (IEA) Hydrogen Technology Collaboration Programme, Chehade et al. (2019) performed a similar analysis and identified 192 PtX demonstration projects in 32 countries. The authors focused on the different fields of applications and objectives (economic or non-economic) and various hydrogen storage technologies, and also assessed the efficiency of the electrolyzers. They did not include projects that have only been projected or announced. This confirms the conditions for previous years, but does not reflect current or even future perspectives.

Although these articles offer a good overview of the development of PtX technologies, they stopped collecting data in early 2018 (Chehade et al., 2019) and late 2018 (Thema et al., 2019), respectively. However, in 2019 and at the beginning of 2020, several multi-MW projects were announced, which offer a perspective for the future. Lab-scale projects as well as projects initiated before 2000 have been excluded from this article to focus on recent developments. Furthermore, all previous reviews show that Europe has been the leading region for these technology concepts for several years now. Therefore, only European projects are considered here. We also discuss qualitative trends in terms of certain countries or technological features using examples of different projects. This overview clearly shows how the scope of a review can influence the results. Chehade et al. (2019) provided a review on a global scale, which also included lab-scale projects.

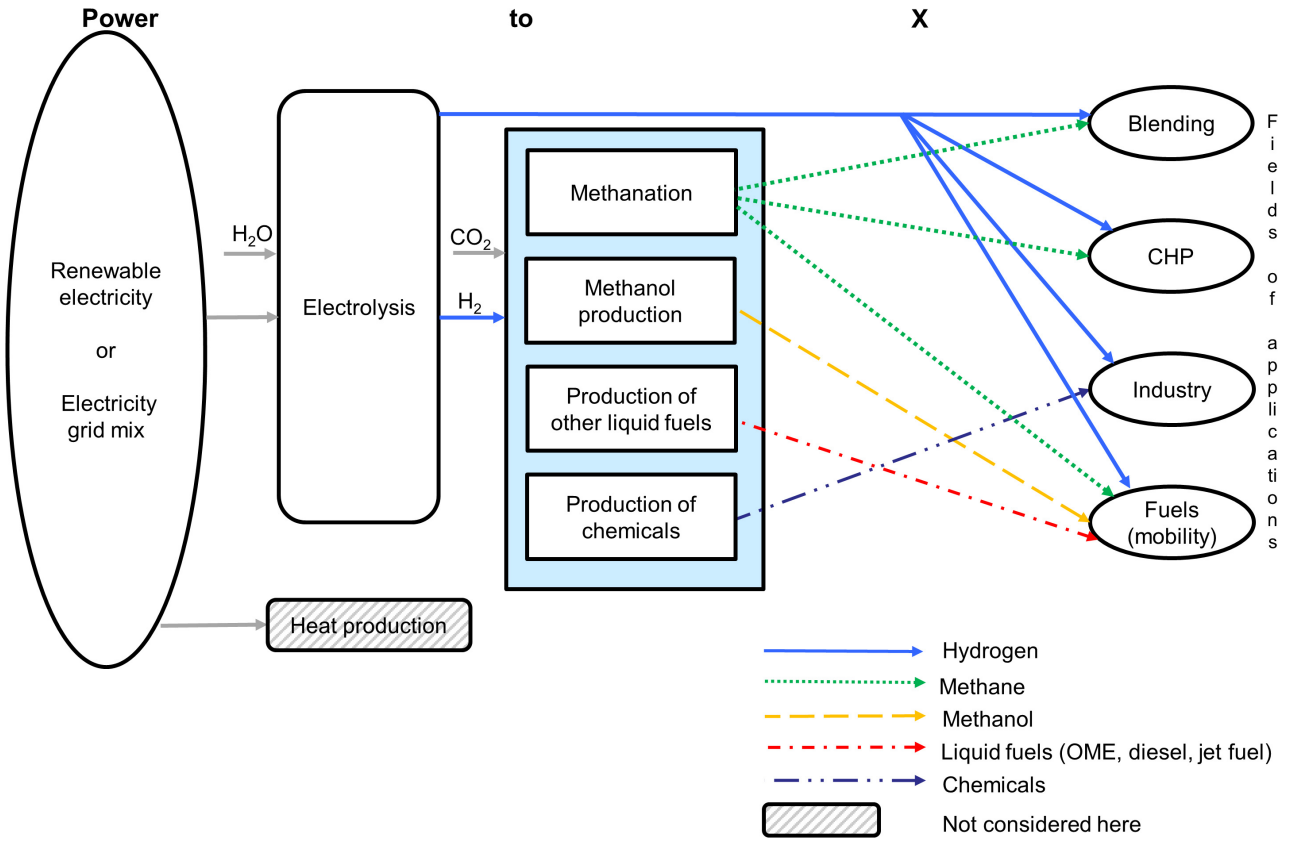

FIGURE 1 | Overview of Power-to-X process chains based on hydrogen. CO_2, carbon dioxide; H_2, hydrogen; H_2O, water; CHP, combined heat and power; OME, polyoxymethylene dimethyl ether.

For the years 2010–2014, they identified 78 eligible projects, while only 37 are taken into account here. As 80% of the projects they identified are European, the consideration of lab-scale projects can be seen as the major difference.

METHODOLOGY

Power-to-X projects were identified through extensive internet research. Many sources took the form of press releases from companies announcing a new project. Frequently used publications included *BWK Das Energie-Fachmagazin*, the German Hydrogen and Fuel-Cell Association (DWV) Mitteilungen (membership magazine), the project database of the German Energy Agency (dena, 2020), and the German Technical and Scientific Association for Gas and Water (DVGW, 2019). Non-German literature reporting frequently about new PtX projects is – to the best of our knowledge – not available. While these sources provided an initial indication of a new project, we also sought out announcements of each project in English. The same applies for publications in French, Danish, and other European languages, although this was not always available.

To qualify as a project for this publication, the project must be located in Europe, have been initiated after the year 2000, and have a technology readiness level of five or higher (EU, 2014). The other review articles mentioned in the introduction were used to validate the data before 2018.

The analyzed topics can be arranged into three categories:

- General information: location (country base), year of commissioning (electrolyzer), out of operation (yes/no).
- Technical specifications: power and carbon dioxide supply, type of electrolyzer, capacity of electrolyzer, type of hydrogen processing (e.g., catalytic methanation).
- Field of application: gaseous or liquid fuels, industrial application, heat and power generation, blending into the natural gas grid.

RESULTS AND DISCUSSION

For the analysis, 220 projects that meet the set criteria were identified by June 2020. Twenty different countries are currently undertaking PtX projects, with an increasing number becoming interested in these technological concepts. A complete list of these projects can be found in the **Supplementary Material**. This section is structured into three sections according to the categories mentioned above. The first section provides an overview of the historical development of PtX in the different countries and discusses how they use different strategies. The

second section features a discussion of current and planned installed electrolyzer technologies as well as their capacities. The third and final section takes a look at the design of the X phase and which electrolyzer technology is used for what purpose.

General Information

From **Figure 2**, it can be seen that 2018 was the year with the most commissioned projects so far in Europe. In the years to come, fewer projects will be initiated, but the data also shows that installed capacity is still growing rapidly. It also seems that PtX development is following a wave-like pattern with peaks in 2015, 2018, and 2020. Experience has shown, however, that some of the projects scheduled for 2020 will be delayed to 2021 due to technical difficulties and delayed approvals as well as the special circumstances surrounding the global COVID-19 crisis. The year 2024 is also expected to stand out, due to a situation specific to Germany. It had been assumed that the regulatory sandboxes (*Reallabore*) funded by the German Federal Ministry for Economic Affairs and Energy[1] that can be classified as PtX projects (ten out of 20) would be commissioned in 2024, if they were yet to have published a commissioning year. Furthermore, the three HyPerformer projects (NOW, 2019) are expected to begin in 2025, which is also a conservative estimation since these projects received their notification of funding in December 2019. It has been generally assumed that commissioning takes place in the penultimate year of the project, based on the experience of earlier projects.

Twenty European countries are engaged in PtX projects. Furthermore, one pan-European project including the Netherlands, Denmark, and Germany is currently being planned, in which hydrogen is to be produced offshore in the North Sea right next to wind parks with connections to bordering countries (NSWPH, 2019). The country with the most PtX projects is Germany, representing 44% of all identified projects. In the first few years, PtX projects were developed in several different countries. Since 2011, however, Germany has started to increase its interest in this technology, with at least four new projects per year and 13 new projects in 2020.

[1]https://www.bmwi.de/Redaktion/EN/Dossier/regulatory-test-beds-testing-environments-for-innovation-and-regulation.html

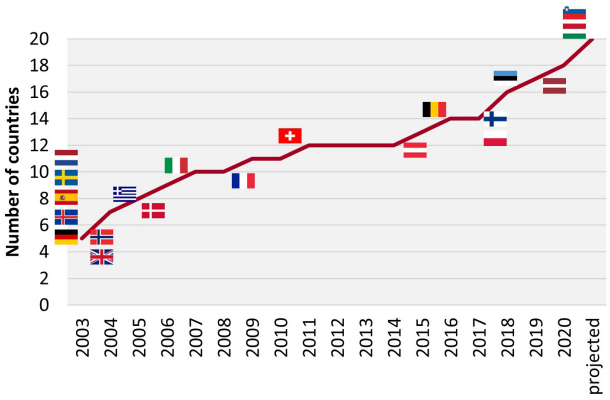

FIGURE 3 | Historical development of the involvement of countries in Power-to-X projects.

The interest of different countries in PtX projects has been growing constantly over the last few years (see **Figure 3**). However, in the years to come, the only new countries to launch PtX projects will be Hungary and Slovenia.

Figure 4 shows the installed capacities of European countries in the last five years and the next five years. As expected, due to its large number of projects (**Figure 2**), Germany has had the largest installed capacity over the last five years and this is set to increase significantly in the next five years. Demonstration projects have also been realized in several other countries. However, it appears that in the future, these technologies will be implemented by fewer countries but with a higher intensity.

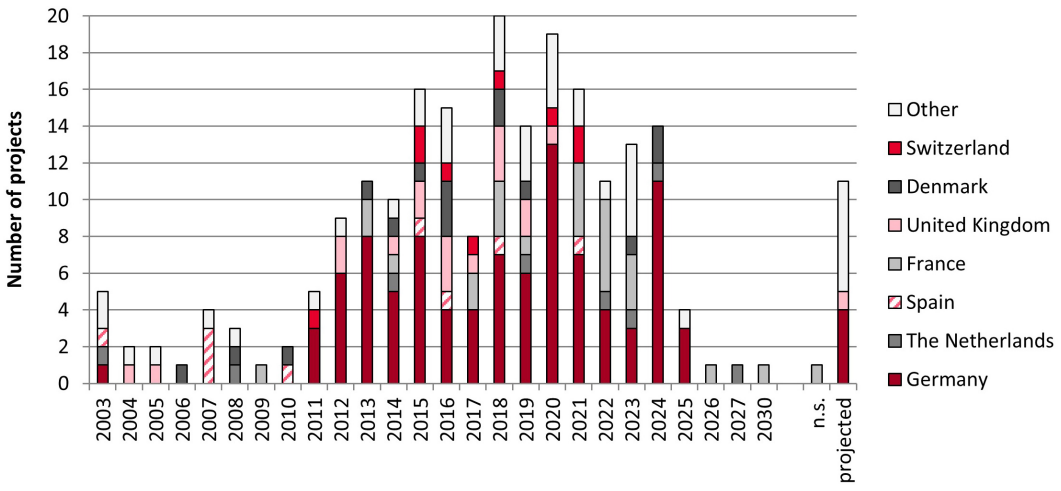

FIGURE 2 | Historical development of Power-to-X projects commissioned in Europe with regard to the countries involved; year for commissioning not specified (n.s.).

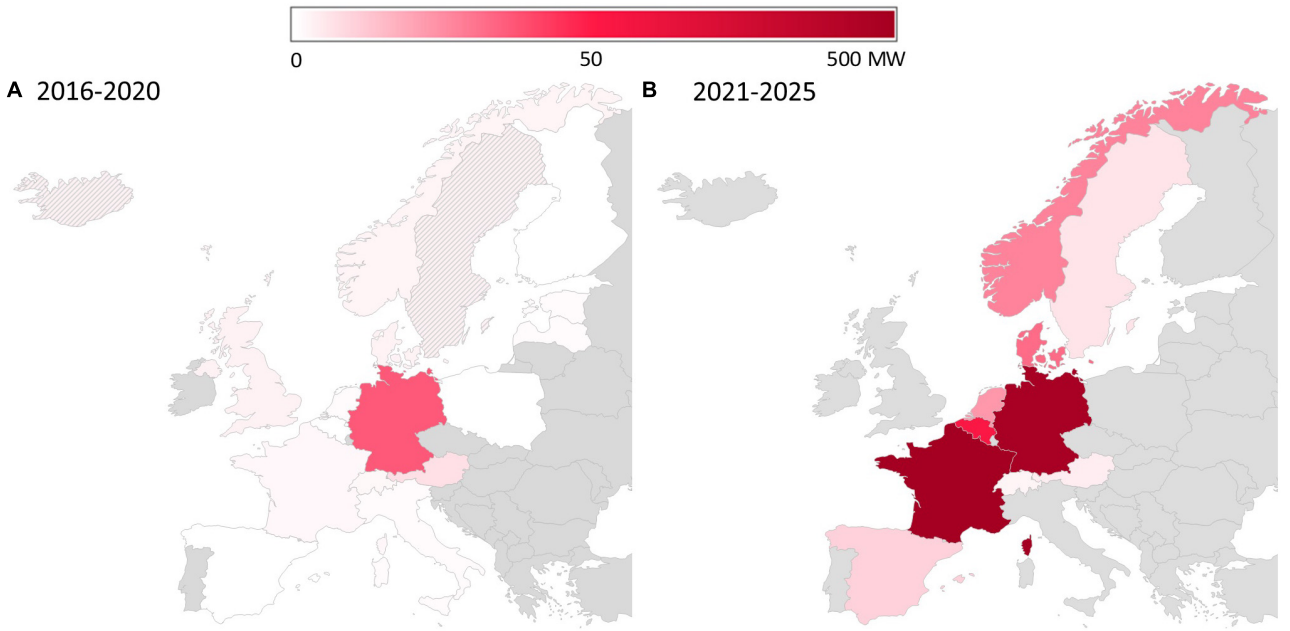

FIGURE 4 | Newly installed capacities of Power-to-X projects in Europe, **(A)** commissioned between 2016 and 2020, **(B)** planned for 2021–2025. Shaded countries: installed capacity not specified, gray countries: no Power-to-X projects.

Germany, France, the Netherlands, Belgium, and Denmark stand out in particular. Over the next five years, 494 MW of installed electrolyzer capacity is scheduled in Germany. In addition, there are plans for seven more projects, which have not yet specified their electrolyzer capacity, but which will likely also be on the multi-MW scale. In France, 514 MW are projected to be installed in this time period. It is also worth mentioning that in France, this capacity will largely be achieved by two projects alone. The developer H2V PRODUCT (Meillaud, 2019; H2V, 2020) is set to install 500 MW of capacity. In contrast, seven hydrogen projects for fuel provision (hydrogen refueling stations) funded by ADEME (Agence de l'environnement et de la maîtrise de l'énergie) are rather minor (around 1 MW) (FuelCellsWorks, 2020a). In Germany, 28 projects are scheduled for this period. Here, the main drivers of installed capacity are the aforementioned regulatory sandboxes [6 of the 10 projects will have a capacity of 220 MW (BMWi, 2019]). Surprisingly, the United Kingdom has only announced one new PtX project (ITM, 2020a), despite having been relatively active in the past. Furthermore, the United Kingdom's Committee on Climate Change has called for an increased national effort when it comes to using hydrogen in industry and other sectors (Stark et al., 2019). One reason for this might be that in the United Kingdom, hydrogen production from steam methane reforming, which is connected to carbon capture and storage/use in the long term, is being discussed (Bottrell Hayward, 2020). Belgium is an example of a country that has shown little interest in this kind of technology (one project with only 130 kW installed capacity), but is now announcing relatively major projects (one with a capacity of 25 MW and another with a capacity of 50 MW). In Spain, a similar development can be observed. In the 2000s, small projects were developed, whereas the target is now for capacities on the multi-MW scale. Eastern European countries rarely invest in PtX projects. Only Poland, Estonia, and Latvia currently have active projects. Latvia and Estonia are following the same pathway as the countries involved in the Clean Urban Transport for Europe (CUTE) project (Binder et al., 2006) in 2003, initiating their hydrogen activities with an EU project [H2Nodes (FuelCellsWorks, 2020b)] for fuel cell buses. However, the EU has established a new funding scheme – Important Project of Common European Interest (IPCEI) – that aims to support countries that are not yet active in PtX development. Furthermore, an IPCEI on hydrogen is currently under development and aims to close the gap between research and development projects and commercialization (Hydrogen for Climate Action, 2020). The first projects should be approved by the end of 2020. The central idea behind many of these projects is to produce hydrogen (further processing is not yet planned) in sunny and windy regions, to use some of the hydrogen for local mobility applications, and to export the rest of the hydrogen to other countries.

If available, data about the decommissioning of the projects were also gathered (see **Supplementary Material**). However, such data are hard to come by and too incomplete to allow for a meaningful analysis. In some R&D projects, even the installed technologies are passed on to a follow-up project, for example MefCO$_2$ and FReSMe (2017).

Technical Specifications

The analyzed technical specifications include a power and carbon dioxide supply, electrolyzer types, and capacities, as well as technologies for hydrogen processing.

Energy Sources

Energy sources have a major impact on PtX. One argument for PtX is the storage of intermittent energy sources of VRE. Almost half (105) of the projects consider a supply by direct RE technologies, such as wind, photovoltaics, geothermal, or hydropower plants. There is no clear trend as to which renewable technology is preferred, neither in connection to specific electrolyzer types, nor to capacity sizes, nor to countries. Twelve projects describe their PtX benefit as being able to store surplus energy from renewables, which would be retailed otherwise. This line of argumentation can be mainly seen with German projects. It remains uncertain what the real amount of surplus energy is and what its availability will look like in the future, but the key message is to use RE sources. This is especially true for projects in countries with a high share of electricity produced from fossil fuels as well as all planned projects that rely on certificates (Hulshof et al., 2019). However, almost 13% (28) of the projects do not include an energy source. They either use electricity from the national grid (whose share of renewables might be quite low) or do not specify the energy source. In particular, during the last decade, Germany, Denmark, and the United Kingdom have had several projects, in which the demonstrator was connected to the grid. One project explicitly focuses on the peak shaving of the national grid (Hänel et al., 2019). Most other projects focus on the feasibility of hydrogen production or processing for different applications, rather than demand side management or the demonstration of VRE electricity storage potential. **Figure 5** shows the development of different energy source options, making a distinction between direct RE technologies, certificates for RE electricity, surplus RE electricity, and the national grid (not specified sources are included here for simplification).

Considering the countries with the highest number of projects (Germany, France, Denmark, and United Kingdom), no preference for a specific type of electricity supply can be identified. However, there is a clear trend toward including RE sources in projects.

Carbon Dioxide Source

About one third of the projects (70) process hydrogen into other gases, liquid fuels, or chemicals (see section "Hydrogen processing"), predominantly in Germany (38). The capture of the required carbon dioxide is also included in the PtX project in the majority of cases (60). The sources of the carbon dioxide, however, vary from project to project. To underline the notion of non-fossil carbon sources, the majority (27) of projects obtain carbon dioxide from biogas or biomass plants. In Iceland, the country-specific option of geothermal carbon dioxide is used. A small number of projects (seven) obtain carbon dioxide from nearby industry sites or even lignite power plants. These large point sources already have capture technologies installed and are seeking utilization options (CCU), since storage options (CCS) are not currently available for these sources. This might be a temporary solution, as large industrial carbon dioxide emitters, such as the steel industry in the case of Sweden, and especially the electricity generation industry will have to change to a low carbon future. However, right now, they can provide carbon dioxide in considerable amounts [e.g., 7.2 t CO_2/day (Moser et al., 2018)]. These projects provide an insight into the handling and purification requirements of future industrial carbon dioxide sources, which will still exist due to process-related reactions, such as for the cement industry. Projects from the Exytron Group (Schirmer, 2020) require one filling of carbon dioxide from an external source, with carbon dioxide then being captured and recycled from CHP plants using synthetic methane produced through PtX. In addition, carbon dioxide emissions will be emitted in the future during wastewater treatment and waste incineration. Therefore, nine projects include such facilities as a carbon dioxide source. An industry-independent source is provided by DAC. Ambient air generally flows through a filter where either adsorption, absorption, or mineralization removes carbon dioxide from air. Due to the very low carbon dioxide content of air and its resulting high energy demand (heat and electricity), this concept has proven controversial (Fasihi et al., 2019).

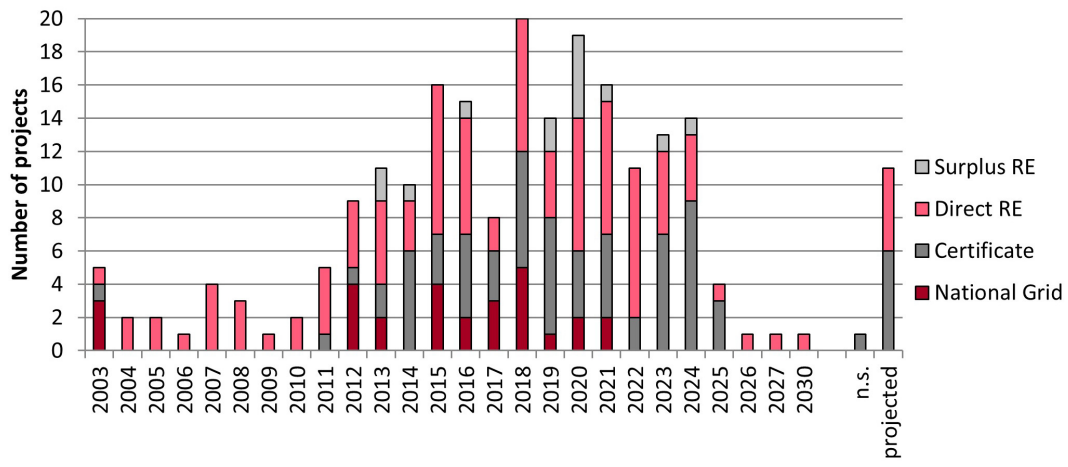

FIGURE 5 | Historical development of Power-to-X projects with regard to electricity supply. RE, renewable energy.

Nevertheless, this Climeworks AG technology is included in seven out of eight projects, often in combination with solid oxide electrolyzer cell (SOEC) electrolyzers using the synergy of thermal integration in the concept.

Electrolyzer Type and Capacity

Alkaline electrolyzers have been used in previous projects and will continue to be used in future projects, thus indicating the constant development of this technology. Since 2015, polymer electrolyte membrane (PEM) electrolyzers have gained high shares of the market due to their good partial load range and dynamic behavior. Four projects aim to compare these two technologies and integrate both into their system design. Several attempts have been made to use SOECs in PtX projects, but this technology remains at a much lower technology readiness level. A more uncommon technology is the alkaline solid polymer electrolyte electrolyzer, which is a hybrid between a PEM and an alkaline electrolyzer. This technology was used in three projects. However, the installed capacities are rather small and future demonstration projects using this technology have yet to be announced. From 2022 onward, the share of projects with no dedicated electrolyzer technology is set to increase, which is understandable, since it has not yet been decided which technology is used. Unfortunately, over the past few years, the electrolyzer technology used has not been specified, which results in a total of 24% of the projects with no information about the technology.

The cumulative installed capacity (see **Figure 6**[2]) shows a constant increase with a noticeably higher rise from 2021 onward. Until the end of 2020, 93 MW of electrolyzer capacity is planned to be installed. The biggest projects (all with 6 MW of capacity) are the Audi e-gas project (commissioned 2013, alkaline electrolyzer) (Köbler, 2013), the Energiepark Mainz (commissioned 2015, PEM electrolyzer) (Energiepark Mainz, 2016) both in Germany, and the new H2Future project (commissioned 2019, PEM electrolyzer) in Austria (voestalpine, 2019). The expected capacities for the upcoming years are presented. They are all based on project announcements, many of which have secured funding. Until 2025, the biggest projects will have a capacity of 100 MW. Four projects fall under this category: Element Eins (scheduled for 2022) (E1, 2019) and hybridge (2019) (scheduled for 2023) – both in Germany – as well as H2V59 (also scheduled for 2022) (H2V, 2020), and the second H2V PRODUCT project – both in France – with 400 MW of capacity (planned for 2022/23) (Meillaud, 2019). From 2026 onward, even bigger projects have been announced, increasing the total installed capacity for electrolyzers to 1.8 GW. The largest single project is HyGreen Provence 2 with 435 MW of installed capacity planned in the final stage by 2030 in France (Le Hen, 2019; Saveuse, 2020). Thema et al. (2019) predicted exponential growth of cumulative installed capacity. Based on the published project data, this appears to be a considerable underestimation, even for the near future. For 2026, they predicted roughly 300 MW of installed capacity worldwide. The research presented here, however, shows that in Europe alone, 1410 MW is expected to be installed by 2026. The main drivers behind this acceleration of growth are the publicly funded projects in many sectors in Germany and several high-investment industry projects in France, for example H2V PRODUCT (Le Hen, 2019).

A closer look at the years between 2012 and 2020 with regard to installed capacity and the electrolyzer technology used is also shown in **Figure 6**. It demonstrates the growing importance of PEM technology for hydrogen production. Not only is the number of projects utilizing PEM electrolyzers constantly growing (**Figure 7**) but so too the installed capacities. 2019 was the first year in which more PEM electrolyzer capacity was installed than alkaline electrolyzer capacity (cumulatively). However, alkaline electrolyzers will play an important role again. For example, the 100 and 400 MW PtX projects in France, which are part of the H2V PRODUCT project, will be equipped with

[2]Many projects do not announce when they have shut down. For this reason, no information about active projects is available and capacities are cumulative; projects using PEM and alkaline electrolyzers are counted separately according to the technology used; due to the small number of projects using alkaline SPE, they have been excluded from this diagram.

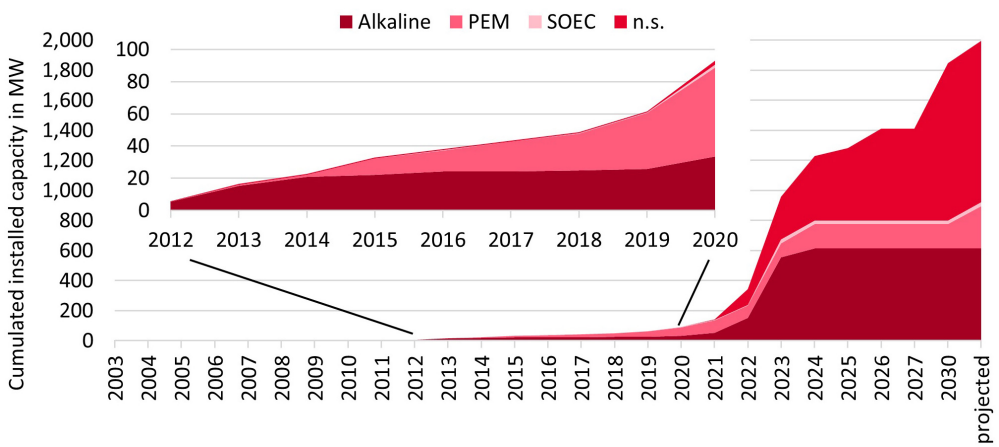

FIGURE 6 | Cumulative installed capacity according to electrolyzer type. n.s., not specified; PEM, polymer electrolyte membrane; SOEC, solid oxide electrolyzer cell.

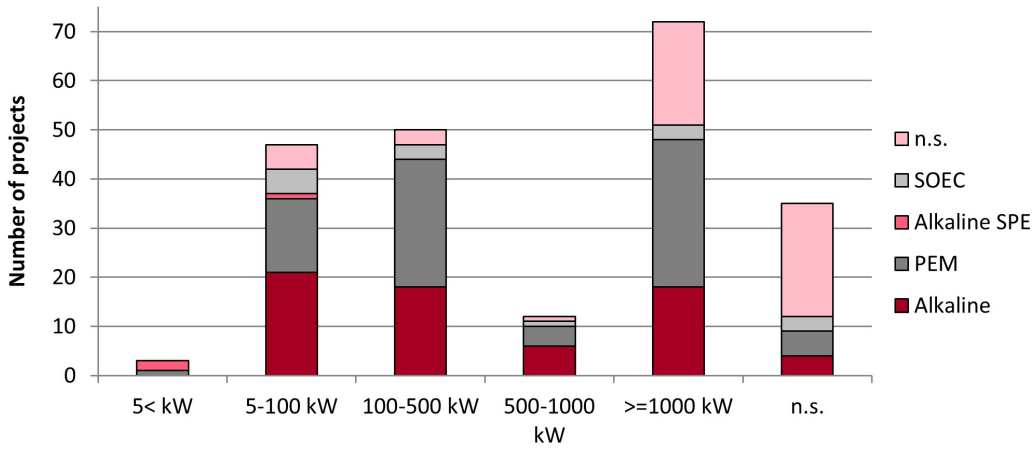

FIGURE 7 | Electrolyzer types according to capacity. PEM, Polymer electrolyte membrane; SOEC, solid oxide electrolyzer cell; SPE, solid polymeric electrolyte.

alkaline electrolyzers (HydrogenPro, 2019). Due to the level of technological development, only a low level of capacity has been installed for SOECs over the last few years. This technology still needs to demonstrate its usability beyond niche applications. The MultiPLHY project aims to install a 2.6 MW SOEC electrolyzer in a biorefinery (European Commission, 2020). In the same year (2023), an industrial project with a 20 MW electrolyzer capacity is set to be installed in Herøya, Norway to produce jet fuel using the Fischer–Tropsch process (Norsk e-Fuel, 2020). This would be a much faster technological development from a multi-MW scale to greater than 10 MW than was the case for PEM or alkaline electrolyzers. For alkaline electrolyzers, it took ten years from the first demonstration projects to achieve a multi-MW scale and another eight years to reach 10 MW. For PEM, it took seven years to achieve the first multi-MW scale and another five years to reach 10 MW. For SOECs, the first step of technological development took nine years – in contrast to PEM and alkaline electrolyzers – the second step, however, is expected to follow instantly.

In **Figure 7**, the distribution of electrolyzer capacities is depicted. The smallest class of electrolyzers (below 5 kW) is used extremely rarely, because they are too small for demonstration projects and are only considered for laboratory use. For electrolyzers below 100 kW, alkaline electrolyzers tend to be used. This is because of earlier projects, during which small capacities were installed and the preferred technology was alkaline electrolysis due to its higher maturity back then. On the other hand, the Exytron projects (Schirmer, 2020) – most of which have a capacity of 100 kW or below – will all use alkaline electrolyzers, stating the cost advantages of this technology due to its higher maturity. At present, SOECs are predominantly installed at a capacity between 100 and 500 kW, although they are less developed than PEM and alkaline electrolyzers. A trend toward smaller capacities might have been expected due to the lower level of technological development. Electrolyzers with a capacity between 0.5 and 1.0 MW are rarely used. Electrolyzer developers decided to opt directly for a size bigger than 1 MW. For sizes above 1 MW, more PEM electrolyzers are installed than alkaline electrolyzers. A relatively high share of projects, which have not yet defined their electrolyzer technology, are set to install multi-MW electrolyzers. Furthermore, a significant number of projects have not yet made a decision on electrolyzer type or capacity.

Hydrogen Processing

At present, only around one third of the projects are processing hydrogen into other fuels and products (see **Figure 8**). If hydrogen is treated further, mainly methane is produced that can be easily injected into the natural gas grid. Methanation can be realized in a catalytic and biological way. Biological methanation, for example, can be used if biogas or sewage gas needs to be upgraded to biomethane by injecting hydrogen into the biogas. A good example of the holistic use of PtX is its application in wastewater treatment plants. In the Swisspower Hybridkraftwerk project (Viessmann, 2019), hydrogen is used to enhance the methane content in the sewage gas. In another PtX project – LocalHy in Germany – the additional oxygen produced is used directly for wastewater treatment (localhy, 2019). Denmark is another country with several biological methanation projects. Catalytic methanation shows higher efficiencies, but it is also more complex from a technical perspective. However, the Exytron projects – seven projects with CHP production in residential buildings – show that catalytic methanation is on its way toward commercialization (Schirmer, 2020). Although the number of projects suggest a balance between catalytic and biological methanation, catalytic methanation is more commonly used in bigger projects, as Thema et al. (2019) have also stated (twice as much capacity for catalytic methanation). The trend becomes even more apparent when considering very recent projects. In the foreseeable future, 19 MW of installed electrolyzer capacity will be connected to biological methanation, and 122 MW to catalytic methanation. Furthermore, 100 MW alone will be installed in the efossil project (hybridge, 2019) in Germany. Only several projects are attempting to develop technologies for liquid fuel production. Methanol is the one most likely to be used. The George Olah Plant 1 in Iceland already

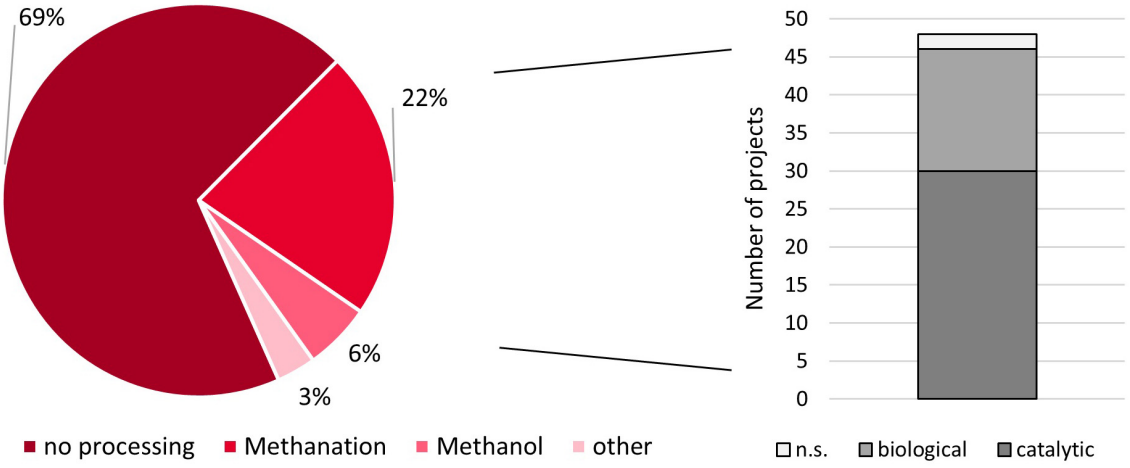

FIGURE 8 | Process steps of Power-to-X projects in Europe with a focus on methanation technologies, n.s., not specified.

proved in 2011 that this is a technically feasible option. The second most used technology is the Fischer–Tropsch process to produce mainly diesel or jet fuel (five projects) and other carbon-based co-products. They all use SOECs for hydrogen production. The four smaller projects are all located in Germany, but the most recently announced and largest project is situated in Norway (Norsk e-Fuel, 2020) due to the high availability of electricity from renewable sources. Other products include DME (Moser et al., 2018) and industrial products like waxes (Karki, 2018) or formic acid (Bär, 2014). However, in the future, no other projects are planned that go beyond methanol or Fischer–Tropsch fuels. Since liquid fuels based on electricity will have to play a major role in future energy systems (e.g., Ram et al., 2019), there have been greater efforts to develop these technologies.

Fields of Application

Fields of application include the blending of the produced gas – mainly hydrogen or methane – into the national gas grids; the production of fuels for mobility applications, for example hydrogen in fuel cell electric vehicles, methane, methanol, or Fischer-Tropsch fuels in internal combustion engines; use of the produced gases in CHP plants and use of the gases in industry, for example refineries or steel plants. For some projects, no such purpose was detected[3].

Although projects were already being developed in the early 2000s whose main field of application was fuel production, the dominance of such projects is a rather recent trend. In our previous article from 2018 (Wulf et al., 2018), blending gases into the natural gas grid was the most common form of application. In that article, we mentioned that the interest in industrial applications is growing, a trend which has proven to be true. Although no further CHP projects are scheduled for after 2023, this does not mean they will no longer be implemented. If the Exytron projects and the Vårgårda housing project prove to be successful, similar projects will arise. However, these projects have rather small installed electrolyzer capacities (below 500 kW) and are easily overlooked.

As can be seen in **Figure 9**, in the context of fuel production, PtX is the most common field of application in Europe with a 37% share of all projects. In some countries, there is a preference for certain applications. This is most apparent in the United Kingdom, for instance, where fuels are produced in the majority (67%) of the projects. The main driver behind this trend in the United Kingdom is ITM Power (ITM, 2020b), a company which produces electrolyzers as well as owning and operating several hydrogen refueling stations in the United Kingdom and France. In Germany, the greatest number of projects are also in the field of fuel production (32%). However, significant numbers of projects are found in all fields of application. Compared to other countries, industrial-based PtX projects are of higher interest. The trend toward industrial PtX applications is also likely to increase, as one of the aims of Germany's National Hydrogen Strategy (Die Bundesregierung, 2020) is to foster industrial applications. Furthermore, in the field of mobility, aviation, shipping, and heavy-duty vehicles are more likely to be funded than individual mobility. Denmark is another country with a clear preference for a certain technological purpose. In Denmark, 57% (8) of all projects are blending the produced gas into the natural gas grid. A methanation plant is used in seven out of the eight Danish projects, primarily biological methanation. However, these projects were all commissioned in the past; in the future, they will also focus on industrial applications and fuel production. In the Netherlands, the focus is on blending and industrial projects. The development of industrial applications is a rather recent trend of the 2020s. Based on the number of projects in France, the most common field of application is fuels. The seven recently approved ADEME projects (see section "General information") will contribute significantly to this development. Based on the installed capacities, fuels are also important with the HyGreen Provence projects (Le Hen, 2019). Furthermore, in future projects, multiple fields of application

[3]For this analysis, only one main purpose is counted, despite the fact that several projects use hydrogen for several purposes.

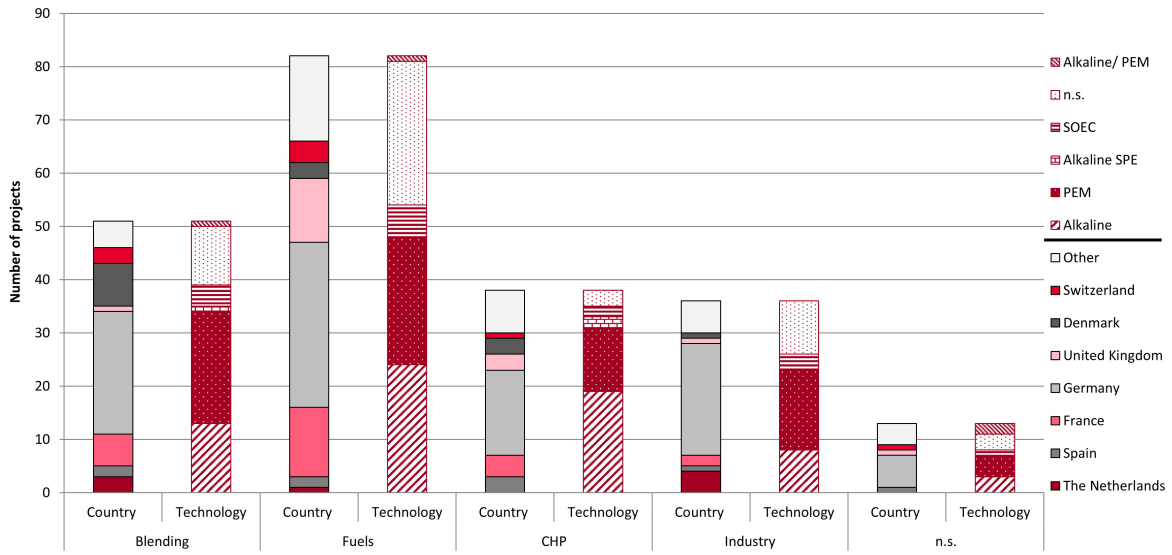

FIGURE 9 | Fields of application for Power-to-X projects according to countries and technologies. PEM. polymer electrolyte membrane; SOEC, solid oxide electrolyzer cell; SPE, solid polymeric electrolyte.

are increasingly being targeted, for example Norddeutsches Reallabor (BMWi, 2019). Such projects are listed in the **Supplementary Material**.

Certain types of electrolyzer are preferred for different fields of application (see **Figure 9**). For CHP purposes, an alkaline electrolyzer is used in almost 50% of the projects, whereas for industrial applications, a PEM electrolyzer is used in 47% of the projects. However, the use of industrial applications and PEM electrolyzers has increased significantly in recent years (**Figure 10**), which explains the correlation between these two parameters. The trend toward the renewed usage of alkaline electrolyzers in the upcoming years is mainly driven by the CHP Exytron projects (Schirmer, 2020). They all use alkaline electrolyzers, since they are more technically mature and less expensive. Furthermore, this is one of the few cases where customers are already starting to see economic viability (Schirmer, 2020). As the SOEC technology is less mature than PEM and alkaline electrolyzers, it is not surprising that this type of electrolyzer has yet to find a preferred field of application. Many projects planned for the future have not yet specified the type of electrolyzer used, which leads to the assumption that there is no strong connection between electrolyzer technology and fields of application. However, this line of argumentation is contradicted by the fact that some companies, such as Exytron, are using alkaline electrolyzers for CHP, while Sunfire is using SOECs and Fischer–Tropsch for fuel production in numerous projects.

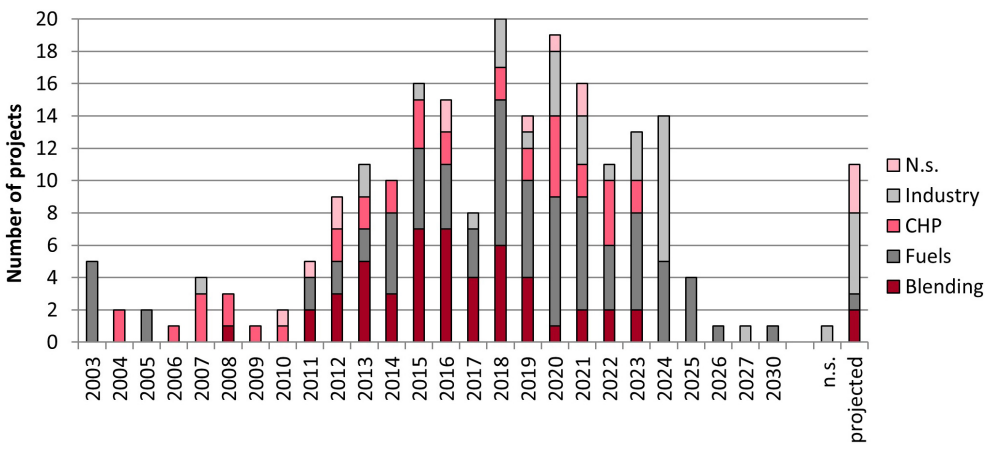

FIGURE 10 | Historical development of Power-to-X projects with regard to fields of application. CHP, combined heat and power, n.s., not specified.

As mentioned above, CHP projects most often have installed electrolyzer capacities below 500 kW. No such correlation can be drawn for fuel production, however, since it might refer to onsite hydrogen production at one hydrogen refueling station (e.g., Løkke and Simonsen, 2017) or centralized e-fuel production (e.g., Thomsen, 2019).

CONCLUSION

This analysis has shown that the development of PtX technologies is progressing quickly and will continue to do so in the near future. The planning and commissioning of PtX projects is expanding at a rapid rate. A new project is announced almost every week. This review therefore provides merely a snapshot of this development. Although the maximum number of commissioned plants was already reached in 2018 and fewer projects will be initiated in the upcoming years, installed electrolyzer capacities are getting larger and larger. This indicates that a consolidation is taking place, as fewer projects are closer to commercialization. The development of PEM and alkaline electrolyzer technologies has been good and these technologies are used very often, although there seems to be an apparent preference for the more mature alkaline technology in the future. Solid oxide electrolyzer cells are catching up in their technological development with multi-MW projects. However, the development of commercial applications is limited to one company (Sunfire), whereas several companies are involved in the development of PEM and alkaline electrolyzers. Methanation is used in many applications and has proven its feasibility for hydrogen processing. The choice between biological and catalytical methanation seems to be more a question of the project's aim rather than one of its technical maturity. Only a handful of projects are focusing on the production of liquid fuels, despite the fact that such fuels will be crucial for defossilized energy systems (Ram et al., 2019; Bauer and Sterner, 2020). Greater effort needs to be made in terms of liquid fuel production. The different technological developments of PtX technologies gives reason to believe that in the future we will see a division of major projects fostering technologies on the edge of commercialization. However, small projects will focus on technological development rather than large-scale implementation. This might also include the valorization of co-products, in particular oxygen. Very little effort has been made in terms of the use of oxygen, for example in wastewater treatment plants and innovative heat integration strategies.

Most of the discussed projects are dependent on public funding. However, the different technologies are getting closer to commercialization. This is also underlined by the introduction of the IPCEI on hydrogen. This should allow new countries, for example Portugal and eastern European countries, to participate in PtX projects. Furthermore, these projects will ensure the installation of sufficient capacities of RE, mainly wind and photovoltaics. The roll-out of new RE generation facilities is a prerequisite for many countries to enable the nationwide use of PtX technologies for the defossilization and decarbonization of the future economy; whether PtX is directly coupled with the generation of electricity or the use of RE sources is ensured by certificates.

Although 220 projects in 20 different countries have been identified in Europe, a clear regional focus has been established with France and Germany as the leading countries. Both countries plan to install around 500 MW of capacity by 2025. In Germany, this capacity will be reached through many different projects with various purposes and motives. In France, however, it is an altogether more concentrated effort involving one company. With PtX technologies still in the pre-commercialization stage, the diversified strategy with distributed risks appears to be the more sustainable one. Other very active countries are Denmark and the Netherlands. Both countries border on the North Sea, where the large potential for offshore and onshore wind can guarantee the efficient production of hydrogen and other PtX products.

AUTHOR CONTRIBUTIONS

CW conducted the research and undertook most of the writing. PZ helped to conceptualize the manuscript, as well as support the analysis, and give a critical review. AS helped with the research and gave a critical review. All authors contributed to the article and approved the submitted version.

FUNDING

This work was funded by the Helmholtz Association of German Research Centres.

SUPPLEMENTARY MATERIAL

The Supplementary Material for this article can be found online at: https://www.frontiersin.org/articles/10.3389/fenrg.2020.00191/full#supplementary-material

REFERENCES

Andika, R., Nandiyanto, A. B. D., Putra, Z. A., Bilad, M. R., Kim, Y., Yun, C. M., et al. (2018). Co-electrolysis for power-to-methanol applications. *Renew. Sustain. Energy Rev.* 95, 227–241. doi: 10.1016/j.rser.2018.07.030

Bailera, M., Lisbona, P., Romeo, L. M., and Espatolero, S. (2017). Power to Gas projects review: lab, pilot and demo plants for storing renewable energy and CO2. *Renew. Sustain. Energy Rev.* 69, 292–312. doi: 10.1016/j.rser.2016.11.130

Bär, L. (2014). *CO2RRECT Schlussbericht*. Erlangen: Siemens AG.

Bauer, F., and Sterner, M. (2020). Power-to-X im kontext der energiewende und des klimaschutzes in Deutschland. *Chem. Ing. Tech.* 92, 85–90. doi: 10.1002/cite.201900167

Bauer, S. (2016). *Underground Sun Storage: Den Sonnenschein speichern*. Vienna: RAG Rohöl-Aufsuchungs Aktiengesellschaft.

BIGH2IT (2017). *Building Innovative Green Hydrogen Systems in Isolated Territories*. Zaragoza: Fundación Hidrógeno Aragón.

Binder, M., Faltenbacher, M., Kentzler, M., and Schuckert, M. (2006). *Clean Urban Transport for Europe Project No. NNE5-2000-00113: Final Report*. Ulm: EvoBus GmbH.

BMBF (2018). *Modulare und Autarke Technologien zur Umsetzung von Synthesegas in Kohlenwasserstoff und langkettige Alkohole*. Berlin: German Federal Ministry of Education and Research.

BMWi (2019). *Gewinner des Ideenwettbewerbs „Reallabore der Energiewende" – Steckbriefe –*. Berlin: German Federal Ministry of Economic Affairs and Energy.

Bottrell Hayward, N. (2020). K gears up for hydrogen heating, H2. *Int. J. Hydrogen Fuel Cells* 48–49.

Büssers, A. (2019). *Grüner Wasserstoff aus Wyhlen: Behörden Geben Grünes Licht*. Laufenburg: Energiedienst Holding AG.

Chehade, Z., Mansilla, C., Lucchese, P., Hilliard, S., and Proost, J. (2019). Review and analysis of demonstration projects on power-to-X pathways in the world. *Int. J. Hydrogen Energy* 44, 27637–27655. doi: 10.1016/j.ijhydene.2019.08.260

dena (2020). *Vorreiter Deutschland: Projektkarte*. Berlin: Deutsche Energie-Agentur GmbH (dena).

Die Bundesregierung (2020). *Die Nationale Wasserstoffstrategie*. Berlin: German Federal Ministry of Economic Affairs and Energy.

DVGW (2019). *Wo aus Wind und Sonne grünes Gas wird . Eine Übersicht der Power-to-Gas-Projekte in Deutschland*. Bonn: Deutscher Verein des Gas- und Wasserfaches.

E1 (2019). *Element Eins: Energiewende Mit Sektorkopplung - Intelligent. Innovativ. Effizient*. Dortmund: Thyssengas GmbH.

Energiepark Mainz (2016). *Turning Wind into Gas*. Mainz: Stadtwerke Mainz.

EU (2014). *G. Technology readiness levels (TRL)", in: Horizon 2020 - Work Programme 2014-2015: General Annexes*. Brussels: European Commission.

European Commission (2020). *Multimegawatt High-Temperature Electrolyser to Generate Green Hydrogen for Production of High-Quality Biofuels*. Luxembourg: Publications Office of the European Union.

Exytron (2019). *Nachhaltige Energieversorgung für Bestands- und Neubauten im Natur- und Freizeitgebiet BernsteinSee*. Rostock: EXYTRON Vertrieb GmbH.

Fasihi, M., Efimova, O., and Breyer, C. (2019). Techno-economic assessment of CO2 direct air capture plants. *J. Clean. Prod.* 224, 957–980. doi: 10.1016/j.jclepro.2019.03.086

FReSMe (2017). *From Residual Steel Gases to Methanol*. Madrid: I-deals Innovación & Tecnología Venturing Services.

FuelCellsWorks (2020a). *France: ADEME Supports 10 New Hydorgen Mobility Projects*. Available online at: https://fuelcellsworks.com/news/france-ademe-supports-10-new-hydrogen-mobility-projects/ (accessed June 04, 2020).

FuelCellsWorks (2020b). *Hydrogen-Powered Trolleybuses put into Service in Riga*. Available online at: https://fuelcellsworks.com/news/hydrogen-powered-trolleybuses-put-into-service-in-riga/ (accessed June 10, 2020).

Gahleitner, G. (2013). Hydrogen from renewable electricity: an international review of power-to-gas pilot plants for stationary applications. *Int. J. Hydrogen Energy* 38, 2039–2061. doi: 10.1016/j.ijhydene.2012.12.010

H&R (2017). *Hansen & Rosenthal Weiht Weltgrössten Elektrolyseur Für Umweltfreundlichen Wasserstoff ein*. Hamburg: H&R Gruppe.

H2V (2020). *H2V59 - Concertation Préalable*. Paris: H2V59-Concertation par H2V.

Hänel, G., Krautz, H.-J., and Weber, H. (2019). *Referenzkraftwerk – Lausitz: Vom Braunkohlenkraftwerksstandort zum Energie- und Industriepark für neue Technologien: Speicherkraftwerk mit Sektorenkopplung*. Spremberg: Zweckverband Industriepark Schwarze Pumpe.

Hendriksen, P. V. (2015). *Synfuel*. Roskilde: Technical University of Denmark.

Hulshof, D., Jepma, C., and Mulder, M. (2019). Performance of markets for European renewable energy certificates. *Energy Policy* 128, 697–710. doi: 10.1016/j.enpol.2019.01.051

hybridge (2019). *Sektorkopplung auf Systemebene*. Dortmund: Amprion GmbH.

Hydrogen for Climate Action (2020). *IPCEI on Hydrogen*. Brussels: European Commission.

HydrogenPro (2019). *H2V Industry and HydrogenPro Join Forces!*. Porsgrunn: HydrogenPro.

HyFLEET:Cute (2009). *Electrolysis*. Fremantle: Fontaine Publishing Group.

ITM (2020a). *Industrial Scale Renewable Hydrogen Project Advances to next phase*. Sheffield: ITM Power.

ITM (2020b). *Swindon Hydrogen Station*. Sheffield: ITM Power.

Karki, J. (2018). *Demonstration of bio-CO2 products with Novel Research Platform*. Espoo: VTT.

Köbler, J. (2013). *Audi Future Lab: Mobility*. Ingoldstadt: Audi.

Le Hen, A. (2019). *Hygreen Provence: Production, stockage massif et valorisation d'H2 vert*. Marseille: Durance Luberon Verdon Agglomération.

localhy (2019). *localhy - The Real Energy Transition*. Erfurt: donner+friends UG (haftungsbeschränkt) & Co. KG.

Løkke, J. A., and Simonsen, B. (2017). *Awarded Contract for Hydrogen Electrolyser and Fueling Station in Estonia*. Oslo: Nel Hydrogen Solutions.

MefCO2 (2019). *MefCO2: Methanol fuel from CO2*. Madrid: I-deals Innovación & Tecnología Venturing Services, S.L.

Meillaud, L. (2019). *Le Projet d'usine de H2V Soumis à Concertation en Normandie*. Paris: H2V Industry.

Moser, P., Wiechers, G., Schmidt, S., Stahl, K., Majid, M., Heberle, A., et al. (2018). "Demonstrating the CCU-chain and sector coupling as Part of ALIGN-CCUS - dimethyl ether from CO2 as chemical energy storage, fuel and feedstock for industries," in *Proceedings of the Greenhouse Gas Control Technologies (GHGT) conference* (Melbourne: GHGT).

Norsk e-Fuel (2020). *Norsk e-Fuel is Planning Europe's first Commercial Plant for hydrogen-Based Renewable Aviation Fuel in Norway*. Oslo: Norsk e-Fuel.

NOW (2019). *HyLand Presskit*. Berlin: National Organisation Hydrogen and Fuel Cell Technology.

NSWPH (2019). *Modular Hub-and-Spoke Concept to Facilitate Large Scale Offshore Wind*. Dogger Bank: NSWPH.

Pearce, A. (2015). *Energy storage | clean fuel | clean air Green Comission* Sheffield: ITM Power.

Ram, M., Bogdanov, D., Aghahosseini, A., Gulagi, A., Oyewo, S. A., Cild, M., et al. (2019). *Global Energy System based on 100% Renewable Energy – Power, Heat, Transport and Desalination Sectors*. Berlin: Energy Watch Group.

Rubio, J., Cortés, P., Escudero, M. T., de Godos, I., Lana, J. A., Navarro, R., et al. (2016). "RENOVAGAS: process for the production of renewable natural gas," in *Proceedings of the 21st World Hydrogen Energy Conference* (Zaragoza: WHEC).

Saveuse, H. (2020). *HyGreen Provence : GRDF rejoint le Consortium D'entreprises Partenaires du Projet*. Marseille: Travaux Publics & Bâtiment du Midi.

Schirmer, K. (2020). *RE: AW: EXYTRON - AW: Review of Power-to-Gas Projects in Europe*. Type to C. Wulf.

Stark, C., Thompson, M., Andrew, T., Beasley, G., Bellamy, O., Budden, P., et al. (2019). *Net Zero The UK's Contribution to Stopping Global Warming*. London: Committee on Climate Change.

Sveinbjörnsson, D., and Münster, E. (2017). *WP1: Gas Conditioning and Grid Operation - Upgrading of Biogas to Biomethane with the Addition of Hydrogen from Electrolysis*. Skørping: PlanEnergi.

Thema, M., Bauer, F., and Sterner, M. (2019). Power-to-gas: electrolysis and methanation status review. *Renew. Sustain. Energy Rev.* 112, 775–787. doi: 10.1016/j.rser.2019.06.030

Thomsen, T. L. (2019). *GreenLab to be Catalyst for Global P2X MARKET*. Spøttrup: GreenLab.

Viessmann. (2019). *Grünes Licht für Erste Industrielle Power-to-Gas-Anlage im SCHWEIZERISCHEN DIETIKOn. Deutsche Technologie- und Entwicklungspartner sind die beiden Viessmann Tochterunternehmen microbEnergy und Schmack Biogas sowie Siemens*. Allendorf: Viessmann Werke GmbH & Co. KG.

voestalpine (2019). *H2FUTURE: World's largest "green" hydrogen pilot facility successfully Commences Operation*. Linz: voestalpine AG.

Wang, L., Rao, M., Diethelm, S., Lin, T.-E., Zhang, H., Hagen, A., et al. (2019). Power-to-methane via co-electrolysis of H2O and CO2: the effects of pressurized operation and internal methanation. *Applied Energy* 250, 1432–1445. doi: 10.1016/j.apenergy.2019.05.098

Wulf, C., Zapp, P., and Linßen, J. (2018). Review of power-to-gas projects in Europe. *Energy Procedia* 15, 367–378. doi: 10.1016/j.egypro.2018.11.041

Conflict of Interest: The authors declare that the research was conducted in the absence of any commercial or financial relationships that could be construed as a potential conflict of interest.

frontiers in Energy Research

ORIGINAL RESEARCH
published: 09 November 2020
doi: 10.3389/fenrg.2020.533850

Life Cycle Assessment of Power-to-Syngas: Comparing High Temperature Co-Electrolysis and Steam Methane Reforming

Andrea Schreiber[1]*, *Andreas Peschel*[2], *Benjamin Hentschel*[2] and *Petra Zapp*[1]

[1]Institute of Energy and Climate Research - Systems Analysis and Technology Evaluation (IEK-STE), Forschungszentrum Jülich, Jülich, Germany, [2]Research & Development - Process Development (RDP), Linde Aktiengesellschaft, Linde Engineering, Pullach, Germany

To achieve the European Union's ambitious climate targets, not only the energy system must be transformed, but also other sectors such as industry or transport. Power-to-X (PtX) technologies enable the production of synthetic chemicals and energy carriers using renewable electricity, thus contributing to defossilization of economy. Additionally, they provide storage capacity for renewable energy. Detailed life cycle assessments (LCA) of PtX is required, to prove the environmental advantages to fossil-based benchmark technologies. An emerging PtX technology for syngas production is the high temperature co-electrolysis (HT-co-electrolysis), which produces syngas. Aim of this LCA is the evaluation of syngas production by HT-co-electrolysis at its early stage of development to derive incentives for further research. For comparison, a small-scale steam methane reforming process (SMR) serves as today's fossil-based benchmark. The required CO_2 is obtained via direct air capture. The by-far most important input for the HT-co-electrolysis is electricity. Hence, several future electricity mixes are considered, representing two different climate protection targets (CPT80, CPT95) for the energy system in 2050. For each CPT, an additional distinction is made regarding full load hours, which depend on the availability of renewable energy. The results show lower global warming potential (GWP) and fossil fuel depletion for HT-co-electrolysis compared to SMR if mostly renewable power is used. Exclusively renewable operated HT-co-electrolysis even achieve negative net GWPs in cradle-to-gate LCA without considering syngas use. If HT-co-electrolysis shall operate continuously (8,760 h) additional fossil electricity production is needed. For CPT80, the share of fossil electricity is too high to achieve negative net GWP in contrast to CPT95. Other environmental impacts such as human toxicity, acidification, particulate matter or metal depletion are worse in comparison to SMR. The share of direct air capture on the total environmental impacts is quite noticeable. Main reasons are high electricity and heat demands. Although plant construction contributes to a minor extent to most impact categories, a considerable decrease of cell lifetime due to higher degradation caused by flexible operation, would change that. Nevertheless, flexibility is one of the most important factors to apply PtX for defossilization successfully and reinforce detailed research to understand its impacts.

OPEN ACCESS

Edited by:
David Parra,
Université de Genève, Switzerland

Reviewed by:
Xun Liao,
École Polytechnique Fédérale de Lausanne, Switzerland
Johannes Lindorfer,
Energy Institute at Johannes Kepler University, Austria

***Correspondence:**
Andrea Schreiber
a.schreiber@fz-juelich.de

Specialty section:
This article was submitted to Process and Energy Systems Engineering, a section of the journal Frontiers in Energy Research

Received: *10 February 2020*
Accepted: *01 October 2020*
Published: *09 November 2020*

Citation:
Schreiber A, Peschel A, Hentschel B and Zapp P (2020) Life Cycle Assessment of Power-to-Syngas: Comparing High Temperature Co-Electrolysis and Steam Methane Reforming. Front. Energy Res. 8:533850. doi: 10.3389/fenrg.2020.533850

Keywords: life cycle assessment, power-to-syngas, small-scale steam methane reforming, high-temperature co-electrolysis, solid oxide electrolysis cell, direct air capture

INTRODUCTION

In most countries, climate change is at the top of today's political and technological agenda. The challenge of climate change can only be met by a fundamental transformation of the energy system. The aim is to transform the current system, which is highly dependent on fossil fuels, into a mostly greenhouse gas neutral energy system based on renewable energies. The European Union has established three key targets for 2030 already in 2014: 1) reducing greenhouse gas (GHG) emissions at least by 40% compared to 1990 levels, 2) increasing the share of renewable energy at least to 32%, and 3) improving energy efficiency at least by 32.5% (European Council, 2014).

Currently, the European Commission has proposed a European climate law (the green deal) to reduce GHG emissions even by 50–55% compared to 1990 levels by 2030 and to achieve climate neutrality by 2050 (European Commission, 2020).

To reach these not only the energy system must be transformed, but also other sectors, like industry or transport. All the same, carbon-based energy carriers and raw materials will still be needed in the future, especially for the chemical industry. Hence, a full decarbonization of all sectors is very unlikely. Even more, defossilization of sectors by substitution of fossil fuels with renewables is mandatory. Power-to-X (PtX) technologies allow the production of synthetic chemicals and energy carriers using renewable electricity. By coupling sectors, PtX contributes to the overall defossilization (Heinemann et al., 2019; Bauer and Sterner, 2020). However, renewable electricity will continue to be a limited resource in the near future, since it can be used for competing PtX technologies such as Power-to-Heat, Power-to-Gas, Power-to-Fuels or Power-to-Chemicals. Processes with highest environmental benefits per kWh renewable electricity must be identified. In the past years specific efforts were taken to promote the development of PtX technologies, driving low technology readiness levels (TRL) of one to three toward demonstration plants (TRL 6–7) (Wulf et al., 2018; Chehade et al., 2019; RWE, 2019; Thema et al., 2019; Uniper SE, 2019).

The German Kopernikus project "P2X," funded by the German Federal Ministry of Education and Research, meets the challenge to improve PtX competitiveness (Ausfelder et al., 2019). In an emerging PtX technology, known as high temperature solid oxide co-electrolysis (HT-co-electrolysis; HT-SOEC), water is split and simultaneously CO_2 is activated to form syngas (Foit et al., 2016). Syngas is a mixture of carbon monoxide (CO) and hydrogen (H_2) in various compositions and therefore an important intermediate product of numerous chemical synthesis such as methanol synthesis, Fischer-Tropsch synthesis, and hydroformylation. The annual production of syngas is estimated to approx. 598 million tons for 2018 (Khan, 2018). Coal (48.3%) and natural gas (46.5%) are the two dominant feedstocks. Petcoke, refinery residue and coke oven gas serve as 4.3% syngas feedstock. Biomass and waste constitute less than 1% (Khan, 2018). HT-co-electrolysis is able to generate tailor-made syngas of variable compositions, which are relevant for industrial applications in the range of H_2/CO ratio of one–three by variation of operating parameters (temperature, current, feed gas composition). HT-co-electrolysis takes place at temperatures around 800°C. Syngas can be produced with current densities up to 2 A/cm^2 (Zheng et al., 2017), although they are often lower in practice, and with high cell efficiencies (Foit et al., 2016).

Detailed analyses are already required at a very low TRL, since PtX products are not a priori more sustainable than their well-established fossil benchmarks. The overall performance depends on various criteria, e.g., expenditures for electricity, water and CO_2 supply, efficiencies of the new synthesis routes as well as costs (Bracker, 2017). Comprehensive reviews on HT-co-electrolysis including basic principles, required materials, cell and stack design, fabrication and scale up, performance measurements, degradation issues, and economic feasibility were given by Zheng et al. (2017) and Foit et al. (2016). An in-depth insight into optimal energy system layout and conditions for economic feasibility was provided by Morgenthaler et al. (2020). Syngas, as an important intermediate of the chemical industry, is neither transported nor directly sold as a final product, in contrast to H_2 (Peschel, 2020). This might be the reason that only one life cycle assessment (LCA) study was found analyzing solely the production of syngas so far (Sternberg and Bardow, 2016). The authors analyzed Power-to-Gas processes to synthetic natural gas (Power-to-SNG) by Sabatier reaction in comparison to Power-to-syngas by reverse water gas shift (rWGS) and dry reforming of methane (DRM). They pointed out that both Power-to-Syngas pathways have a higher environmental benefit than Power-to-SNG. Syngas production by DRM has lower GHG emissions than by rWGS. Some other LCA studies are available that analyze processes using CO_2-based syngas as intermediate feedstock for chemicals (Anicic et al., 2014; Luu et al., 2015; Al-Kalbani et al., 2016) and fuels (van der Giesen et al., 2014; Baltrusaitis and Luyben, 2015).

Several LCA studies have been conducted for different PtX pathways. In a recent review Koj et al. (2019) compared 32 LCA studies analyzing environmental, technological, as well as methodological aspects of PtX systems. The electricity source and the methodological concept of CO_2 consideration are crucial drivers of environmental impacts. Sternberg and Bardow (2015) presented an environmental comparison of Power-to-Power, -to-Mobility, -to-Heat, -to-Fuel, and -to-Chemical feedstock. Reiter and Lindorfer (2015) compared H_2 and methane (CH_4) production from renewable electricity via Power-to-Gas technology to conventional natural gas supply. A study from van der Giesen et al. (2014) examined rWGS process as intermediate step for the production of liquid hydrocarbon fuels (Power-to-Fuel) as an alternative to diesel. In the study from Liu et al. (2020) CO_2 emissions from direct air capture

(DAC) and Fischer-Tropsch fuel production were assessed by LCA. CO_2 based C1-chemicals (e.g. formic acid, CO, methanol, CH_4) by hydrogenation (Power-to-Chemical feedstock) are focus of the study from Sternberg et al. (2017). The environmental comparison of different CO_2 sources (e.g., captured CO_2 from chemical plants, natural gas processing, paper mills, power plants, iron and steel plants) for Power-to-Chemicals processes is the focus of the study by von der Assen et al. (2016). Zhang et al. (2017) discussed many system variations of Power-to-Gas technologies. Power-to-Gas can reduce GHG emissions, depending on the electricity supply and CO_2 source, compared to conventional gas production technologies. A global assessment of the climate change mitigation potential of carbon capture and utilization (CCU) in the chemical industry is provided in studies by Artz et al. (2018) and Kätelhön et al. (2019).

Aim of this LCA study is to evaluate the environmental competitiveness of syngas production by HT-co-electrolysis at an early stage of development, to derive incentives for further research and development directions. For the electrolysis process, different electricity supply mixes representing various future energy scenarios are considered. The required CO_2 is captured by DAC. Coal gasification (Khan, 2018) and steam methane reforming (SMR) of natural gas (Rostrup-Nielson, 2005) can be regarded as today's most utilized fossil benchmark technologies. However, gasification is used for very large scales (>10 kNm^3/h often even >100 kNm^3/h syngas) and is not built on a small scale for technical and economic reasons. As HT-co-electrolysis is still at an early developing stage and will be employed only on small scale and in a decentralized way in the near future, a small-scale SMR with an output of just 330 m^3/h syngas is used as fossil reference for a meaningful comparison. However, since not all measures of heat integration are economically useful for small scale, its efficiency is lower than that for large-scale SMRs usually used.

METHOD

LCA is a comprehensive method to assess environmental impacts of products and processes (International Organization for Standardization, 2006a; International Organization for Standardization, 2006b). According to the ISO standards, LCA is subdivided into four steps. First, in the goal and scope definition the object, the system boundaries, and the functional unit (FU) of the analysis are described. Second, in the life cycle inventory (LCI), material and energy inputs and their subsequent outputs are compiled along the process chains considered. Third, in the life cycle impact assessment (LCIA), the potential environmental impacts are evaluated. Fourth, the results are summarized and conclusions are drawn to give recommendations for improvement in the final interpretation step.

Goal and Scope Definition

Goal of this paper is the comparison of environmental impacts of syngas production by HT-co-electrolysis and by the corresponding small-scale SMR process. Therefore, LCIs of syngas production by HT-co-electrolysis and small-scale SMR as well as CO_2 supply by DAC are compiled In addition, detailed LCIs of construction of HT-co-electrolysis and small-scale SMR and their environmental impacts is carried out in order to sensitize the technology developers to critical materials at an early stage and to derive further research incentives. In case of HT-co-electrolysis, balance-of-plant (BoP) components, stack materials and single cells are published for the first time and can serve as a basis for further analyses in the PtX field.

System Boundaries and Functional Unit

Figure 1 presents the system boundaries of the two syngas production pathways considered in an attributional cradle-to-gate LCA. The functional unit (FU) is 1 kg of syngas produced, with a molar H_2/CO ratio of 2, at 20 bar, 40°C and a CO_2 molar fraction below 0.1 mol%. The molar ratio of two is chosen, since many chemical processes and synthetic fuels require such a syngas feed. Syngas use is not included in this analysis.

Tables 2-4 present the LCI data of HT-co-electrolysis, small-scale SMR, and DAC construction and operation. Detailed information about construction is provided in the **Supplementary Material**.

For electricity as the most important input of the HT-co-electrolysis, four different electricity supply mixes are used for the year 2050, which are specified in detail in the background system "*Electricity Supply Mixes*." The electricity mixes take into account two different climate protection targets (CPT) based on 80% and 95% CO_2 reduction (CPT80, CPT95). For each CPT, an additional distinction is made regarding full load hours, which depend on the availability of renewable energy. The availability represents hours of exclusively renewable generated electricity (Bareiß et al., 2018; Bareiß et al., 2019). This results in four scenarios: 1) CPT80, 8,760 h; 2) CPT80, 3,000 h; 3) CPT95, 8,760 h; 4) CPT95, 6,500 h) (**Table 5**). The lower the number of full load hours, the lower the quantities of syngas produced per year. While for 8,760 h, 147 t of syngas are produced per year, for 3,000 h (CPT80) and 6,500 h (CPT95), 50.3 and 109 t of syngas are produced, respectively (**Table 2**). For small-scale SMR as today's conventional technology of syngas production, an 8,760 h operation with the German electricity mix 2014 is considered.

Data Sources

For process chain modeling, the LCA software GaBi version 9.2.0.58 (thinkstep, 2018) was used. Background LCI data are taken from both the ecoinvent 3.5 database (Ecoinvent, 2016) and the GaBi Professional 9.2 database. Most of the LCI data of the syngas production technologies (so called foreground data) are provided by Kopernikus project partners:

(1) cell and stack construction of HT-co-electrolysis: Forschungszentrum Jülich GmbH - Institute of Energy and Climate Research (IEK-1, IEK-3), - Central Institute of Engineering, Electronics and Analytics (ZEA)
(2) small-scale SMR process design and simulation, HT-co-electrolysis overall system design and process simulation: Linde Aktiengesellschaft (AG), Linde Engineering, Research & Development, Process Development

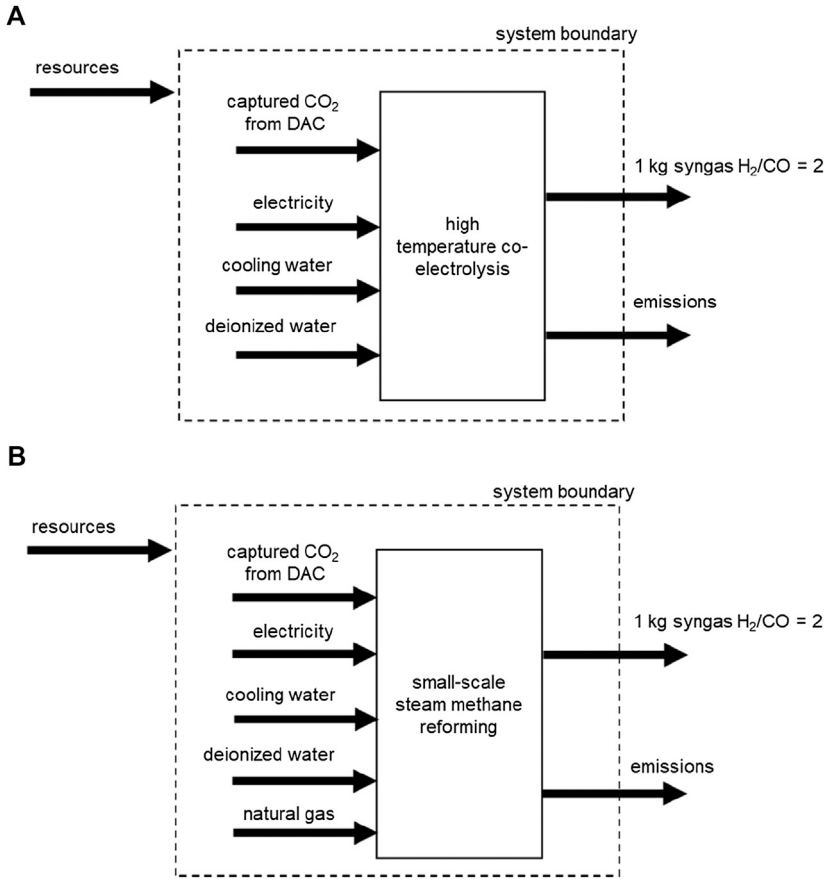

FIGURE 1 | System boundaries of cradle-to-gate syngas production pathways considered: **(A)** syngas production by HT-co-electrolysis, **(B)** conventional syngas production by small-scale SMR.

(3) DAC: Climeworks AG
(4) electricity supply models: Technical University Munich - Institute for Renewable and Sustainable Energy Systems.

Limitations

The construction of the syngas production units as well as of the DAC unit is considered. The lifetime is 20 years. Components with lower lifetime (e.g., cells) are replaced. Decommissioning of the production units or other end-of-life processes are neglected. To simplify the calculation it was assumed, that the intermittent renewable electricity is provided continuously to HT-co-electrolysis. This is, of course, not the case. However, a consequential ramp up and shut down of the HT-co-electrolysis most likely would affect the performance and life time of the unit. This effects have not been investigated yet and are topic of further research. Processing and use of syngas for a specific industrial application is out of the presented scope. Nevertheless, results can be taken for LCAs of further products based on syngas with H_2/CO ratio of 2.

Allocation

If more than one product is produced in a process, it is necessary to divide the environmental impacts between the products according to ISO 14040 (International Organization for Standardization (ISO), 2006a; b). Although syngas and oxygen are produced during the HT-co-electrolysis, no allocation was carried out between the two products. Oxygen is neither purified, nor stored or used. Before the oxygen is released from the system, it is diluted with air to mitigate safety concerns. Therefore, it is considered as waste and no allocation is necessary.

The assessment of the various impacts of CO_2 supply as well as the best way to account for expenditures for the capture process has been topic of several controversial studies and lies beyond the scope of this study (Müller et al., 2020). In case of DAC it is not necessary to consider the primary CO_2 emitter (air). CO_2 is considered as an elementary flow (see *Life Cycle Inventory of High Temperature Co-Electrolysis*). We completely allocate all expenditures for DAC (e.g., electricity, heat) and emissions to the both syngas production systems. Additionally, the amount of CO_2 removed from the atmosphere is credited to the syngas production via HT-co-electrolysis and via small-scale SMR process.

Environmental Impact Categories

The environmental impacts are determined according to the ReCiPe methodology for LCIA version 2016 v1.1 Midpoint (Hierarchist) (Goedkoop, 2009) with one exception considering abiotic resource depletion. The two considered syngas production pathways are compared based on the following eight impact categories:

(1) Climate change (GWP) (kg CO_2 eq.),
(2) Fossil depletion (FD) (kg oil eq.),
(3) Fine Particulate Matter Formation (PM) (kg $PM_{2.5}$ eq.),
(4) Terrestrial Acidification (AP) (kg SO_2 eq.),
(5) Photochemical Ozone Formation, Ecosystems ($POCP_{eco}$) (kg NO_x eq.),
(6) Photochemical Ozone Formation, Human Health ($POCP_{human}$) (kg NO_x eq.), and
(7) Human toxicity, cancer (HTP) (kg 1,4-DB eq.)
(8) Abiotic resource depletion (ADP) (kg Sb eq.).

The first seven categories are chosen because they reflect electricity driven impact categories and thus represent the motivation for PtX. Due to the use of rare earth elements (REEs) for the single cells in the HT-co-electrolysis unit, the impact category "Abiotic Depletion (ADP elements)" (kg Sb eq.) supplied by CML method version CML2001 - Jan. 2016 is used additionally. For this method, Adibi et al. (2019) estimated new characterization factors (CFs) for 15 REEs. Despite the high criticality, individual REEs are not covered appropriately by any LCIA methods so far. To develop the CFs, the authors collected a wide range of data from U.S. Geological Survey (USGS) and other mining reports for 11 large REE deposits. For this study, we integrated the new CFs of the REEs in the ADP category of CML. ADP and HTP are often important for the supply of steel, nickel, copper and other metals like REEs or chromium.

Specification of Foreground Systems

High Temperature Co-Electrolysis

Technical Description of High Temperature Co-Electrolysis

HT-co-electrolysis is a further development of HT-solid oxide electrolysis (HT-SOEC) for H_2 production. In the HT-co-electrolysis, the two reactions of electrolytic H_2 production and CO production by rWGS run simultaneously in one reactor. Operation at high temperatures offers thermodynamic advantages. On stack level, this results in lower energy requirements combined with increased efficiency by better kinetics compared to low temperature electrolysis. A complex fully heat integrated HT-co-electrolysis process at commercial scale, however, has not been built so far. This results in a lower system efficiency compared to the stack efficiency. The simulated 150 kW HT-co-electrolysis analyzed in this study operates at 800°C with an efficiency of approx. 75% (**Figure 2**). The process design was done by Linde AG deriving a fully heat integrated process, so that no steam input and export is required. Since CO_2 and steam are not fully converted in the electrolyzer, CO_2 needs to be separated from the syngas and recycled. CO_2 separation is carried out by pressure swing adsorption (PSA). The syngas output has the same composition and properties as the one from the small-scale SMR described below. The output amounts to 16.8 kg/h and is therefore only 10% of the syngas output supplied by the small-scale SMR (159 kg/h). Additional losses in efficiency caused by transformer, rectifier and power electronics are not yet included in the HT-co-electrolysis analysis. These losses usually are below 5%.

Currently, a degradation of 1%/1,000 h in contrast to the much lower degradation of solid oxide fuel cells (SOFC) (0.3%/1,000 h) is taken into account. This results in a total cell replacement after 10 years. It is assumed that most of the stack material (Crofer22APU) can be reused. However, system efficiency losses due to lower cell efficiency over time is not considered in power demand. It should be noted that the current degradation of 1%/1,000 h will probably result in overcharged maintenance and replacement costs which makes industrial applications rather unrealistic. Although it can be assumed that degradation will decrease when the TRL increases, degradation remains a major development task for HT-co-electrolysis. It is still uncertain whether lower degradation can be achieved.

Table 1 presents the main cell, stack and operating parameters. The numbers of cell levels and single cells for a 150 kW unit are calculated to 227 and 908, respectively. For simplification, two stacks with 120 levels each and 960 single cells are assumed.

The so-called Jülich F^Y10 is a robust stack design based on 2.5–5 mm thick interconnectors (IC) consisting of Crofer22APU (Fang et al., 2015; Frey et al., 2018). This vacuum-cast alloy has a composition of 22% chromium, 0.4% manganese, 0.07% titanium, 0.08% lanthanum, and 77.45% iron and was developed by Quadakkers et al. (2004). The major stack components are shown in **Figure 3** (Fang et al., 2015). Each repeating unit consists of one IC, one frame, together with the cell and a nickel mesh. The anode side of the IC is coated with a 100 µm chromium poisoning protection layer consisting of $Mn_{1.0}Co_{1.9}Fe_{0.1}O_4$ (MCF). The coating is performed by atmospheric plasma spraying (APS). The glass-cermet used as sealant is discussed in Groß-Barsnick et al. (2018). The slurry contains glass powder, yttrium stabilized zirconia (YSZ) fibers, and organics.

Figure 3 shows a schematic illustration of an anode-supported cell (ASC in SOFC mode) which is considered here, in contrast to the other main concept of electrolyte-supported cells (ESC). The cell and stack concept analyzed in this study is mainly based on activities at Forschungszentrum Jülich (Menzler et al., 2014; Schafbauer et al., 2014; Frey et al., 2018), but using a thinner IC (2.5 mm) as described in Harboe et al. (2020). Due to its mechanical strength, 8 mol% YSZ (8YSZ) is used as an electrolyte. The anode consists of (La, Sr) (Co, Fe)O_3 perovskite (LSCF) and the contact layer consist of $La_1Mn_{0.45}Co_{0.35}Cu_{0.2}O_3$ (LCC10). The cathode is a nickel cermet (NiO/8YSZ). Gadolinium doped ceria (CGO) is used as barrier layer and is screen printed between electrolyte and anode. Typical cell manufacturing processes are tape casting (for the substrate layer), screen printing (for all other layers) and various sintering processes for each layer at optimized

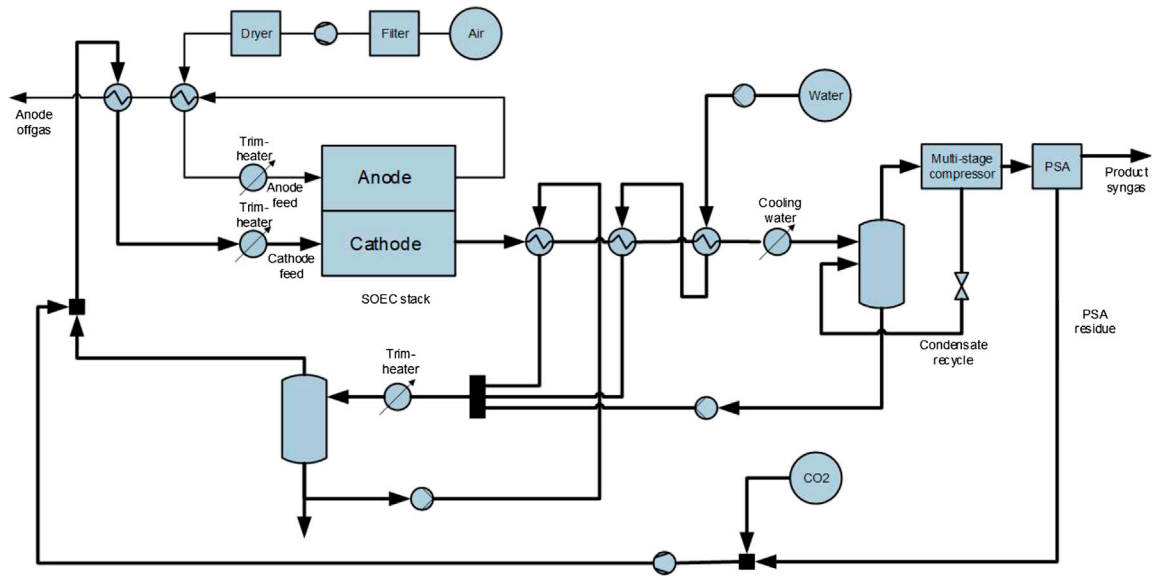

FIGURE 2 | Simplified process flow diagram of HT-co-electrolysis.

TABLE 1 | Cell, stack and operating parameters of HT-co-electrolysis.

HT-co-electrolysis parameter	Unit	Value
Cell dimension	cm	10*10
Active area per cell	cm^2	80
Active area per level	cm^2	320
Cell thickness	µm	500
Cell resistance	$\Omega*cm^2$	0.29
Current density	A/cm^2	1.5
Cell voltage	V	1.375
Power density	W/cm^2	2
Cell power	W	165
Power per stack level	W	660
Number of levels	—	2*120
Number of single cells	—	960
Temperature at stack	°C	800
Steam utilization	—	0.5
Degradation	%/1,000 h	1

temperature (Menzler et al., 2014). The production route of these cells is discussed in detail in Menzler et al. (2014).

Life Cycle Inventory of High Temperature Co-Electrolysis

For the production of 1 kg of syngas, 1.38 kg of CO_2, 1.13 kg of deionized H_2O and 8.82 kWh of electricity are required. The separated oxygen leaves the plant without any ecological impact (see "*Goal and Scope Definition*"). Depending on the full load hours, various shares of single cells, stacks, and BoP pieces are assigned to the process. The smaller the number of full load hours due to the assumed electricity supply mix, the smaller the amounts of syngas produced per year. This results in larger shares of single cells, stacks, and BoP pieces assigned to 1 kg of syngas (**Table 2**). The amount of syngas reduces from 147 t/y to 109 t/y (CPT95) and finally to 50 t/y (CPT80) when the full load hours drop from 8,760 to 6,500 and 3,000 (**Table 2**).

For stack production approx. 530 of kg Crofer22APU, 20 kg of nickel mesh, 20 kg of glass-ceramic sealant, and 3 kg of MCF are required for one stack. Further material processing such as form-shaping steps (e.g., milling of fuel gas and air manifolds, creep-feed grinding of the air channels, laser-cutting of outline), application of the chromium protecting layer MCF by APS and annealing of the stack at high-temperature are also considered in terms of their energy demand (Harboe et al., 2020). Argon and H_2 needed for annealing are not considered due to missing data on gas consumption. In case of cells, materials and energy required for the sintering steps are included in the LCI. Further information about cell and stack construction as well as BoP can be found in **Supplementary Tables S4–S7**.

According to the BoP of a 100 kW_{el} SOFC plant in Pehnt (2002) and data from Primas (2007), the BoP for the 150 kW HT-co-electrolysis was calculated. Approx. 1.9 t of steel are required for water evaporator, compressor, heat exchanger and piping. Moreover, an inverter, electricity and fuels for heating were used (**Supplementary Table S7**). The construction material for the PSA could not be taken into account because no data was available.

Small-Scale Steam Methane Reforming

Technical Description of Small-Scale Steam Methane Reforming

The process design of the small-scale SMR was carried out by Linde AG within the Kopernikus P2X project. For a meaningful comparability to the HT-co-electrolysis, a small-scale SMR process is modeled with typical heat integration and process set-up for small-scale. The syngas output is 330 Nm^3/h (with 0.481 kg/m^3 for a syngas with a molar ratio of H_2/CO of 2) and

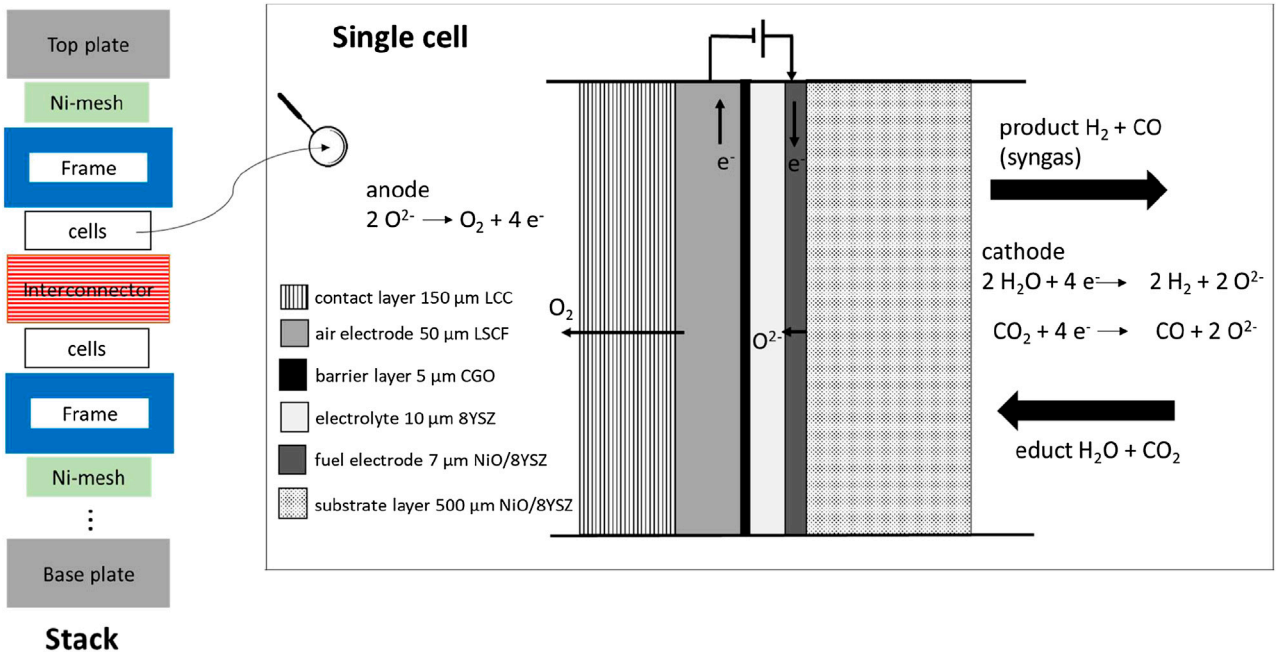

FIGURE 3 | Schematic illustration of the Jülich F[Y]10 stack design based on Fang et al. (2015) and an included single cell (Menzler et al., 2014; Harboe et al., 2020).

TABLE 2 | Operation of HT-co-electrolysis to produce 1 kg of syngas (molar ratio H_2/CO = 2) under consideration of different electricity mixes.

CPT	Unit	CPT80 CPT95	CPT80	CPT95
Full load hours	h	8,760	3,000	6,500
Syngas per year	t	147	50.3	109
Input				
CO_2 From DAC	kg	1.38	1.38	1.38
RER: Water production and supply, deionized[a]	kg	1.13	1.13	1.13
Electricity (depending on energy model)	kWh	8.82	8.82	8.82
Cells	Pieces	2.0E-03	6.0E-03	2.8E-03
Stack	Pieces	1.4E-06	4.0E-06	1.8E-06
BoP	Pieces	3.4E-07	9.9E-07	4.6E-07
Output				
Syngas[b]	kg	1	1	1
O_2	kg	1.5	1.5	1.5

[a]*Ecoinvent 3.5 process;*
[b]*20 bar, 40°C.*

TABLE 3 | Operation of small-scale SMR to produce 1 kg of syngas (molar ratio H_2/CO = 2).

Inputs and Outputs	Unit	Value
Input		
DE: Natural gas mix, ts[a]	kg	0.826
DE: Market for electricity, low voltage[b]	kWh	0.23
RER: Water production and supply, deionized[b]	kg	0.35
Small-scale steam reformer 330 m^3 syngas/h[c]	Pieces	3.6E-8
CO_2 From DAC	kg	0.33
Output[d]		
Syngas[e]	kg	1
Carbon dioxide (inorganic emissions to air)	kg	1.07
Carbon monoxide (Inorganic emissions to air)	g	0.0163
Dinitrogen monoxide (ecoinvent long-term to air)	g	4.8E-03
Dust (PM2.5) (particles to air)	g	2.9E-03
Methane [organic emissions to air (group VOC)]	g	9.6E-03
Nitrogen oxides (Inorganic emissions to air)	g	0.342
NMVOC (unspecified) (Group NMVOC to air)	g	0.048
Sulfur dioxide (Inorganic emissions to air)	g	4.8E-03

[a]*ts = GaBi dataset from thinkstep.*
[b]*Ecoinvent 3.5 process.*
[c]*Assuming 8,760 h per year.*
[d]*All emissions are direct process emissions.*
[e]*20 bar, 40°C.*

therefore considerably lower than the usual industrial SMR processes between 20,000 and 200,000 Nm^3/h. The process design is adapted to obtain syngas in a H_2/CO ratio of two from a small-scale SMR for H_2 production (Linde AG, 2019). The process performance is obtained from process simulations using UniSim Design® and physical property data. Such a small-scale SMR differs significantly from large-scale reformers in terms of process design and hence process efficiency. In case of large-scale reformers, a tailored heat recovery is economically reasonable. For small scale this would increase the specific investment costs per Nm^3 product. Therefore, a simpler heat integration is used. By reason of small scale, the process is designed without steam export. Excess thermal energy is dissipated via cooling water. The efficiency of the small-scale SMR process is about 63% related to the lower heating value (LHV) of used natural gas

(49.085 MJ/kg). Thus, the energy efficiency is more than 10%-points lower than for large-scale SMR plants.

The German natural gas mix from the GaBi Professional database (thinkstep, 2018) was selected for suppling the small-scale SMR. Because data for natural gas supply from the GaBi database stand for a LHV of 45.5 MJ/kg, the required quantity is converted by the LHV used for SMR modeling. The produced syngas consists of 66.4 mol% H_2, 33.2 mol% CO and traces of CO_2, nitrogen, H_2O and hydrocarbons and has a LHV of 23.59 MJ/kg. The modeling data and process design of the small-scale SMR process supplied by Linde AG is confidential and cannot be presented in detail.

Life Cycle Inventory of Small-Scale Steam Methane Reforming

Table 3 specifies the inputs and outputs of 1 kg of syngas production by small-scale SMR. For SMR operation, 8,760 full load hours are assumed. Approx. 25% of the natural gas input serves as fuel for the burner. The calculation of the natural gas combustion emissions in the burner is based on the ecoinvent report 06.V (Faist-Emmenegger et al., 2007).

For the construction of the small-scale SMR including BoP material, 100 t of concrete, approx. 31 t of various steel types and 0.5 t of nickel are required (**Supplementary Table S8**). It should be noted that these values are only a first rough estimation. Furthermore, these values cannot be used to calculate the construction materials for a large-scale plant due to a significantly different design. In contrast to HT-co-electrolysis, no metalworking steps for the reformer components could be included due to missing information. As the results of the HT-co-electrolysis show, the metalworking steps have only a marginal impact on the results.

Specification of Background Systems

For the comparison of the HT-co-electrolysis and the small-scale SMR process, the background processes considered are identical. Both pathways need CO_2, electricity, deionized water, and cooling water. Cooling water consumption is neglected because it is usually circulated and has only minor effects.

Supply of CO_2 by Direct Air Capture

Technical Description of Direct Air Capture

The required CO_2 can be supplied from different sources. Larger point sources, for example from CO_2 wash systems as employed in chemical processes (e.g., ethylene oxide production), have the advantage of high CO_2 concentrations and often high flow rates. In the long term, CO_2 from biomass, waste gasification or obtained via DAC are favorable sources for a defossilization of the entire system. Keeping this long-term perspective in mind and to be as independent as possible from local conditions, DAC is considered as CO_2 source in this study.

DAC is a geo-engineering method that separates CO_2 from air. The concept was first introduced by Klaus Lackner in 1999 (Sanz-Pérez et al., 2016). Since that time, DAC caused many pro and cons analyses whether it is (or is not) an important and viable option for reducing greenhouse gases. In the last 10 years DAC is a rapidly growing environmental technology with several start-ups pushing this technology from lab scale to demonstration and pilot scale (Sanz-Pérez et al., 2016), although the second-law thermodynamic efficiency is likely to be significantly below 10% (House et al., 2011). In contrast, efficiency for amine based flue gas scrubbing reaches 20–25% (House et al., 2011). During the DAC process, ambient air flows through a filter where either adsorption, absorption or mineralization removes CO_2 from air. In this study, the DAC technology of Climeworks AG is considered. This technology uses an adsorption-desorption process with a special cellulose-based filter material. Amine based solid sorbents are often proposed for DAC. The CO_2 is chemically bound to the filter material along with air moisture (Fasihi et al., 2019). When the filter is saturated with CO_2, it is heated up to around 100°C mainly by low-grade heat as an energy source. The CO_2 is released from the filter and collected as concentrated CO_2 gas to supply customers. The process is operated in continuous cycles. The filter is reused and lasts several thousand cycles (Climeworks, 2017). A full cycle takes 4–6 h with an output of >99% pure CO_2 flow (Lozanovski, 2019). Data of this process represents the Climeworks DAC plant in Hinwil (Switzerland). It started operation in 2017 and is situated on top of a waste incineration plant. Eighteen air filter modules extract 900 t of CO_2 per year, which is sold to a nearby fruit and vegetable grower for use in its greenhouse. The waste incineration plant provides the low-grade heat for stripping the CO_2. This accounts for approx. 80% of the DAC's total energy requirements (Fasihi et al., 2019). Climeworks seeks to reduce the current energy demand of 500 kWh of electricity and 1,500 kWh of heat per ton of CO_2 by 40% in the future (Evans, 2017).

TABLE 4 | Operation of DAC to produce 1 t of CO_2.

Inputs and Outputs	Unit	Value
Input		
Electricity (depending on the electricity supply mix)	kWh	500
CH: Market for heat, district or industrial, natural gas[a]	kWh	1,500
RER: Market for anionic resin[a]	kg	3.75
Direct air capture plant	Pieces	9.3E-5
Output		
CO_2	kg	1,000

[a]*Ecoinvent 3.5 process.*

Life Cycle Inventory of Direct Air Capture

Table 4 shows the required inputs to produce 1 t of CO_2 by DAC. Main inputs for the process are electricity, heat and amine based sorbents. We assumed the ecoinvent process "RER: market for anionic resin" for the production of the amine based solid sorbents. Although the low-grade heat for the DAC plant in Hinwil is provided by the waste incineration plant, we considered a more general heat supply, using the ecoinvent process "CH: market for heat, district or industrial, natural gas." This constitutes a worse case due to the heat supply from natural gas. Ecological improvements can be achieved by an advantageous heat supply instead of natural gas (e.g., waste heat from waste incineration as in Hinwil or from industrial processes).

TABLE 5 | Electricity supply mixes assumed for 2050 based on data from TUM (Bareiß et al., 2018; Bareiß et al., 2019).

	CPT80	CPT80	CPT95	CPT95
CPT compared to 1990 (%)	80	80	95	95
Available full load hour (h)	8,760	3,000	8,760	6,500
Combined cycle natural gas power plant	40	—	5	—
Hard coal	—	—	—	—
Lignite	—	—	—	—
Photovoltaics	21	35	29	30
Wind	39	65	66	70

To calculate the expenditures to build a DAC plant, 900 t of CO_2 produced per year and a lifetime of 12 years were assumed. For construction 52 t of concrete, 93 t of gravel, 90 t of sand, 66.6 t of steel, 26.2 t of aluminum, 1.7 t of copper, 8.7 t of isolation material, and 1.1 t of sealing compound were considered (Lozanovski, 2019). Recycling of aluminum and steel was taken into account with recycling rates of 92% and 90%, respectively. We applied the usual avoided burden approach by giving the system a credit for possible metal recycling and thus avoiding the production of virgin metal. Further detailed LCI data regarding construction can be found in **Supplementary Table S3**.

Electricity Supply Mixes

The main energy input for the HT-co-electrolysis is electricity, which plays an important role. Hence, several future electricity supply mixes are considered, representing different assumptions for a future energy system. For the year 2050, four different electricity supply mixes were assumed, elaborated by the project partner TUM (**Table 5**). The electricity supply mixes base on two different CO_2 reduction scenarios taken from the German Climate Action Plan 2050 (BMU, 2016). The calculations consider the specified target corridors of 80 and 95% greenhouse gas reduction up to 2050 compared to 1990 (climate protection target: CPT80, CPT95) (Repenning et al., 2015). A power plant deployment model is applied with spatial and hourly resolution for the German federal states. An economic optimization of the overall system is carried out to determine the power generation capacity (fossil power plants, expansion of renewable energies). The entire derivation of the electricity supply mixes as well as all assumptions and parameters are listed in the studies from TUM (Bareiß et al., 2018; Bareiß et al., 2019). Furthermore, for each CPT, an additional distinction is made regarding full load hours, which depend on the availability of renewable energy. The hours of generation of renewable electricity was calculated using the model of TUM (**Table 5**). The CPT with higher reduction targets results in a higher share of renewables and consequentially in higher operation hours of renewable technologies, 6,500 h (CPT95) compared to 3,000 h (CPT80). An operation of 8,760 h allows maximum capacity utilization of the HT-co-electrolysis. In case of the small-scale SMR, the German electricity mix 2014 is considered, because it represents today's conventional technology. Thus, the LCA of the small-scale SMR represents the worst case in terms of the electricity supply mix.

More detailed information about LCI and LCIA of the electricity supply mixes are listed in **Supplementary Tables S1 ans S2**.

RESULTS AND DISCUSSION OF THE LIFE CYCLE IMPACT ASSESSMENT

Comparison of Syngas Production by High-Temperature Co-electrolysis and Small-Scale Steam Methane Reforming

The comparison of the environmental categories between small-scale SMR and HT-co-electrolysis per kg of syngas produced is shown in **Figure 4** (see **Supplementary Table S9** for raw data). The figure visualizes the main process segments including expenditures for CO_2 provision by DAC, energy and water supply as well as the construction of the unit to show their contribution to the impacts. Additionally, for HT-co-electrolysis, the differences regarding the four electricity supply mixes, described above, are presented. In case of the small-scale SMR, natural gas supply as well as direct emissions during syngas production were considered supplementary. To display all impacts (unit: kg-eq.) in a single diagram, some of them had to be multiplied or divided by factors (e.g., 10, 100, 1,000; this procedure is applied for **Figures 4, 6, and 10**). The results show lower impacts for HT-co-electrolysis in terms of FD and GWP (**Figure 4**), while all other impacts are higher. For HT-co-electrolysis the electricity supply of approx. 9 kWh/kg syngas (**Table 2**) is the crucial segment regardless of the electricity supply mix. The emissions most contributing due to electricity supply are chromium (+VI) emissions into water (HTP), SO_2 and NO_x into air (AP), NO_x into air (both POCPs), SO_2 and particles (<2.5 μm) into air (PM) as well as indium (60%), silver (14%), cadmium (7%) and copper (4.5%) as resources (ADP). The ADP impacts occur during mining of raw materials and construction of power plants (fossil and renewable) and not during electricity generation. ADP for photovoltaics is highest followed by wind turbines and natural gas combined cycle power plants. The share of construction is higher for HT-co-electrolysis than for small-scale SMR, especially for ADP and HTP. The DAC is also clearly visible while the deionized water supply is negligible.

In case of the small-scale SMR, construction of the SMR plant and deionized water supply are negligible and are even lower in case of steel and nickel recycling. Direct process emissions are considerable for both POCPs and GWP. In case of POCP, direct NO_x emissions account for 30% and NO_x emissions caused by natural gas supply contribute to approx. 40% of the total POCP. Direct NO_x emissions can be further reduced by enhanced burner technology and use of a $DeNO_x$ unit. It should be mentioned again that the LCIA is based on emission calculation and not on measured plant data. The share of CO_2 supply by DAC on the total environmental impacts is quite noticeable and reaches approx. 40% for ADP and HTP, 30% for AP and still 26% for PM. The main reasons are the high electricity (0.5 kWh/kg CO_2)

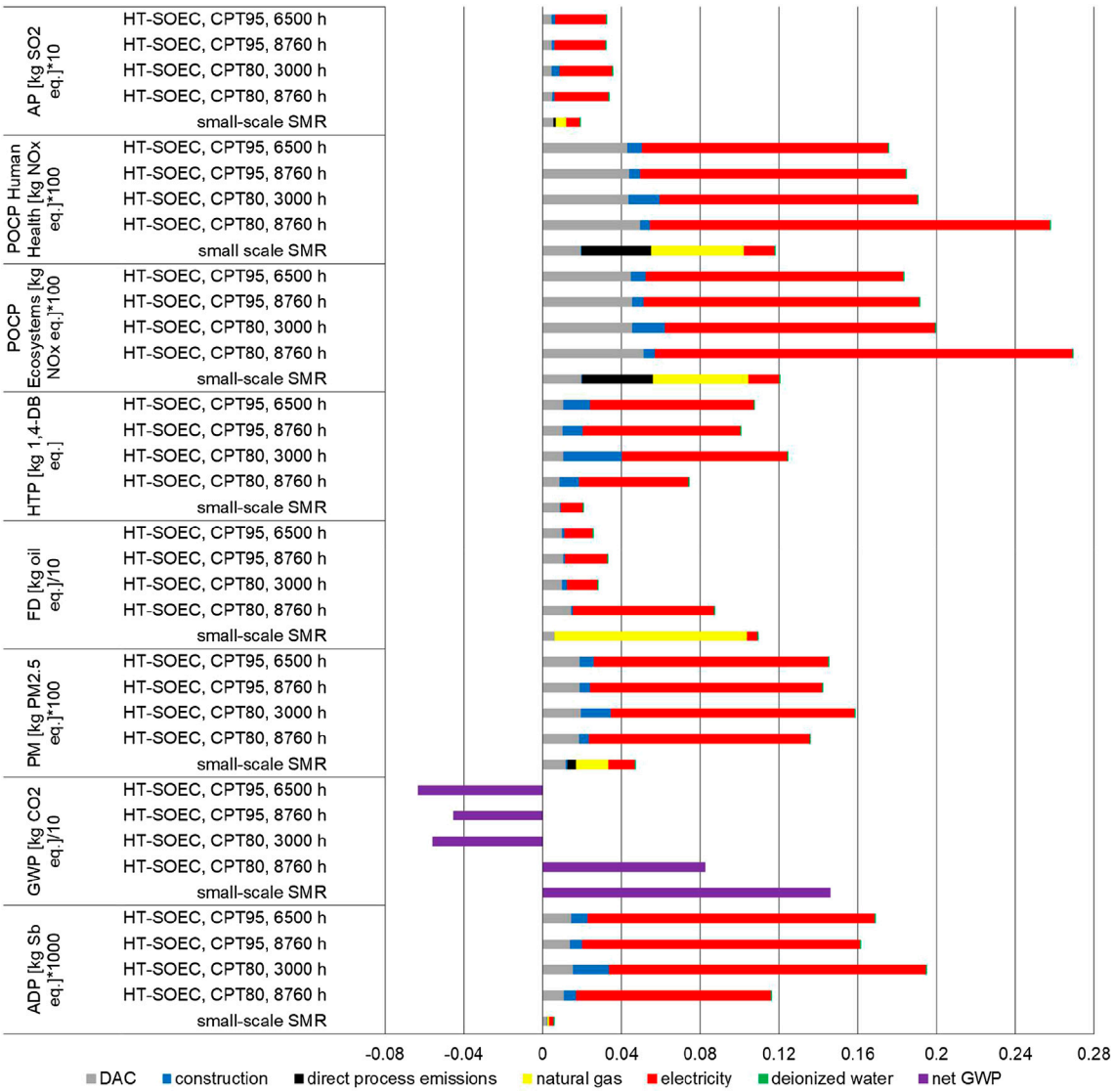

FIGURE 4 | Environmental impacts of small-scale SMR and HT-co-electrolysis for 1 kg of syngas (molar ratio $H_2/CO = 2$).

and heat demands (1.5 kWh/kg CO_2) for DAC (**Table 4**). Natural gas supply is the main cause for FD (approx. 90%) and contributes significantly to the other impacts too. It should be kept in mind that almost all values will be lower by more than 10% in case of large-scale reformer due to enhanced efficiency. In addition, FD and GWP will be significantly lower in case of biogas instead of natural gas as feed. As mentioned before, power supply is calculated with today's electricity mix in case of the small-scale SMR. Hence, GWP and FD will become lower in case of applying a greener electricity mix.

For the 80% and 95% reduction scenarios, the energy supply mixes result in a reduction of conventional CHP from 40% to 5% and a considerable increase of wind (27%-points) and a smaller increase of photovoltaics (8%-points) (**Table 5**). This leads to an improvement of most environmental impacts. Only HTP, PM and ADP worsen, as gas supply has much lower impacts here than wind and photovoltaic electricity production. For CPT80, 8,760 h, 75% of the total ADP is caused by photovoltaics supply chain, 54% of HTP by wind power supply chain, an equal contribution of all to PM, and 61% of both POCPs by the natural gas-fired CHP. These contributions change for CPT95, 8,760 h to 73% photovoltaic to ADP, 64% wind to HTP, 50% photovoltaics to PM, and 48% photovoltaics and 41% wind, respectively, to both POCPs.

Differences between the full load hours are more prominent for CPT80. In case of CPT95, the differences in terms of environmental impacts are only marginal. The most obvious difference can be found in the share of plant construction, which increases for lower full load hours.

In summary, CPT95, 6,500 h shows the lowest environmental impacts in most categories, except for HTP, PM and ADP, where the change to more renewables has higher impacts. From a

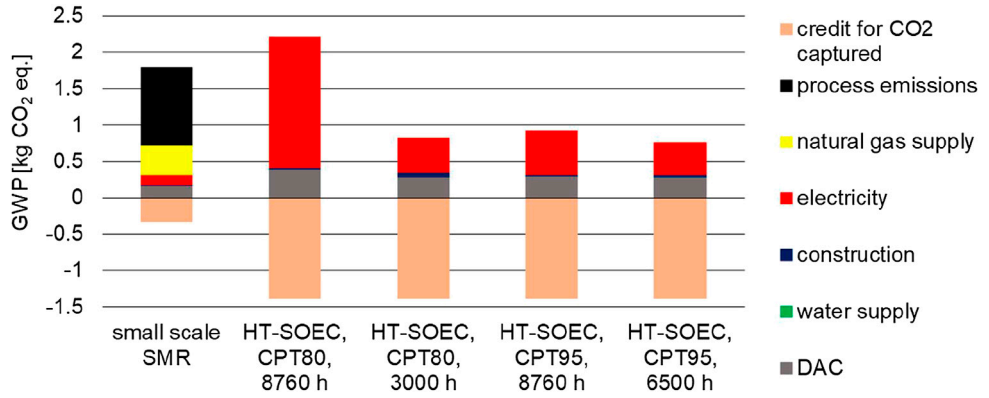

FIGURE 5 | Share of process chain stages on the total GWP of 1 kg syngas (molar ratio $H_2/CO = 2$) production by small-scale SMR and HT-co-electrolysis.

technical point of view, however, operation with less operation hours for HT-co-electrolysis is questionable, due to less syngas production, higher degradation and a shorter lifetime of cells and stacks. These aspects have not been considered in the calculation so far. In addition, operating the HT-co-electrolysis in dynamic mode results in severe technical challenges on plant operation, such as keeping temperature gradients low during ramp up and shut-down, which have not been solved by far. Nevertheless, flexibility of the HT-co-electrolysis is one of the most important factors to apply this technology for GWP reduction successfully, so further detailed assessment of fluctuation effects is mandatory. In order to bridge the fluctuations of renewable energies to achieve a high capacity utilization of HT-co-electrolysis, the use of temporary electricity storage is necessary. This is again associated with higher costs (Morgenthaler et al., 2020) and additional environmental impacts.

The discussion above shows the strong dependence of HT-co-electrolysis from the future electricity supply mix deployed, which depends on the CPT agreed upon. Using today's German electricity mix with approx. 0.48 kg CO_2 eq. per kWh in 2017 (Juhrich, 2017) means that HT-co-electrolysis would not be competitive compared to the SMR. The GWP of HT-co-electrolysis would be 6.5 kg CO_2 eq./kg syngas in contrast to 1.5 kg CO_2 eq./kg syngas for small-scale SMR. In addition, all other impact categories would be worse than for small-scale SMR. This analysis underlines the necessity to switch to sustainable power production and also to produce additional green power for PtX processes.

The GWP due to the production of the syngas is reduced by the amount of CO_2 separated from the atmosphere by DAC. In some cases the net GWP even becomes negative if the credit for CO_2 capture from DAC is higher than the CO_2 emissions from syngas production. To visualize this effect, **Figure 5** focusses on GWP. The lowest GWP achieves HT-co-electrolysis using exclusively renewables in the CPT95 scenario. This is followed by the CPT80, 3,000 h, the CPT95, 8,760 h scenario and the small-scale SMR. Last is operation in the CPT80, 8,760 h scenario due to a high share of natural gas (40%) in this electricity supply mix. The share of natural gas in the electricity supply mix CPT95, 8,760 h amounts only to 5%. This low natural gas utilization is the reason for the low GWP, which is comparable to exclusively renewable operation (**Supplementary Table S2**).

In **Figure 5**, GWP is divided into the individual process chain segments like plant construction as well as electricity, natural gas, and water supply. Also the expenditures to capture CO_2 as well as the credit for the captured CO_2 are displayed. The share of construction is hardly noticeable, and the supply of deionized water is not identifiable at all. In case of the small-scale SMR, the direct CO_2 emissions caused by natural gas burning during syngas production have the highest share on the total GWP, followed by emissions caused by natural gas supply. The credit given for CO_2 capture from atmosphere by DAC is higher for HT-co-electrolysis than for the small-scale SMR, due to the higher CO_2 demand for producing 1 kg of syngas by HT-co-electrolysis (1.38 kg of CO_2/kg syngas) than by small-scale SMR (0.33 kg of CO_2/kg syngas) (**Tables 2**, **3**). Incorporating the credit given for CO_2 capture from atmosphere by DAC, the exclusively renewable operation (CPT80 and CPT95) and the HT-co-electrolysis operated by the CPT95, 8,760 mix achieve negative net GWP's (purple bar in **Figure 4**).

Operating 8,760 h for CPT95 is the most favored scenario due to high syngas production capacity and acceptable environmental impacts.

Results Regarding Construction

Construction of both plants plays only a minor role in the overall environmental performance of syngas production (**Figure 4**). Nevertheless, it is necessary for developers of new technologies to be aware of possible risks posed by materials used. Details of material use for HT-co-electrolysis (**Figure 6**) and small-scale SMR (**Figure 10**) are presented. **Figure 7** represents separated HT-co-electrolysis details for BoP components, **Figure 8** for stack materials, and **Figure 9** for single cells.

Construction of High-Temperature Co-Electrolysis

In case of HT-co-electrolysis, the BoP has almost always a share of more than 80% on the total environmental effects of plant construction with the exception of ADP (70%) and HTP (50%) (**Figure 6**).

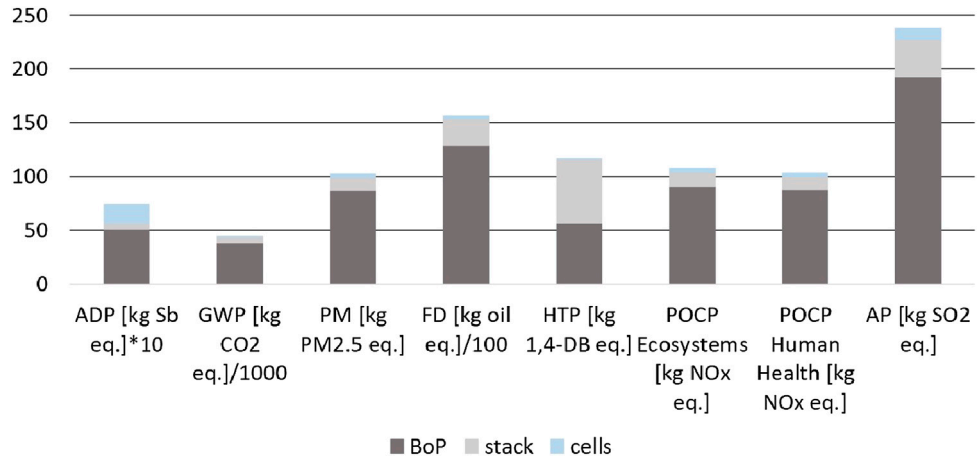

FIGURE 6 | Environmental impacts of the HT-co-electrolysis subdivided in BoP, stack and single cells.

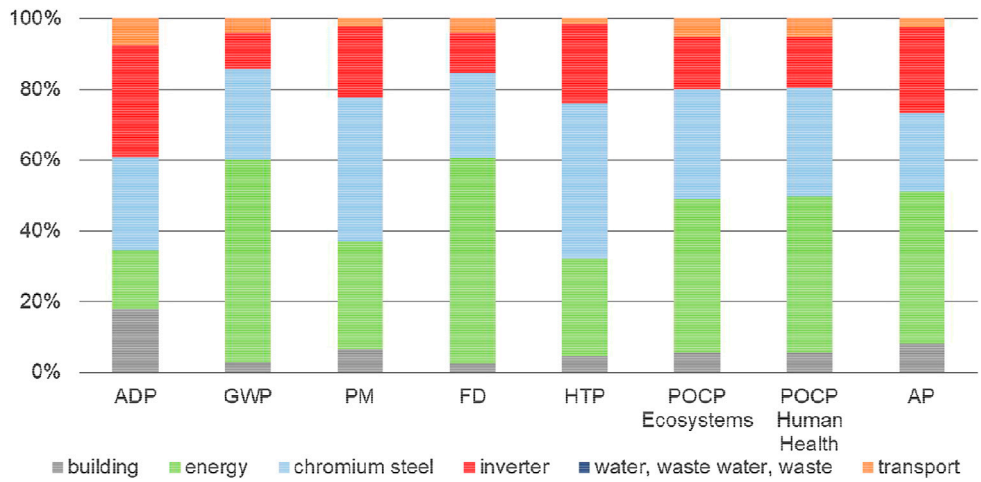

FIGURE 7 | Share of materials and energy demand on the total environmental impacts of the BoP construction for HT-co-electrolysis.

For BoP construction, 17% (ADP) up to 58% (GWP and FD) of all impacts are due to energy supply (**Figure 7**). Chromium steel causes 22% (AP)–44% (HTP) of the total impacts of BoP and 10–32% are caused by the inverter (**Figure 7**). The impacts associated with the building are low and only noticeable in the case of ADP (20%).

On the overall plant construction the stacks cause 8–16% on the total impacts with the exception of HTP (50%) (**Figure 6**). Reason for the latter is the high chromium content in the stack material Crofer22APU (**Figure 8**). Within the stack, approx. 40% of the resource depletion (ADP) are allotted to the glass-ceramic sealant due to the use of yttrium oxide (67%), barium oxide (25.5%) and 6% zirconium oxide (**Figure 8**). Gas and electricity demand required for stack construction (e.g., laser cutting, annealing, grinding of gas channels, sand blasting, ultrasonic cleaning, APS-coating, spot welding, assembly) accounts to 20–40% except for ADP (6%) and HTP (3%). Nickel, which is required for the nickel meshes, is responsible for approx. 20% of AP and PM. The chromium content in the Crofer22APU is the main causer of almost all impact categories.

The single cells are only responsible for less than 5% of each impact on the total construction impacts with the exception of ADP (23%) (**Figure 6**). The main contributor for this is yttrium oxide used in 8YSZ for substrate, electrolyte, and cathode material (**Figures 3**, **9**). The other REE's (cerium, gadolinium, lanthanum) and metal oxides of strontium, zirconium, cobalt and iron account for only 7% of the ADP and 1–2% of the other impacts. During cell production, NMVOC and NO_x are emitted due to losses of solvent and nitric acid, respectively. These emissions are responsible for both POCP impacts. Again, the nickel supply chain is the main contributor to AP (75%) and PM (70%). Nickel is required for the nickel cermet NiO/8YSZ used as substrate and cathode material. Although some sintering

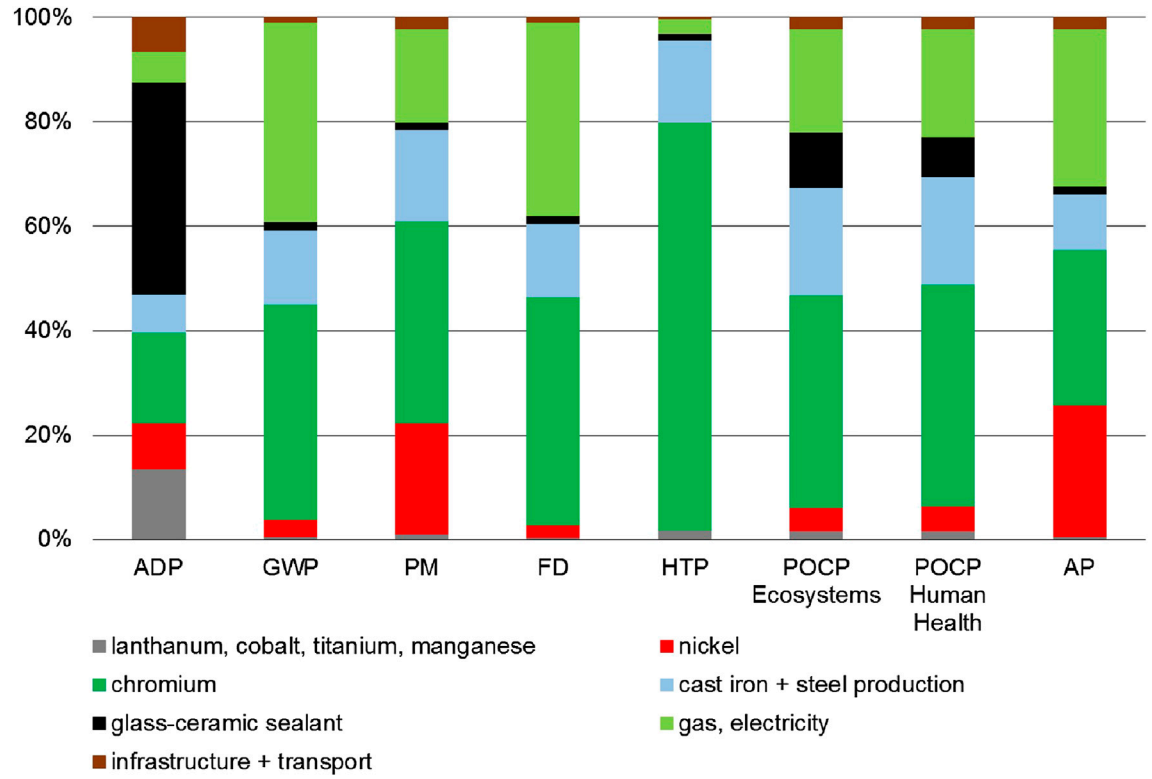

FIGURE 8 | Share of stack materials, energy demand and others on the total environmental impacts of the stack construction for HT-co-electrolysis.

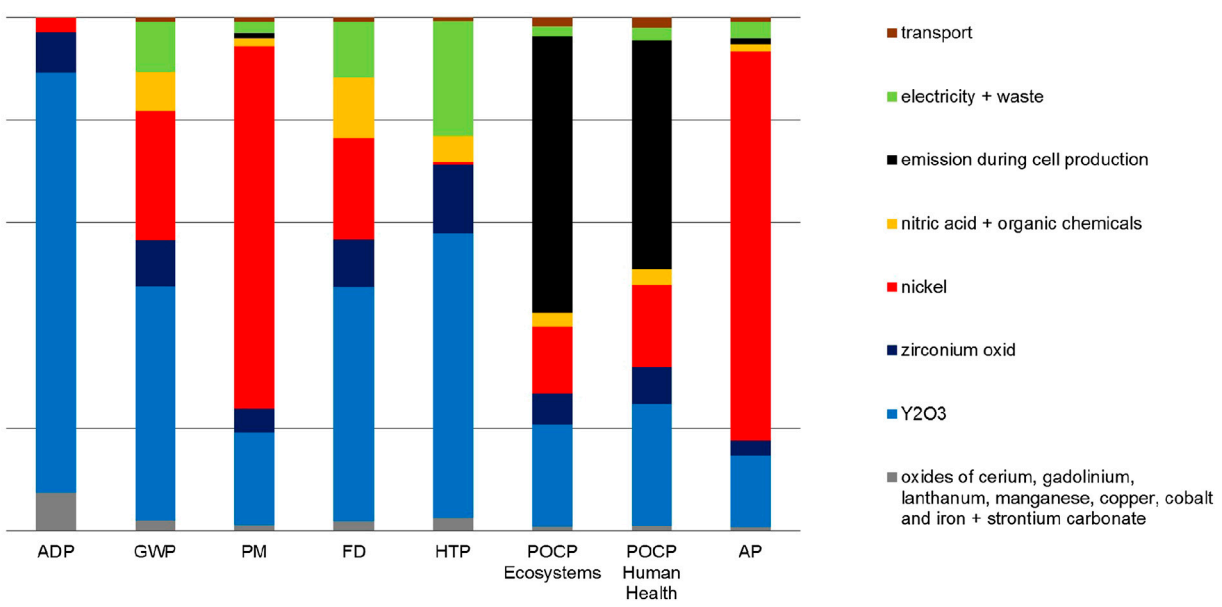

FIGURE 9 | Share of cell materials, energy demand and others on the total environmental impacts of single cell construction for HT-co-electrolysis.

processes at high temperature are required for single cell production, the electricity demand is hardly visible for almost all impact categories.

Summarizing, a significant reduction of environmental impacts regarding construction can be achieved by reducing the quantity of steel. Here other stack concepts, for example

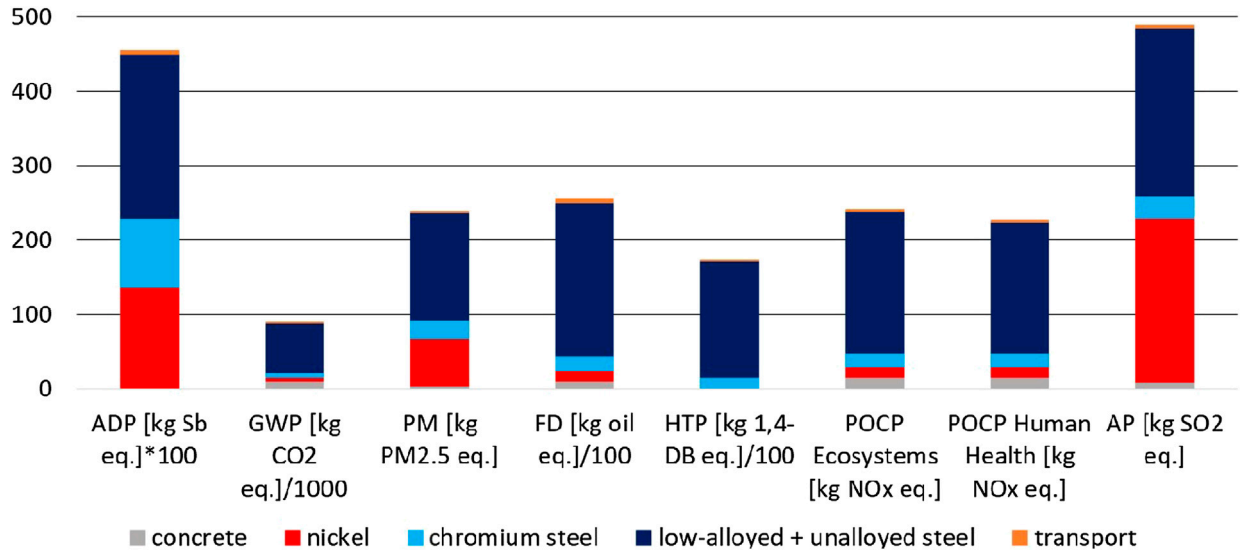

FIGURE 10 | Environmental impacts of the small-scale SMR plant subdivided according to the materials used.

with thinner interconnectors, and material recycling could be helpful.

Construction of Small-Scale Steam Methane Reformer

In case of small-scale SMR construction, the main part of the environmental impacts are caused by 34.5 tons of low-alloyed and unalloyed steel. Five hundred kg of nickel causes 30% of PM and ADP, and even 45% of AP. One thousand four hundred kg of chromium steel are responsible for 6% AP, 10% PM and HTP, and 20% ADP. One hundred tons of concrete have a considerable effect on GWP (10%) (**Figure 10**). In case of steel and nickel recycling, the small impacts of construction (**Figure 4**) can be reduced even further.

CONCLUSION

In this paper, we analyzed the following two Power-to-syngas production pathways: HT-co-electrolysis as a new PtX technology with a low TRL and SMR as their well-established fossil-based counterpart designed as a small-scale system for decentralized operation. This smaller type of SMR has a lower efficiency than the large SMR plants, because it is less energetically optimized for economic and technical reasons. The evaluation of the environmental performance of HT-co-electrolysis at an early stage of development was used to derive incentives for further research. In a HT-co-electrolysis, syngas is synthesized from conversion of CO_2 and steam. As CO_2 source, we considered DAC as a future capture technology to keep the long-term perspective of PtX in mind and be independent of local CO_2 sources. Due to the high importance of electricity as main input for HT-co-electrolysis, we included various future electricity supply mixes taking into account different CO_2 reduction targets and different full load hours due to the availability of renewable energies. This resulted in four different electricity supply scenarios.

The results of cradle-to-gate LCA without considering syngas use indicate advantages of HT-co-electrolysis compared to the small-scale SMR in terms of GWP and FD if mostly renewable energy is used. Exclusively renewable operated HT-co-electrolysis achieves negative specific net GWPs, however resulting in lower operation hours and therefore less syngas production per year. In case of CPT80, only 3,000 h operation hours are achieved, which would hinder market penetration of a novel technology. In addition, the investment costs would be high and too many load changes would make operation difficult, which would have a negative effect on the lifetime of cell and plant. Subsequent syngas using processes such us Fischer-Tropsch require higher and continuous amounts of syngas. If HT-co-electrolysis shall operate continuously (8,760 h) additional fossil-based electricity is needed. For CPT80, the share of fossil electricity is still high, so that negative net GWPs cannot be achieved. Targeting CPT95 requires a higher share of renewable electricity, which results in negative net GWP also for 8,760 h. Using today's German electricity mix, HT-co-electrolysis would be far from competitive with respect to GWP of 6.5 kg CO_2 eq./kg syngas compared to that of the SMR even at small-scale (1.5 kg CO_2 eq./kg syngas All other environmental impacts are lower for small-scale SMR, particularly due to the high electricity demand of the HT-co-electrolysis and the associated renewable electricity supply chains. While wind and PV technologies produce no emissions during electricity generation, they are associated with impacts during construction.

Besides electricity supply, the CO_2 supply is also crucial for the environmental performance of Power-to-syngas pathways. The syngas production can achieve lower global warming impacts if, e.g., CO_2 is captured from flue gases or from chemical process, which would emit the CO_2 otherwise. Using existing capture technologies, the energy demand for separation at industrial sites

is lower than for DAC. The contribution of the CO_2 supply would be reduced accordingly. This holds true for both HT-co-electrolysis and SMR.

One frequently used argument pro PtX is the potential to balance the power production and consumption in case of a large share of renewable power production. Intermittent renewable electricity could be directly used by HT-co-electrolysis, especially when more renewables have to be fed into the grid. However, offering flexibility must be carefully examined and decided on a case-by-case basis (Ausfelder et al., 2019). The advantage of flexible operation can turn into a disadvantage, as it results in higher cell and plant degradation and a shorter lifetime as well as more complicated operation and difficult integration with downstream production. Although degradation was not further analyzed in this paper, the need to focus further research on materials and processing which lower degradation potentials can be pointed out.

To use our results in a discussion about potentials of defossilization of the economy, the syngas production needs to be integrated into a wider picture. The subsequent processing of syngas to chemicals and fuels should be considered in further analysis in order to assess the full potential of HT-co-electrolysis. In addition, alternative PtX pathways need to be analyzed on the same basis and compared to each other.

Overall, the results show that HT-co-electrolysis is a promising technology to integrate renewable electricity into the chemistry and transport sector and to decrease dependence on fossil feedstock. Together with changes in the electricity sector, HT-co-electrolysis can contribute to the overall defossilization of the economy. Other technology options using captured CO_2 for syngas production such as rWGS or dry reforming with additional H_2 import produced from renewable power may also contribute to the defossilization. Hence, HT-co-electrolysis is one technological option for defossilization of the economy among others. Further sustainability assessments of various PtX technologies need to follow.

DATA AVAILABILITY STATEMENT

All datasets generated for this study are included in the manuscript/**Supplementary Material**.

AUTHOR CONTRIBUTIONS

AS: conceptualization, life cycle assessment and writing. AP and BH: technical calculation. PZ: project administration and validation.

FUNDING

The authors gratefully acknowledge funding by the German Federal Ministry of Education and Research (BMBF) within the Kopernikus Project P2X: Flexible use of renewable resources–exploration, validation and implementation of "Power-to-X" concepts.

ACKNOWLEDGMENTS

The information and advice applied from L. Blum (Institute of Energy and Climate Research, IEK-3, Electrochemical Process Engineering), N.H. Menzler (Institute of Energy and Climate Research, IEK-1, Materials Synthesis and Processing) and N. Margaritis (Central Institute for Engineering, Electronics and Analytics, ZEA-1, Engineering and Technology) from Forschungszentrum Jülich are gratefully acknowledged.

SUPPLEMENTARY MATERIAL

The Supplementary Material for this article can be found online at: https://www.frontiersin.org/articles/10.3389/fenrg.2020.533850/full#supplementary-material

REFERENCES

Adibi, N., Lafhaj, Z., and Payet, J. (2019). New resource assessment characterization factors for rare earth elements: applied in NdFeB permanent magnet case study. *Int. J. Life Cycle Assess*. 24, 712–724. doi:10.1007/s11367-018-1489-x.

Al-Kalbani, H., Xuan, J., García, S., and Wang, H. (2016). Comparative energetic assessment of methanol production from CO_2: chemical versus electrochemical process. *Appl. Energy* 165, 1–13. doi:10.1016/j.apenergy.2015.12.027.

Anicic, B., Trop, P., and Goricanec, D. (2014). Comparison between two methods of methanol production from carbon dioxide. *Energy* 77, 279–289. doi:10.1016/j.energy.2014.09.069.

Artz, J., Müller, T. E., Thenert, K., Kleinekorte, J., Meys, R., Sternberg, A., et al. (2018). Sustainable conversion of carbon dioxide: an integrated review of catalysis and life cycle assessment. *Chem. Rev.* 118 (2), 434–504. doi:10.1021/acs.chemrev.7b00435.

Ausfelder, F., Bareiß, K., Deutz, S., Dura, H., Forster, S., Fröhlich, T., et al. (2019). "Roadmap des Kopernikus-Projekts "Power-to-X": flexible Nutzung erneuerbarer Ressourcen (P2X)," in *Optionen für ein nachhaltiges Energiesystem mit Power-to-X Technologien. Nachhaltigkeitseffekte – potenziale Entwicklungsmöglichkeiten*. F. Ausfelder and H. Dura (Editors) (Frankfurt am Main: DECHEMA Gesellschaft für Chemische).

Baltrusaitis, J., and Luyben, W. L. (2015). Methane conversion to syngas for gas-to-liquids (GTL): is sustainable CO_2 reuse via dry methane reforming (DMR) cost competitive with SMR and ATR processes? *ACS Sustain. Chem. Eng.* 3 (9), 2100–2111. doi:10.1021/acssuschemeng.5b00368.

Bareiß, K., de la Rua, C., Möckl, M., and Hamacher, T. (2019). Life cycle assessment of hydrogen from proton exchange membrane water electrolysis in future energy systems. *Appl. Energy* 237, 862–872. doi:10.1016/j.apenergy.2019.01.001.

Bareiß, K., Schönleber, K., and Hamacher, T. (2018). *Szenarien für den Strommix zukünftiger, flexibler Verbraucher am Beispiel von P2X-Technologien*. Munich: Technische Universität München, Lehrstuhl für Erneuerbare und Nachhaltige Energiesysteme).

Bauer, F., and Sterner, M. (2020). Power-to-X im Kontext der Energiewende und des Klimaschutzes in Deutschland. *Chem. Ing. Tech.* 92 (1–2), 85–90. doi:10.1002/cite.201900167.

BMU (2016). *Klimaschutzplan 2050 – klimaschutzpolitische Grundsätze und Ziele der Bundesregierung*". Bundesministerium für Umwelt, Naturschutz, Bau und

Reaktorsicherheit. . Available at: https://www.bmu.de/fileadmin/Daten_BMU/Download_PDF/Klimaschutz/klimaschutzplan_2050_bf.pdf.

Bracker, J. (2017). *An outline of sustainability criteria for synthetic fuels used in transport - policy paper for Transport & Environment*. Freiburg, Germany: Öko-Institut e.V.

Chehade, Z., Mansilla, C., Lucchese, P., Hilliard, S., and Proost, J. (2019). Review and analysis of demonstration projects on power-to-X pathways in the world. *Int. J. Hydrogen Energy* 44 (51), 27637–27655. doi:10.1016/j.ijhydene.2019.08.260.

Climeworks (2017). Available at: http://www.climeworks.com/. (Accessed April 04, 2019) (Online).

Ecoinvent (2016). *Life cycle inventory database Version 3.3* (St. Gallen (Switzerland): Swiss Center for Life Cycle Inventory).

European Commission (2020). Proposal for a regulation of the European Parliament and of the Council establishing the framework for achieving climate neutrality and amending Regulation (EU) 2018/1999 (European climate law) (Brussels: COM). (Accessed April 03, 2020). COM(2020) 80 final.

European Council (2014). Agreement on climate framework until 2030. Available at: https://www.bundeskanzlerin.de/bkin-de/angela-merkel/terminkalender/reiseberichte/einigung-auf-klimarahmen-bis-2030-426584. (Accessed April 10, 2019) (Online).

Evans, S. (2017). Available at: https://www.carbonbrief.org/swiss-company-hoping-capture-1-global-co2-emissions-2025. (Accessed June 22, 2020) (Online).

Faist-Emmenegger, M., Heck, T., Jungbluth, N., and Tuchschmid, M. (2007). "Erdgas," in *Sachbilanzen von Energiesystemen: grundlagen für den ökologischen Vergleich von Energiesystemen und den Einbezug von Energiesystemen in Ökobilanzen für die Schweiz. Final report ecoinvent No. 6-V*. R. Dones (Editor) (Dübendorf, Switzerland: Paul Scherrer Institut Villigen, Swiss Centre for Life Cycle Inventories).

Fang, Q., Blum, L., Peters, R., Peksen, M., Batfalsky, P., and Stolten, D. (2015). SOFC stack performance under high fuel utilization. *Int. J. Hydrogen Energy* 40 (2), 1128–1136. doi:10.1016/j.ijhydene.2014.11.094.

Fasihi, M., Efimova, O., and Breyer, C. (2019). Techno-economic assessment of CO2 direct air capture plants. *J. Clean. Prod.* 224, 957–980. doi:10.1016/j.jclepro.2019.03.086.

Foit, S. R., Vinke, I. C., de Haart, L. G. J., and Eichel, R.-A. (2016). Power-to-Syngas – an enabling technology for the transition of the energy system? *Angew. Chem. Int. Ed.* 56 (20), 5402–5411. doi:10.1002/anie.201607552.

Frey, C. E., Fang, Q., Sebold, D., Blum, L., and Menzler, N. H. (2018). A detailed post mortem analysis of solid oxide electrolyzer cells after long-term stack operation. *J. Electrochem. Soc.* 165 (5), F357–F364. doi:10.1149/2.0961805jes.

Goedkoop, M., Heijungs, R., Huijbregts, M. A. J., De Schryver, A., Struijs, J., and Van Zelm, R. (2009). "ReCiPe 2008. A life cycle impact assessment method which comprises harmonised category indicators at the midpoint and the endpoint level," in *Report I: characterisation factors*. 1st Edn. (Den Haag, Netherlands: Ministerie van Volkshuisvesting, Ruimtelijke Ordening en Milieubeheer (VROM)). Available at: www.vrom.nl

Groß-Barsnick, S.-M., Margaritis, N., Haart, U. d., Huczkowski, P., and Quadakkers, W. J. (2018). "Interaction of a barium-calcium-silicate glass composite sealant with Sanergy HT 441," in Proceedings of the 13th European SOFC & SOE forum. E. Ivers-Tiffée, C. Endler-Schuck, A. Leonide, A. Weber, A. Häffelin, J.-C. Njodzefon, et al. (Editors). (Lucerne, Switzerland: European Fuel Cell Forum AG), 9–18.

Harboe, S., Schreiber, A., Margaritis, N., Blum, L., Guillon, O., and Menzler, N. H. (2020). Manufacturing cost model for planar 5 kWel SOFC stacks at Forschungszentrum Jülich. *Int. J. Hydrogen Energy* 45 (15), 8015–8030. doi:10.1016/j.ijhydene.2020.01.082.

Heinemann, C., Kasten, P., Bauknecht, D., Bracker, J. F., Bürger, V., Emele, L., et al. (2019). "Die Bedeutung strombasierter Stoffe für den Klimaschutz in Deutschland. Zusammenfassung und Einordnung des Wissenstands zur Herstellung und Nutzung strombasierter Energieträger und Grundstoffe," in *Kopernikus-Projekt: ENSURE – neue EnergieNetzStruktURen für die Energiewende* (Freiburg, Berlin, Darmstadt: Öko-Insitut), Förderkennzeichnen 03SFK1TO.

House, K. Z., Baclig, A. C., Ranjan, M., van Nierop, E. A., Wilcox, J., and Herzog, H. J. (2011). Economic and energetic analysis of capturing CO_2 from ambient air. *Proc. Natl. Acad. Sci. Unit. States Am.* 108 (51), 20428–20433. doi:10.1073/pnas.1012253108.

International Organization for Standardization (ISO) (2006a). *ISO 14040: environmental management - life cycle assessment - principles and framework*". Geneva, Switzerland: ISO.

International Organization for Standardization (ISO) (2006b). *ISO 14044: environmental management - life cycle assessment - requirements and guidelines*. Geneva, Switzerland: ISO.

Juhrich, K. (2017). *Spezifische Emissionsfaktoren für den deutschen Strommix*. Umweltbundesamt.

Kätelhön, A., Meys, R., Deutz, S., Suh, S., and Bardow, A. (2019). Climate change mitigation potential of carbon capture and utilization in the chemical industry. *Proc. Natl. Acad. Sci. Unit. States Am.* 116 (23), 11187–11194. doi:10.1073/pnas.1821029116.

Khan, H. (2018). *Global syngas overview - 2018*. (Houston, Brussels, Singapore: Stratas Advisors).

Koj, J. C., Wulf, C., and Zapp, P. (2019). Environmental impacts of power-to-X systems - a review of technological and methodological choices in Life Cycle Assessments. *Renew. Sustain. Energy Rev.* 112, 865–879. doi:10.1016/j.rser.2019.06.029.

Linde, A. G. (2019). HYDROPRIME®-Wasserstoffgeneratoren [Online]. Available at: https://www.linde-engineering.com/de/process-plants/furnaces_fired_heaters_incinerators_and_t-thermal/steam_reformer_furnaces/index/hydroprime.html (Accessed September 16, 2019).

Liu, C. M., Sandhu, N. K., McCoy, S. T., and Bergerson, J. A. (2020). A life cycle assessment of greenhouse gas emissions from direct air capture and Fischer–Tropsch fuel production. *Sustain. Energy Fuels* 4 (6), 3129–3142. doi:10.1039/C9SE00479C.

Lozanovski, A. (2019). Life cycle assessment of a commercial scale CO_2 - direct air capture plant," in 17th international conference on carbon dioxide utilization (ICCDU). (Aachen, Germany: DECHEMA).

Luu, M. T., Milani, D., Bahadori, A., and Abbas, A. (2015). A comparative study of CO_2 utilization in methanol synthesis with various syngas production technologies. *J. CO_2 Util.* 12, 62–76. doi:10.1016/j.jcou.2015.07.001.

Menzler, N. H., Malzbender, J., Schoderböck, P., Kauert, R., and Buchkremer, H. P. (2014). Sequential tape casting of anode-supported solid oxide fuel cells. *Fuel Cells* 14 (1), 96–106. doi:10.1002/fuce.201300153.

Morgenthaler, S., Kuckshinrichs, W., and Witthaut, D. (2020). Optimal system layout and locations for fully renewable high temperature co-electrolysis. *Appl. Energy* 260 (15). doi:10.1016/j.apenergy.2019.114218.

Müller, L. J., Kätelhön, A., Bachmann, M., Zimmermann, A., Sternberg, A., and Bardow, A. (2020). A guideline for life cycle assessment of carbon capture and utilization. *Front. Energy Res.* 8 (15). doi:10.3389/fenrg.2020.00015.

Pehnt, M. (2002). Ganzheitlichen Bilanzierung von Brennstoffzellen in der Energie- und Verkehrstechnik," in *Fortschrittsberichte VDI, reihe 6, energietechnik, Nr. 476* (Düsseldorf: VDI Verlag).

Peschel, A. (2020). Industrial perspective on hydrogen purification, compression, storage, and distribution. *Fuel Cells* 20 (4). doi:10.1002/fuce.201900235

Primas, A. (2007). Life cycle inventories of new CHP systems," in *Ecoinvent report* (Basler & Hofmann AG, Dubendorf, & Zurich: Swiss Centre for Life cycle Inventories).

Quadakkers, W. J., Pirón-Abellán, J., and Shemet, V. (2004). Metallic materials in solid oxide fuel cells. *Mater. Res.* 7**,** 203–208. doi:10.1590/S1516-14392004000100027

Reiter, G., and Lindorfer, J. (2015). Global warming potential of hydrogen and methane production from renewable electricity via power-to-gas technology. *Int. J. Life Cycle Assess.* 20 (4), 477–489. doi:10.1007/s11367-015-0848-0.

Repenning, J., Emele, L., Blanck, R., Böttcher, H., Dehoust, G., Förster, H., et al. (2015). *Klimaschutzszenario 2050 - 2. Endbericht* (Berlin, Karlsruhe: Studie im Auftrag des Bundesministeriums für Umwelt, Naturschutz, Bau und Reaktorsicherheit).

Rostrup-Nielson, J. R. (2005). "Natural gas: fuel or feedstock?," in Sustainable strategies for the upgrading of natural gas: fundamentals, challenges, and opportunities. Proceedings of the NATO advanced study Institute, Vilamoura, Portugal, July 6–18, 2003. E.G. Derouane, V. Parmon, F. Lemos, and F. R. Ribeiro (Editors) (Dordrecht, Netherlands: Springer Netherlands).

RWE (2019). Niederaußem ist Schauplatz wichtiger technologischer fortschritte [Online]. Köln, 28.05.2019. Available at: https://www.group.rwe/presse/rwe-power/2019-05-28-niederaussem-ist-schauplatz-wichtiger-technologischer-fortschritte (Accessed January 15, 2020).

Sanz-Pérez, E. S., Murdock, C. R., Didas, S. A., and Jones, C. W. (2016). Direct capture of CO_2 from ambient air. *Chem. Rev.* 116 (19), 11840–11876. doi:10.1021/acs.chemrev.6b00173.

Schafbauer, W., Menzler, N. H., and Buchkremer, H. P. (2014). Tape casting of anode supports for solid oxide fuel cells at Forschungszentrum Jülich. *Int. J. Appl. Ceram. Technol.* 11 (1), 125–135. doi:10.1111/j.1744-7402.2012.02839.x.

Sternberg, A., and Bardow, A. (2016). Life cycle assessment of power-to-gas: syngas vs methane. *ACS Sustain. Chem. Eng.* 4 (8), 4156–4165. doi:10.1021/acssuschemeng.6b00644.

Sternberg, A., and Bardow, A. (2015). Power-to-what?–environmental assessment of energy storage systems. *Energy Environ. Sci.* 8 (2), 389–400. doi:10.1039/C4EE03051F.

Sternberg, A., Jens, C. M., and Bardow, A. (2017). Life cycle assessment of CO_2-based C1-chemicals. *Green Chem.* 19 (9), 2244–2259. doi:10.1039/C6GC02852G.

Thema, M., Bauer, F., and Sterner, M. (2019). Power-to-Gas: electrolysis and methanation status review. *Renew. Sustain. Energy Rev.* 112, 775–787. doi:10.1016/j.rser.2019.06.030.

thinkstep (2018). GaBi (ganzheitliche bilanzierung) version 8.7.018. Available: https://www.thinkstep.com/software/gabi-lca/ [Dataset].

Uniper SE (2019). Methanisierungsanlage in Falkenhagen geht in Betrieb und liefert synthetisches Methan – weiterer Schritt für eine erfolgreiche Energiewende [Online]. Düsseldorf. Available at: https://www.uniper.energy/news/methanisierungsanlage-in-falkenhagen-geht-in-betrieb-und-liefert-synthetisches-methan–weiterer-schritt-fur-eine-erfolgreiche-energiewende/ (Accessed January 15, 2020).

van der Giesen, C., Kleijn, R., and Kramer, G. J. (2014). Energy and climate impacts of producing synthetic hydrocarbon fuels from CO_2. *Environ. Sci. Technol.* 48 (12), 7111–7121. doi:10.1021/es500191g.

von der Assen, N., Müller, L. J., Steingrube, A., Voll, P., and Bardow, A. (2016). Selecting CO_2 sources for CO_2 utilization by environmental-merit-order curves. *Environ. Sci. Technol.* 50 (3), 1093–1101. doi:10.1021/acs.est.5b03474.

Wulf, C., Linßen, J., and Zapp, P. (2018). Review of power-to-gas projects in Europe. *Energy Procedia* 155, 367–378. doi:10.1016/j.egypro.2018.11.041.

Zhang, X., Bauer, C., Mutel, C. L., and Volkart, K. (2017). Life Cycle Assessment of Power-to-Gas: approaches, system variations and their environmental implications. *Appl. Energy* 190, 326–338. doi:10.1016/j.apenergy.2016.12.098.

Zheng, Y., Wang, J., Yu, B., Zhang, W., Chen, J., Qiao, J., et al. (2017). A review of high temperature co-electrolysis of H_2O and CO_2 to produce sustainable fuels using solid oxide electrolysis cells (SOECs): advanced materials and technology. *Chem. Soc. Rev.* 46 (5), 1427–1463. doi:10.1039/C6CS00403B.

Conflict of Interest: The authors AP and BH were employed by the company Linde AG.

The remaining authors declare that the research was conducted in the absence of any commercial or financial relationships that could be construed as a potential conflict of interest.

frontiers in Energy Research

ORIGINAL RESEARCH
published: 26 November 2020
doi: 10.3389/fenrg.2020.509052

Characterisation of a Nickel-iron Battolyser, an Integrated Battery and Electrolyser

John P. Barton[1,2]*, *Rupert J. L. Gammon*[1] and *Abdulla Rahil*[1,3]

[1]Institute of Energy and Sustainable Development (IESD), De Montfort University, Leicester, United Kingdom, [2]Centre for Renewable Energy Systems Technology (CREST), School of Mechanical, Electrical and Manufacturing Engineering, Loughborough University, Loughborough, United Kingdom, [3]The Centre for Automotive & Power Systems Engineering (CAPSE), Faculty of Computing, Engineering and Science, University of South Wales, Pontypridd, Wales, United Kingdom

Electricity systems require energy storage on all time scales to accommodate the variations in output of solar and wind power when those sources of electricity constitute most, or all, of the generation on the system. This paper builds on recent research into nickel-iron battery-electrolysers or "battolysers" as both short-term and long-term energy storage. For short-term cycling as a battery, the internal resistances and time constants have been measured, including the component values of resistors and capacitors in equivalent circuits. The dependence of these values on state-of-charge and temperature have also been measured. The results confirm that a nickel-iron cell can hold 25% more than its nominal charge. However, this increased capacity disappears at temperatures of 60°C and may be dissipated quickly by self-discharge. When operating as an electrolyser for long-term energy storage, the experiments have established the importance of a separation gap between each electrode and the membrane for gas evolution and established the optimum size of this gap as approximately 1.25 mm. The nickel-iron cell has acceptable performance as an electrolyser for Power-to-X energy conversion but its large internal resistance limits voltage efficiency to 75% at 5-h charge and discharge rate, with or without a bubble separation membrane.

Keywords: nickel-iron battery, hydrogen, battolyser, electrolysis, Edison cell, equivalent circuit model

OPEN ACCESS

Edited by:
Valerie Eveloy,
Khalifa University,
United Arab Emirates

Reviewed by:
Mariano Martín,
University of Salamanca, Spain
Surendra Kumar Martha,
Indian Institute of Technology Hyderabad, India

Correspondence:
John Barton
j.p.barton@lboro.ac.uk

Specialty section:
This article was submitted to Process and Energy Systems Engineering, a section of the journal Frontiers in Energy Research

Received: *31 October 2019*
Accepted: *26 October 2020*
Published: *26 November 2020*

Citation:
Barton JP, Gammon RJ L and Rahil A (2020) Characterisation of a Nickel-iron Battolyser, an Integrated Battery and Electrolyser. Front. Energy Res. 8:509052. doi: 10.3389/fenrg.2020.509052

INTRODUCTION

Energy storage is becoming an increasingly critical component of low-carbon energy systems at all scales, from national networks down to micro-grids. At the smaller end of this range, batteries are routinely used at the heart of household or community-level energy supply networks, typically powered by solar photovoltaics and wind turbines, especially in remote and Developing World applications. However, it is often the battery that is the weakest part of a stand-alone mini-grid as it is the most vulnerable, and yet most expensive, element of the system (Wiemann et al., 2011; Innovation Energie Développement (IED), 2013; Crossland et al., 2015; Danish Energy Management, 2019). Industrialised nations also are installing batteries, in their national grids, for the purposes of frequency response and peak lopping.

Just one battery chemistry, nickel-iron (Ni-Fe), stands out from the rest for its durability and robustness. Lead-acid batteries are degraded by high temperatures and by being stored in a partially discharged state (Ruetschi 2004). Lithium-ion batteries are more expensive and are degraded by high temperatures, deep cycling and by being stored at a high state-of-charge (SOC) (Ecker et al., 2014).

Ni-Fe batteries are also more expensive than lead-acid, and have several drawbacks, for example a low round-trip efficiency of 50%–80%, and a high self-discharge rate of 1%–2% per day at 25°C and much faster at higher temperatures (Chakkaravarthy et al., 1991; Shukla et al., 1994). Nevertheless, Ni-Fe batteries continue to occupy a niche in the battery market where ultra-reliability and long cycle life are required (Dougherty et al., 1995). The service life can be 20 or 25 years (Chakkaravarthy et al., 1991) and there are examples of Ni-Fe batteries lasting for 40 years (Soutar, 2018). Research in Ni-Fe batteries has continued (Hariprakash et al., 2005; Gaffor et al., 2010; Kong et al., 2020) including an innovation to improve the power density (Wang et al., 2012).

Wind and solar power outputs vary on all timescales, as does energy demand. Batteries are practical for storing and delivering energy over diurnal cycles, but weekly patterns of demand, weather-related variation over several days or weeks, and seasonal variations are more difficult to cope with. Hydrogen has long been proposed as a long-term energy storage medium for such cases (Borgschulte, 2016). Such hydrogen production is an example of Power-to-X in its own right and an input for sustainable production of synthetic fuels such as methanol, methane and ammonia.

Recently, there has been renewed interest in using Ni-Fe technology as a combined battery and electrolyser, a so-called "battolyser" (Mulder and Weninger, 2016; Mulder et al., 2017). As well as being potentially well suited to the mini-grid applications discussed above, such a device might also be scaled up for large-capacity energy storage on national-scale energy networks.

While the focus of Mulder et al. (2017) was to verify that the Ni-Fe device can operate as both a battery and an electrolyser, the present paper explores how it might perform under a wider envelope of temperatures and charge rates and discharge rates in the real world, and considers some of the design parameters of a practical device. The present paper also measures the transient response of a Ni-Fe cell and thereby establishes an equivalent circuit that will be useful when designing a battolyser or Ni-Fe cell.

The aim of the experiment was to simulate the operation of a battolyser where the maximum power input as an electrolyser is much greater than the power input or output as a battery. This design philosophy maximises the value of the capital investment by maximising the useful energy throughput.

It is anticipated that such a battolyser will produce hydrogen for high-power and high-energy loads such as cooking and water heating, while also storing electrical power for lower power and lower energy loads such as lighting, mobile phone charging, televisions, radios and computers. The intended application is in mini-grids for communities in the developing world that are not connected to the national grid. The hydrogen will provide a sustainable alternative to liquefied petroleum gas as a cooking gas, and an alternative to biogas for communities without sufficient biological feedstocks. Clean cooking fuels are an essential part of achieving the UN Sustainable Development Goals (SDG), especially SDG 7 (United Nations 2019).

Materials and Methods describes the experiments performed. *Results* shows the results and discusses them. *Discussion* describes the next steps and the design modifications necessary in a practical, commercial device.

MATERIALS AND METHODS

Experiments were conducted at small laboratory scale and the apparatus was similar to that of Mulder et al. (2017) as described below.

Electrodes

The present experiments used electrodes extracted from a commercially sold Ni-Fe cell, manufactured by the Sichuan Changhong Battery Co., Ltd. The cell was the smallest size available, with a nominal capacity of 10 Ah and voltage of 1.2 V. The cell consisted of pocket-plate electrodes of alternating polarity. Three negative (iron containing) anode plates were interspersed between with four positive (nickel containing) cathode plates. This cell was chosen because it was readily available and provided plates of an appropriate size for benchtop experimentation. The construction of a battolyser cell using components from a commercial battery offers an easier route to market than the construction of components within house.

In order to convert the cell from a battery to a battolyser, it was necessary to insert a bubble separation membrane between the plates and to collect gas produced by electrolysis. For simplicity, just one electrode plate of each type was used in the present experiments. Since just two out of the seven original plates were used, the new cell capacity was estimated as 3 Ah. The physical size of each electrode was 7 cm by 7 cm, and therefore the maximum current density achievable was just over 200 mA cm^{-2} using a 10 A power supply.

Electrolyte

This assembly was placed in potassium hydroxide solution at 30% concentration by weight. Unlike the experiments of Mulder et al. (2017), the electrolyte did not include any sodium hydroxide or lithium hydroxide. Only potassium hydroxide solution was used, because it is easier to obtain and more similar to the electrolyte used in an alkaline electrolyser (Hydrogenics, 2013; NEL Hydrogen, 2020; Keçebaş et al., 2019). In future tests, the long-term durability of the battolyser may be improved by the addition of lithium hydroxide to protect the positive electrode against migrated ferric hydroxide (Shukla et al., 1994).

Membrane

The bubble separation membrane was the same material as used by Mulder et al. (2017): Zirfon-Perl-UTP500 from Agfa Speciality Products. This was chosen because it is an available, low-cost asbestos free membrane material.

Data Acquisition

Currents and voltages were measured using handheld meters. Gases were collected over water using measuring beakers. The

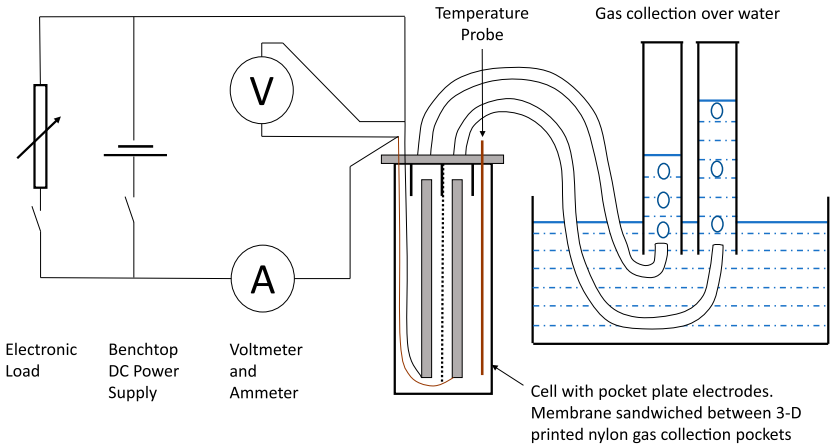

FIGURE 1 | Experimental setup.

temperature of the cell was measured using a k-type thermocouple probe. A diagram of the experimental set-up is shown in **Figure 1**. The voltmeter was placed directly on the cell terminals to minimise the effect of contact resistances.

It was not possible to determine whether the cell capacity was limited by the positive or negative electrodes since no reference electrode was available and electrode voltages were not measured relative to a reference voltage.

Experiments

The experiments were designed to test the battolyser at low and high current densities to simulate the intended application in mini-grids. Electrical charging and discharging were conducted at currents of 0.6 A (C/5 rate) and 1.5 A (C/2 rate). Electrolysis tests were conducted at up to 10 A (3.3C rate).

The experiments were conducted in 2 phases. In the first phase, the gap between the electrodes and membrane was varied and its effect on cell electrical efficiency and electrolysis efficiency were measured. This was done to establish the optimum gap, which is a trade-off between length of electrical conduction path and the ability of bubbles to escape during electrolysis.

In the second phase, the experimental cell was rebuilt to enable gas collection. The temperature, charge rate and discharge rate were varied, to explore the effects of high ambient temperature and high renewable energy input rates that might be encountered in a larger battery as part of a practical energy storage system. Experiments at 20°C were carried out with no temperature control other than the room thermostat. Experiments at 40 and 60°C were carried out with the cell in a thermostatically controlled water bath. The heat dissipated inside the cell during charging and discharging was 3 W or less. The heat dissipated during electrolysis was 30 W or less for a much shorter period. The thermal mass of the cell and the large, uninsulated surface area were such that the temperature rise of the experimental cell due to self-heating was negligible, as confirmed by the temperature probe inside the cell.

In phase 2, the additional cell capacity observed by Mulder et al. (2017) and electrolysis gas volumes were measured to establish the real cell capacity and total energy efficiency.

Measurements Taken

Electrical measurements were used to measure the total charge entering and leaving the cell and voltage as a function of time and charge level. Thus, as the cell was cycled, the charge efficiency (Coulombic efficiency) and overall energetic efficiency were measured.

Cell Equivalent Circuit and Interruption Tests

During the cell cycling, the charging and discharging was periodically interrupted to establish the transient response of the cell (Stroe et al., 2016). From this, the component values of an equivalent circuit with two RC networks (Tian et al., 2014; Zhang C et al., 2018) were calculated, as shown in **Figure 2**. In order to fully model the transient characteristics of the cell, an equivalent circuit with two resistor-capacitor pairs was chosen and found to

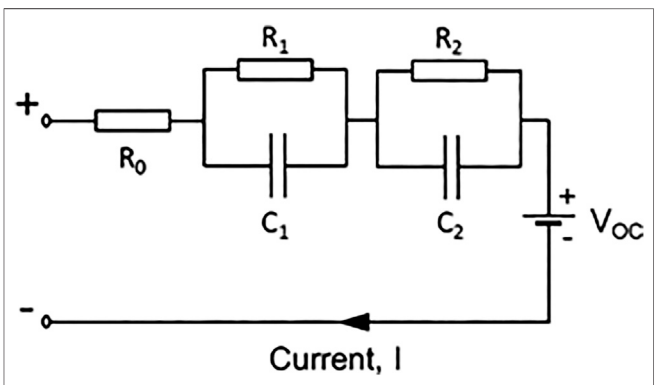

FIGURE 2 | Equivalent circuit of the Ni-Fe cell.

be a good fit to the data. With this model, it will be possible to calculate the ability of a Ni-Fe battery to meet transient loads of various sizes and durations.

Each of the parameters was calculated from measurements and in some cases found to be functions of state-of-charge (SOC), temperature and cell construction. Open circuit voltage (V_{OC}) also exhibits hysteresis between charging and discharging.

Interruption tests were used to calculate the component values of the equivalent circuit. Data was measured every 10 s for 5 min as shown in the enlarged insets of **Figure 3** curve was fitted to the data as a sum of two decaying exponential terms, **Eqs 1–7**.

$$V = V_{OC} + IR_0 + A_1 e^{-t/\tau_1} + A_2 e^{-t/\tau_2} \quad (1)$$

Constants τ_1 and τ_2 are the time constants of the resistor-capacitor circuits:

$$\tau_1 = R_1 C_1 \quad (2)$$

$$\tau_2 = R_2 C_2 \quad (3)$$

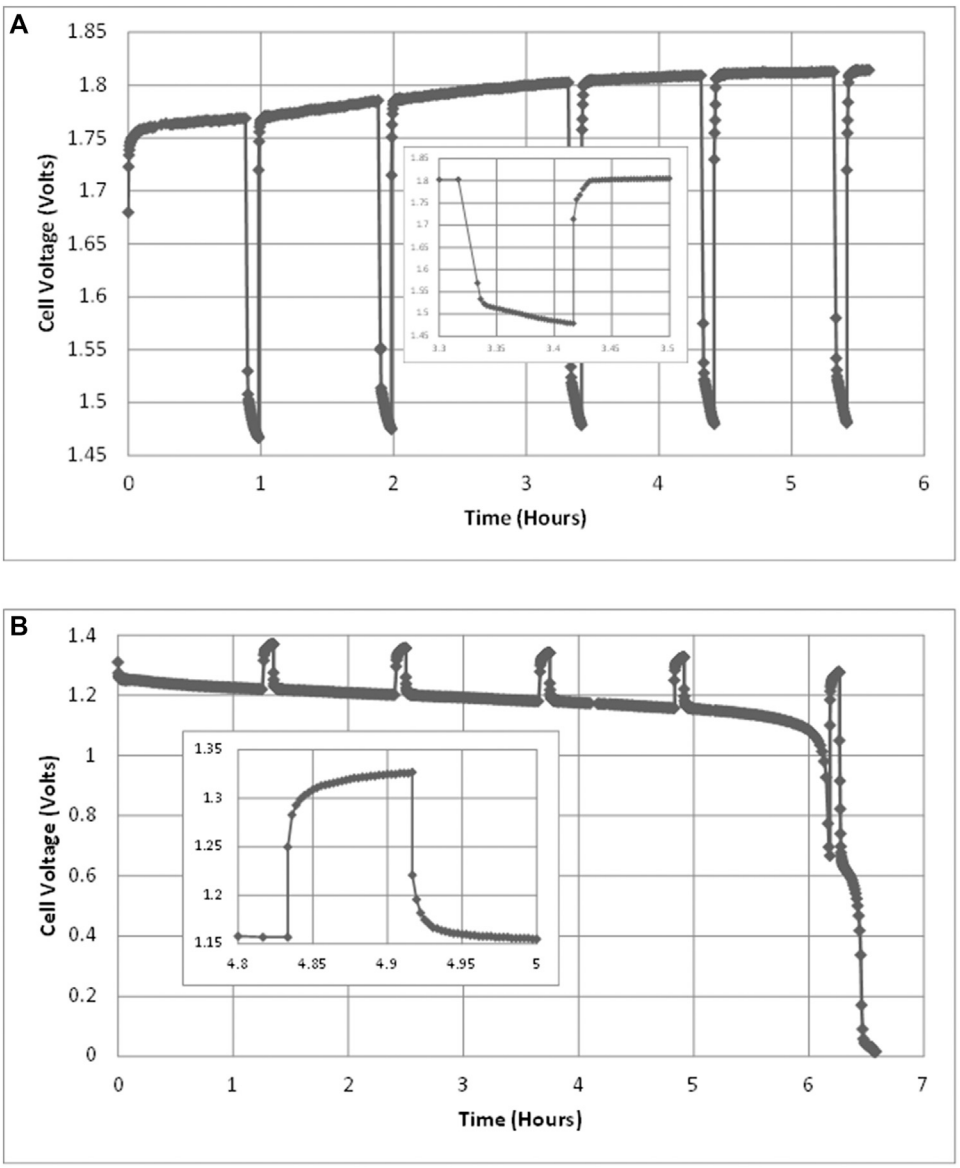

FIGURE 3 | Cell voltages during **(A)** charging test at 1.5 A, 40°C and **(B)** discharging test at 0.6 A, 40°C. Each test includes five interruption tests of 5 min each. An example interruption is shown in each, enlarged and inset.

Taking the example of an interruption during charging, the voltage before interruption (time t = 0) is V_0. In a fully stabilised cell, the capacitors have zero current flowing through them, and therefore:

$$V_0 = V_{OC} + IR_0 + IR_1 + IR_2 \quad (4)$$

The initial values of the curve-fit functions are found by extrapolation of the components $V_1 = A_1 e^{-k_1 t}$ and $V_2 = A_2 e^{-k_2 t}$ back to time t = 0, the instant of current interruption. Thus:

$$R_0 = (V_0 - V_1 - V_2 - V_{OC})/I \quad (5)$$

$$R_1 = V_1/I \quad (6)$$

$$R_2 = V_2/I \quad (7)$$

When resistances R_1 and R_2 have been established, the capacitances can also be calculated using **Eqs 2** and **3**:

$$C_1 = \tau_1/R_1 \quad \text{and} \quad C_2 = \tau_2/R_2$$

The components of the equivalent circuit can also be calculated from the recovery period after interruption. However, the method is not as easy, or as accurate, for the following reasons:

(1) After just 5 min of interruption, the capacitances of the equivalent circuit have not fully discharged. The conditions at the time of reconnection are not fully known and therefore, a curve fit of data over the following 5 min would not be as accurate.
(2) When recovering to a state of charging or discharging, the open-circuit voltage of the cell, V_{OC}, is continuously changing. There is no fixed asymptote to which the cell recovers.

Electrolysis Tests

When fully charged, and also when not fully charged, the cell was tested as an electrolyser by increasing the applied voltage. The voltage was increased from 1.5 V in steps of 0.05–3.0 V or until a current of just over 10 A was achieved. These tests simulate periods surpluses of power in a mini-grid, caused for example by an increase in wind turbine power or midday solar PV power.

Where possible, the volume of hydrogen was measured separately from the volume of oxygen. However, there was an inadequate seal between the two halves of the cell and only a total volume of gas could be measured.

Measurements of Cell Electrical Capacity

The capacity of the cell was measured during discharge by Coulomb counting, i.e., an integration of current drawn from the cell between full and empty. The starting point for discharge was a high SOC, soon after the end of charging. This "full" SOC has no clear markers, other than the point during charging at which the cell voltage plateaus and stops rising. An indefinite amount of charge can still be inserted into the fully-charged cell, but no longer results in the storage of more electrical charge. Instead, energy is consumed in hydrogen production and a much smaller amount is dissipated through side reactions of the cell, **Eq. 8**:

$$\textit{Full Charge Current} = \textit{Side Reactions} + \textit{Hydrogen Production} \quad (8)$$

One way to detect the fully charged condition is to wait until the cell voltage has not increased by more than 1 mV in 5 min (in constant-current mode). Another way is to wait until cell current has not dropped by more than 10 mA in 5 min (constant-voltage mode). A third way is simply to leave the cell charging overnight. All these methods have been tried in the tests described here.

Discharge was not cut off at the point of voltage collapse since that event is not well defined and very dependent on the discharge rate. Discharge was continued with a terminal voltage very close to zero. A more repeatable end point for discharging can be defined as when the voltage has collapsed, the cell has been shorted out and the current has dropped to a very low level (typically below 0.15 A). At this "empty" point, the current is dropping and exponentially approaching zero. The cell always carries some residual charge, and to completely flatten it would take an unfeasibly long time. The best way to estimate this residual charge is therefore to fit an exponential function to the measured discharge current and to integrate this function, **Eqs 9** and **10**.

$$\textit{Residual Discharge Current} = A_3 e^{-t/\tau_3} \quad (9)$$

$$\textit{Residual Charge} = \int_0^\infty A_3 e^{-t/\tau_3} = \left[A_3 \tau_3 e^{-t/\tau_3}\right]_0^\infty = A_3 \tau_3 \quad (10)$$

The parameters τ_3 and A_3 are found by curve fitting. The residual charge was found to be relatively small compared to the total cell capacity and was added onto the cell SOC determined by coulomb counting.

RESULTS

The sections below describe the results of charging, discharging and electrolysis tests together with the calculated cell model parameter values.

Cell Voltage

As described above, charging and discharging tests were interrupted in order to measure the internal resistance of the cell. Therefore, the raw voltage measurements over time typically look like those in **Figure 3** for a charging test and for a discharge test.

Excluding the interruptions and excluding the period of voltage stabilisation after each interruption test, charge and discharge curves were created. These have been plotted as a function of cumulative charge, for example **Figure 4**. Some noise appears on the curves, both due to the interruption tests and because in phase 1 the variable resistor required repeated adjustment to achieve constant current.

It appears that the capacity of the cell increased as it was cycled, and that the actual capacity was greater than the nominal 3 Ah. It can also be seen that the total internal resistance of the cell reduced on second and subsequent cycles.

Open Circuit Voltages

The open-circuit voltages, V_{OC}, were calculated, being the asymptote of each interruption test. V_{OC} is plotted against cumulative cell charge for tests from phase 2 in **Figure 5**. Phase 1 tests are excluded from **Figure 5** because the corrosion of the copper wires may have affected the apparent cell voltage. V_{OC} exhibits some scatter, reflecting uncertainty in the calculation of the asymptote of voltage. Nevertheless, some patterns do emerge:

(1) There is a hysteresis, or difference, between charging V_{OC} and discharging V_{OC}. Either this is a genuine difference that depends on the direction of the most recent current, or the voltage stabilisation takes longer than can be measured in a 5-min interruption test due to internal resistances.
(2) The hysteresis is larger at low SOC than high SOC.
(3) When charging at ambient temperature, V_{OC} is higher than in other tests. However, the cell may not have fully stabilized after being rebuilt. Some discharging tests at ambient temperature were excluded from **Figure 5** for this reason.
(4) There is no strong correlation of V_{OC} with temperature.

Ohmic Resistance

The ohmic resistance (R_0) of the cell and its electrical connections was calculated from the initial voltage rise, or fall, of an interruption test. For most tests, R_0 was about 0.2 Ω. Four observations can be made:

(1) When the SOC is very low, the R_0 for discharging is much higher than in other cases, up to 0.8 Ω. This is consistent with the surface area of the active chemical species, iron and nickel oxyhydroxide, being reduced as their abundance is depleted.
(2) When the cell has a membrane but no gap each side of the membrane, R_0 is higher than in the other tests, up to values between 0.3 and 0.5 Ω, especially during charging and toward high SOC. This could be because of bubble blinding, where bubbles are trapped against the electrodes and unable to escape by buoyancy. These bubbles obstruct the flow of ions through the electrolyte.
(3) When the cell has a membrane and a gap of 2.5 mm each side, R_0 is slightly higher than when the gaps are just 1.25 mm. This is as expected, due to the increased length of the conduction path through the electrolyte.
(4) When the cell had no membrane, R_0 was not significantly reduced. The addition of a membrane does not therefore significantly impact on the function of the cell as a battery.

Time Constants and R-C Equivalent Circuit Component Values

When each of the parameters in each test were plotted against SOC, no strong trends were evident except for an increase in resistances at very low SOC; cell construction and temperature made very little difference. Therefore, average values have been given, **Table 1**. Each parameter was averaged across all

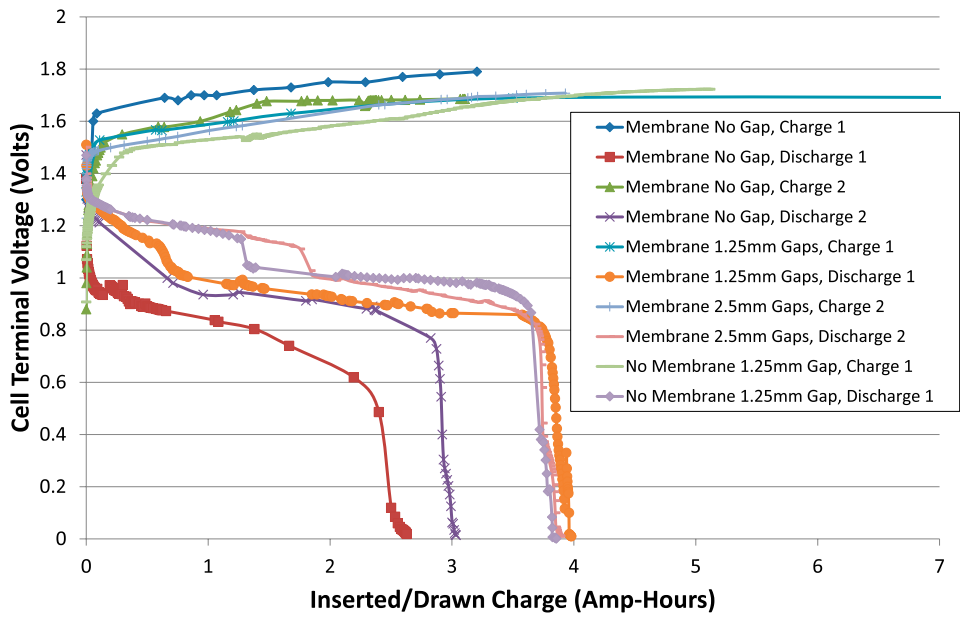

FIGURE 4 | Cell voltages during charge and discharge excluding interruptions. The current was ± 0.6 A (C/5 rate) and the cell temperature was room temperature, about 20°C.

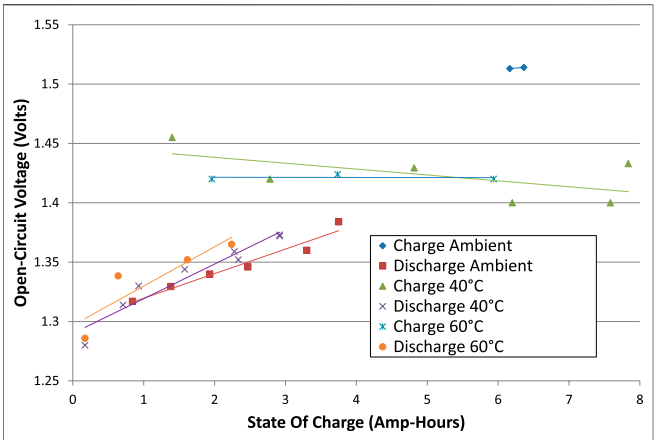

FIGURE 5 | Open circuit voltages (VOC) for all tests, comparing charging with discharging, and comparing the effect of cell temperatures.

interruptions of charging and discharging across all tests of phase 2, excluding very low values of SOC and excluding a few outlying values. The test program did not allow time for long-term cycling of the battery to see how these parameters change over time.

Most parameters of the equivalent circuit exhibit insignificant differences between charging and discharging, but the long time constant, τ_2 is slightly larger and the larger capacitance, C_2 is significantly larger during charging. This could be because bubbles of gas form inside the electrodes and act as a form of energy storage, causing the cell to temporarily perform as an alkaline fuel cell for a few minutes when the charging current is disconnected.

Cell Capacity

The approximate charge capacity of the cell can be observed from the total ampere-hours delivered in each discharge test at the point of voltage collapse, for example the discharge tests of **Figures 3** and **4**. However, the time of voltage collapse depends on the discharge current: a slower discharge results in later voltage collapse. Therefore, discharge was continued at very low voltage until the current also dropped to a very low level, approximately 0.1 A, while counting ampere-hours. Since current continued to fall exponentially and asymptotically, **Eq. 10** was used to estimate the residual cell capacity at the end of each test. Residual capacity added only a small fraction of total charge, in most cases about 1% of capacity and never more than 3.3%.

At ambient temperatures, the total cell capacity was 3.87 ± 0.2 Ah. At 40°C, the total cell capacity was very similar at 3.79 ± 0.12 Ah. Thus, the observed total cell capacity was about 30% greater than the expected nominal value of 3 Ah, and about 25% greater at the point of voltage collapse, **Figure 4**. There are various reasons for this. Firstly, the cell becomes conditioned by repeated cycling. Any net oxidation of both electrodes is removed by the liberation of more oxygen than hydrogen over the first few cycles. Secondly, the measured cell capacity included a second plateau of lower voltage where further oxidation of iron electrodes takes place, **Eq. 11**:

$$3Fe(OH)_2 + 2NiOOH \leftrightarrow 2Ni(OH)_2 + Fe_3O_4 + 2H_2O \qquad (11)$$

However, the plateau, visible in **Figure 3B** only adds about 2% to cell capacity. Therefore, the actual cell capacity appears to be larger than nominal. The charging process behaves as a logistic function (Mulder et al., 2017). With the exception of the first two charge-discharge tests carried out, the charge inserted was much greater than the nominal capacity and was continued until the cell voltage had stopped rising, indicating that no more charge was being stored.

At 60°C, the total cell capacity was 2.46 ± 0.04 Ah, which is 18% below nominal capacity and 35% below the capacity at ambient temperature despite the inserted charge being at least as great as in tests at lower temperatures. These observed differences could be due to cell self-discharge and its dependence on both SOC and temperature. At moderate temperatures, self-discharge is slow enough for the cell to temporarily hold a full charge, whereas at elevated temperature the initial self-discharge rate is very high. However, self-discharge tests were not carried out to confirm or refute this theory. Self-discharge does not necessarily result in a high rate of energy loss, since it can result in the release of hydrogen and oxygen gases (Weninger and Mulder, 2019). The production of gases during the charging process was not measured during the long capacity tests, but was measured in the combined charging-electrolysis tests described in *Charge Efficiency During Electrolysis Tests*, *Energy Efficiency During Full Charging*

TABLE 1 | Time constants of interruption tests and equivalent circuit component values measured in phase 2 with a gap of 1.25 mm on each side of the membrane.

	Charging		Discharging	
Equivalent circuit parameter	**Average value**	**Standard deviation**	**Average value**	**Standard deviation**
Ohmic resistance, R_0 (mΩ)	158	14	178	15
Short time constant, τ_1 (s)	13	6.7	17	4.4
Smaller resistance, R_1 (mΩ)	36	12	27	4.9
Smaller capacitance, C_1 (F)	498	245	425	131
Long time constant, τ_2 (s)	187	15	140	26
Larger resistance, R_2 (mΩ)	32	6.3	54	18
Larger capacitance, C_2 (F)	6,010	1,300	2,840	1,050
Total cell resistance, R_{TOT} (mΩ)	236	23	269	41

and Discharging Cycles, and *Energy Efficiency When Electrolysing at Full Charge*.

Electrolyser Performance Comparing Different Cell Constructions

Electrolyser tests have been performed at least once with every cell configuration. The maximum current is 10 A, and the working cell area of the cell is 50 cm^2, corresponding to a current density of 200 mA/cm^2, which is a modest maximum for an electrolyser.

A hysteresis effect was observed: electrolysis voltage is slightly higher when stepping up the voltage than when stepping down, indicating a slightly lower resistance when decreasing voltage and current. Also, when a second, repeated electrolysis test was performed, it usually resulted in higher current at a given voltage than in the first test, indicating a further reduction in resistance. This is due to the action of the self-forming catalysts, nickel oxy-hydroxide in the oxygen evolution reaction and metallic iron in the hydrogen evolution reaction (Mulder et al., 2017) that reduce the overpotential at each electrode. A second test also resulted in less difference between the increasing and decreasing tests. Therefore, where possible, only the second electrolysis test of each cell configuration is presented and compared in subsequent analyses. The increasing and decreasing portions of each electrolysis test were then averaged to minimise hysteresis effects.

Comparing the second electrolysis tests (where available) for all the cell configurations of phase 1, **Figure 6**, the cell configurations can be ranked in order of performance as an electrolyser.

The cell with no gaps is the worst performing and can be discounted as a realistic option for a battolyser. With no gap on each side of the membrane, the voltage was much higher than other configurations, implying that the internal resistance was consistently higher. Therefore, it is imperative to have at least a small gap on each side of the membrane. It is thought that this is necessary to allow bubbles to escape efficiently, to avoid "bubble blinding."

The cell with lowest resistance is the one with no membrane and just one spacer, giving a gap of 1.25 mm. This can also be discounted as a realistic option for a battolyser since the membrane is needed to separate hydrogen and oxygen gases. However, the no-membrane case can be used to estimate the electrical resistance of the membrane itself.

When a 1.25 mm spacer on each side of the membrane is compared with a 2.5 mm spacer on each side, the smaller gaps create a cell with a smaller internal resistance. Therefore, for current passing between the electrodes, the effect of reduced resistance of a shorter pathway through the electrolyte more than offsets any increase in bubble blinding due to a smaller gap, even at maximum current density.

The difference between the lines in **Figure 6** can be used to estimate the electrolyte resistivity. The lines are almost linear between 4 and 10 A, where the gradients have been calculated as shown in **Table 2**.

The difference in pathway length through the electrolyte in a cell with a gap of 2.5 mm on each side and that of a cell with a gap of 1.25 mm on each side is a total of L = 2.5 mm, and the increase in resistance, R, is 0.0939 − 0.0797 = 0.0142 Ω. The working area, A, is still approximately 50 cm^2, or 0.005 m^2.

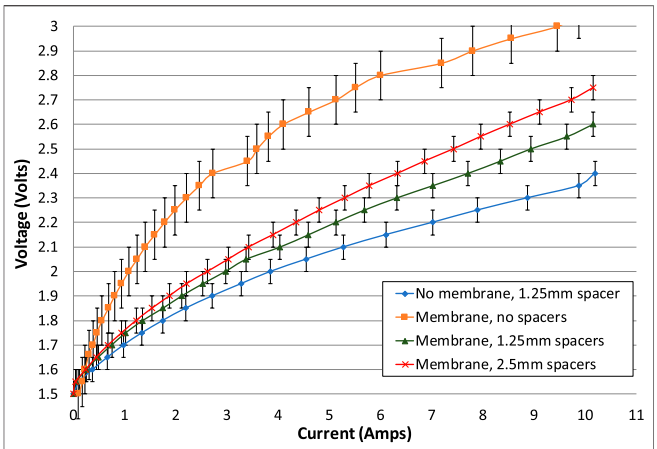

FIGURE 6 | Electrolysis tests for all cell configurations of phase 1 testing. The increasing and decreasing portions of the electrolysis tests have been averaged. With the exception of the test of a membrane with no spacers, the second electrolysis test is shown. Error bars added indicate variation in test repeatability.

$$Resistivity,\ \rho = \frac{RA}{L} = \frac{0.0142 \times 0.005}{0.0025} = 0.0284\ \ \Omega m \qquad (12)$$

The conductivity is the inverse of this, 35.2 Sm^{-1}, or 352 $mScm^{-1}$. This corresponds reasonably well with published results of 550 $mScm^{-1}$ for 35 wt.% KOH at 25°C (Allebrod et al., 2012).

Given this resistivity, it is possible to estimate the resistance that the no-membrane cell would have had if a membrane were present, as follows:

Resistance of cell with membrane and 1.25 mm gaps = 0.0797 Ω, Thickness of membrane itself = 0.45 mm, Length of pathway through electrolyte in cell with no membrane = 1.25 mm, Length of pathway through electrolyte in cell with membrane is 1.25 + 0.45 + 1.25 = 2.9 mm, Reduction in resistance due to reduced width is 0.0142 × 1.7/2.5 = 0.009656 Ω, Resistance of no-membrane cell if it had a membrane is therefore 0.0797 − 0.009656 = 0.070044 Ω, Actual resistance of no-membrane cell = 0.0594 Ω.

Therefore, added resistance of membrane itself is 0.070044 − 0.0594 = 0.0106 Ω, or just 10.6 mΩ.

Given the 50 cm^2 cell area, this equates to a specific resistance of 0.53 Ωcm^2 at 20°C, which agrees fairly well with the

TABLE 2 | Gradients and intercepts of electrolysis voltage curves, indicating ohmic resistance and voltage at which significant electrolysis first takes place.

Cell configuration	Gradient (mΩ)	Intercept (V)
No membrane	59.4	1.7804
Membrane, no gaps	76.5	2.2994
Membrane, 1.25 mm gaps	79.7	1.7879
Membrane, 2.5 mm gaps	93.9	1.798

manufacturer's stated resistance of 0.3 Ωcm^2 for 30 wt.% KOH solution at 30°C.

The added resistance of membrane plus increased cell width is 20.3 mΩ, which is only 8% of average total cell internal resistance, **Table 1**. The internal resistance is dominated by the resistance within the electrodes themselves and the addition of a membrane is only a small efficiency or power penalty.

Electrolysis at Elevated Temperatures

In phase 2 tests, the cell had a fixed configuration of a membrane and a gap of 1.25 mm on each side. Electrolysis tests were carried out as before, increasing and decreasing the voltage in steps of 0.05 V. Tests were performed at ambient laboratory temperature of approximately 20°C, then 40°C and finally 60°C. At each temperature, electrolysis was repeated, ramping the current and voltage up and down twice.

As before, the increasing and decreasing portions of each electrolysis test have been averaged, and the second electrolysis test is used wherever one was available, **Figure 7**. The lower voltage gradient in the phase 1 test is due to the lower resistance of its contact wires within the cell. The results show that voltage at a given current is reduced with increasing temperature. To a good approximation, the cell voltage is uniformly reduced by 0.1 V for a temperature increase of 40°C.

The cell was rebuilt between phase 1 and phase 2 testing, with a new lid for gas collection and new electrical connections to the electrodes. The new electrical connections are expected to have some effect on the ohmic resistance of the cell. In phase 1, the electrode connectors were stranded copper wires that became corroded where they were exposed to the potassium hydroxide electrolyte. The wires were clamped onto the electrode with nylon nuts and bolts. The surface connection resistance may have been poor but the electrical conductivity of the wires themselves was good. Each wire had a measured resistance of 0.01 Ω. In total, the connections to both electrodes are therefore estimated to have a total resistance of at least 0.02 Ω.

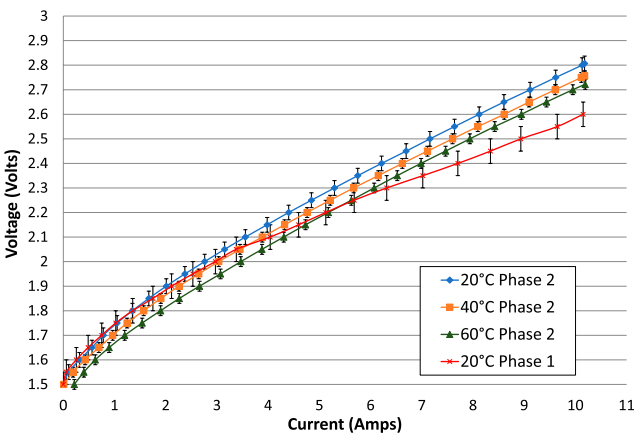

FIGURE 7 | Comparison of electrolysis tests at different temperatures and also compared with the equivalent test in phase 1, all with 1.25 mm spacers on each side of the membrane. The increasing and decreasing portions of the electrolysis tests have been averaged. With the exception of the 60°C test, the second (repeated) electrolysis test is shown.

In phase 2, the electrode connectors were solid stainless steel, each with a length of about 200 mm and diameter of 3 mm. The resistivities of stainless steels are between 69 and 80 μΩ-cm, (AZOMaterials, 2018; Ugur, 2018; California Fine Wire Co, 2020). Using a typical value of 75 μΩ-cm, the resistance of each wire would be 0.021 Ω, and the total resistance added to the cell would be 0.042 Ω, which is slightly larger than in phase 1. A back-to-back comparison of the electrolysis current-voltage characteristics of the cell in phase 1 and phase 2 at ambient temperature is shown in **Figure 7**.

The phase 2 cell obviously has a higher internal resistance, resulting in a higher gradient of voltage vs. current. In **Figure 7**, the cell voltage at a current of 10 A is about 0.2 V higher in phase 2 than in phase 1, indicating an apparent increase in resistance of 0.02 Ω. This is consistent with the calculated increase in resistance that should result from swapping from copper wires to stainless steel wires, and within the margin of experimental error.

The design of the experimental cell included wires to the base of each electrode so that the electrical connection did not have to pass through the gas collection pockets. Further research and design work are required to achieve a multi-cell stack with minimal electrical resistance between cells.

Gas Production Rates

The total gas production rates were measured for some of the electrolysis tests. There was too much gas cross-over from oxygen to hydrogen or vice versa to measure the volume of each gas independently, but the total gas volume was successfully measured. One important reason for the gas cross-over was the insufficient depth of gas collection pockets at the top of the cell, as the proportion of gas emerging from each of the tubes was dependent on small changes to the depth of submersion in the water collection bath. The overall sealing of the cell was also inadequate for very accurate gas volume measurements, given that some bubbles were often observed emerging from the edges of the cell lid and around the temperature probe. Lessons are learned for future cell design, including problems of electrolyte frothing at high gas production rates.

Nevertheless, total gas volumes from both collection cylinders were measured, added together and converted into the number of moles of gas using measured temperature and known atmospheric pressure on the day (Time and Date AS, 2020). The gas volume was adjusted for humidity, assuming 100% relative humidity at the temperature of the water bath (TLV A Steam Specialist Company, 2020).

To investigate the effect of SOC, some electrolysis tests took place when the cell was fully charged, whereas others took place when the cell was almost completely discharged. When the cell was fully charged, it was expected that all electrical charge would be used to make hydrogen and oxygen, but when the cell was charged rapidly from empty, the charge is divided between charging the cell and producing gases, both of which were measured.

The measured total gas production rates depended mainly on the cell voltage, regardless of the SOC, **Figure 8**. Gas production is negligible below a cell voltage of 1.5 V.

There is some evidence suggesting that gas production rates are higher when the cell is fully charged than when it is empty, but the data was only sufficient to show this effect at elevated temperatures, and the effect is secondary to the voltage.

Charge Efficiency During Electrolysis Tests

The charge balances of all the electrolysis tests are shown in **Figures 9** and **10**. They show the charge balance of electrolysis tests in units of millimoles of electrons in, and millimoles of electrons used in gas production, according to the overall chemical equation for electrolysis.

$$H_2O \underset{4e^-}{\rightleftharpoons} 2H_2 + O_2 \quad (13)$$

Using the stoichiometry, **Equation 11**, each 3 mol of gas requires 4 mol of electrons to make it. If the electrical charges were fully accounted for, the "charge input" and "gas output" bars of **Figure 9** would be equal in height for each test. However, in practice the measured charge efficiency (Faraday efficiency) is quite variable and usually less than 100%. When starting from a full cell, the charge efficiency varies between 73% and 107% with an average of 87%. Apart from measurement error and gas leakage, possible sources of difference include temporary over-charging of the cell and leakage current.

When starting with an almost-empty cell, **Figure 10**, the sum of "gas output" and "charge out" should be equal to the preceding "charge input" for each test, if all charge were accounted for. However, the charge efficiency is even more variable for these tests, with a minimum of 65%, a maximum of 174% and an average of 112%. In these tests, apart from all the sources of error and difference measured above, it is also difficult to know if the cell returned to the same SOC at the end of the experiment as it was at the beginning. The most commonly used methods for estimating SOC in other batteries (Zeng et al., 2018; Zhang R et al., 2018) are not available for our Ni-Fe cell. Considering each possible method in turn: Ampere-hour counting is an output of this experiment, not an input that can be used to determine SOC; V_{OC} is too variable to be used and the time constants associated with the cell are too long; The internal impedances do not exhibit any clear relationship with SOC; An electrochemical model is not available; The equivalent circuit model does not show clear relationships with SOC; Kalman filter algorithms are not available for this cell. Upon disconnection of a load, V_{OC} slowly returns to a plateau at about 0.7 V, and then another plateau at 1.2 V. The characteristics of the battery are not well enough known for impedance spectroscopy or modeling methods to be used. The method of estimation of residual charge described by **Eq. 10** makes the reasonable assumption that short-circuit current is proportional to residual charge but may not be accurate enough.

From the charge stored in the cell when performing a short electrolysis/charge test from an almost-empty state, it appears that there is a maximum rate-of-charge for the Ni-Fe cell.

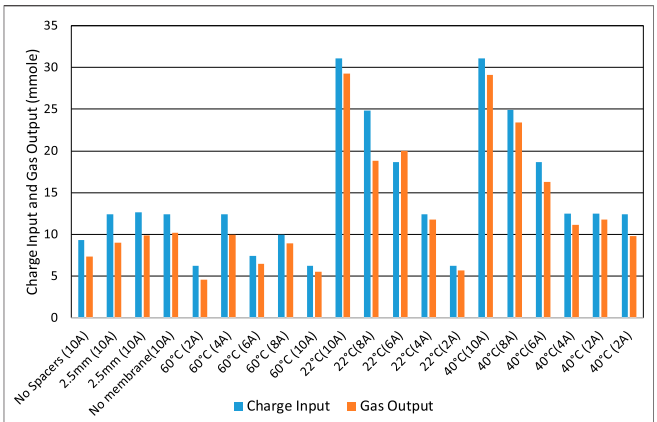

FIGURE 9 | Electrolysis tests starting with a fully charged cell. Charge input and equivalent gas output in terms of effective charge used and at different charge rates.

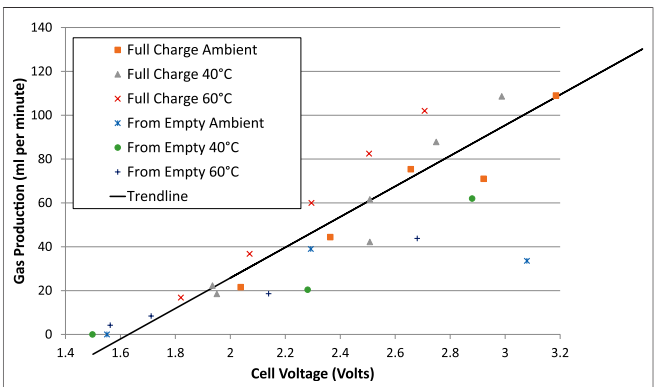

FIGURE 8 | Electrolysis total gas production rates vs. cell voltage averaged over the test. Cells had 1.25 mm spacers each side of the membrane.

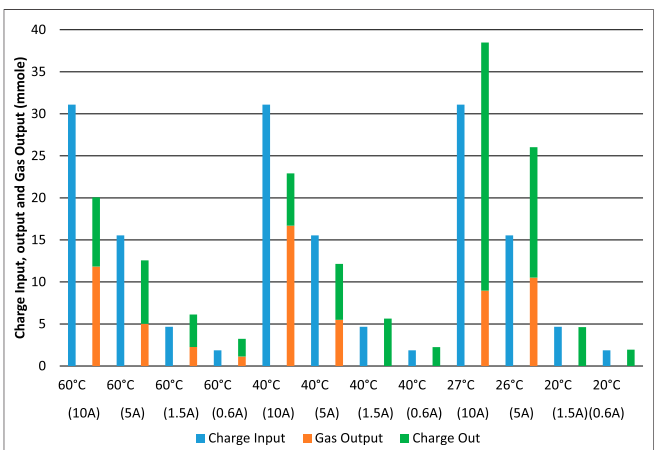

FIGURE 10 | Electrolysis tests starting with an almost-empty cell. Charge input, charge output and equivalent gas output in terms of effective charge used and at different charge and discharge rates.

Excluding tests where the charge output exceeded the charge input, and therefore focusing on tests at 40 and 60°C, it is possible to divide the charge output by the duration of the charging test to calculate an effective charging current as a function of average cell voltage, **Figure 11**. It appears that the maximum charge rate is limited to about 2.5 A, corresponding to 50 $mAcm^{-2}$, no matter how high the voltage or the electrolysis current is. That is a charge rate of just under 1C in this 3 Ah cell.

Energy Efficiency During Full Charging and Discharging Cycles

During the long charge and discharge cycles, the overall energy balance is impossible to establish since the gas volumes were not measured. As seen above, as the cell approaches a fully charged state, the rate of electrolysis increases but the chemical energy associated with the hydrogen gas was not accounted for during the long charging tests. The plateau voltages, **Figures 3** and **4**, show the cell charging at between 1.5 and 1.8 V, then discharging between 1.3 and 0.7 V. The electrical energy efficiency was therefore about 70% when charged and discharged at 0.6 A (12 mA/cm^2) and closer to 40% when charged and discharged at 1.5 A (30 mA/cm^2) but these figures include the large resistances of contact wires inside the cell. the efficiency penalty due to addition of the membrane is estimated to be up to 10%. Therefore, the battolyser's performance as a battery is compromised.

Energy Efficiency When Electrolysing at Full Charge

The higher heating value (HHV) of the chemical energy in the hydrogen gas produced has been compared with electrical energy input and integrated over the time duration of the tests, **Figures 12** and **13**. When starting from a fully-charged cell, **Figure 12**, the energy efficiency may be as high as 70% when the current is only 2 A and the cell voltage is only 1.9 V, but is less than 40% when the current is up to 10 A and the voltage is up to 3 V. The main cause of low efficiency is, again, high cell voltage, which again includes the voltage drop in the wires inside the cell of up to 0.4 V.

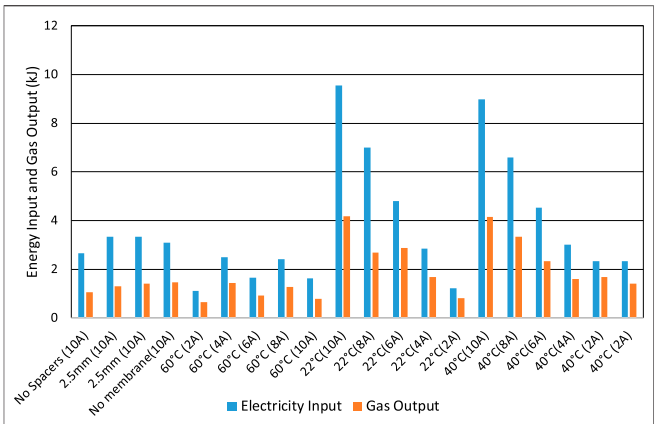

FIGURE 12 | Electrolysis tests starting with a fully charged cell. Electrical energy input compared to calorific heat energy of gas output (HHV).

When starting from an almost-empty cell, **Figure 13**, the energy efficiency is again much lower than the charge efficiency, **Figure 10**, due to the high voltage during electrolysis, especially when the current is as high as 10 A with an associated high cell voltage of up to 3 V including the resistance of wires inside the cell.

DISCUSSION

The high internal resistances of the cell, **Table 1**, and hysteresis of V_{OC}, **Figure 5**, result in poor voltage efficiency. When the charge and discharge rate is C/5, the stabilized terminal voltages are typically 1.6 and 1.2 V respectively, resulting in a voltage efficiency of 75%. When the charge and discharge rate is C/2, the stabilized terminal voltages are typically 1.82 and 0.98 V respectively, resulting in

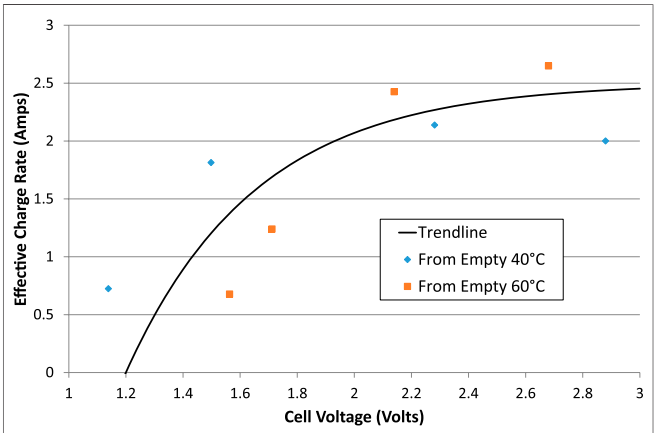

FIGURE 11 | Effective charge rate during electrolysis tests that start with an empty cell. Asymptotic trend line added.

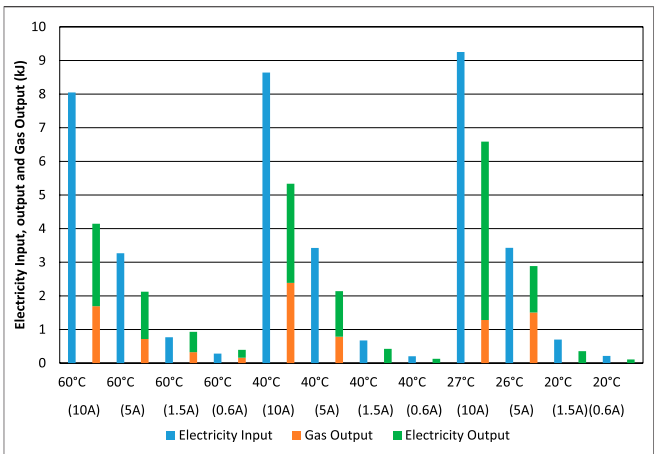

FIGURE 13 | Electrolysis tests starting with an almost-empty cell. Electrical energy input compared to calorific heat energy of gas output (HHV) and electrical energy output.

a voltage efficiency of 54%. These voltage efficiencies are similar to but slightly lower than those observed by Mulder et al. (2017). Side reactions and poorer performance at very high or low SOC reduce electrical efficiency still further. In any case, the maximum charge rate is limited to less than 1C, **Figure 11**. The role of Ni-Fe batteries in electricity systems is therefore primarily for long duration storage, diurnal cycling rather than peak lopping for example.

The present experiments used only one pair of electrodes whereas a battery uses a stack of interleaved electrodes. The present experiments also added a membrane and increased the conduction path length. The relatively small increases in resistance caused by these changes, **Table 2**, indicate that the high internal resistance are intrinsic to the chemistry of Ni-Fe cells and that the present changes make only a small compromise to the performance of a Ni-Fe battolyser as a battery.

As an electrolyser, the energy efficiency is also relatively low at typically 50%, **Figure 12**. Given the thermo-neutral voltage of electrolysis at ambient pressure and temperature of 1.48 V (Mori et al., 2013), the voltage efficiency at a current density of 200 mA/cm^2 and 60°C is just 55% **Figure 7**. The measured current density at an efficiency of 70% (or 2.11 V) is just 83 mA/cm^2 compared to 500 mA/cm^2 for alkaline electrolysers and 2000 mA/cm^2 for PEM electrolysers (Ayers et al., 2010). The electrolysis efficiency of 80% at a current density of 100 mA/cm^2 measured by Mulder et al. (2017) is slightly higher than the present result but still lower than commercial electrolysers.

Given the proposed application of using surplus renewable electricity at low capacity factors, low cost and durability are more important than efficiency. The United Kingdom retail price of Ni-Fe batteries is £440/kWh, which is lower than other batteries of long cycle life such as lithium titanate or lithium iron phosphate (Bimble Solar Ltd., 2020) but higher than deep-cycle lead acid batteries, which have shorter cycle life. The example current density of 83 mA/cm^2 is equivalent to a battery charge rate of 1.4C in the tested two-electrode cell, or 2.8C if many electrodes are interleaved in a stack and operated as double-sided electrodes. If a thermal efficiency of 70% is expected, then capital cost per kW as an electrolyser is comparable or lower than that of commercial electrolysers but excludes the cost of gas collection and compression. If a lower efficiency is tolerated, then the capital cost of the stack on its own can be lower.

Further research is required to optimize the Ni-Fe battolyser for its dual role:

- Long cycle-life testing is required to establish the durability of a Ni-Fe battolyser as repeated overcharging is known to change the crystal structure of the positive electrode (Shukla et al., 1994). Damage to electrodes and partial disintegration of the electrode materials was observed but the cause was unknown.
- Existing Ni-Fe electrodes are designed to minimise hydrogen and oxygen evolution. The battolyser may therefore benefit from a different formulation of electrodes and surface coatings to enhance gas production.
- The gas collection system and balance of plant need to be engineered to be affordable yet durable.

CONCLUSIONS

The tests confirm that a Ni-Fe cell can be used as a battery-electrolyser or battolyser. It can be used for both storage of electrical energy and hydrogen production as a Power-to-X sustainable fuel.

An equivalent circuit model of a Ni-Fe cell has been constructed from interruption tests conducted during charging and discharging of the experimental cell, with approximate values of equivalent circuit components. The equivalent circuit has two R-C loops. The shorter time constant is approximately 15 s in either charging or discharging but the longer time constant is 187 s during charging and 140 s during discharging. The open-circuit voltage exhibits a hysteresis effect, depending on whether the cell is charging or discharging, especially at low states-of-charge. Alternatively, this may be evidence of an even longer time required for cell voltage stabilisation.

The total cell capacity is confirmed to be greater than the nominal cell capacity by approximately 25%. To make use of this extra capacity, the cell has to be overcharged for a significant period of time and may need to be discharged immediately after charging to avoid loss of energy by self-discharge.

Results are consistent with the Ni-Fe cell having a high self-discharge rate, and that self-discharge is increased at elevated temperature.

The bubble separation membrane increases the cell's internal resistance by 0.53 Ω cm^2 at 20°C, which is consistent with the membrane manufacturer's specifications. Together with the required increase in separation between electrodes, the addition of a membrane results in an increase in cell resistance during electrolysis of 34%. The increase in total internal resistance of the cell as a store of electricity is only 8%. The electrical performance of a Ni-Fe battolyser is therefore almost as good as a Ni-Fe battery.

Elevated temperature reduces the measured cell capacity by a modest amount, but also reduces the voltage at which electrolysis takes place, thereby improving the efficiency of electrolysis.

There is an optimum separation gap between the cell electrodes and each side of the bubble separation membrane. This should be large enough to avoid "bubble blinding" but small enough that the extra electrolyte layer does not increase internal resistances significantly. In the cell studied, the best results were observed with gaps of 1.25 mm or 2% of cell height.

There appears to be a maximum cell charge rate of the order of 50 mA cm^{-2}, regardless of the cell voltage.

Ni-Fe batteries appear to be a good choice for electricity storage in off-grid microgrids powered by intermittent renewable energy, especially where long battery life is required at elevated ambient temperatures. Ni-Fe battolysers appear to be a cost-effective technology of providing hydrogen for other energy uses and longer-term energy storage, provided they can be manufactured in a low-cost yet robust way.

DATA AVAILABILITY STATEMENT

The datasets generated for this study are available on request to the corresponding author.

AUTHOR CONTRIBUTIONS

JB and RG contributed conception and methodology of the experiments; RG secured funding, supervised and administered the project; AR and JB assembled the laboratory equipment and performed the experiments; AR organized the database of results; JB wrote the first draft of the manuscript; JB, RG and AR contributed to manuscript revision, read and approved the submitted version.

FUNDING

This research was funded by HEIF (grant HE0010 - 15.A.7HU) and by the Modern Energy Cooking Services (MECS) project, UK Foreign, Commonwealth and Development Office (FCDO) (IATI Identifier: GB-GOV-1-300123).

ACKNOWLEDGMENTS

The authors would like to thank colleagues at De Montfort University for their help in this study. Special thanks go to the mechanical engineering workshop for use of machining equipment, electrical engineering workshop for loan of test equipment, the materials design department for 3D printed parts, and the chemistry department for the loan of laboratory equipment. The authors would also like to thank Dr Richard Blanchard, Head of Renewable Energy for Development Group, and Dr Murray Thomson, Senior Lecturer in Electrical Networks and Systems, at CREST, Loughborough University for enabling the publication of this paper.

SUPPLEMENTARY MATERIAL

The Supplementary Material for this article can be found online at: https://www.frontiersin.org/articles/10.3389/fenrg.2020.509052/full#supplementary-material

REFERENCES

Allebrod, F., Chatzichristodoulou, C., Mollerup, P. L., and Mogensen, M. B. (2012). Electrical conductivity measurements of aqueous and immobilized potassium hydroxide. *Int. J. Hydrogen Energy.* 37, 16505–16514. doi:10.1016/j.ijhydene.2012.02.088

Ayers, K. E., Anderson, E. B., Capuano, C., Carter, B., Dalton, L., Hanlon, G., et al. (2010). Research advances towards low cost, high efficiency PEM electrolysis. *ECS Trans.* 33 (1), 3–15. doi:10.1149/1.3484496

AZOMaterials (2018). Stainless steel - grade 316 (UNS S31600). Available at: https://www.azom.com/properties.aspx?ArticleID=863 (Accessed March 9, 2018).

Bimble Solar Ltd. (2020). Bimble solar. Available at: https://www.bimblesolar.com/batteries/nifebatteries (Accessed October 5, 2020).

Borgschulte, A. (2016). The hydrogen grand challenge. *Front. Energy Res.* 4 (11). doi:10.3389/fenrg.2016.00011

California Fine Wire Co. (2020). Stainless steel 308 material #: 100193. Avilable at: http://www.calfinewire.com/datasheets/100193-stainlesssteel308.html (Accessed September 30, 2020).

Chakkaravarthy, C., Periasamy, P., Jegannathan, S., and Vasu, K. I. (1991). The nickel/iron battery. *J. Power Sources.* 35 (1), 21–35. doi:10.1016/0378-7753(91)80002-f

Crossland, A. F., Anuta, O. H., and Wade, N. S. (2015). A socio-technical approach to increasing the battery lifetime of off-grid photovoltaic systems applied to a case study in Rwanda. *Renew. Energy.* 83, 30–40. doi:10.1016/j.renene.2015.04.020

Danish Energy Management (2019). Batteries - a key constraint for off-grid solar. Available at: https://www.dem.dk/wp-content/uploads/2019/11/Discussion-paper-05_Batteries.pdf (Accessed September 30, 2020).

Dougherty, B. J., Tanzella, F. L., I International, S. R., Ave, R., and Park, M. (1995). "Some nickel -iron, and nickel - metal hydride, cell cycling results," in Proceedings of the tenth annual battery conference on applications and advances. Long Beach, CA: IEEE, 199–205. doi:https://doi.org/10.1109/BCAA.1995.398538

Ecker, M., Nieto, N., Käbitz, S., Schmalstieg, J., Blanke, H., Warnecke, A., et al. (2014). Calendar and cycle life study of Li(NiMnCo)O_2-based 18650 lithium-ion batteries. *J. Power Sources.* 248 (15), 839–851. doi:10.1016/j.jpowsour.2013.09.143

Gaffor, S. A., Haripraksh, B., and Shukla, A. K. (2010). "Nickel-iron battery-based electrochemical energy storage systems for rural/remote area telecommunication," in INTELEC, international telecommunications energy conference (proceedings), Orlando, FL: IEEE, 1–6. doi:10.1109/INTLEC.2010.5525702

Hariprakash, B., Martha, S. K., Hegde, M. S., and Shukla, A. K. (2005). A sealed, starved-electrolyte nickel-iron battery. *J. Appl. Electrochem.* 35, 27–32. doi:10.1007/s10800-004-2052-y

Hydrogenics (2020). Electrolysis. Available at: https://www.hydrogenics.com/technology-resources/hydrogen-technology/electrolysis/ (Accessed March 19, 2020).

Innovation Energie Développement (IED) (2013). Identifying the gaps and building the evidence base on low carbon mini-grids final. Francheville. Available at: https://www.gov.uk/dfid-research-outputs/support-study-for-dfid-low-carbon-mini-grids-identifying-the-gaps-and-building-the-evidence-base-on-low-carbon-mini-grids-final-report (Accessed November 10, 2020).

Keçebaş, A., Kayfeci, M., and Bayat, M. (2019). "Alkaline electrolyzer," in *Solar hydrogen production: processes, systems and technologies*. Editors F. Calise, M. Dentice D'Accadia, M. Santarelli, A. Lanzini, and D. Ferrero, 1st Edition. Elsevier Academic Press, 586. Available at: https://www.sciencedirect.com/topics/engineering/alkaline-water-electrolysis.

Kong, D., Wang, Y., Huang, S., Zhang, B., Lim, Y. V., Sim, G. J., et al. (2020). "3D printed compressible quasi-solid-state nickel-iron battery." *ACS Nano.* 14 (8), 9675–9686. doi:10.1021/acsnano.0c01157

Mori, M., Mržljak, T., Drobnič, B., and Sekavčnik, M. (2013). Integral characteristics of hydrogen production in alkaline electrolysers. *Strojniski Vestnik/J. Mech. Eng.* 59 (10), 585–594. doi:10.5545/sv-jme.2012.858

Mulder, F. M., Weninger, B. M. H., Middelkoop, J., Ooms, F. G. B., and Schreuders, H. (2017). Efficient electricity storage with a battolyser, an integrated Ni-Fe battery and electrolyser. *Energy Environ. Sci.* 10 (3), 756–764. doi:10.1039/c6ee02923j

Mulder, F., and Weninger, B. (2016). *Hybrid battery and electrolyser*. US10297890B2. Issued 2016. Available at: https://patents.google.com/patent/US10297890B2/en.

NEL Hydrogen (2020). Atmospheric alkaline electrolyser. Available at: https://nelhydrogen.com/product/atmospheric-alkaline-electrolyser-a-series/ (Accessed March 19, 2020).

Ruetschi, P. (2004). Aging mechanisms and service life of lead-acid batteries. *J. Power Sources.* 127 (1–2), 33–44. doi:10.1016/j.jpowsour.2003.09.052

Shukla, A. K., Ravikumar, M. K., and Balasubramanian, T. S. (1994). Nickel/iron batteries. *J. Power Sources.* 51, 29–36. doi:10.1016/0378-7753(94)01953-3

Soutar, I. (2018). The Edison nickel iron cell. Available at: http://www.nickel-iron-battery.com/ (Accessed October 11, 2018).

Stroe, D.-I., Swierczynski, M., Stroe, A.-I., and Knudsen Kær, S. (2016). Generalized characterization methodology for performance modelling of lithium-ion batteries. *Batteries* 2 (4), 37. doi:10.3390/batteries2040037

Tian, Y., Xia, B., Wang, M., Sun, W., and Xu, Z. (2014). Comparison study on two model-based adaptive algorithms for SOC estimation of lithium-ion batteries in electric vehicles. *Energies* 7 (12), 8446–8464. doi:10.3390/en7128446

Time and Date AS (2020). Past weather in Leicester, England, United Kingdom. Available at: https://www.timeanddate.com/weather/uk/leicester/historic (Accessed September 30, 2020).

TLV A Steam Specialist Company (2020). Calculator: saturated steam table by temperature. Available at: https://www.tlv.com/global/UK/calculator/ (Accessed September 30, 2020).

Ugur, U. (2018). "Resistivity of steel," in *The physics factbook*. Brooklyn, NY: Glenn Elert is Science Research Coordinator, Midwood High School. Available at: https://hypertextbook.com/facts/2006/UmranUgur.shtml (Accessed March 9, 2018).

United Nations (2019). "Sustainable development goals," in *Sustainable development goals knowledge platform*. New York, NY: UN Department of Economic and Social Affairs (UNDESA). Available at: https://sustainabledevelopment.un.org/?menu=1300.

Wang, H., Liang, Y., Gong, M., Li, Y., Chang, W., Tyler, M., et al. (2012). An ultrafast nickel-iron battery from strongly coupled inorganic nanoparticle/nanocarbon hybrid materials. *Nat. Commun.* 3 (917). doi:10.1038/ncomms1921

Weninger, B. M. H., and Mulder, F. M. (2019). Renewable hydrogen and electricity dispatch with multiple Ni-Fe electrode storage. *ACS Energy Lett.* 4 (2), 567–571. doi:10.1021/acsenergylett.8b02488

Wiemann, M., Rolland, S., and Guido, G. (2011). *Hybrid mini-grids for rural electrification: lessons learned*. Brussels, Belgium. Brussels, Belgium: Alliance for Rural Electrification Available at: https://www.ruralelec.org/sites/default/files/hybrid_mini-grids_for_rural_electrification_2014.pdf.

Zeng, Z., Tian, J., Dong, L., and Tian, Y. (2018). An online state of charge estimation algorithm for lithium-ion batteries using an improved adaptive cubature kalman filter. *Energies* 11 (1), 59. doi:10.3390/en11010059

Zhang, C., Allafi, W., Dinh, Q., Ascencio, P., and Marco, J. (2018). Online estimation of battery equivalent circuit model parameters and state of charge using decoupled least squares technique. *Energy* 142 (1), 678–688. doi:10.1016/j.energy.2017.10.043

Zhang, R., Xia, B., Li, B., Cao, L., Lai, Y., Zheng, W., et al. (2018). State of the art of lithium-ion battery SOC estimation for electrical vehicles. *Energies* 11 (7), 1820. doi:10.3390/en11071820

Conflict of Interest: The authors declare that the research was conducted in the absence of any commercial or financial relationships that could be construed as a potential conflict of interest.

GLOSSARY

A_1, A_2 Volts Scale factors of exponential terms associated with the RC networks of the equivalent circuit

A_3 Amps Scale factor of exponential decay of residual current

C/5, C/2, 1C $hour^{-1}$ Hourly charge or discharge rate of the cell

C_1, C_2, F Polarisation capacitances of the RC networks of the equivalent circuit

mΩ Ohmic resistance

Ni-Fe Nickel-iron

R_1, R_2, mΩ Polarisation resistances of the RC networks of the equivalent circuit

R_{TOT}, mΩ Total resistance of the cell. $R_{TOT} = R_0 + R_1 + R_2$

SOC, % State Of Charge of batteries or cells

V_1, V_2, Volts Voltages of the RC networks of the equivalent circuit

V_{OC}, Volt Open Circuit Voltage

τ_1, τ_2, seconds Time constants of the RC networks of the equivalent circuit

τ_3, seconds Time constant of exponential decay of residual current

frontiers in Energy Research

REVIEW
published: 17 December 2020
doi: 10.3389/fenrg.2020.570887

Direct Methanation of Biogas—Technical Challenges and Recent Progress

*Adelaide S. Calbry-Muzyka and Tilman J. Schildhauer**

Division Energy and Environment, Paul Scherrer Institute, Thermochemical Processes Group, Villigen, Switzerland

The direct methanation of biogas using hydrogen from electrolysis is a promising pathway for seasonal storage of renewables in the natural gas network. It offers particular advantages over the methanation of carbon dioxide separated from biogas, as it eliminates a costly and unnecessary carbon dioxide separation step. The key implementation challenges facing direct methanation of biogas are reviewed here: 1) treatment of biogas impurities; 2) competing reactor concepts for methanation; and 3) competing process concepts for final upgrading. For each of these three aspects, the state of the art is reviewed, focusing especially on results which have been validated at a high Technology Readiness Level (TRL) at recent long-duration demonstrations. The different technology solutions have advantages and disadvantages which may fit best to different technical and economic boundary conditions, which are discussed. As a final outlook, TRL 8 demo plants will be necessary to show the full potential of these systems, and to obtain consistent operation data to allow a cost comparison.

Keywords: biogas, catalytic methanation, biological methanation, gas cleaning, upgrading, long duration tests

OPEN ACCESS

Edited by:
Valerie Eveloy, Khalifa University, United Arab Emirates

Reviewed by:
Alain Bengaouer, Commissariat à l'Energie Atomique et aux Energies Alternatives (CEA), France
Bruna Rego de Vasconcelos, Université de Sherbrooke, Canada

****Correspondence:***
Tilman J. Schildhauer
tilman.schildhauer@psi.ch

Specialty section:
This article was submitted to Carbon Capture, Storage, and Utilization, a section of the journal Frontiers in Energy Research

Received: *09 June 2020*
Accepted: *20 November 2020*
Published: *17 December 2020*

Citation:
Calbry-Muzyka AS and Schildhauer TJ (2020) Direct Methanation of Biogas—Technical Challenges and Recent Progress. Front. Energy Res. 8:570887. doi: 10.3389/fenrg.2020.570887

INTRODUCTION

The shift from fossil power production to the use of renewable energy sources such as wind, hydropower and photovoltaic systems requires new energy storage concepts due to the less controllable character of these technologies, which in the case of hydropower and photovoltaics also have a seasonal imbalance in temperate zones.

While daily and weekly imbalances between power demand and supply can be bridged by pumped hydro storage power plants, batteries and compressed air energy storage, for seasonal energy storage Power-to-Gas processes are often suggested (Bach et al., 2019; Panos et al., 2019; Store and Go, 2019). In these processes, electricity that cannot be used at the time and location of its production is used for water electrolysis to produce hydrogen (H_2) as an energy carrier and oxygen. The H_2 can be directly used, for instance as the fuel for fuel cell vehicles, or it can be stored in tanks for later use. To some extent, H_2 can also be injected into the natural gas grid; however, in many countries, injection is limited to few percentage points. To fully exploit the advantages of the natural gas infrastructure, including pipelines, cavern storage etc., conversion of H_2 to methane (CH_4) is needed. For this reaction, referred to as methanation, a source of carbon is needed, such as carbon monoxide (CO)

Abbreviations: GC, gas chromatograph; ppb_v/ppm_v, parts per billion/million on a volume basis, which for an ideal gas mixture is equivalent to a molar basis; SCD, sulfur chemiluminescence detector; SNG, synthetic natural gas; TCD, thermal conductivity detector; TRL, technology readiness level; VOC, volatile organic compound.

originating from gasification or pyrolysis among others, or (more typically) carbon dioxide (CO_2), which can be found in exhaust gases from combustion, fermentation, anaerobic digestion or could be captured from air.

Due to its high concentration of CO_2 (30–50%) and its biogenic origin, raw biogas is often used as a CO_2 source for methanation, usually by adding the methanation as a separate process step after the existing biogas upgrading or separation of the CO_2 with membranes or scrubbers. Examples of this concept were realized in the 3 MW_{CH4} plant in Werlte/Germany (Specht et al., 2016) or in Solothurn/Switzerland (Store and Go, 2020). The use of pure CO_2 offers some advantage with respect to gas conditioning and reactor size. The drawback is the necessary CO_2 separation, which is connected to investment and operational costs. Therefore, the direct methanation of biogas without prior separation of the CO_2 is also investigated, converting the CO_2 in the biogas in the presence of CH_4. This methanation process can be achieved either by thermochemical means using a transition metal catalyst, or biologically using appropriate micro-organisms. In these processes, the CO_2 separation can be omitted, however, now the conversion reactor encounters the complete biogas including trace compounds and impurities, and the process must be able to handle the connected challenges.

This article reviews the efforts in direct methanation of biogas in the past few years and reports on recent progress. Important challenges such as impurities in biogas, potential gas cleaning technologies and upgrading are highlighted, and several methanation reactor concepts and their performance in long duration tests are compared.

The focus of this review is on the production of grid-ready biomethane in particular, as this is likely to be a principal first target for direct methanation of biogas. Biomethane as produced from direct methanation of biogas could alternatively be used locally (i.e., without transiting through the natural gas network) to generate heat and electricity and heat; it could also be used for a variety of other downstream applications including conversion to value-added chemicals. These have different quality requirements for biomethane than the natural gas network (broadly, less stringent requirements for local combustion, more stringent requirements for conversion to value-added chemicals). However, local production of heat and electricity can be achieved already today from the direct combustion of biogas even with a high CO_2 content, without a methanation step. Meanwhile, conversion of methane to value-added chemicals or other downstream processes is likely to still require a connection through the natural gas network to allow for sufficiently large downstream plants taking advantage of the economy of scale. Finally, one of the key advantages of the direct methanation of biogas is to enable seasonal storage of renewable electricity via the natural gas network; as such, this network's quality requirements will remain the likely standard to be met.

Several authors have recently reviewed various related elements of the Power-to-CH_4 process chain. Water electrolysis, which forms the first part of the process chain and is the source of the H_2 necessary for methanation, includes alkaline, proton exchange membrane (PEM) and solid oxide electrolysis solutions. While alkaline electrolysis has the highest technological maturity of these, PEM electrolysis is also relatively mature and especially well-adapted to the quick start-up times which can be necessary with intermittent biogas production, while solid oxide electrolysis, despite a lower technological readiness, offers good efficiency advantages (Buttler and Spliethoff, 2018). Reviews have also summarized the technical status of Power-to-Gas generally (Götz et al., 2016; Bailera et al., 2017; Thema et al., 2019; Hidalgo and Martín-Marroquín, 2020), the catalytic materials and mechanisms underlying the methanation of CO_2 (Younas et al., 2016), the potential of combining methanation and high temperature electrolysis (Biswas et al., 2020), or biological methanation mechanisms (Dumas et al., 2020).

However, the direct methanation of biogas brings specific challenges, in particular relating to highly variable biogas composition — both bulk composition, affecting the methanation performance, and trace composition, affecting the degree of pretreatment needed to protect the methanation reactor — which have not been previously reviewed in detail. These are largely issues which can only be identified and addressed at scaled-up plants over long-duration tests rather than in lab environments where conditions can be held constant; therefore, this review focuses in particular on recent progress at high TRL.

BIOGAS COMPOSITION: BULK AND TRACE COMPOUNDS

The major components of biogas are CH_4 (50–70%v) and CO_2 (30–50%v). In addition to these, biogas can contain minor amounts of nitrogen (N_2) and oxygen (O_2) (0–5%v generally, although reaching ~10%v in some cases), as well as trace amounts (ppb_v–ppm_v levels) of sulfur compounds including hydrogen sulfide (H_2S), mercaptans/thiols, sulfides, and others; silicon compounds (siloxanes, silanes); ammonia; halogenated compounds; and other volatile organic compounds (VOCs). Additionally, untreated biogas is quite wet, generally being saturated with moisture at the temperature of the anaerobic digester (35–40°C for mesophilic digesters, >50°C for thermophilic digesters) or at the temperature of the downstream processes (for example, a gas transfer line exposed to the ambient air after the digester).

The degree to which trace compounds exist in a specific biogas source depends on a variety of factors. The type of primary substrate and co-substrates which are used in the anaerobic digestion process directly affect the trace compounds which exist in the biogas. The digester conditions (operating temperature, digester type, retention time) will also have an effect. Additionally, in-digester desulfurization methods (by micro-aeration or addition of iron compounds) can be used to reduce H_2S levels in the biogas.

The concentration of trace compounds in biogas is therefore highly variable (Rasi et al., 2007; Rasi et al., 2011). Sulfur is present primarily as H_2S, which can be expected in concentrations from ~10 ppm_v (Salazar Gómez et al., 2016) to

several thousands of ppm_v (for example, nearly 7,000 ppm_v from agricultural biogas, Saber and Cruz, 2009). Trace volatile organic sulfur compounds, including mercaptans/thiols, sulfides, disulfides, can exist in concentrations up to 10 ppmv (for methyl mercaptan) or lower (for others) (Saber and Cruz, 2009).

Silicon-containing compounds are particularly found in biogas from wastewater treatment, where concentrations span from undetectable to ~60 mg/m^3 (Rasi et al., 2010). Although they are not usually expected in biogas from agricultural or food waste, they have been identified in low concentrations in at least one set of gases produced from grass and maize (Rasi et al., 2013).

Landfill gas is not a primary focus of this review. In comparison with biogas from anaerobic digestion, landfill gas can contain significantly higher concentrations of halogenated compounds in particular (Rasi et al., 2011), along with sulfur compounds, silicon compounds (with an order of magnitude lower concentration than in biogas from wastewater treatment, Kuhn et al., 2017), and other VOCs.

GAS CLEANING TECHNIQUES FOR BIOGAS POWER-TO-METHANE

Successful operation of a methanation plants asks for appropriate gas cleaning to avoid catalyst deactivation by impurities in the biogas. The challenges are 1) to know which impurities at which concentration are problematic for the chosen catalyst, 2) to measure the impurities in the raw gas and also in the cleaned gas, 3) to have appropriate gas cleaning steps whose performance was verified by sufficiently realistic testing.

Biogas Purity Requirements for Methanation Processes

As summarized in Section "*Biogas Composition: Bulk and Trace Compounds*," biogas contaminants can include sulfur-containing compounds (H_2S and otherwise), silicon-containing compounds, and other large organic molecules (terpenes, large alkanes and alkenes, aromatics, furans, alcohols, etc.). The degree to which each of these classes of compounds needs to be removed from biogas in a Power-to-CH_4 process chain depends on the sensitivity of the downstream process.

For catalytic thermo-chemical methanation, the most sensitive downstream process is generally the methanation catalyst itself. Methanation catalysts based on nickel are known to be deactivated by even a few tens or hundreds of ppb_v of sulfur in the gas, regardless of whether this sulfur is present as H_2S (Erekson and Bartholomew, 1983) or bound to a larger, organic sulfur molecule (Struis et al., 2009; Witte et al., 2019).

Although no known studies have examined the effect of silicon-containing compounds in catalytic methanation, siloxanes have been observed to decompose at the methanation-relevant temperatures of ≥400°C (Finocchio et al., 2008; Montanari et al., 2010), and high-temperature fuel cells have shown a marked performance decrease even under 70 ppb_v of siloxanes in biogas (Madi et al., 2015). It is therefore reasonable to assume that a near-total removal of siloxanes is necessary for catalytic methanation.

Due to the similarities in the sensitivity to biogas contaminants (especially to sulfur- and silicon-compounds) of catalytic methanation reactors and high-temperature fuel cells, biogas cleaning strategies that have been developed for the latter can often be applied to the former.

Biochemical methanation is generally acknowledged to be insensitive to common biogas contaminants (Seifert et al., 2013; Götz et al., 2016). Nevertheless, the product gas must still fulfill natural gas grid injection requirements concerning impurities. In Europe, the recently developed regulation EN 16723 covers the injection of biomethane into the natural gas network (European Organization for Standardization, 2016) and its use as automotive fuel (European Organization for Standardization, 2017). It specifies that total sulfur in biomethane must remain $<5\ mg_S/m^3$ and that total volatile silicon must remain $<0.3\ mg/m^3$. In biochemical methanation, the most sensitive downstream process is therefore the local natural gas grid, or rather the gas-burning furnaces, stoves, etc. which are connected to the natural gas grid.

Finally, although the focus in this paper is on biogas cleaning technology to remove trace compounds, the possible presence of the minor compounds O_2 and N_2 in biogas should not be neglected. On the one hand, some trace O_2 is desirable for many desulfurization processes, as it improves the H_2S retention ability of activated carbons (Primavera et al., 1998) and of biotrickling filters (Dannesboe et al., 2019). On the other hand, O_2 and N_2 levels in biomethane must both be kept low to enable injection of the produced biomethane into the natural gas grid. Very high (>5%v) O_2 and/or N_2 levels are often associated with landfill gas rather than biogas from anaerobic digestion. Nevertheless, as a recent report of 19%v N_2 and 4%v O_2 in biogas from household waste demonstrates (Salazar Gómez et al., 2016), it is possible (though unusual and often tied to poor biogas plant operation) for high O_2 and N_2 levels to exist in biogas from anaerobic digestion.

Gas Cleaning Technology Options for Biogas Power-To-Methane

In the last years, a number of different gas cleanings solutions has been suggested and tested; in the following sections, the different technical solutions and their costs (as far as known) are reported.

Technical Solutions

Figure 1 illustrates the possible gas cleaning steps which may be used to treat biogas for direct methanation in a Power-to-CH_4 process. No standard solution yet exists for these systems, in large part due to the site-to-site variabilities found in biogas contamination levels, requiring some amount of redesign at each site. Nevertheless, some trends can be summarized.

Even prior to individual gas cleaning process steps, it is worth mentioning that many biogas production sites already utilize in-digester desulfurization techniques. This can include injection of air or O_2 (also known as "micro-aeration," see the review of

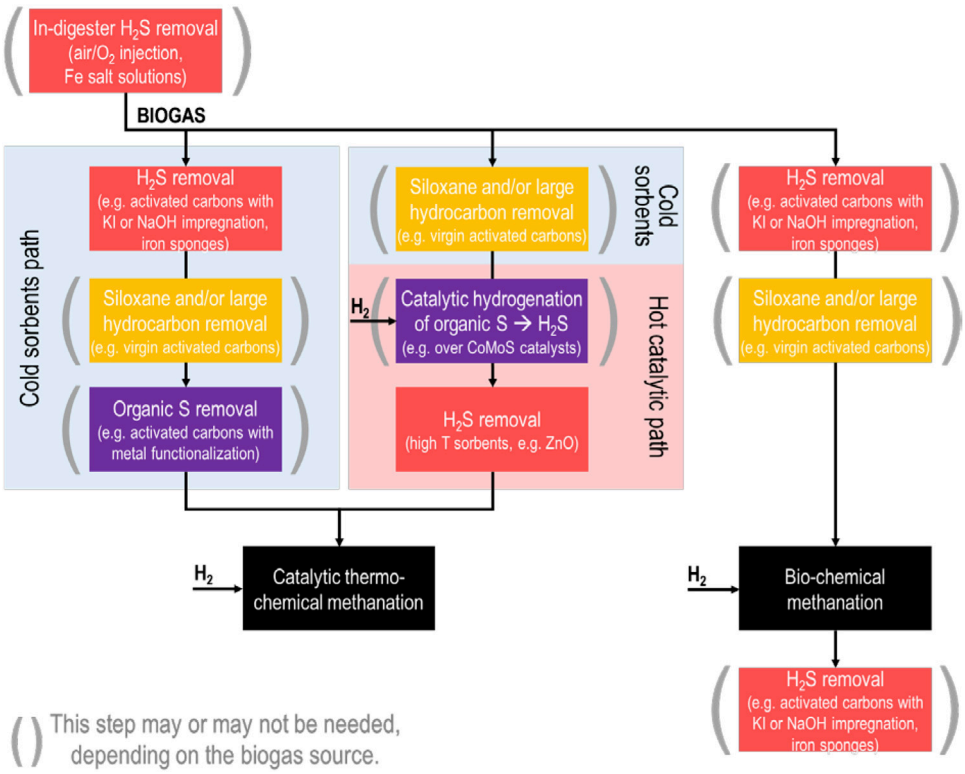

FIGURE 1 | Broad overview of biogas cleaning steps which may be needed, depending on the biogas source, for Power-to-CH_4 conversion of biogas. Biogas cleaning needs for bio-chemical methanation are dictated by natural gas grid purity requirements rather than the methanation process.

Krayzelova et al., 2015), which is used by micro-organisms in the digester to convert H_2S to elemental sulfur deposits (Díaz et al., 2011). Iron-based salt solutions are also used, with the effect of precipitating iron sulfide. These techniques are effective for reducing H_2S concentration in the produced biogas; however, the extent to which they may be effective to reduce other trace sulfur compounds is not fully understood. One study has found that while iron chloride successfully reduces H_2S and several volatile organic sulfur compounds from biogas (Park and Novak, 2013); meanwhile, another study noted that the volatile compound dimethyl sulfide is not affected (Andersson, 2004).

Techniques for bulk H_2S removal from biogas are technologically mature and well-studied, and readers are referred to the review by Abatzoglou and Boivin (2008) for a detailed overview. These would apply to any biogas pre- or post-desulfurization for biochemical methanation. In broad terms, bulk H_2S removal can be achieved by adsorption onto activated carbons (unmodified/virgin or modified by chemical impregnation, with the modified carbons achieving significantly higher capacity), onto iron oxide materials, or by reaction in biological processes such as bio-trickling filters. Solvent-based solutions (for example, alkaline aqueous solutions) would not be considered advantageous for a Power-to-CH_4 process, as they remove significant amounts of CO_2 from the biogas in addition to H_2S.

Siloxane removal from biogas has been reviewed by several authors (Ajhar et al., 2010; Soreanu et al., 2011; de Arespacochaga et al., 2015) and it is generally achieved with ambient temperature, solid sorbents. This predominantly includes activated carbons, where siloxane capacity is correlated with larger BET surface area and with larger pore volumes of pores >0.7 nm (Cabrera-Codony et al., 2014). Other sorbents such as silica gels, zeolites, and alumina have also been used.

The removal of trace sulfur compounds from biogas is not as well studied as H_2S removal. Here, work done on deep desulfurization of natural gas for fuel cells is helpful. The sulfur compounds dimethyl sulfide (DMS), carbonyl sulfide (COS), and carbon disulfide (CS_2) are particularly difficult to remove using ambient temperature sorbents (Dannesboe et al., 2019). Activated carbons incorporating transition metals such as iron (Fe) (de Aguiar et al., 2017) or copper (Cu) (Barelli et al., 2015) can be effective for this, as can certain zeolites if the biogas is maintained relatively dry (Calbry-Muzyka et al., 2019a).

It should be taken into account that the presence of other compounds in biogas, moisture (Calbry-Muzyka et al., 2019b) and large VOCs (Kajolinna et al., 2015) especially, can have a competitive effect with the impurities targeted by certain sorbents, causing a much earlier breakthrough of the target impurities than expected.

Apart from low-temperature sorbents, which are operationally simple but can suffer from strong competitive effects from other

biogas contaminants, high-temperature catalytic/adsorption processes should also be considered for catalytic methanation. Hydro-desulfurization catalytic processes as used in the oil and gas industry can be used to convert organic sulfur compounds to H_2S, after which the produced H_2S can be retained by a high-temperature sorbent (such as zinc oxide, ZnO). This has been suggested as a possible solution to trace sulfur compounds in the review of Lanzini et al., (2017) on biogas cleaning for fuel cells, and it has been demonstrated in field tests for fuel cells in several past projects (He et al., 1997; Spiegel et al., 2003). In these projects, one or more cold sorbent steps are nevertheless used before the catalytic steps, for siloxane and/or VOC removal. However, there have been successful demonstrations of siloxane removal by high-temperature (400°C) alumina (Finocchio et al., 2008), indicating that it may be possible to do a full clean-up at elevated temperatures. For future biogas Power-to-CH_4 projects using catalytic methanation, it would be important to demonstrate that hydro-desulfurization processes can be controlled well under variable sulfur concentrations in the biogas, in particular by testing different H_2 feed rates to the hydro-desulfurization step. Alternatively, a ZnO based sorbent with promoters, operated at 400°C in presence of H_2, was able to protect a methanation catalyst for 1,000 h from any deactivation (Dannesboe, 2019).

Costs

The costs of gas cleaning techniques are also a key factor for biogas Power-to-CH_4 projects. Abatzoglou and Boivin estimated that biogas can be treated for bulk H_2S removal for \$0.03 USD/Nm^3 using iron-based or activated carbon sorbents (Abatzoglou and Boivin, 2008). In a study of H_2S and siloxane removal from biogas to protect a fuel cell, it was estimated that biogas cleaning would cost from 0.04–0.10 €/Nm^3 of biogas where H_2S removal accounted for 46–65% of capital costs and 75–95% of operating costs for a starting H_2S concentration between 200 and 3,000 ppmv (de Arespacochaga et al., 2013). Similarly, a separate study of the costs of biogas cleaning for fuel cells estimated gas cleaning at \$0.018 USD/kWh_e (Papadias et al., 2012), corresponding to \$0.06 USD/Nm^3 of biogas with 60%v CH_4 content. Although these are only a few studies, they can be used as an estimate of the costs of bulk H_2S removal (for biochemical methanation) and of deep biogas cleaning (for catalytic methanation), especially at large scale.

Learning From Monitored Field Tests

The key difficulty with using lab-based results to inform a choice of biogas cleaning technology for any system scale-up is that real biogas—in comparison to lab-based model gas mixtures—varies strongly in trace contaminant concentration site-to-site and day-to-day. This means that field-based demonstrations, where biogas comes from a real biogas source, are essential to understanding and validating gas cleaning processes.

The ability to monitor and quantify key compounds, ideally online, is not straightforward at these low concentrations. Often, gas sampling is performed on-site for off-site analysis of trace compounds, which carries the risk of analyte loss, with no single sampling vessel type (bags, containers, adsorption tubes) having been found to be appropriate for all biogas contaminants (Arrhenius et al., 2017). This necessarily leads to a piecemeal approach, where only a subset of compounds is measured, often non-continuously.

Then, many field tests are performed to demonstrate a technology which comes downstream of any gas cleaning process, which means that the gas cleaning step is intentionally oversized with large safety factors to ensure that the downstream unit is not harmed. However, this then makes it difficult to accurately represent the capacity of sorbent-based gas cleaning systems, where the accumulative nature of the process means that the capacity will not be known until a breakthrough has occurred.

Testing of biogas cleaning units until full breakthrough can bring significant insight into the performance and failings of the system under real conditions. From field tests in biogas, it has been shown that iron-based sorbents are able to remove H_2S at efficiencies >98% despite inlet concentrations varying from 104 to 1,852 ppm_v (de Arespacochaga et al., 2013), that high levels of moisture can reduce a promising zeolite-based sorbent's trace sulfur capacity to nearly zero (Calbry-Muzyka et al., 2019a), that non-H_2S sulfur compounds such as carbonyl sulfide (COS), carbon disulfide (CS_2), and dimethyl sulfide break through desulfurization steps much earlier than H_2S (Calbry-Muzyka et al., 2019a; Dannesboe et al., 2019), and that siloxanes (especially the light siloxanes L2-L4) can be measured to break through activated carbon beds much earlier than expected from single-contaminant lab tests due to the competitive presence of other volatile organic compounds in real biogas (Arnold and T. Kajolinna, 2010).

The coupling of competitive adsorption between the many dozens of biogas trace compounds and of the concentration fluctuations of specific compounds can be understood, along with their effect on adsorptive biogas cleaning techniques, by the example in **Figure 2**. Here, a two-stage biogas cleaning process is used: 1) bulk H_2S removal using a commercial sorbent based on copper oxide (CuO); 2) trace sulfur removal using a commercial sorbent based on a ceramic-activated-carbon composite. The biogas, which originated from agricultural, food, and green wastes, contained no detectable siloxanes. H_2S was monitored online using a portable gas chromatograph (GC) with thermal conductivity detector (TCD) (microGC-TCD, see method details in Calbry-Muzyka et al., 2019a). The remaining sulfur compounds were monitored online as total sulfur using a sulfur chemiluminescence detector (SCD) (Calbry-Muzyka et al., 2019b). This field test was performed to evaluate the gas cleaning alone; no methanation reactor was used downstream. This allowed a full study of the breakthrough behavior.

Although no H_2S breakthrough was ever detected in this test, management of trace organic sulfur compounds was much more difficult. Even though the sorbent for trace sulfur removal had been chosen based its good desulfurization performance in lab studies using variable gas humidity and variable concentrations of VOCs in the feed gas, its performance in the field was significantly impeded. The breakthrough plot in **Figure 2** shows a clear concentration roll-up effect, where the concentration at the bed outlet exceeds that at the bed inlet.

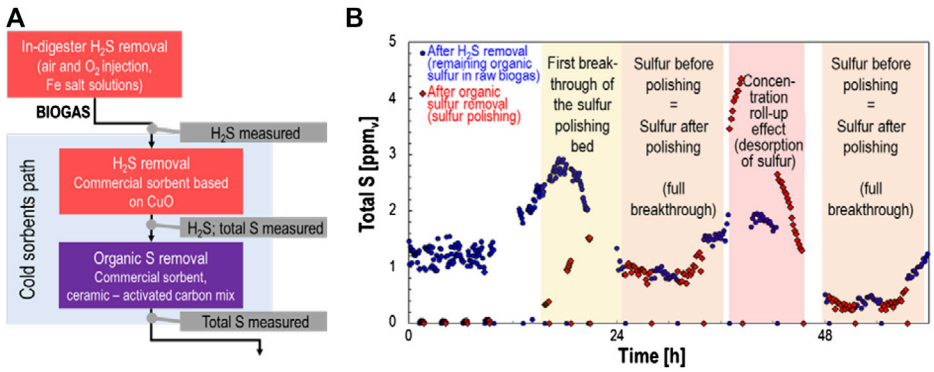

FIGURE 2 | Example of the use of a field test to evaluate the capacity of sorbents for trace sulfur compounds in biogas. The biogas was produced from agricultural waste and food/green waste and contained undetectable levels of siloxanes. **(A)** Shows a schematic representation of the biogas treatment steps, and **(B)** shows the resulting total sulfur measurements after different stages of biogas treatment.

This indicates a competitive adsorption effect, for example from much higher concentrations of VOCs than had been expected in the gas. As result, practically all organic sulfur adsorbed in the first 20 h is desorbed between 36 and 48 h of test duration. Events such as these must be avoided when scaling up methanation technology. For this reason, field testing of biogas cleaning steps with monitoring and with a bypass of downstream catalytic reactors must be done to demonstrate robustness to real biogas.

SYNTHESIS AND UPGRADING OF BIOMETHANE

The production of biomethane downstream of the gas cleaning consists of at least two steps: the main conversion and the gas upgrading leading to injectable gas. A prerequisite for these two processes is the supply of cleaned biogas and of hydrogen; further, a good integration of all processes is needed to improve plant performance and to minimize costs.

As discussed in the last section, the quality of biogas is changing over time; moreover, also the biogas production itself shows (e.g., seasonal) fluctuations depending on the plant and the feedstock availability. On the other hand, renewable electricity production as well as the electricity price strongly depend on varying and sometimes even stochastic phenomena such as the weather and the interplay between supply and demand. This results in the desire to, at least partly, adapt the hydrogen production by water electrolysis according to the electricity prices. This explains why many Power-to-Gas projects apply PEM-electrolysis that specifically was developed for fast load changes. The biogas production however follows other time patterns.

In the short term, the discrepancy can be solved by a hydrogen tank at intermediate pressures close to the pressure of the electrolysis (30–50 bar) to avoid additional compression (Gorre et al., 2020). The tank allows decoupling of the hydrogen production and its consumption for several days. A methanation technology comprising deep part load and at least moderately fast load changes allows for smaller hydrogen tanks or for longer transitory periods. Some biogas plants also have intermediate gas storages that allow them to store the produced gas for a few hours.

To overcome longer periods of unavailability or high costs of hydrogen, an even more flexible plant integration is needed. A recent study showed that the same membrane system can be used for two modes of operation of a biogas Power-to-Gas plant: as upgrading for the product enabling H_2 recycle in case of direct methanation of biogas in times when cheap renewable electricity and H_2 are available, or as classical biogas separation system in other times. This allows to avoid the necessity to buy expensive H_2 in times when renewable electricity is scarce and the hydrogen tank is not sufficient to close the gap. Moreover, such a system also represents a back-up solution for uninterrupted biomethane production in times of maintenance or operation stop of electrolysis or methanation (Gantenbein et al., 2020).

Another important aspect of plant integration is the use of heat flows. Both electrolysis and methanation are exothermic; the optimal use of these heat flows depends however on the available temperature level. Alkaline and PEM electrolysis as well as biological methanation operate at moderate temperatures of 30–65°C which limits the heat use to (pre-)warming of digesters etc. Higher temperature heat demand, e.g., for des-infective treatment of feedstock or to reach the required temperature level in digesters or for regeneration in sorption based gas up-grading plants, can be supplied by catalytic methanation operating at >300°C (see next section). Alternatively, the high temperature heat of methanation reactors can also be used to raise steam for solid oxide electrolysis, which allows for a significantly higher efficiency of the electrolysis step and therefore of the overall process (Dannesboe, 2019).

Methanation

The reaction of CO_2 with H_2, detected by Sabatier and Senederens in 1902, is strongly exothermic and limited by thermodynamic equilibrium:

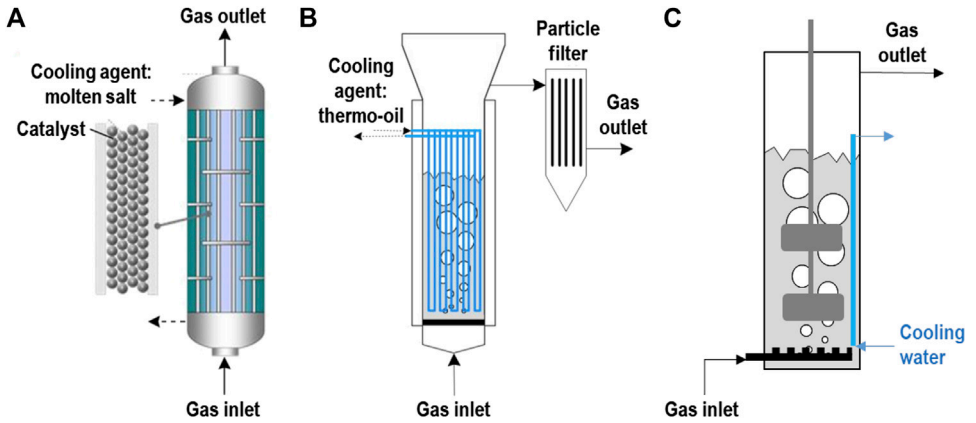

FIGURE 3 | Important methanation reactor concepts: **(A)** Cooled fixed bed **(left)**, **(B)** Catalytic bubbling fluidized bed **(middle)**, **(C)** Stirred bubble column for biological methanation **(right)**.

$$CO_2 + 4H_2 \leftrightarrow CH_4 + 2H_2O, \qquad \Delta H_r = -165\,\mathrm{kJ/mol}.$$

This implies that the heat of reaction has to be removed to allow for high conversion. The presence of CH_4 from the raw biogas dampens the temperature increase compared to reactors fed with pure CO_2 and H_2; however, hot spots of up to 680°C can easily be reached in adiabatic reactors.

Furthermore, the methanation reaction needs to be catalyzed, by either suitable microorganisms or chemical catalysts such as nickel, ruthenium, iron etc. This necessitates appropriate contact between the reacting gases and the solid catalysts or the microorganisms living in water phase. Because of these two challenges (heat and mass transfer), a number of different reactor concepts have been developed (Götz et al., 2016; Rönsch et al., 2016; Schildhauer, 2016), see **Figure 3**.

Biological Methanation

When microorganisms are used as catalysts, the reactor contains a water phase, which serves both as the habitat for the microorganisms and as the solvent for the nutrients necessary for the growth of the microorganisms, such as Na_2S and NH_3. The microorganisms metabolize the CO_2 and the H_2; CH_4 is then a waste by-product. The water produced in the methanation reaction adds to the volume of the water phase, i.e., the excess has to be separated while not losing too much of the (expensive) nutrients. Nutrient recovery is therefore an important research topic (Hafenbradl, 2020). The heat of reaction is produced at the temperature level that is suitable for the microorganisms (35–70°C). To avoid overheating of the reactor, the water phase easily can be cooled either internally by immersed cooling coils or in an external heat exchanger fed with cooling water, which limits the further use of this heat flow. On the other hand, biological methanation reactors have to be protected from freezing during winter.

The big challenge for biological methanation is to provide sufficient contact between the gas phase and the water phase. CO_2 dissolves to some extent in water; H_2 however only very weakly. Therefore, the reactor systems developed so far try to maximize gas-liquid interface area by applying stirred bubble columns. These induce additional energy consumption of 2–2.5% of the electricity used in the electrolysis, leading to an efficiency loss of the same order of magnitude (Heller, 2016; Hafenbradl, 2020).

As an alternative, counter-current trickling bed reactors are under development (Rachbauer et al., 2016) that allow large gas-liquid interfaces without stirring. Instead, the pump for the recirculation of the liquid has to be operated.

Catalytic Methanation

While biological methanation was investigated to some extent already in the 1970s and reconsidered a few years ago, catalytic methanation has been continuously used since decades and further developed. Methanation of small traces of carbon oxides in the H_2 flow to ammonia synthesis reactors is state of the art; further catalytic methanation for the production of synthetic natural gas (SNG) from coal gasification gas has been scaled-up to the GW-scale and is still in operation in the US and especially in China (Schildhauer, 2016). Decentralized methanation of biomass-based gas streams has been under development since nearly 20 years, especially for the conversion of wood gasification based gas (Rabou and Bos, 2012; Held, 2016; Rabou et al., 2016; Schildhauer, 2016; Schildhauer and Biollaz, 2016; Thunman et al., 2018). Since about 10 years, the methanation of CO_2 and biogas for Power-to-Gas applications has been considered (Specht et al., 2016).

Catalytic methanation proceeds at temperatures above 200–300°C on supported metal catalysts, where an active metal, for example nickel or ruthenium, is distributed over the large (inner) surface of porous ceramic support materials such as alumina and silica. Well performing commercial catalyst exist since more than 50 years; a recent article reviews the progress in synthesis of suited catalysts for CO_2 methanation (Lv et al., 2020). The challenge in catalytic methanation reactors is to remove the significant heat of reaction from the reactor to avoid catalyst sintering and conversion limitation due to the thermodynamic

equilibrium. The high temperature level allows the recovery of two heat flows at favourable temperature levels: the heat of reaction (above 250–300°C) and the heat of condensation of the produced water (depending on the pressure level, but usually above 150°C), see (Witte et al., 2018a).

For the classical reactor system, the adiabatic fixed bed reactor, a temperature increase to a certain level (550°C or 700°C depending on the applied catalyst) is considered acceptable, and is controlled by the recirculation of cooled product gas. As the temperature increase impedes full conversion, one further reactor and at least one third reactor after condensation is necessary.

In the last 2 decades, cooled fixed bed reactors have been developed (e.g., Hashimoto et al., 1999; Specht et al., 2016) that allow the removal of the heat of reaction in the reactor and to realize a temperature profile that favors high conversion, also by different cooling zones (Specht et al., 2016; Moioli et al., 2019). To avoid high pressure drop, catalyst particles in the range of a few millimetres diameter are usually used. As the radial heat transfer in reactors filled with coarse catalyst particles is limited, several fixed bed reactor concepts with high internal heat transport by thermal conduction have been developed. The necessary large amount of conducting metal is implemented in the reactors either as wrapped metal monoliths or by metal plates which form channels in the sub millimetre range (LeViness et al., 2014; Dittmeyer et al., 2017; Bengaouer et al., 2018; Neuberg et al., 2019; Chwoła et al., 2020) that are coated with catalyst or filled with catalyst powder. Further, metal foams (Frey et al., 2016; Bengaouer et al., 2018) and static mixer type packings (Schildhauer et al., 2009; Sudiro et al., 2010) and recently also 3D printed metal structures are discussed (Danaci et al., 2018).

A completely different approach is followed by reactor systems that allow the movement of the catalyst by fluidization, either in the up-flowing gas stream (bubbling gas-solid fluidized beds, Friedrichs et al., 1985, Schildhauer and Biollaz, 2016) or in an inert liquid with fine, suspended catalyst powder (three-phase gas-liquid-solid bubble columns, Frank et al., 1976; Lefebvre et al., 2015). The advantage of the fluidization is dual: 1) due to the movement of the catalyst particles, the heat production is spread over the complete volume of the reactor where it can be removed by immersed heat exchangers; 2) due to the movement, the local heat transfer rate to the immersed surface is increased. As a result, both reactor types operate close to isothermal conditions and allow for relatively fast load changes (in the range from 30 to 100%, Friedrichs et al., 1985) without significantly changing temperature profiles and thus without the connected thermal stress to the catalyst. The challenges in the bubble column reactor is the low gas-liquid mass transfer (similar as in most biological reactors). For the bubbling gas-solid fluidized bed reactor, a sufficiently stable catalyst has to be applied to avoid loss of catalyst material due to attrition.

Upgrading

The regulations for unlimited injection of biomethane into the gas grid differ over Europe. While in the North-West of Germany and in the Netherlands, natural gas from the Groningen field with a relatively low CH_4 content dominates, in most part of Europe, CH_4 contents for injected gas of >96% are mandatory. A further differentiation is caused by the limitations with respect to residual H_2 content, which is 5% in Spain, 2% in Germany and Switzerland and even below 0.5% in Italy.

Most reactor concepts do not or not easily allow for full conversion with low residual H_2 contents, either due to mass transfer limitation (biological stirred tank reactors or catalytic gas-liquid-solid bubble columns) or to thermodynamic equilibrium at the temperatures necessary for sufficient catalytic activity (all catalytic reactors). In case of mass transfer limitations, lower gas throughput helps, but leads to larger reactor volumes (Hafenbradl, 2020). For catalytic reactors, the necessary gas quality can be achieved by either a reactor zone with low temperature and an (expensive) low temperature-active noble metal catalyst (Moioli et al., 2019), or by condensation to remove water and a second reactor (Specht et al., 2016; Witte et al., 2018a; Dannesboe, 2019; Guilera et al., 2019) which however necessitates a further heat exchanger system.

An alternative that can be used for any reactor system is the use of a membrane that separates unreacted H_2 and CO_2 from the CH_4. For this, commercial biogas-upgrading membranes can be used. In state of art polymeric membranes, most of the product CH_4 stays on the high pressure side of the membrane (retentate). Humidity and a fraction of the CH_4 permeate together with H_2 and CO_2 to the low-pressure side of the membrane and have to be recycled to the reactor to avoid loss of valuable H_2 and CH_4.

Due to the low residual amounts of H_2 and CO_2 after well-performing catalytic reactors (below 10 and 2%, respectively (Specht et al., 2016; Witte et al., 2019), the permeate can consist of CH_4 up to more than 60%. This raises the question of cost optimization as the CH_4 recompression is connected to operational costs and higher capital costs that add to the membrane costs. Witte et al. (2018b) compared the costs of a co-current membrane system to the costs of a second catalytic reactor and did not find a significant difference based on the available cost information from literature. A recent experimental study showed however that counter-current membrane operation allows for smaller membrane areas and/or lower pressure gradients which opens room for further optimization (Gantenbein et al., 2020).

Successful Long Duration Tests

In the last years, a number of long duration tests (mostly at a Technology Readiness Level of 5) were conducted in Germany (Heller, 2016; Specht et al., 2016), Denmark (Dannesboe, 2019; Hafenbradl, 2020), Spain (Guilera et al., 2019), Austria (Rachbauer et al., 2016) and Switzerland (Witte et al., 2019) to demonstrate the technical feasibility of direct methanation of real biogas. These tests cover several reactor concepts (catalytic: cooled fixed bed (Specht et al., 2016), fluidized bed (Witte et al., 2019), micro-structured heat exchange reactor (Guilera et al., 2019); biological: stirred bubble columns, trickle bed (Heller, 2016; Rachbauer et al., 2016; Hafenbradl, 2020) and biogas sources. **Table 1** gives an overview of the tests for which detailed public information is available.

The volume of the main reactor ranges from around few liters (catalytic) to several cubic meters (biological), while the produced

TABLE 1 | Overview long duration testing of direct biogas methanation.

Company/ Institution	Solarfuel/etogas (today: Hitachi Zosen inova)	Paul Scherrer Institut	Haldor Topsøe A/S	Ineratec GmbH	Electrochaea	Microbenergy	University for natural resources and life sciences (Boku), Vienna
Location of pilot plant	Hessen, Germany	Zürich-Werdhölzli Switzerland	Foulum, Denmark	Sabadell, Spain	Avedøre, Denmark	Allendorf, Germany	Tulln, Austria
Raw gas source	Anaerobic digestion	Commercial anaerobic digestion of sewage sludge and green waste	Anaerobic digestion of agricultural waste and manure	Commercial anaerobic digestion of sewage sludge	Commercial anaerobic digestion of sewage sludge	Commercial anaerobic digestion	Pilot scale anaerobic digestion of manure and sucrose
Reactor type	2 cooled tubular fixed bed in series with intermediate condensation	Bubbling fluidized bed	2 cooled tubular fixed bed in series with intermediate condensation	2 micro-structured heat exchange reactors in series with intermediate condensation	Stirred bubble column	Stirred bubble column	Countercurrent trickle bed
Technology readiness level	5	5	5	5	7	7	3–4
Catalyst	Nickel/alumina	860 g Nickel/alumina	Nickel/alumina	105 g of Ni/CeO_2/alumina, 400–500 μm, diluted with SiC	Specific archaea type	Mixed micro-organisms	Mixed micro-organisms
Cooling system	Double shell with thermooil plus gas recycle loop	TRL 5: Cold air in double shell; pilot scale: Thermooil	Boiling water	Water evaporation 1st stage, air cooling 2nd stage	Cooling water	Cooling water	External cooling of recirculated liquid
Reactor temperature	250–550°C	320–360°C	280–680°C	475–375°C (1st), 375–275°C (2nd)	60–65°C	60–70°C	37 ± 2°C
Reactor pressure	6 barg	6 barg	20 barg	2.5–8 bar, mainly 5 barg	10 bar	5–10 bar	Ambient
H_2/CO_2 molar ratio	Ca. 4	3.95–4.2	3.75–4.15	4	Around 4	4	During 840 h: 3.7–4.1 During 672 h: 4.4–6.7
Additional CH_4 production	14 kW_{HHV}	0.6–0.84 Nm^3/h = 6.6–9.2 kW_{HHV}	4 Nm^3/h = 45 kW_{HHV}	Ca.1.4 Nm^3/h = 15.4 kW_{HHV}	50 Nm^3/h = 550 kW_{HHV}	15 Nm^3/h = 165 kW_{HHV}	0.6 L/h = <0.01 kW_{HHV}
CH_4 concentration after main reactor	Unknown	85–90% CH_4	94.6%	72.66%	>97%	>98%	94–99%
CH_4 concentration after upgrading	>91%, <4% H_2	97%, <2% H_2	97.9%, <2% H_2	93.48%, <5% H_2	No upgrading	No upgrading	No upgrading
Volume main reactor	Few liters catalyst	<1 kg catalyst, ca. 2 L volume; total reactor: 13 L	Length 2.3 m, diameter not disclosed	2 reactors of 29.5 cm × 15 cm × 33.5 cm = 2 × 14.8 L	Ca. 7 m^3 (3600 L liquid)	5 m^3	Length 1.5 m, 8 cm diameter; ca. 7.5 L content
Type upgrading	Condensation and second reactor	Polymer membrane and H_2 recycle	Condensation and second reactor	Condensation and second reactor	None	None	None
Duration of test	Unknown (several weeks)	1150 h	1,000 h	Unknown	>500 h	Several 1000 h experience	>1500 h
Gas cleaning measures	"Fine gas cleaning", no further information	Drying at 4°C, cold sorbents: Mixed metal oxides, active carbon functionalized with metal oxides, metal oxide on high surface support	Bio-trickling filter, active carbon, hot ZnO with promoters	Drying at 5°C; active carbon filters at ambient condition, active carbon at elevated pressure and ZnO at 250°C	Unknown	Unknown	None
Steam addition	Yes	Yes: CO_2/H_2O = 2:1	None	0.5% O_2 and 2,000 ppm H_2O = <1% steam	None	None	None
Additional information					Electricity consumption stirrer 3 W/l = 1.3–2.5% of electrolyser-input	Electricity consumption stirrer 2–2.5% of electrolyser-input	
Refs.	Specht et al. (2016)	(Witte et al., (2019), Calbry-Muzyka et al. (2019a)	Dannesboe (2019)	Guilera et al. (2019)	Hafenbradl (2020)	Heller (2016)	Rachbauer et al. (2016)

CH_4 ranges from 6.6 to 550 kW_{HHV} (Hafenbradl, 2020). Due to the limited information available, a clear order of methanation capacity per reactor volume is not possible, but the catalytic reactors outperform the biological ones by about one order of magnitude.

Nickel-based catalysts dominate in catalytic reactors, while both specialized archaea and mixed cultures are used in biological plants. The operation conditions with respect to H_2 to CO_2 molar ratio (around the stoichiometric value of 4) and pressure (5–10 bar) are quite similar in all reactors; only the fixed bed reactor concept by Haldor Topsøe A/S operates at 20 bar (Dannesboe, 2019).

The temperature range is very specific for each reactor type where the difference of the reactor concepts leads to diverse temperature range situation. The biological reactors operate at the temperature range suitable for meso- and thermophilic microorganisms at 35–65°C leading to the above mentioned limitations of using this heat. The catalytic reactors with very high internal heat transport properties (microchannel reactor, Guilera et al., 2019) show relatively flat temperature profiles with maximum 100 K gradient, while the fixed bed reactors are characterized by a hot spot above 550°C at the reactor inlet (Specht et al., 2016). The fluidized bed proved to be nearly isothermal around 350°C (Witte et al., 2019).

Unfortunately, not all projects explain their gas cleaning in detail, but the well-described ones are quite different due to the varying biogas sources. In the test in Zurich, Switzerland, mixed gas from sewage sludge digestion (80%) and green waste digestion (20%) was converted, which has a moderate level of terpenes and siloxanes, but a significant amount of organic sulfur species (Witte et al., 2019). Here, a combination of cold adsorbers with metal oxides and impregnated activated carbon reached the goal to keep sulfur concentrations in the feed to the catalytic methanation significantly below 1 ppm_v (Calbry-Muzyka et al., 2019a). In Foulum/Denmark, biogas from digestion of agricultural waste and manure was used (Dannesboe, 2019). The gas cleaning concept consists of a bio-trickling filter with oxygen addition, active carbon at ambient temperatures and a promoted ZnO bed at elevated temperatures. The plant in Spain applied activated carbons at two pressure levels and a hot ZnO bed (Guilera et al., 2019).

All of the reactors were operated for several hundreds to more than 1,000 h and reached the necessary gas quality for the injection into the local gas grid, for which the conditions differ significantly within Europe. Most catalytic process concepts include an upgrading step, either a second reactor after intermediate condensation or a membrane to recycle unreacted gas, especially H_2. Biological reactors can reach the necessary gas quality in one step due to the favourable thermodynamics at low temperatures, when the throughput is not too high, i.e., the reactor is sufficiently large.

DISCUSSION

This overview of different process concepts for direct methanation of biogas shows very different answers to the three main challenges in this process chain: management of impurities in the raw biogas, heat removal in the main reactor (where the exothermic reaction takes place), and up-scaling options and market implementation.

Gas Cleaning

The impurities in the biogas strongly depend on the feedstock and the chosen operation conditions. While siloxanes are the challenge in the otherwise relatively clean gas from anaerobic sewage sludge digestion, green waste digestion increases the amount of aromatics and terpenes. Although terpenes themselves are not necessarily a problem in the catalytic methanation reactors, they can impede the removal of sulfur species in adsorption beds. With respect to sulfur species, it is reasonable to expect, besides significant amounts of H_2S, up to a few ppm_v of carbonyl sulfide and organic sulfur species (mercaptans and thioethers). The latter is no problem in biological methanation, but is detrimental to catalyst stability in catalytic methanation. Therefore, thorough non-H_2S sulfur removal to the sub-ppm level is absolutely necessary. To avoid high specific costs, the processes developed for small-scale biogas methanation do not utilize the gas cleaning steps as found at large scale in refineries and coal gasification plants, but rather use gas drying at low temperatures combined with several sorbents based on activated carbon and metal oxides, partly at elevated temperatures.

Due to the varying composition of the biogas, no standard gas cleaning solution seems to have been developed so far. Further development in this field and cost optimization will be necessary, accompanied by developing standard methods for analytics. The latter is needed both for determining the biogas composition to control the H_2/CO_2 molar ratio, and for impurity measurement. Finally, it was shown that long duration tests of the chosen gas cleaning measures with the real gas (and thus with the varying concentrations of impurities) are of utmost importance to verify the gas cleaning performance.

Concepts for Methane Synthesis and Upgrading

The challenge of removing heat from the methanation reactor has led to a relatively large number of reactor concepts, of which several have been tested at TRL 5 or greater for direct methanation of real biogas. Reactors with liquid hold-up or moving catalyst particles, i.e., the biological and the fluidized bed reactors, allow for nearly isothermal operation. Reactors with fixed catalyst beds experience significant temperature gradients and hot spots, which might lead to catalyst damage and necessitates measures such as recirculation cooling. Strong temperature gradients can be a problem when changing the gas load, as then the temperature profile moves within the reactor. In such cases, too fast local temperature changes have to be avoided in order not to compromise the catalyst stability. While solutions for fast load changes (within few minutes) are discussed in the scientific literature (Bremer et al., 2017; Kreitz et al., 2019; Theurich et al., 2019), in reality a tank for H_2 storage can significantly dampen this necessity. To limit the size of this

H_2 tank, however, relatively low part load or even simple stop and restart of the methanation reactor operation are helpful. Here, biological methanation reactors have shown an impressive ability to interrupt for hours the H_2 feed without any problem (Hafenbradl, 2020).

All process concepts discussed here allowed the attainment of the gas quality (minimum CH_4 content, maximum H_2 content) necessary for the injection into the respective local grid, which is easier to achieve in areas such as the north-west of Germany and in Spain (<5% H_2) than in areas such as Switzerland or the south of Germany (<2% H_2). Biological methanation reactors at moderate throughput reach this gas quality due to low operating temperatures and the inherent, favourable thermodynamics, without further upgrading (besides the drying and odoration steps that are mandatory for all processes). Catalytic reactors need an intermediate condensation step and a second reactor or a membrane for recirculation of unreacted gas; in other words, compared to biological methanation, more units are needed. On the other hand, the higher temperature level in catalytic reactors enable the further use of the heat of reaction and the heat of water condensation, which improves the potential synergies with the biogas plant, the overall efficiency and therefore the process economics.

Costs

Generally, Power-to-Gas plant costs are dominated by the electricity costs and the capital costs of the electrolyser (Witte et al., 2018b). The costs of electrolysers are expected to decrease markedly in future: studies estimate the average costs of alkaline electrolysers at 1,300 €/kW_{el} in 2017 dropping to <500 €/kW_{el} by 2050, of PEM electrolysers at 1,900 €/kW_{el} in 2017 dropping to 500 €/kW_{el} in 2050, and of high-temperature electrolysers at 3,570 €/kW_{el} in 2017 dropping to 535 €/kW_{el} in 2050 (Thema et al., 2019). Costs of biogas cleaning to a level acceptable for methanation have been estimated in the range of 0.03–0.10 €/Nm^3 of biogas, as discussed earlier in section "*Costs*".

In the methanation step itself, capital costs for the reactor, the compressor and heat exchangers have the most significant impact as well as the electricity costs for stirrers and compressors. Different from electrolysers, the specific costs of these units are strongly depending on the plant size with a tendency that they decrease by a factor of more than two for a ten times larger plant. It therefore does not make sense to indicate absolute numbers for the general discussion, while it is possible to consider the differences between the respective technologies.

To withstand the temperatures or the corrosive potential of CO_2 dissolved in water, all methanation reactors require a stainless steel system at elevated pressure (at least PN 16), therefore the number and size of the reactor(s) and heat exchangers has direct importance for the costs. Here catalytic reactors with limited heat transfer (fixed beds) and biological reactors are at a disadvantage in comparison with, for example, fluidized beds. Compressor costs can be minimized by lower pressure drop through the reactor, and by lower recirculation rates, for instance by improved heat transfer in externally cooled fixed bed reactors, or due to more selective membranes in case of membrane based upgrading. Stirrer costs in biological reactors can be optimized by well-designed gas injection systems; due to the disadvantageous scaling rules for the energy consumption of stirred tank reactors, the stirring requirements might however limit the feasible diameter of this reactor type. Furthermore, the direct methanation of biogas itself has already an energy advantage over state-of-the art biogas Power-to-Gas plants, as these first separate the CO_2 from CH_4 before feeding to the methanation unit, which represents a continuous energy loss.

So far, a consistent, detailed cost comparison for the overall process (total cost of ownership) for biological and catalytic methanation is missing; only the cost differences between catalytic fixed bed and fluidized bed processes have been investigated (Witte et al., 2018b), showing a slight advantage for fluidized bed reactors over cooled fixed beds. From this comparison and the aspects above, it can be expected that the real cost differences will only be known once demonstration plants of each technology have been built and operated for several years.

Upscaling and Market Implementation

To reach the demonstration phase (TRL 8), most technologies have to undergo upscaling. While stirred bubble columns for biological methanation have been built up to 350 $kW_{HHV,CH4}$ (TRL 7), biological trickle bed reactors have not yet reached the pilot scale (TRL 6,7). In Dietikon, Switzerland, planning and initial construction work is ongoing for a stirred biological reactor from microbenergy that will convert the H_2 from a 2.5 MW_{el} electrolyser. At this site, there exists not only a waste water treatment plant delivering the biogas, but also a source of renewable electricity which can be used without paying a grid use fee.

Several catalytic systems have been extensively tested for methanation of pure CO_2 or producer gas from wood gasification: Adiabatic fixed bed reactors at 20 $MW_{HHV,CH4}$ in the GoBiGas plant (Held, 2016); cooled fixed bed reactors at 3 $MW_{HHV,CH4}$ in Werlte/Germany (Specht et al., 2016); catalytic fluidized bed reactors at 1 $MW_{HHV,CH4}$ in Güssing/Austria (EU-project BioSNG, Schildhauer and Biollaz, 2016); catalytically coated monoliths at >500 $kW_{HHV,CH4}$ and micro-structured heat exchanger reactors at up to 90 $kW_{HHV,CH4}$ within the EU project Store and Go Roadmap (2019). Based on this experience, it will be possible (but has not yet been realized) to test these reactor types in pilot scale with biogas and to demonstrate their options for flexible load gradients and low part load. Additionally, the interaction of methanation reactors with upgrading membranes needs further investigation. Therefore, an important gap on the way to market implementation is the erection and operation of demonstration plants, which under the current market situation (high price for renewable electricity including grid use fees, too low value of renewable gas) needs support measures.

OUTLOOK

When comparing different Power-to-Methane process concepts, the direct methanation of biogas is closest to economic feasibility

as it combines the conversion of (relatively expensive) renewable H_2 with the upgrading of (relatively cheaper raw biogas) to valuable biomethane. This is an important advantage over schemes that work with CO_2 which must first be separated from biogas, air or flue gas (Biollaz et al., 2017). With respect to life cycle green house gas emission, direct methanation outperforms the methanation of CO_2 separated from biogas (Zhang et al., 2020) due to the avoided effort. This is especially significant, if a pressure swing adsorption was used for the CO_2 separation because of its relatively high methane emissions. Still, due to the absence of noble metal catalyst or similarly rare materials in the methanation and gas cleaning, the life cycle greenhouse gas emission are completely dominated by the electrolysis and to the largest extent by the CO_2 intensity of the used electricity.

While most biogas plants are relatively small with scales of 1 to few MW, there is generally a large number of waste water treatment plants that are close to the natural gas grid. In addition, the number of biogas plants with green and agricultural waste and manure is increasing. At the same time, the subsidies for electricity production from biogas are decreasing in many countries, which further enlarges the potential market for direct methanation of biogas.

To exploit this market potential, on the technical side the most important steps are gaining a better understanding and cost optimization of the gas cleaning as well as demonstration plants for the different methanation and upgrading technologies. In the coming years, the specifications with respect to residual H_2 in biomethane injected into the natural gas network might move to higher values, which would facilitate the operation of biogas production and decrease the upgrading effort. On the economic side, besides more consistent comparison of technologies at demo-scale operation, the potential synergies within the biogas sites should be the focus: the use of heat flows from the methanation plant for the biomass handling, efficient high-temperature electrolysis or neighbored plants; furthermore, synergies with respect to services and trained staff; and finally flexibility options with respect to time of electricity consumption.

AUTHOR CONTRIBUTIONS

All authors agree to be accountable for the content of the work. AC-M focused on the gas cleaning part, TS on the methanation/upgrading part and the discussion.

FUNDING

Our research was financially supported by the Swiss Innovation Agency lnnosuisse and is part of the Swiss Competence Center for Energy Research SCCER BIOSWEET. The authors would like to acknowledge financial and other support from the Swiss Federal Office for Energy (SFOE), FOGA and the ESI Platform at PSI.

ACKNOWLEDGMENTS

The authors would like to thank all colleagues of the Thermochemical Processes group at PSI as well as their industrial collaborators for valuable discussions.

REFERENCES

Abatzoglou, N., and Boivin, S. (2008). A review of biogas purification processes. *Biofuels Bioprod. Biorefin.* 3 (1), 42–71. doi:10.1002/bbb.117

Ajhar, M., Travesset, M., Yüce, S., and Melin, T. (2010). Siloxane removal from landfill and digester gas—a technology overview. *Bioresour. Technol.* 101 9, 2913–2923. doi:10.1016/j.biortech.2009.12.018

Andersson, F. A., Karlsson, A., Svensson, B. H., and Ejlertsson, J. (2004). Occurrence and abatement of volatile sulfur compounds during biogas production. *J. Air Waste Manag. Assoc.* 54 (7), 855–861. doi:10.1080/10473289.2004.10470953

Arnold, M., and Kajolinna, T. (2010). Development of on-line measurement techniques for siloxanes and other trace compounds in biogas. *Waste Manag.* 30 (6), 1011–1017. doi:10.1016/j.wasman.2009.11.030

Arrhenius, K., Yaghooby, H., Rosell, L., Büker, O., Culleton, L., Bartlett, S., et al. (2017). Suitability of vessels and adsorbents for the short-term storage of biogas/biomethane for the determination of impurities—siloxanes, sulfur compounds, halogenated hydrocarbons. *BTEX. Biomass and Bioenergy* 105, 127–135. doi:10.1016/j.biombioe.2017.06.025

Bach, C., Beuse, M., Georges, G., Held, M., Heselhaus, S., Korba, P., et al. (2019). *Perspectives of Power-to-X technologies in Switzerland: a white paper*. Editors T. Kober and C. Bauer, 2nd Edn. Villigen, Switzerland: Paul Scherrer Institute. doi:10.3929/ethz-b-000352294

Bailera, M., Lisbona, P., Romeo, L. M., and Espatolero, S. (2017). Power to Gas projects review: lab, pilot and demo plants for storing renewable energy and CO_2. *Renew. Sustain. Energy Rev.* 69, 292–312. doi:10.1016/j.rser.2016.11.130

Barelli, L., Bidini, G., Desideri, U., Discepoli, G., and Sisani, E. (2015). Dimethyl sulfide adsorption from natural gas for solid oxide fuel cell applications. *Fuel Process. Technol.* 140, 21–31. doi:10.1016/j.fuproc.2015.08.012

Bengaouer, A., Ducamp, J., Champon, I., and Try, R. (2018). Performance evaluation of fixed-bed, millistructured, and metallic foam reactor channels for CO_2 methanation. *Canad. J. Chem. Eng.* 96, 1937–1945. doi:10.1002/cjce.2314

Biollaz, S., Calbry-Muzyka, A., Schildhauer, T. J., Witte, J., and Kunz, A. (2017). Final Report BfE-Projekt SI/501284-04. Direct methanation of biogas. Available at: https://www.aramis.admin.ch/Texte/?ProjectID=36924 (Accessed June 1, 2020).

Biswas, S., Kulkarni, A. P., Giddey, S., and Bhattacharya, S. (2020). A review on synthesis of methane as a pathway for renewable energy storage with a focus on solid oxide electrolytic cell-based processes. *Front. Energy Res.* 8, 570112. doi:10.3389/fenrg.2020.570112

Bremer, J., Rätze, K. H. G., and Sundmacher, K. (2017). CO_2 methanation: optimal start-up control of a fixed-bed reactor for power-to-gas applications. *AIChE J.* 63, 23–31. doi:10.1002/aic.15496

Buttler, A., and Spliethoff, H. (2018). Current status of water electrolysis for energy storage, grid balancing and sector coupling via power-to-gas and power-to-liquids: a review. *Renew. Sustain. Energy Rev.* 83 (3), 2440–2454. doi:10.1016/j.rser.2017.09.003

Cabrera-Codony, A., Montes-Morán, M. A., Sánchez-Polo, M., Martín, M. J., and Gonzalez-Olmos, R. (2014). Biogas upgrading: optimal activated carbon properties for siloxane removal. *Environ. Sci. Technol.* 48 (12), 7187–7195. doi:10.1021/es501274a

Calbry-Muzyka, A. S., Gantenbein, A., Schneebeli, J., Frei, A., Knorpp, A. J., Schildhauer, T. J., et al. (2019a). Deep removal of sulfur and trace organic compounds from biogas to protect a catalytic methanation reactor. *Chem. Eng. J.* 360, 577–590. doi:10.1016/j.cej.2018.12.012

Calbry-Muzyka, A. S., Indlekofer, J., Schneebeli, J., and Biollaz, S. M. A. (2019b). Online measurement of sub-ppmv total sulfur in biogas by chemiluminescence. *Energy Fuel.* 33 (10), 9859–9869. doi:10.1021/acs.energyfuels.9b01778

Chwoła, T., Spietz, T., Więcław-Solny, L., Tatarczuk, A., Krótki, A., Dobras, S., et al. (2020). Pilot plant initial results for the methanation process using CO_2 from amine scrubbing at the Łaziska power plant in Poland. *Fuel* 263, 116804. doi:10.1016/j.fuel.2019.116804

Danaci, S., Protasova, L., Snijkers, F., Bouwen, W., Bengaouer, A., and Marty, P. (2018). Innovative 3D-manufacture of structured copper supports post-coated with catalytic material for CO_2 methanation. *Chem. Eng. Process.* 127, 168–177. doi:10.1016/j.cep.2018.03.023

Dannesboe, C. (2019). Catalytic upgrading of CO2 in biogas. PhD thesis. Aarhus (Denmark): University of Aarhus.

Dannesboe, C., Hansen, J. B., and Johannsen, I. (2019). Removal of sulfur contaminants from biogas to enable direct catalytic methanation. *Biomass Conv. Bioref.* doi:10.1007/s13399-019-00570-7

de Aguiar, M. F., and Coelho, G. L. V. (2017). Adsorption of sulfur compounds from natural gas by different adsorbents and desorption using supercritical CO_2. *J. Environ. Chem. Eng.* 5 (5), 4353–4364. doi:10.1016/j.jece.2017.07.079

de Arespacochaga, N., Valderrama, C., Mesa, C., Bouchy, L., and Cortina, J. L. (2013). Biogas deep clean-up based on adsorption technologies for Solid Oxide Fuel Cell applications. *Chem. Eng. J.* 255, 593–603. doi:10.1016/j.cej.2014.06.072

de Arespacochaga, N., Valderrama, C., Raich-Montiu, J., Crest, M., Mehta, S., and Cortina, J. L. (2015). Understanding the effects of the origin, occurrence, monitoring, control, fate and removal of siloxanes on the energetic valorization of sewage biogas—a review. *Renew. Sustain. Energy Rev.* 52, 366–381. doi:10.1016/j.rser.2015.07.106

Díaz, I., Pérez, S. I., Ferrero, E. M., and Fdz-Polanco, M. (2011). Effect of oxygen dosing point and mixing on the microaerobic removal of hydrogen sulphide in sludge digesters. *Bioresour. Technol.* 102 (4), 3768–3775. doi:10.1016/j.biortech.2010.12.016

Dittmeyer, R., Boeltken, T., Piermartini, P., Selinsek, M., Loewert, M., Dallmann, F., et al. (2017). Micro and micro membrane reactors for advanced applications in chemical energy conversion. *Current Opinion in Chemical Engineering* 17, 108–125. doi:10.1016/j.coche.2017.08.001

Dumas, C., Ottosen, L. D. M., Escudié, R., and Jensen, P. (2020). Biological methanation or (Bio/Syn)-gas upgrading. *Front. Energy Res.* 8, 30. doi:10.3389/fenrg.2020.00030

Erekson, E. J., and Bartholomew, C. H. (1983). Sulfur poisoning of nickel methanation catalysts: II. effects of H2S concentration, CO and H_2O partial pressures and temperature on deactivation rates. *Appl. Catal.* 5 (3), 323–336.

European Organization for Standardization (2016). *EN 16723-1—natural gas and biomethane for use in transport and biomethane for injection in the natural gas network—part 1: specifications for biomethane for injection in the natural gas network*. Brussels, Belgium: European Organization for Standardization.

European Organization for Standardization (2017). *EN 16723-2—natural gas and biomethane for use in transport and biomethane for injection in the natural gas network—part 2: automotive fuels specifications*. Brussels, Belgium: European Organization for Standardization.

Finocchio, E., Garuti, G., Baldi, M., and Busca, G. (2008). Decomposition of hexamethylcyclotrisiloxane over solid oxides. *Chemosphere* 72 (11), 1659–1663. doi:10.1016/j.chemosphere.2008.05.032

Frank, M. E., Sherwin, M. B., Blum, D. B., and Mednick, R. L. (1976). "Liquid phase methanation—shift PDU results and pilot plant status," in Proceeding of eighth synthetic pipeline gas symposium, Chicago, IL, October 1976 (Chigago, IL: American Gas Association), 159–179.

Frey, M., Romero, T., Roger, A.-C., and Edouard, D. (2016). Open cell foam catalysts for CO_2 methanation: presentation of coating procedures and *in situ* exothermicity reaction study by infrared thermography. *Catal. Today* 273, 83–90. doi:10.1016/j.cattod.2016.03.016

Friedrichs, G., Proplesch, P., Wismann, G., and Lommerzheim, W. (1985). *Methanisierung von Kohlenvergasungsgasen im Wirbelbett Pilot Entwicklungsstufe, Technologische Forschung und Entwicklung—Nichtnukleare Energietechnik*. Duisburg, Germany: Thyssengas GmbH prepared for Bundesministerium fuer Forschung und Technologie.

Gantenbein, A., Witte, J., Biollaz, S., Kröcher, O., and Schildhauer, T. J. (2020). Flexible application of biogas upgrading membranes for hydrogen recycle in power-to-methane processes. *Chem. Eng. Sci.* 229, 116012. doi:10.1016/j.ces.2020.116012

Gorre, J., Ruoss, F., Karjunen, H., Schaffert, J., and Tynjäläb, T. (2020). Cost benefits of optimizing hydrogen storage and methanation capacities for Power-to-Gas plants in dynamic operation. *Appl. Energy* 257, 113967. doi:10.1016/j.apenergy.2019.113967

Götz, M., Lefebvre, J., Mörs, F., McDaniel Koch, A., Graf, F., Bajohr, S., et al. (2016). Renewable Power-to-Gas: a technological and economic review. *Renew. Energy* 85, 1371–1390. doi:10.1016/j.renene.2015.07.066

Guilera, J., Andreu, T., Basset, N., Boeltken, T., Timm, ., Mallol, I., et al. (2019). Synthetic natural gas production from biogas in a waste water treatment plant. *Renew. Energy* 146, 1301–1308. doi:10.1016/j.renene.2019.07.044

Hafenbradl, D. (2020). "Biological methanation," Presentation at of the store & go final conference, Karlsruhe, Germany, February 2020.

Hashimoto, K., Yamasaki, M., Fujimura, K., Matsui, T., Izumiya, K., Komori, M., et al. (1999). Global CO_2 recycling—novel materials and prospect for prevention of global warming and abundant energy supply. *Mater. Sci. Eng. A* 267, 200–206. doi:10.1016/S0921-5093(99)00092-1

He, C., Herman, D. J., Minet, R. G., and Tsotsis, T. T. (1997). A catalytic/sorption hybrid process for landfill gas cleanup. *Ind. Eng. Chem. Res.* 36 (10), 4100–4107. doi:10.1021/ie970252h

Held, J. (2016). "SNG from wood, the GoBiGas project," in *Synthetic natural gas from coal, dry biomass, and power-to-gas applications*. Editors T. J. Schildhauer, and S. M. A. Biollaz (New York, NY: Wiley & Sons), 77–159.

Heller, T. (2016). BioPower2Gas—power-to-gas with biological methanation. Presentation at of the Biomass for Swiss Energy Future Conference, Brugg, Switzerland, September 2016.

Hidalgo, D., and Martín-Marroquín, J. M. (2020). Power-to-methane, coupling CO_2 capture with fuel production: an overview. *Renew. Sustain. Energy Rev.* 132, 110057. doi:10.1016/j.rser.2020.110057

Kajolinna, T., Aakko-Saksa, P., Roine, J., and Kåll, L. (2015). Efficiency testing of three biogas siloxane removal systems in the presence of D5, D6, limonene and toluene. *Fuel Process. Technol.* 139, 242–247. doi:10.1016/j.fuproc.2015.06.042

Krayzelova, L., Bartacek, J., Díaz, I., Jeison, D., Volcke, E. I. P., and Jenicek, P. (2015). Microaeration for hydrogen sulfide removal during anaerobic treatment: a review. *Rev. Environ. Sci. Biotechnol.* 14 (4), 703–725. doi:10.1007/s11157-015-9386-2

Kreitz, B., Friedland, J., Güttel, R., Wehinger, G. D., and Turek, T. (2019). Dynamic methanation of CO_2—effect of concentration forcing. *Chem. Ing. Tech.* 91, 576–582. doi:10.1002/cite.201800191

Kuhn, J. N., Elwell, A. C., Elsayed, N. H., and Joseph, B. (2017). Requirements, techniques, and costs for contaminant removal from landfill gas. *Waste Manag.* 63, 246–256. doi:10.1016/j.wasman.2017.02.001

Lanzini, A., Madi, H., Chiodo, V., Papurello, D., Maisano, S., Santarelli, M., et al. (2017). Dealing with fuel contaminants in biogas-fed solid oxide fuel cell (SOFC) and molten carbonate fuel cell (MCFC) plants: degradation of catalytic and electro-catalytic active surfaces and related gas purification methods. *Prog. Energy Combust. Sci.* 61, 150–188. doi:10.1016/j.pecs.2017.04.002

Lefebvre, J., Götz, M., Bajohr, S., Reimert, R., and Kolb, T. (2015). Improvement of three-phase methanation reactor performance for steady-state and transient operation. *Fuel Process. Technol.* 132, 83–90. doi:10.1016/j.fuproc.2014.10.040

LeViness, S., Deshmukh, S. R., Richard, L. A., and Robota, H. J. (2014). Velocys fischer–tropsch synthesis technology—new advances on state-of-the-art. *Top. Catal.* 57, 518–525. doi:10.1007/s11244-013-0208-x

Lv, C., Xu, L., Chen, M., Cui, Y., Wen, X., Li, Y., et al. Recent progresses in constructing the highly efficient Ni based catalysts with advanced low-temperature activity toward CO_2 methanation, *Front. Chem.* 8, 269, 2020. doi:10.3389/fchem.2020.00269

Madi, H., Lanzini, A., Diethelm, S., Papurello, D., Van herle, J., Lualdi, M., et al. (2015). Solid oxide fuel cell anode degradation by the effect of siloxanes. *J. Power Sources* 279, 460–471. doi:10.1016/j.jpowsour.2015.01.053

Moioli, E., Gallandat, N., and Züttel, A. (2019). Model based determination of the optimal reactor concept for Sabatier reaction in small-scale applications over Ru/Al_2O_3. *Chem. Eng. J.* 375, 121954. doi:10.1016/j.cej.2019.121954

Montanari, T., Finocchio, E., Bozzano, I., Garuti, G., Giordano, A., Pistarino, C., et al. (2010). Purification of landfill biogases from siloxanes by adsorption: a study of silica and 13X zeolite adsorbents on hexamethylcyclotrisiloxane separation. *Chem. Eng. J.* 165 (3), 859–863. doi:10.1016/j.cej.2010.10.032

Neuberg, S., Pennemann, H., Shanmugam, V., Thiermann, R., Zapf, R., Gac, W., et al. (2019). CO_2 Methanation in microstructured reactors—catalyst development and process design. *Chem. Eng. Technol.* 42 (10), 2076–2084. doi:10.1002/ceat.201900132

Panos, E., Kober, T., and Wokaun, A. (2019). Long term evaluation of electric storage technologies vs alternative flexibility options for the Swiss energy system. *Appl. Energy* 252, 113470. doi:10.1016/j.apenergy.2019.113470

Papadias, D. D., Ahmed, S., and Kumar, R. (2012). Fuel quality issues with biogas energy—an economic analysis for a stationary fuel cell system. *Energy* 44 (1), 257–277. doi:10.1016/j.energy.2012.06.031

Park, C. M., and Novak, J. T. (2013). The effect of direct addition of iron(III) on anaerobic digestion efficiency and odor causing compounds. *Water Sci. Technol.* 68 (11), 2391–2396. doi:10.2166/wst.2013.507

Primavera, A., Trovarelli, A., Andreussi, P., and Dolcetti, G. (1998). The effect of water in the low-temperature catalytic oxidation of hydrogen sulfide to sulfur over activated carbon. *Appl. Catal. Gen.* 173 (2), 185–192. doi:10.1016/S0926-860X(98)00178-1

Rabou, L. P. L. M., and Bos, L. (2012). High efficiency production of substitute natural gas from biomass. *Appl. Catal. B Environ.* 111-112, 456–460. doi:10.1016/j.apcatb.2011.10.034

Rabou, L. P. L. M., Van der Drift, B., Van Dijk, E. H. A. J., Van der Meijden, C. M., and Vreugdenhil, B. J. (2016). "MILENA indirect gasification, OLGA tar removal, and ECN process for methanation," in *Synthetic natural gas from coal, dry biomass, and power-to-gas applications*. Editors T. J. Schildhauer and S. M. A. Biollaz (New York, NY: Wiley & Sons), 77–159.

Rachbauer, L., Voitl, G., Bochmann, G., and Fuchs, W. (2016). Biological biogas upgrading capacity of a hydrogenotrophic community in a trickle-bed reactor. *Appl. Energy* 180, 483–490. doi:10.1016/j.apenergy.2016.07.109

Rasi, S., Lehtinen, J., and Rintala, J. (2010). Determination of organic silicon compounds in biogas from wastewater treatments plants, landfills, and co-digestion plants. *Renew. Energy* 35 (12), 2666–2673. doi:10.1016/j.renene.2010.04.012

Rasi, S., Läntelä, J., and Rintala, J. (2011). Trace compounds affecting biogas energy utilisation—a review. *Energy Convers. Manag.* 52, 3369–3375. doi:10.1016/j.enconman.2011.07.005

Rasi, S., Seppälä, M., and Rintala, J. (2013). Organic silicon compounds in biogases produced from grass silage, grass and maize in laboratory batch assays. *Energy* 52, 137–142. doi:10.1016/j.energy.2013.01.015

Rasi, S., Veijanen, A., and Rintala, J. (2007). Trace compounds of biogas from different biogas production plants. *Energy* 32 (8), 1375–1380. doi:10.1016/j.energy.2006.10.018

Rönsch, S., Schneider, J., Matthischke, S., Schlüter, M., Götz, M., Lefebvre, J., et al. (2016). Review on methanation—from fundamentals to current projects. *Fuel* 166, 276–296. doi:10.1016/j.fuel.2015.10.111

Saber, D. L., and Cruz, K. M. H. (2009). *Pipeline quality biomethane: north American Guidance Document for introduction of dairy waste derived biomethane into existing natural gas networks: task 2*. Des Plaines, IL: Gas Technology Institute.

Salazar Gómez, J. I., Lohmann, H., and Krassowski, J. (2016). Determination of volatile organic compounds from biowaste and co-fermentation biogas plants by single-sorbent adsorption. *Chemosphere* 153, 48–57. doi:10.1016/j.chemosphere.2016.02.128

Schildhauer, T. J., Newson, E., and Wokaun, A. (2009). Closed cross flow structures—improving the heat transfer in fixed bed reactors by enforcing radial convection. *Chem. Eng. Process: Process Intensif.* 48 (1), 321–328. doi:10.1016/j.cep.2008.04.009

Schildhauer, T. J., and Biollaz, S. M. A. (2016). "Fluidized bed methanation for SNG production—process development at the Paul-Scherrer Institut," in *Synthetic natural gas from coal, dry biomass, and power-to-gas applications*. Editors T. J. Schildhauer, and S. M. A. Biollaz (New York, NY: Wiley & Sons), 221–229.

Schildhauer, T. J. (2016). "Methanation for SNG production—chemical reaction engineering aspects," in *Synthetic natural gas from coal, dry biomass, and power-to-gas applications*. Editors T. J. Schildhauer and S. M. A. Biollaz (New York, NY: Wiley & Sons), 77–159.

Seifert, A. H., Rittmann, S., Bernacchi, S., and Herwig, C. (2013). Method for assessing the impact of emission gasses on physiology and productivity in biological methanogenesis. *Bioresour. Technol.* 136, 747–751. doi:10.1016/j.biortech.2013.03.119

Soreanu, G., Béland, M., Falletta, P., Edmonson, K., Svoboda, L., Al-Jamal, M., et al. (2011). Approaches concerning siloxane removal from biogas—a review. *Can. Biosyst. Eng.* 53, 1–18.

Specht, M., Brellochs, J., Frick, V., Stürmer, B., and Zuberbühler, U. (2016). "The power-to-gas (P2G®) process: storage of renewable energy in the natural gas grid via fixed bed methanation of CO_2/H_2," in *Synthetic natural gas from coal, dry biomass, and power-to-gas applications*. Editors T. J. Schildhauer and S. M. A. Biollaz (New York, NY: Wiley & Sons), 77–159.

Spiegel, R. J., and Preston, J. L. (2003). Technical assessment of fuel cell operation on anaerobic digester gas at the Yonkers, NY, wastewater treatment plant. *Waste Manag.* 23 (8), 709–717. doi:10.1016/S0956-053X(02)00165-4

Store and Go Roadmap (2019). Innovative large-scale energy storage technologies and Power-to-Gas concepts after optimization, Roadmap for large-scale storage based PtG conversion in the EU up to 2050. Available at: https://www.storeandgo.info/fileadmin/dateien/STORE_GO_power_to_gas_roadmap.pdf (Accessed June 1, 2020).

Store and Go (2020). European Union project. Available at: https://www.storeandgo.info/ (Accessed September 21, 2020).

Struis, R. P., Schildhauer, T. J., Czekaj, I., Janousch, M., Biollaz, S. M. A., and Ludwig, C. (2009). Sulphur poisoning of Ni catalysts in the SNG production from biomass: a TPO/XPS/XAS study. *Appl. Catal. Gen.* 362 (1-2), 121–128. doi:10.1016/j.apcata.2009.04.030

Sudiro, M., Bertucco, A., Groppi, G., and Tronconi, E. (2010). "Simulation of a structured catalytic reactor for exothermic methanation reactions producing synthetic natural gas," in *Computer aided chemical engineering*. Editors S. Pierucci and G. B. Ferraris (Amsterdam, Netherlands: Elsevier), 691–696.

Thema, M., Bauer, F., and Sterner, M. (2019). Power-to-Gas: electrolysis and methanation status review. *Renew. Sustain. Energy Rev.* 112, 775–787. doi:10.1016/j.rser.2019.06.030

Theurich, S., Rönsch, S., and Güttel, R. (2019). Transient flow rate ramps for methanation of carbon dioxide in an adiabatic fixed-bed recycle reactor. *Energy Technol.* 8, 1901116. doi:10.1002/ente.201901116

Thunman, H., Seemann, M., Berdugo Vilches, T., Maric, J., Pallares, D., Ström, H., et al. (2018). Advanced biofuel production via gasification—lessons learned from 200 man-years of research activity with Chalmers' research gasifier and the GoBiGas demonstration plant. *Energy Sci. Eng.* 6, 6–34. doi:10.1002/ese3.188

Witte, J., Calbry-Muzyka, A. S., Hottinger, P., Biollaz, S. M. A., and Schildhauer, T. J. (2019). Demonstrating direct methanation of real biogas in a fluidized bed reactor. *Appl. Energy* 240, 359–371. doi:10.1016/j.apenergy.2019.01.230

Witte, J., Settino, J., Biollaz, S. M. A., and Schildhauer, T. J. (2018a). Direct catalytic methanation of biogas—part I: new insights into biomethane production using rate-based modelling and detailed process analysis. *Energy Convers. Manag.* 171, 750–768. doi:10.1016/j.enconman.2018.05.056

Witte, J., Kunz, A., Biollaz, S. M. A., and Schildhauer, T. J. (2018b). Direct catalytic methanation of biogas—part II: techno-economic process assessment and feasibility reflections. *Energy Convers. Manag.* 178, 26–43. doi:10.1016/j.enconman.2018.09.079

Younas, M., Kong, L. L., Bashir, M. J. K., Nadeem, H., Shehzad, A., and Sethupathi, S. (2016). Recent advancements, fundamental challenges, and opportunities in catalytic methanation of CO_2. *Energy Fuel.* 30 (11), 8815–8831. doi:10.1021/acs.energyfuels.6b01723

Zhang, X., Witte, J., Schildhauer, T., and Bauer, C. (2020). Life cycle assessment of power-to-gas with biogas as the carbon source. *Sustain. Energy Fuels* 4, 1427–1436. doi:10.1039/c9se00986h

Conflict of Interest: The authors declare that the research was conducted in the absence of any commercial or financial relationships that could be construed as a potential conflict of interest.

Advantages of publishing in Frontiers

OPEN ACCESS
Articles are free to read for greatest visibility and readership

FAST PUBLICATION
Around 90 days from submission to decision

HIGH QUALITY PEER-REVIEW
Rigorous, collaborative, and constructive peer-review

TRANSPARENT PEER-REVIEW
Editors and reviewers acknowledged by name on published articles

Frontiers
Avenue du Tribunal-Fédéral 34
1005 Lausanne | Switzerland

Visit us: www.frontiersin.org
Contact us: frontiersin.org/about/contact

REPRODUCIBILITY OF RESEARCH
Support open data and methods to enhance research reproducibility

DIGITAL PUBLISHING
Articles designed for optimal readership across devices

FOLLOW US
@frontiersin

IMPACT METRICS
Advanced article metrics track visibility across digital media

EXTENSIVE PROMOTION
Marketing and promotion of impactful research

LOOP RESEARCH NETWORK
Our network increases your article's readership